https://doi.org/10.35662/unine-thesis-2664

UNIVERSITÉ DE
NEUCHÂTEL

Doctoral Dissertation

Modeling heat and fluid flow in discrete fracture networks: Application to fluid-driven seismicity and engineered geothermal systems

Gunnar Jansen

Accepted on the recommendation of

Prof. Dr. Stephen Andrew Miller
Centre for Hydrogeology and Geothermics
Université de Neuchâtel

Prof. Dr. Benoît Valley
Centre for Hydrogeology and Geothermics
Université de Neuchâtel

Prof. Dr. Thomas Driesner
Institute of Geochemistry and Petrology
ETH Zürich

Defended on March 14, 2018

Gunnar Jansen
Modeling heat and fluid flow in discrete fracture networks: Application to fluid-driven seismicity and engineered geothermal systems
Doctoral Dissertation, March 14, 2018

Université de Neuchâtel
Faculty of Science
Centre for Hydrogeology and Geothermics
Laboratory for Geothermics and Geodynamics
Rue Emile-Argand 11
2000 Neuchâtel

UNIVERSITÉ DE
NEUCHÂTEL

Faculté des Sciences
Secrétariat-décanat de Faculté
Rue Emile-Argand 11
2000 Neuchâtel – Suisse
Tél : + 41 (0)32 718 21 00
E-mail : secretariat.sciences@unine.ch

IMPRIMATUR POUR THESE DE DOCTORAT

La Faculté des sciences de l'Université de Neuchâtel
autorise l'impression de la présente thèse soutenue par

Monsieur Gunnar JANSEN

Titre:

"Modeling heat and fluid flow in discrete fracture networks: Application to fluid-driven seismicity and engineered geothermal systems"

sur le rapport des membres du jury composé comme suit:

- Prof. Stephen A. Miller, directeur de thèse, Université de Neuchâtel, Suisse
- Prof. ass. Benoît Valley, co-directeur de thèse, Université de Neuchâtel, Suisse
- Prof. Thomas Driesner, ETH Zürich, Suisse

Neuchâtel, le 19 avril 2018

Le Doyen, Prof. R. Bshary

Abstract

Understanding the dynamics of naturally fractured systems and fractured reservoirs in terms of flow, heat transport and fracture stability (e.g. earthquakes) is important for a range of applications including geothermal systems, waste water injection and natural fluid-driven seismicity. Many numerical codes exist that can simulate aspects of these dynamics, but in general require either expensive licences or their utility is limited mostly to the developers. In this thesis I present an open source MATLAB package for efficient numerical simulations of the coupled processes in fractured systems. I take advantage of the embedded discrete fracture model that accounts for discrete fractures that are computationally efficient.

In a numerical thermo-elasticity study, I investigate the effect of cold fluid injection on the reservoir and the resulting thermal stress change on potential shear failure in the reservoir. I observe a strong influence of the hydraulic reservoir properties on thermal stress propagation. I also find that thermal stress change can lead to induced shear failure on non-optimally oriented fractures. The results suggest that thermal stress changes should be taken into account in all models for long-term fluid injections in fractured reservoirs.

Furthermore, I use the developed model to investigate an earthquake sequence that occurred in Mogul west of Reno, Nevada, USA in late February 2008. It culminated in a magnitude 4.9 main-shock after a foreshock-rich period of approximately 2 months on a previously unidentified fault structure. Here I show that the foreshock sequence may have been driven by a fluid pressure intrusion into this preexisting structure and find a strong correlation between high fluid pressure fronts and foreshock hypocenters.

Finally, I present a simple and efficient algorithm to generate hexahedral meshes from a geological model to be used in numerical simulation tools. Using binary space partitioning of the input geometry and octree refinement on the grid, a successive increase in accuracy of the mesh is achieved. The algorithm provides a new method for hexahedral mesh generation in geological settings. It generates high accuracy discretizations with cell counts suitable for state-of-the-art subsurface simulators.

Keywords: Geothermal Energy, numerical modeling, heat transport, fluid flow, discrete fracture networks, fluid-driven seismicity, hexahedral mesh generation

Résumé

La compréhension de la dynamique des systèmes naturels et des réservoirs fracturés en termes des écoulements, des transferts de la chaleur ou de stabilité de fractures (p. ex. les tremblements de terre) est importante pour diverses applications telles que les systèmes géothermiques et la séismicité naturelle induite par des fluides. Aujourd'hui, beaucoup de codes numériques existent pour simuler certains aspects de ces dynamiques, mais en général, ils sont très couteux ou alors leur utilisation n'est possible que par leurs développeurs eux-mêmes. Dans cette thèse, je présente une solution open-source MATLAB efficace pour des simulations numériques de processus couplés dans les systèmes fracturés. J'utilise le modèle des fractures discrètes intégrées.

Dans une étude numérique thermoélastique, je cherche à comprendre l'effet de l'injection de fluides froids dans un réservoir plus chaud et plus spécifiquement les changements des contraintes associées aux variations de température. Ces changements induisent des ruptures en cisaillement dans le réservoir. J'ai observé une influence très forte des propriétés hydrauliques du réservoir sur l'évolution des contraintes thermiques. De plus, j'ai trouvé que le changement des contraintes thermiques peut conduire à du cisaillement sur des fractures orientées non optimalement pour la rupture.Ces résultats suggèrent que les changements des contraintes thermiques devraient être pris en compte dans tous les modèles lors d'injections de fluides de longue durée dans des réservoirs fracturés.

J'utilise le modèle développé pour comprendre une séquence de tremblements de terre qui prit place à l'Ouest de Reno, Mogul, Nevada, aux États-Unis à la fin février 2008. Après 2 mois de séismes précurseurs répétés près d'une structure de faille inconnue préalablement, un tremblement de terre de magnitude 4.9 a eu lieu. Ici, je montre que la séquence de séismes précurseurs a pu être engendrée par l'intrusion de fluides à haute pression dans la structure de faille préexistante et j'ai trouvé une forte corrélation entre le front de pression et l'hypocentre des événements sismiques.

Finalement, je présente un algorithme simple et efficace pour générer des maillages hexahedraux à partir d'un modèle géologique utilisable par n'importe quels simulateurs numériques. En utilisant la méthode de «binary space partitioning» et d'«octree refinement» sur la géométrie importée, un maillage précis est créé. L'algorithme fournit une nouvelle méthode pour la création de maillages hexahedraux pour toutes configurations géologiques.

Mots clés: systèmes géothermiques, simulations numériques, transport de chaleur, écoulement des fluides, fractures discrètes, séismicité induite par des fluides, génération des meillages hexahedraux

Acknowledgement

I would like to express my gratitude to Prof. Stephen A. Miller for supervising my doctorate, and his guidance and support throughout many long and regular discussions during my work at the Centre for Hydrogeology and Geothermics (CHYN). I admire his enthusiasm and refreshing look on science and the friendly atmosphere he creates including a healthy respect for personal free time that allows me to be both creative and productive.

Thanks are due to Prof. Benoît Valley who has always had an open ear for my questions despite a busy schedule and provided me with advice and views from applied geophysics and engineering.

I thank Prof. Thomas Driesner for valuable discussions on various occasions in relation to my project, the management of the joint research project financing my work, and last but not least for accepting to be part of my doctoral defense jury.

Additional thanks go to all my colleagues at the CHYN. In particular, I want to express my gratitude to Reza, my personal French teacher and good friend.

Further thanks are due to my friends in Bern, Katja, Elena, Marius, Eva, Matthias, Amadeo, Lisa, Dominik and Lorenz, for countless good memories.

I would like to thank my family for their encouragement and guidance in life.

Finally, I am especially thankful to Marilena whose support over the last years was invaluable. She is always there for me, gives me comfort and peace when times are tough and brings joy to my life.

Contents

Introduction

1

> *A journey of a thousand miles started with a first step.*
>
> — **Lao Tzu**

The energy transition motivated by climate change and nuclear phaseout, turning away from fossil fuels and nuclear power, leads to renewable and mainly carbon-free energy production. Geothermal energy provides a renewable and sustainable energy source in this context. It is energy in form of heat produced continuously by natural radioactivity in the crust and heat exchange with the mantle that can be accessed at natural appearances such as volcanoes, geysers and hot springs or by a well-placed borehole. The name geothermal is constituted from the greek words *geo* ("earth") and *therme* ("heat"). Over 99% of our planet exhibits temperatures above 1000°C. On average, only the uppermost 3km are colder than 100°C (Fridleifsson et al., 2008). This corresponds to an average geothermal gradient in the upper crust of 33°C/km or equally an increase of 1°C with each 30m depth.
The world-wide use of geothermal energy is rapidly growing (Bertani, 2007; Bertani, 2016). Depending on their depth, heat transported with water or steam from geothermal energy occurrences or 'geothermal reservoirs' can be used for domestic hot water, district heating, process heat for agriculture and industry and power production. In case of *hydrothermal* occurrences we can use hot water directly from water-bearing layers. *Petrothermal* occurrences on the other hand are characterized by temperatures at depth favorable for electricity production and heating but only limited water content. In this case, cold water is injected into the deep reservoir where the water circulates along cracks and fractures and is heated by the surrounding rock before it is pumped back to the surface.

While many of the natural hydrothermal occurrences are geographically limited, geothermal potential in petrothermal reservoirs is widely available at depths between 2 - 6km . However, petrothermal reservoirs often consist of dry crystalline or dense sedimentary rocks, which do not have high enough natural permeability. Therefore, they require stimulation in order to create artificial permeability through a connected fracture network (Breede et al., 2015). Due to the fact that stimulation is required, these systems are often referred to as enhanced or engineered geothermal systems (EGS). The foundation for EGS was set by experimental studies at the Los Alamos National Laboratory where the "hot dry rock" concept of petrothermal energy production was investigated in the 1970s (Tester et al., 2006). Ever since it has been applied around the world in numerous projects with varying success (e.g. Chen and Wyborn, 2009; Häring et al., 2008; Hickman and Davatzes, 2003; Genter et al., 2010; Kelkar et al., 2016).

Despite its rather long history, technical, economical and social challenges remain with the development of a successful engineered geothermal system. Especially the stimulation or reservoir creation phase is associated with many of the challenges. During this phase, cold fluid is injected into the fractured rock in order to enhance permeability. This is achieved by inducing rock failure due to the high injection pressure and thermal rock contraction. Rock failure, or more specifically the generation of new fractures or the shearing of existing fractures, creates irreversible new or enhanced flow paths (permeability) but also triggers seismicity. Most of the induced seismicity is microseismic and not felt by the local population. However, moderate but strongly felt earthquakes may occur, as was the case in Soultz-sous-

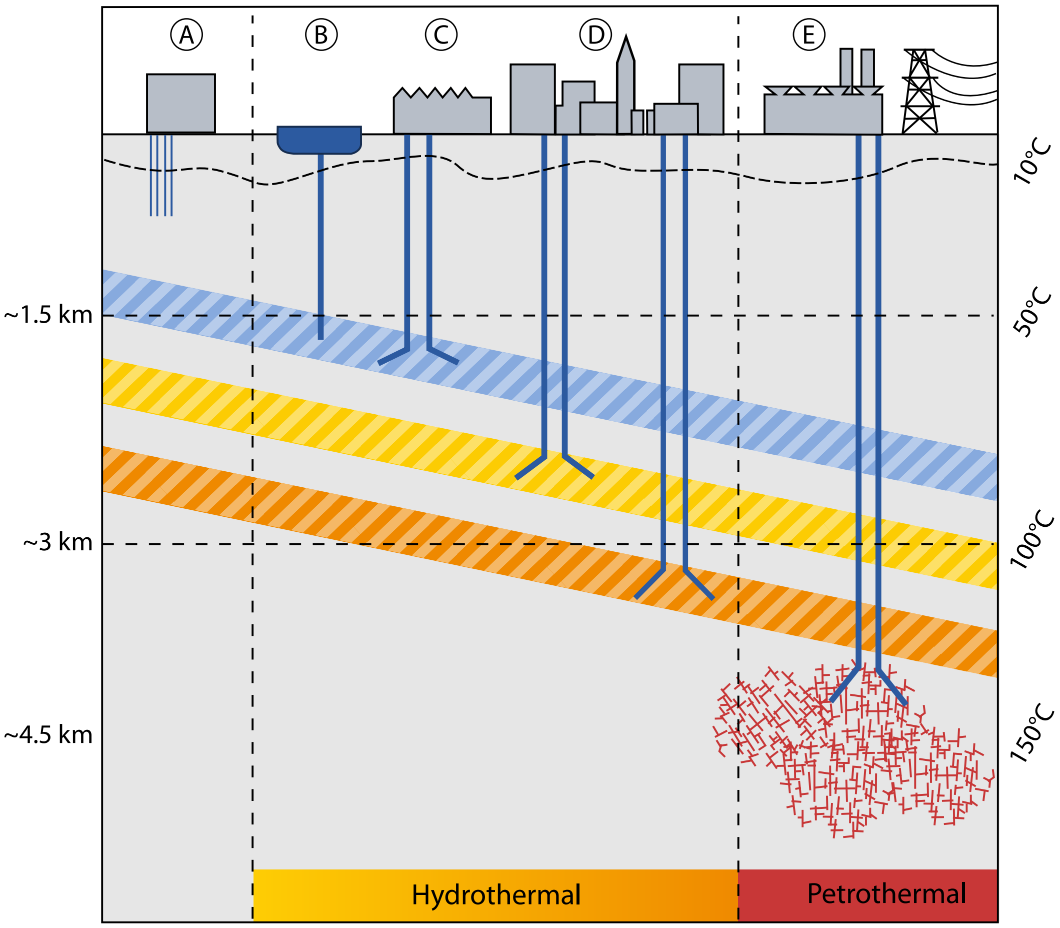

Figure 1.1: Depending on depth geothermal energy has many applications. At shallow depths geothermal energy from hydrothermal reservoirs is used for domestic heat pumps (A). Direct use of geothermal energy at intermediate depths include (B) thermal springs, (C) agricultural/industrial heat and (D) district heating. At large depths, petrothermal reservoirs with >120°C can be utilized for power production (E). Modified from Geothermie-Schweiz.ch, (2018)

Figure 1.2: The world's main hot temperature zones where geothermal power can be harnessed from hydrothermal reservoirs. The zones are located along active plate boundaries or hot spots. Large parts coincide with the *Ring of Fire* in the basin of the Pacific ocean that is associated with numerous earthquakes and volcanic arcs. Based on information from the Icelandic National Energy Authority.

Forêts, 2003 and Basel, 2006 (Majer et al., 2007). This has led to a major concern in the population and raised the issue of public acceptance (Kraft et al., 2009). Additional challenges include exploration methods for deep geothermal resources, deep geothermal drilling technology and reservoir assessment (Rybach, 2010) as well as economical challenges associated with the uncertainty of success in EGS (Gehringer and Loksha, 2012). Nevertheless, by overcoming these challenges, engineered geothermal systems can provide an important contribution in the carbon-free energy production era.

If fluids are circulating in natural faults and fractures, fluid-driven seismicity can occur and actually might be a primary driver of earthquake cycles (Miller, 2013). The significance of fluids in many tectonic processes mostly by the reduction of effective normal stress through high pore pressure has been long recognized (e.g. Hubbert and Rubey, 1959; Nur and Booker, 1972; Hill, 1977). Throughout the scientific literature many fluid-driven earthquake sequences have been documented for example in the Apennines through the release of CO_2 (Miller et al., 2004; Chiarabba et al., 2009; Lucente et al., 2010; Terakawa et al., 2010). Other sequences in countries around the world include Japan (Sibson, 2007; Sibson, 2009; Wang et al., 2012), Ethiopia (Noir et al., 1997) and Sumatra (Waldhauser et al., 2012). Swarms are observed in volcanic environments, hydrothermal systems, and other active geothermal areas. Fluids are certainly involved in these sequences as suggested by studies on the

Bohemian swarms (Fischer and Horálek, 2003; Heinze et al., 2017), Mammoth Mountain (Shelly and Hill, 2011), Yellowstone (Evans et al., 2010) and the East African Rift (Lindenfeld et al., 2012). However, the physical processes connected with the appearance and dissipation of these earthquake swarms is not fully understood due to the complex interactions and feedbacks between fracturing, fluid flow, heat transport and chemical reactions.

Numerical modeling can be a valuable investigation tool for both EGS technology and natural fluid-driven seismicity. Understanding the underlying processes & phenomena and describing them quantitatively is crucial to overcome the challenges described above. In addition to invaluable laboratory and field experimentation, mathematical modeling provides insight into these phenomena. While initially scientists were able to address these problems analytically, it has become necessary for some time now to use numerical modeling to achieve further understanding of the remaining questions (Ismail-Zadeh and Tackley, 2010). This is particularly true for naturally fractured systems with their high degree of inherent complexity. Hence, this thesis seeks to advance our understanding of such systems by numerical modeling.

Thesis Structure

This thesis is structured as follows: Chapter 2: 'Theoretical concepts & related work' lays ground for the work presented in Chapters 3-6 and introduces basic physical concepts for numerical modeling of flow and heat transport in fractured porous media and its challenges as well as numerical discretization of geological models. The contents of Chapters 3 - 6 are presented below as short summaries of their corresponding scientific publication. As each of the Chapters 3 - 6 is a complete research article, there will be sporadic repetitions. Wherever possible I deviated from the original scientific publication and refer to appropriate sections throughout the thesis in order to reduce the repetition of the physical method and used methods. The concluding chapter of my thesis is Chapter 7 and provides a summary of the findings as well as propositions for future work.

Chapter 3:
A MATLAB package for thermo-hydraulic modeling and fracture stability analysis in fractured reservoirs

In this chapter I present the implementation and validation of an open source MATLAB package for efficient numerical simulations of the coupled processes in fractured systems. I take advantage of the embedded discrete fracture model that accounts for discrete fractures in a computationally efficient manner. I perform a series of numerical benchmark experiments to validate the implemented approach against established numerical methods. Finally, I use a simplified geomechanical model and an integrated fracture stability analysis that allows estimating the potential for shear stimulation, and thus a mechanistic assessment of induced seismic risk during stimulation. The open source distribution of the source code and results can be used as a blue print for the re-implementation of the method in a high performance computing (HPC) framework or as a standalone simulation package for investigating TH(m) problems in geothermal reservoirs. The code presented in this chapter can also be further developed by the scientific community.

Chapter 4:
On the role of thermal stresses during hydraulic stimulation of geothermal reservoirs

Massive quantities of fluid are injected into the subsurface during the creation of an Engineered Geothermal System (EGS) to induce shear fracture for enhanced reservoir permeability. In this chapter of my thesis, I analyze the effect of cold fluid injection on the reservoir and the resulting thermal stress change on potential shear failure in the reservoir. I use the methodology presented in Chapter 3 for the coupled simulation of fluid flow, heat transport and thermo-elastic stress changes in a fractured reservoir. I perform a series of numerical experiments to investigate the effects of fracture and matrix permeability as well as fracture orientation on thermal stress changes and failure potential. Finally, I analyze thermal stress propagation in a hypothetical reservoir for the spatial and temporal evolution of possible thermo-hydraulic induced shear failure. I observe a strong influence of the hydraulic reservoir properties on thermal stress propagation. I also find that thermal stress change can lead to induced shear failure on non-optimally oriented fractures. The results suggest that thermal stress changes should be taken into account in all models for long-term fluid injections in fractured reservoirs.

Chapter 5:
Fluid pressure triggered foreshock sequence of the 2008 Mogul earthquake sequence

In Mogul west of Reno, Nevada, USA in late February 2008 an earthquake sequence occurred that culminated in a magnitude 4.9 main-shock after a foreshock-rich period of approximately 2 months on a previously unidentified fault structure. In this chapter I show that the foreshock sequence may have been driven by a fluid pressure intrusion. To this end I use 1082 previously calculated earthquake focal mechanisms to infer the local stress field as well as 1408 relocated foreshock events to determine the required excess fluid pressure field in the source region of the Mogul earthquake sequence to trigger these events. The model of nonlinear pore-pressure diffusion developed throughout this thesis is used to model the fluid flow in a highly fractured subsurface. I find a strong correlation between high fluid pressure fronts and foreshock hypocenters suggesting a natural fluid-driven earthquake sequence.

Chapter 6:
Simple and fast generation of structured hexahedral meshes for improved subsurface simulations

This chapter introduces a new, simple and efficient algorithm to generate hexahedral meshes to be used in simulation tools based on the finite element, finite volume or finite difference methods. The algorithm uses generic STL files describing a geological model. Using binary space partitioning of the input geometry and octree refinement on the grid, a successive increase in accuracy of the mesh is achieved. I present the theoretical basis as well as the implementation procedure for three geological models with varying complexity, providing the basis on which the algorithm is evaluated. The presented algorithm generates high accuracy discretizations with cell counts suitable for state-of-the-art subsurface simulators and provides a new method for hexahedral mesh generation in geological settings.

Theoretical concepts & related work

2

> *The aim of science is... a comprehension, as complete as possible... and... the accomplishment of this aim by the use of the minimum of primary concepts and relations.*
>
> — **Albert Einstein**

The relevance of fractures and their influence on flow and transport covers a wide area, ranging from subsurface water, oil, gas and geothermal reservoirs to storage of nuclear and hazardous wastes as well as geotechnical applications such as mining and tunneling. Research on fracture flow and transport has mainly been motivated by the need for safe repositories for nuclear wastes (Dietrich et al., 2005). Insight into fundamental processes influencing flow and transport in fractured rock was gathered in many study sites including the Grimsel rock laboratory in Switzerland (Dietrich et al., 2005; Majer et al., 1990). Characterization of fractured rock systems is one of the biggest challenges for geologists. Comprehensive reviews on the current state of research on the geological characterization of such systems are available. Such reviews include various aspects such as the effect of heterogeneity, the issue of scaling (e.g. Wang, 1991), as well as the fundamentals of flow and transport through fractured rock systems (e.g. Evans et al., 2001; Bodvarsson et al., 2003; Dietrich et al., 2005). Here I focus on the modeling concepts in fractured porous systems.

Natural geological systems are generally highly complex in both geological structure and the physical processes occurring within. It is extremely difficult to describe such a system in all its detail. Therefore, a conceptual model representing the system's most relevant structures and processes on a given scale is designed. Often a mathematical model is required in order to understand the physical processes in detail. However, analytical solutions are generally not available and the solution is found through numerical models. This transformation inevitably leads to a simplification of the real system. Hence, it is essential to keep in mind that a model is merely an approximation of reality. Any results obtained by the model have to be interpreted with respect to the assumptions and concepts in order to asses its results correctly (Dietrich et al., 2005).
Fractured systems conceptually consist of two distinct separate media, the fractures and the matrix. Different types of reservoirs can be defined that depend on their properties (Nelson, 2001). In EGS, two cases typically prevail:

1. Fractured systems with a low porosity matrix where both the permeability and the storage capacity of the rock mass are controlled by the fractures (cf. type 1 in Nelson, 2001)
2. Fractured *porous* systems with sufficient matrix porosity such that fluid storage is dominated by the matrix while the fractures contain only a small fraction of the fluid but control the permeability (cf. type 2 in Nelson, 2001).

The model developed throughout this thesis is generally concerned with fractured *porous* rock, which can be divided into three components (Dietrich et al., 2005):

- *Fracture network* - A network of (partially) intersecting fractures. The hydraulic properties are characterized by the distribution of fracture size, permeability, spacing and orientation
- *Fracture filling* - Individual fractures may be open or filled with mineral deposits. Open fractures generally represent major fluid pathways while depending on the filling material's composition filled fractures can also act as flow barriers
- *Rock matrix* - The influence of the matrix depends on the permeability contrast between fracture network and matrix. Small scale rock fractures (fissures) can enhance the rock matrix permeability significantly, which in this case is sometimes referred to as *damaged matrix*.

In the following the model concepts of fractured porous media are discussed. The focus lies on the basic ideas and challenges as the coupled thermo-hydraulic model that is used in this thesis' studies is described in detail in Chapter 3. Details on the numerical method and its implementation are omitted at this point and the reader is referred to the following chapters.

2.1 Modeling flow and transport in fractured porous media

As discussed in the introduction to this chapter, a model is always an approximation of reality. Different conceptual models exist for the description of fractured porous media. The appropriate model concept is chosen based on the scale and purpose of the model. In this thesis a combination of the continuum scale and the discrete fracture scale is used. Their basic structures are outlined in this section.

On the continuum scale the concept of the representative elementary volume (REV) as defined by Bear, (1972) is fundamental for a mathematical description of fluid flow and transport in porous media. Through volume averaging, micro-scale properties of the porous medium such as pore-space geometry are represented by equivalent continuum properties on a larger scale (e.g. porosity). The size of the REV has to

be chosen with care so that small-scale fluctuations are averaged but larger spatial variability remains.
A widely used possibility to describe fractured systems on the continuum scale is to transform the matrix and fracture systems on different scales into separate equivalent continua. This approach originally presented by Barenblatt et al., (1960) is mainly used on large scales. Flow and transport between the continua is represented through exchange terms leading to the so called double continuum models. Depending on the type of homogenization used the models are commonly also referred to as double porosity and double permeability models. Double continuum models require an appropriate homogenization of the parameters and exchange terms that are capable of describing the correct physical behavior of the system.

Some natural systems contain dominant fracture networks or shear zones that control flow and transport. In this case it is feasible to describe these features specifically, neglecting the surrounding rock matrix. The resulting models that consider each fracture individually are called *discrete fracture models* (Dietrich et al., 2005). In discrete fracture models the parallel-plate concept is often applied. Natural fractures generally have rough surfaces with asperities. Such asperities are responsible for an irreducible fracture aperture (Figure 2.1a). Conceptual models on the other hand describe fractures often as smooth surfaces or parallel plates between which fluid flow and transport occur. The concept can be applied locally, maintaining a certain variability through the fracture, or globally, leading to a uniform fracture aperture (Figure 2.1b& c). Although it is clear that this approach is a strong simplification of nature, other methods have not yet found general acceptance (Berkowitz, 2002; Dietrich et al., 2005). Based on the parallel-plate model a relationship between fracture aperture and permeability known as the *Cubic law* was defined (Romm, 1966; Witherspoon et al., 1980).

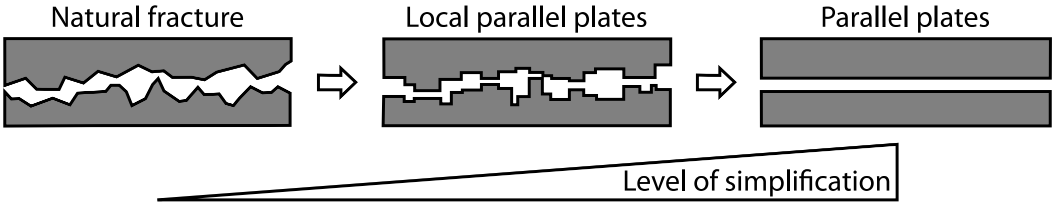

Figure 2.1: From nature to parallel plate model. A natural fracture has a rough surface due to asperities. The local parallel plate model reduces the complexity while maintaining some of the initial heterogeneity. In the parallel plate model all the aperture variability is removed and a single averaged value, representative for the whole fracture, is used. After Dietrich et al., (2005).

In situations where fractures as well as the matrix play a significant role for fluid flow and transport, the domain may not be homogenized accurately by any of the previous approaches. In this case a conceptual model that uses a combination of the continuum model and the discrete fracture model may be preferable. The numerical model based on the embedded discrete fracture model (EDFM) developed and applied in this thesis is such a combined model. The methodology was first introduced by Lee et al., (2001) for single phase problems and later extended through multiple scientific works (e.g. Li and Lee, 2008; Hajibeygi et al., 2011; Karvounis, 2013). The embedded fracture model and presents a suitable tool to study flow and transport in fractured porous systems. The embedded discrete fracture model and its implementation are described in detail in Chapter 3.

2.1.1 Mathematical model for fluid flow

Fluid motion in the porous subsurface is governed by the conservation equations of mass, momentum and energy. Additionally, a set of constitutive equations for the fluid and the porous rock is involved. In this section, the transport of a single phase fluid that occupies the entire void space in a porous medium is considered. A *single phase fluid* describes a fluid that consists of a single component or a homogeneous mixtures of components.

The principle of mass conservation states that for any closed system, the mass of the system must remain constant over time. With the assumption that the mass fluxes due to dispersion and diffusion are sufficiently small compared to the advective mass flux the *mass conservation equation* can be obtained:

$$\frac{\partial \phi \rho}{\partial t} = -\nabla \cdot (\rho \mathbf{v}) + q, \tag{2.1}$$

where $\phi\,[-]$ is porosity, $\rho\,[\frac{kg}{m^3}]$ is the fluid density, $\mathbf{v}\,[\frac{m}{s}]$ the fluid velocity and $q\,[\frac{kg}{s}]$ a source term. The fluid velocity can be replaced by an equation relating it to fluid and rock properties. Equation 2.1 is also known as the *continuity equation*.

Generally, conservation of momentum is governed by the Navier-Stokes equations. For the low velocity flow in porous materials the equations are simplified. Often, the *momentum conservation equation* is given in the form of Darcy's law (Darcy, 1856). This empirically derived law indicates a linear relationship between the fluid velocity relative to the solid and the pressure gradient.

$$\mathbf{v} = -\frac{k}{\mu} \nabla p, \tag{2.2}$$

where $k\ [m^2]$ is the permeability, $\mu\ [\frac{1}{s}]$ the fluid viscosity and p [Pa] is the fluid pressure. The theoretical basis for Darcy's law was provided by Whitaker, (1966), Bear, (1972) and Scheidegger, (1974). An alternative equation is the Forchheimer equations for high velocity flow

$$\nabla p = -\mathbf{v}\frac{\mu}{k} - \frac{\rho}{k_1}\mathbf{v}^2 \tag{2.3}$$

where k_1 is known as inertial permeability factor. The Forchheimer equation is considered appropriate for flows with Reynolds numbers greater than 1 - 10 (Nield and Bejan, 2006). Another alternative is the use of the Brinkman equation, which applies to both porous and non-porous flow:

$$\nabla p = -\mathbf{v}\frac{\mu}{k} + \bar{\mu}\nabla^2\mathbf{v} \tag{2.4}$$

where $\bar{\mu}$ is an effective viscosity. In most applications Brinkman's equation reverts back to Darcy's equations for flow in porous media, since the last term then normally is negligible. It reduces to Stoke's equation for channel flow because the Darcy term of the equation may be neglected in this case.

In the following the Darcy equation is assumed valid for the description of momentum conservation in porous media.

Substituting Darcy's equations (2.2) into the mass conservation equation (2.1) and accounting for gravity yields

$$\frac{\partial(\phi\rho)}{\partial t} = \nabla\cdot(\rho\frac{k}{\mu}\nabla p - \rho g) + q. \tag{2.5}$$

The left hand side (LHS) of this equation may be expanded as

$$\frac{\partial(\phi\rho)}{\partial t} = \rho\frac{\partial\phi}{\partial t} + \phi\frac{\partial\rho}{\partial t}. \tag{2.6}$$

Since porosity and density are functions of pressure only at a constant temperature, the expressions are expanded such that

$$\frac{\partial\phi}{\partial t} = \frac{\partial\phi}{\partial p}\frac{\partial p}{\partial t} \tag{2.7}$$

and

$$\frac{\partial\rho}{\partial t} = \frac{\partial\rho}{\partial p}\frac{\partial p}{\partial t}. \tag{2.8}$$

The pressure dependence of the porosity is expressed through the rock compressibility $\beta_r\,[Pa^{-1}]$ at constant temperature (e.g. Segall and Rice, 1995):

$$\beta_r = \frac{1}{\phi}\left(\frac{\partial\phi}{\partial p}\right)_T. \tag{2.9}$$

A similar relationship can be defined for the fluid compressibility $\beta_f\,[Pa^{-1}]$ at constant temperature:

$$\beta_f = -\frac{1}{V}\left(\frac{\partial V}{\partial p}\right)_T = \frac{1}{\rho}\left(\frac{\partial\rho}{\partial p}\right)_T, \tag{2.10}$$

where V stands for the volume occupied by the fluid. After substitution of these relationships into equations (2.7) and (2.8), equation (2.5) becomes:

$$\phi\rho\left(\beta_f+\beta_r\right)\frac{\partial p}{\partial t}=\nabla\cdot\left[\rho\frac{k}{\mu}(\nabla p-\rho_f g)\right]+q. \tag{2.11}$$

Using the definition of the fluid compressibility and the fact that fluid compressibility is generally very small, equation (2.11) translates to the *single phase flow equation for slightly compressible flow and rock*:

$$\phi\left(\beta_f+\beta_r\right)\frac{\partial p}{\partial t}=\nabla\cdot\left[\frac{k}{\mu}(\nabla p-\rho_f g)\right]+q. \tag{2.12}$$

2.1.2 Mathematical model for heat transfer

Heat transfer in porous media is mainly driven by two basic processes, thermal conduction and convection. Thermal conduction is the transfer of heat by microscopic collisions of particles without movement of the transferring medium. In thermal convection, heat is transferred by movement of fluids. Thermal convection takes place through advection, diffusion or both. Additional heat transfer mechanisms, such as thermal radiation and thermal dispersion exist. Their contributions may be significant in some special cases but their description is beyond the scope of this section. The fundamentals of heat transfer in porous media are also presented in e.g. Nield and Bejan, (2006).

The energy conservation equation expresses the first law of thermodynamics and governs heat transfer in a porous medium in form of a continuity equation. The continuity equation states that the rate of change for a scalar quantity, such as transfer of internal energy (*heat*), in a differential volume is given by flow and diffusion into and out of that volume along with the generation or consumption inside the volume.

Assuming a porous medium that is isotropic and where radiative effects, viscous dissipation and the work done by pressure change are negligible, the heat transfer equation for the solid phase is

$$(1-\phi)(c_{p_r}\rho_r)\frac{\partial T_r}{\partial t}=(1-\phi)\nabla\cdot(\lambda_r\nabla T_r)+(1-\phi)q_r. \tag{2.13}$$

Similarly the fluid phase can be expressed as

$$\phi(c_{p_f}\rho_f)\frac{\partial T_f}{\partial t}+\phi(c_{p_f}\rho_f)\mathbf{V}\cdot\nabla T_f=\phi\nabla\cdot(\lambda_f\nabla T_f)+\phi q_f. \tag{2.14}$$

The subscripts r and f refer to the solid (rock) and fluid phases, respectively. Additionally, the heat capacity $c_p\,[\frac{J}{kgK}]$, the thermal conductivity $\lambda\,[\frac{W}{mK}]$ and internal heat source $q\,[\frac{W}{m^3}]$ of solid and fluid are introduced. The fluid phase equation (2.14) has an additional term due to advective heat transfer that is negligible in the solid phase. The terms of equation (2.13) appear multiplied by the factor $(1-\phi)$ to account for the volume occupied by the solid. Similarly, equation (2.14) is multiplied by ϕ, which is the ratio of the volume occupied by fluid to the total volume. In the fluid phase heat transfer equation (2.14) $\mathbf{V}$ is the intrinsic velocity. Through the Dupuit-Forchheimer relationship it can be related to the Darcy velocity: $\mathbf{v} = \phi\mathbf{V}$. Local thermal equilibrium ($T_r = T_f = T$) can be assumed since the flow in porous media is usually sufficiently slow so that fluid and rock temperatures remain in equilibrium. This allows to express equations (2.13) and (2.14) in a single equation resulting in the *heat conservation equation* in a porous medium:

$$(\phi(c_{p_f}\rho_f)+(1-\phi)(c_{p_r}\rho_r))\frac{\partial T}{\partial t}+c_{p_f}\rho_f\mathbf{v}\nabla T-(\phi\lambda_f+(1-\phi)\lambda_r)\nabla^2 T = \phi q_f+(1-\phi)q_r \tag{2.15}$$

2.2 Challenges in modeling flow and transport

Modeling flow and transport in fractured porous systems is connected to a number of conceptual and computational challenges. One of the biggest challenges, excluding computational challenges, is probably the accurate formulation of the conceptual and corresponding mathematical models. It is obvious that any results obtained from a simulation based on a inaccurate conceptual model are highly questionable. In addition to the fact that conceptual and mathematical models are always a simplification of the complex natural system, multiple approaches can often be utilized to describe the same physical processes. An example for such different approaches was presented earlier in this chapter: The treatment of fractures in numerical models. Double continuum and discrete fracture methods are both used for the description of fractured porous media, yet they are fundamentally different. Both approaches are valid and provide important insight into processes involved in fractured systems. While a discrete fracture model is more suited to provide insight into e.g. aperture changes during hydraulic stimulation and heat exchange between fractures and surrounding matrix, a double continuum model is preferable when detailed information on the fracture network geometry are missing. In the end, the choice of the correct conceptual and mathematical model for the problem at hand is of the utmost importance.

In the following I will present some of the most important computational challenges in connection with flow and transport in fractured systems. Although the focus rests on EGS modeling, a broader field including CO_2 sequestration and nuclear waste deposits is facing similar issues. Additionally, experience shows that overcoming challenges related with one goal often provide unexpected solutions to other applications as well. Most of the challenges presented here were formulated by a working group of the International Partnership for Geothermal Technology (IPGT) and published in a review of Fairley et al., (2010).

Arguably the most important challenge and a research focus is the realistic, fully coupled thermo-hydro-mechanical (THM) modeling of the short-term reservoir performance. This includes reasonable reproduction of borehole stimulation data and reliable predictions of short to medium-term reservoir behavior (e.g. stimulated volume, transmissivity increase and induced seismicity). In order to overcome this challenge an appropriate conceptual model for simulating rock failure and growth of fractures has to be formulated.
On the other hand models are required that can provide insight into dissolution and precipitation processes. These thermo-hydro-chemical (THC) models are most important for the accurate assessment of medium to long-term reservoir behavior. Additionally realistic models of hydrothermal fluids such as saline waters ('brine') or supercritical CO_2 are necessary to accurately model water-rock interactions.
Although the mathematical description is often similar for two and three dimensional models, many modeling frameworks (including the one presented in this thesis) are implemented solely in two dimensions. This is mainly due to the enormous increase in computational effort required in 3D compared to 2D simulations and only rarely associated with limitations of the employed method. In many situations, valuable insight can be obtained from two dimensional modeling. However, in order to understand certain physical processes accurately a 3D model is essential. Tsang and Tsang, (1987) showed that preferential flow paths within natural exist that lead to channeling effects. Channeling can significantly effect the flow and therefore heat transport (e.g. Hirano et al., 2010; Ishibashi et al., 2015; Vogler et al., 2016). Only three dimensional models can be used to investigate channeling and its impact on the reservoir scale accurately.
With the recent advances in computing technology and a widespread availability of supercomputers, the need for numerical codes that are adapted to the simulation of realistic large scale domains arises. Especially high-resolution representations of geological complexities, discrete fractures and fracture networks are becoming increasingly important but are still computationally challenging. Equally challenging is the simulation of processes acting at very different timescales (e.g mechanical and chemical processes) in fully coupled thermo-hydro-mechanical-chemical (THMC) models that include all relevant processes on all time scales (Fairley et al., 2010). Many of today's modeling frameworks are not suited for modern parallel programming techniques that are required to meet these needs.

The challenges listed in this section are not exhaustive. There are other challenges associated with the mathematical description of physical processes as well as general challenges of scientific computing such as parallelization, accurate and stable solvers and visualization. The presented challenges are arguably the most important in modeling flow and transport in fractured porous media. Nonetheless, individual researchers may face other challenges altogether depending on their specific field. In any case novel approaches in simulating fractured porous media and the re-evaluation of existing methods will be inevitable to overcome these challenges.

2.3 Discrete fracture model types

A number of different discrete fracture models (DFM) can be found in literature. Contrary to double continuum methods, discrete fracture models use less assumptions regarding shape and properties of the fractures. Tube network approaches were among the first DFMs (Cacas et al., 1990; Dershowitz and Fidelibus, 1999), but generally neglect flow in the matrix. In consequence other methods that account for flow in the matrix have been developed in which the additional computational cost is outbalanced by the gained accuracy. Such discrete fracture models that treat fractures explicitly and account for flow in the matrix can be categorized into conforming and embedded DFMs. Figure 2.2 visualizes this classification that is based on how the matrix that surrounds discrete fractures is discretized. In conforming DFM approaches the boundaries of the matrix grid cells coincide with the shape of the fracture. In the most complex discrete fracture models, the realistic fracture shapes are fully resolved (Figure 2.2a). This requires an enormous amount of computational effort, which inhibits the simulation of realistic fracture networks. A lower dimensional fracture representation (Figure 2.1b & c) reduces the complexity of the fracture. Consequently, the computational cost is drastically reduced. Both conforming and embedded DFMs benefit from the lower dimensional representation. The main advantage of embedded approaches is that the boundaries of the matrix grid cells do not have to coincide with the shape of the fracture and thus a matrix grid cell may surround a fracture from both sides (Figure 2.2c). Numerous modeling frameworks based on the different types of discrete fracture models exist. Some of the modeling frameworks related to the work in this thesis are presented in the following.

2.4 Related work

Various modeling frameworks for the simulation of fractured porous media in general and geothermal reservoirs in particular exist. An exhaustive review of the current modeling frameworks is out of the scope of this section. Nevertheless, some better known modeling frameworks with a focus on flow and transport that are directly related to the work in this thesis are presented here. Literature reviews of current modeling approaches in geothermal reservoirs and hot dry rock systems

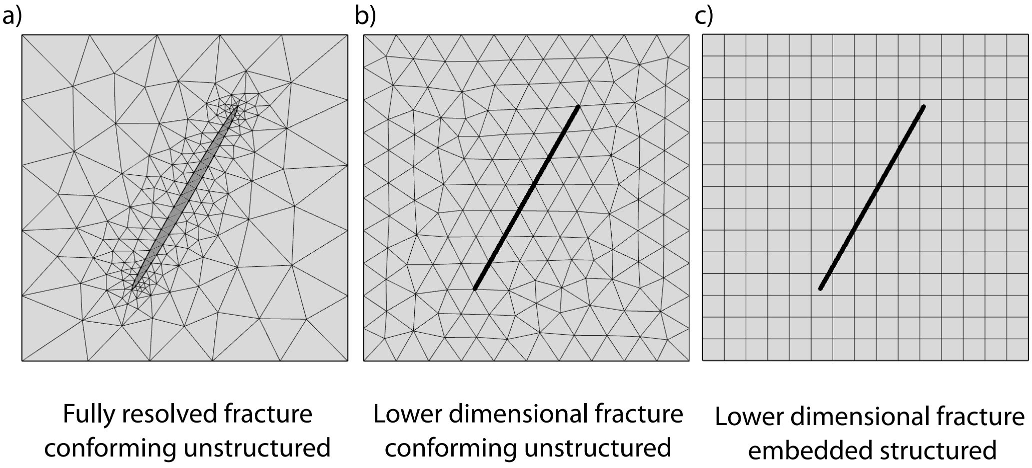

Figure 2.2: Different types of discrete fracture models. The complexity of the fracture representation decreases from left to right. The complexity reduction is accompanied by an significant increase in computational efficiency.

are presented by Willis-Richards and Wallroth, (1995), Sanyal et al., (2000), and O'Sullivan et al., (2001) and White and Phillips, (2015). Following Willis-Richards and Wallroth, (1995) models are classified into reduced and realistic fracture models. Reduced fracture models simplify the treatment of fractures as presented for the double continuum methods. A widely used modeling framework of this type is TOUGH2 that uses integral finite differences in a dual continuum model. It has successfully been applied in geothermal reservoir studies and a wide range of other applications (Pruess, 1991; Wu and Pruess, 2000; Pruess, 2004; Taron et al., 2009; Quinao and Zarrouk, 2018). The coupling of TOUGH2 and the geomechanical modeling framework FLAC has enabled simulations of EGS (Rutqvist et al., 2002; Benato and Taron, 2016). Other modeling frameworks that fall into this category are FEHM (Bower and Zyvoloski, 1997; Zyvoloski, 2007; Kelkar et al., 2014) and FALCON (Podgorney et al., 2010a). Both models have been applied in geothermal studies (e.g. Tenma et al., 2001; Tenma et al., 2003; Podgorney et al., 2010b; Xia et al., 2017).

Realistic fracture models on the other hand do not simplify fractures with respect to their position, orientation and shape. Nevertheless, depending on the type of model fractures are represented as lower dimensional features. In combination with a Darcy-like flow in the fracture this is usually considered an acceptable simplification and used in many DFMs (Kohl and Hopkirk, 1995; Jing et al., 2000; Karimi-Fard et al., 2003; Hajibeygi et al., 2011; Norbeck et al., 2014).

One such fracture network modeling framework is FRACSIM-3D, which includes fluid flow and heat transfer (Jing et al., 2000). In FRACSIM-3D, discrete fractures are treated as a 3D network of 2D planes, from which a representative porous medium of equivalent properties is derived. Strictly speaking the solution procedure belongs to the reduced methods. Since a fracture network can be imposed to derive the averaged properties it is nonetheless included here. It is the extension of a former code FRACSIM-2D (Sanyal et al., 2000) and has been used to model the Hijiori geothermal reservoir (Jing et al., 2014). FRACTure is a discrete-fracture, finite-element code for simulating the coupled hydraulic, thermal and mechanical behavior of fractured media (Kohl and Hopkirk, 1995). The Fluid flow can be modeled using Darcian or turbulent flow equations. Heat transfer includes heat conduction in the matrix and advective transport in the fractures. Thermoelastic and poroelastic effects are included in the porous matrix. Fracture aperture is non-linearly linked to ambient stress conditions. More recently a derivative called HEX-S was presented (Kohl and Mégel, 2007). Both codes have been used amongst others to model the Soultz EGS reservoir (Kohl et al., 2000; Kohl and Mégel, 2005) and geothermal heat storage (Rohner et al., 2005).

A relatively novel fractured reservoir code is GEOS that focuses on the simulation of hydraulic fracturing in the presence of a natural fracture network. The physical processes involved in hydraulic fracturing are addressed as separate modules: a finite element approach for geomechanics in the rock matrix, a finite volume approach for resolving hydrodynamics and linear elastic fracture mechanics elements to resolve fracture propagation (Fu et al., 2011). GEOS has been used to simulate thermal-drawdown induced flow channeling in geothermal reservoirs (Guo et al., 2016).

The code CSMP++, short for "Complex System Modeling Platform", employs a hybrid finite element - finite volume method where fractures are either fully discretized or represented as lower dimensional manifolds (Geiger et al., 2006; Matthäi et al., 2007b; Matthäi et al., 2007a; Coumou et al., 2008). It focuses on the accurate description of multiphase flow and transport. CSMP++ has been successfully applied to geothermal resources, CO_2 injection, oil& gas reservoirs, and used in studies on multiphase thermohaline convection and crack growth (Scott et al., 2015; Scott et al., 2016; Annewandter et al., 2013; Geiger-Boschung et al., 2009; Weis et al., 2014; Paluszny and Matthäi, 2009).

Certain frameworks and simulation platforms can use reduced as well as realistic fracture models. OpenGeoSys is an open-source, multi-platform modeling package based on the finite element method for the simulation of processes in porous and fractured media. It has been used to model the geothermal system performance in the Groß Schönebeck reservoir (Jacquey et al., 2016). Other application areas besides geothermal systems include CO_2 sequestration and waste deposition (Bauer et al., 2012; Rutqvist et al., 2009). A similar framework based on the finite volume method is pflotran that focuses on massively parallel simulation of reactive flow and transport processes (Hammond et al., 2014).

COMSOL Multiphysics and the MOOSE framework are two examples of finite element packages that can be used for a very wide range of numerical simulations (Comsol Inc., 2017; Gaston et al., 2009). Both frameworks include subsurface flow and transport capabilities that have been applied to geothermal systems as well (Saeid et al., 2013; Hu et al., 2017).

As the numerical framework developed throughout this thesis is using an embedded discrete fracture model (EDFM), the current state of research on these models is presented in the following. Embedded discrete fracture models are promising new techniques in modeling the behavior of naturally fractured systems. In these models large and therefore assumed important fractures are treated discretely as lower dimensional manifolds while small fractured are upscaled into the "damaged" matrix (cf. Figure 2.2). The embedded fracture model was first introduced by Lee et al., (2001) for single phase problems and later extended to two-phase flow (Li and Lee, 2008). Recently the method was extended to 3D multiphase problems (Moinfar, 2013). Hajibeygi et al., (2011) developed an embedded fracture model for multi-scale finite volume (MSFV) fracture modeling purposes. One shortcoming of the traditional EDFM is due to the fact that fracture volumes are surrounded only by a single matrix block. Low permeability fractures that act as flow barriers tend to become invisible in the traditional EDFM approach. However, this has just recently been addressed by a projection based embedded fracture method (Ţene et al., 2017). Similar approaches to the embedded discrete fracture method are presented in Sarda et al., (2001) and Vitel and Souche, (2007).

While the embedded multiphase flow methods are mainly directed at the extraction of oil and gas (Li and Lee, 2008; Moinfar, 2013; Shakiba, 2014; Xu, 2015), single phase implementations are also used in the study of geothermal reservoirs (Karvounis, 2013; Norbeck et al., 2016; Karvounis and Jenny, 2016). The first implementation of the heat transport equation in the EDFM can be found in Karvounis, (2013). The embedded fracture model has been applied in combination with a statistical approach to better understand and possibly forecast seismicity induced seismicity by fluid injection during the stimulation phase of an EGS (Karvounis et al., 2014; Karvounis and Wiemer, 2015).

Recently, progress has been made in accounting for deformation processes in embedded fracture models. Different approaches using boundary element methods, multi-point stress approximations (MPSA) and extended finite volume methods (XFVM) were proposed (Norbeck et al., 2016; Ucar et al., 2016; Deb and Jenny, 2016).

Norbeck et al., (2016) use linear fracture mechanics in order to describe the geomechanical processes related to reservoir stimulation, including hydraulic fracturing and shear stimulation. The work is based on the reservoir model introduced by McClure and Horne, (2013) and extended trough the EDF methodology. Fracture and matrix deformation is computed using the boundary element method.

In the work of Ucar et al., (2017), a recently developed cell-centered finite volume method Multi-Point Stress Approximation (MPSA) is used to approximate the fracture deformation in a linear elastic matrix (Ucar et al., 2016; Keilegavlen and Nordbotten, 2017). Fractures are included as internal boundary conditions to the momentum balance equation. However, poroelastic effects in the matrix are neglected (Ucar et al., 2017).

A similar approach is taken by Deb and Jenny, (2017) whom have developed an extended finite volume method (XFVM) in order to model shear failure in fractured reservoirs with a porous matrix. In the XFVM discontinuity basis functions are used to represent shear slip on the embedded fracture manifolds. In case of shear failure, an additional constraint for the frictional constitutive relation is solved.

All in all this sections shows that research on numerical simulation of fractured systems is a very active field. Statistics from peer-reviewed publication records show that the number of publications concerning discrete fracture methods is increasing since the late 1990s (Clarivate Analytics, 2017). The growing interest in engineered geothermal systems, CO_2 sequestration and enhanced oil recovery methods motivates further research on fractured systems and their simulation in the future.

3

A MATLAB package for thermo-hydraulic modeling and fracture stability analysis in fractured reservoirs

> *Talk is cheap. Show me the code.*
>
> — **Linus Torvalds**
> (Creator of the Linux kernel)

The contents of this section are submitted for publication as: Gunnar Jansen, Benoît Valley and Stephen A. Miller, "THERMAID - A MATLAB package for thermo-hydraulic modeling and fracture stability analysis in fractured reservoirs," to Computers & Geosciences. The package is distributed as open-source and can be obtained from `https://github.com/gujans/THERMAID`.

3.1 Introduction

A large fraction of the world's water and energy resources are located in naturally fractured reservoirs within the earth's crust. Understanding the dynamics of such reservoirs in terms of flow, heat transport and fracture stability is crucial to successful application of engineered geothermal systems (also known as enhanced geothermal systems, EGS) for geothermal energy production. Reservoir development characteristics such as permeability creation and induced seismicity largely depend on the properties of preexisting fractures, porosity, permeability and fracture orientation within the local stress field. One of the primary driving mechanisms for permeability creation in EGS involves shear failure induced by fluid injection at high pressures (Barton et al., 1995; Evans et al., 2005; Hickman and Davatzes, 2003). Along sections of the well that are free of natural fractures and in environments with low differential stress (e.g. small shear stresses), tensile fractures may develop if the injection pressure exceeds the minimal principal stress at the borehole wall and the tensile strength of the rock (e.g. fracking). Shear and tensile fracture propagation and reactivation are not exclusive and might occur simultaneously during the stimulation of the reservoir (McClure and Horne, 2014). Clearly, preexisting, critically stressed and optimally oriented fractures provide the most favorable conditions for enhancing permeability of EGS (Barton et al., 1995; Combs et al., 2004; Ghassemi and Kumar, 2007). Induced rock failure triggers micro-seismicity as new fractures

are forming and propagating or preexisting fractures are reactivated in shear. Induced seismicity at levels above that tolerated by the local population, in either frequency or magnitude, is a major concern in the development of an EGS. Reservoir stimulation itself changes the local stress field due to thermo- and poro-elastic effects as well as slip induced stress transfer. Thus fracture stability or criticality is likely to be very heterogeneous in space and time. Therefore, understanding the stress state and its changes in the fractured reservoir is of major importance in order to understand reservoir development and mitigate the risk of induced seismicity.
The basis for EGS are fractured reservoirs, which are usually geothermal plays of the "hot dry rock" type where the available water in the porous medium is considered negligible (Brown et al., 2012). These conditions are found primarily in metamorphic or igneous terrains with low permeability and porosity, containing fractures and faults that provide the major pathways for fluid flow (e.g. Fenton Hill, Soultz, Basel, Cooper basin and Desert Peak (Kelkar et al., 2016; Hooijkaas et al., 2006; Häring et al., 2008; Chen and Wyborn, 2009; Hickman and Davatzes, 2003)). In geothermal energy systems, the fracture's surfaces serve as the main heat exchanger. Fractured reservoirs can be considered to consist of two distinct separate media, the fractures and the matrix, and different types of reservoirs can be defined that depend on their properties (Nelson, 2001). In EGS, two cases typically prevail: 1) reservoirs with low porosity matrix for which both the permeability and the storage capacity of the rock mass are controlled by the fractures (cf. type 1 in (Nelson, 2001)) and 2) reservoir with sufficient matrix porosity such that fluid storage is dominated by the matrix while the fractures contain only a small fraction of the fluid but control the permeability (cf. type 2 in (Nelson, 2001)).

Simulation of flow and transport through fractured porous media is challenging due to the high permeability contrast between the fractures and the surrounding rock matrix. However, accurate and efficient simulation of flow through a fracture network is crucial in order to understand, optimize and engineer reservoirs. Even after decades of research, this is still a very active research topic. Additionally, accurate estimations of the fracture stability are necessary in order to predict permeability evolution and forecast induced seismicity. Discrete fracture models (DFM) have been developed to address the computational problem of scales for fluid flow and heat transport. Yet traditional conforming DFM, where the fractures are explicitly resolved by the numerical grid, suffer from computationally expensive pre-processing in the numerical grid generation and can encounter severe time step restrictions during the simulation when using explicit time-stepping and small cells around the fractures (Norbeck et al., 2014; Sandve et al., 2012).
An alternative approach uses the embedded discrete fracture models (EDFM), which treat fracture and matrix in two separate computational domains. The embedded fracture model was first introduced by Lee et al. for single phase problems and later extended to two-phase flow (Lee et al., 2001; Li and Lee, 2008). The embedded dis-

crete fracture model is a promising technique in modeling the behavior of enhanced geothermal systems. Karvounis, (2013) employs EDFM and a statistical approach to better understand and possibly forecast seismicity induced seismicity by fluid injection during the stimulation phase of an EGS. Norbeck et al. additionally model fracture deformation by linear fracture mechanics (Norbeck et al., 2016).

Slip tendency analysis is used in order to estimate fault reactivation potential in earthquake prone areas as well as fracture stability in geothermal reservoirs (e.g. Morris et al., 1996; Moeck et al., 2009). Slip tendency is the ratio of shear stress to effective normal stress on a surface (Morris et al., 1996), and fracture or fault reactivation is likely to occur when this ratio equals or exceeds the frictional sliding resistance. In general, the stress field is heterogeneous due to the contrast of mechanical properties and the previous slip history along fractures in the rock mass, and stability of the fractures is controlled by the local stress field. However, assessing this local stress field is not trivial. On the other hand, it may not be necessary to determine the local stress field and resolve the complex deformation process during fault slip in order to obtain an indicator for the likelihood of slip. Using slip tendency, predictions on fracture instabilities during the hydraulic stimulation of a fractured reservoir are feasible without solving for the typically non-linear evolution of the stress equilibrium equation.

In this paper we present the to our best knowledge first open source implementation of an embedded discrete fracture model for single phase flow and heat transport with additional capabilities to determine fracture stability in fractured reservoirs. THERMAID, an acronym for "Thermo-Hydraulic Energy Resource Modeling for Application and Development", is a fractured reservoir modeling framework implemented in *MATLAB*, which can be used as a standalone simulation package for TH(m) cases in geothermal reservoirs or as a blue print for the re-implementation of the method e.g. in a high performance computing (HPC) framework. We coin the term TH(m) to indicate a coupled Thermo-Hydraulic code, and we use the lower case (m) to indicate simplified mechanics. Of course, additional model capabilities can be implemented by new users directly in the THERMAID package.
This paper is structured as follows. In the next section we present the methodology of the embedded discrete fracture model, and describe in detail the underlying theory of the fracture stability analysis. The section Implementation focuses on the numerical discretization and the implementation details in *MATLAB*. The implemented model is evaluated in the Results section by comparing it with a widely used numerical model in several test cases. We conclude the paper by illustrating possible applications of the code using some simple examples and a discussion of the findings.

3.2 Methodology

We developed an embedded discrete fracture model (EDFM) using the methodology described in other studies (Hajibeygi et al., 2011; Karvounis, 2013; Pluimers, 2015). The conceptual idea of the EDFM is the distinct separation of a fractured reservoir into a fracture and a matrix domain. We introduce a transfer function to account for coupling effects between the two domains (cf. Figure 3.1), so the fracture and matrix domains are computationally independent except for the transfer function. As the fractures are generally very thin and highly permeable compared to the surrounding matrix rock, the gradient of fracture pressure normal to the fracture is negligible. This allows for a lower dimensional representation of fractures (i.e. 1D objects within a 2D reservoir).

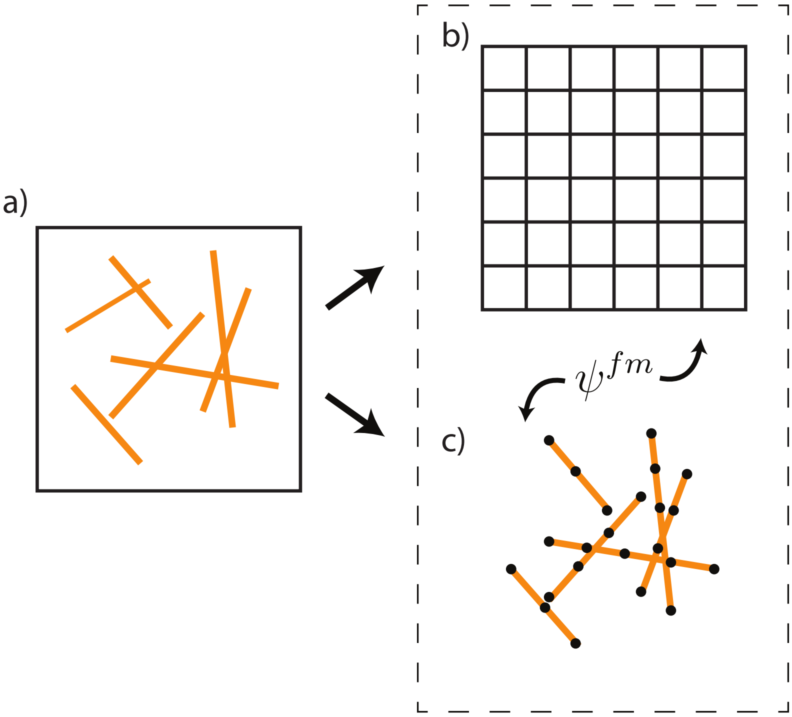

Figure 3.1: A fractured domain a) is separated in a uniform grid b) and a fracture grid c). The two resulting domains are coupled using the transfer function Ψ^{fm} .

3.2.1 Conceptual model

Numerical modeling of fractured reservoirs is not only challenging from the numerical and computational point of view, but also because it involves a variety of coupled thermal, hydraulic, mechanical and chemical (THMC) processes. THERMAID focuses on thermo-hydraulic processes and their coupling, with some additional mechanical processes considered taken within a simplified geomechanical model.

Figure 3.2 shows the conceptual model of the most relevant thermal, hydraulic and mechanical processes in fractured reservoirs. We consider the rock mass consists of a rock matrix crossed by a discrete fracture network. The geometry of the fracture network is static, i.e. propagation of new fractures in not considered. We implemented the processes in Figure 3.2 that are underlined, while relevant processes not yet considered shown as not underlined and between brackets.

The core processes implemented in THERMAID are fluid flow through pressure diffusion in the matrix, and the fracture network that is controlled by fracture aperture or permeability and the accompanying heat transfer by advection and diffusion. Pressure and heat are also exchanged between the rock matrix and the fracture at the fracture walls by pressure and thermal diffusion and thermal advection, respectively. Associated with the thermo-hydraulic processes, numerous thermo-mechanic or thermo-hydraulic processes could be activated, but only a limited amount and simplified processes are currently implemented in THERMAID. Poro-elastic and thermo-elastic deformation of the fractures and of the matrix is currently not implemented in the code. These effects could be important since they will modify the fracture aperture and fracture transmissivity as well as impact pressure diffusion in the matrix. The fluid pressure in the fracture is, however, considered in the compu-

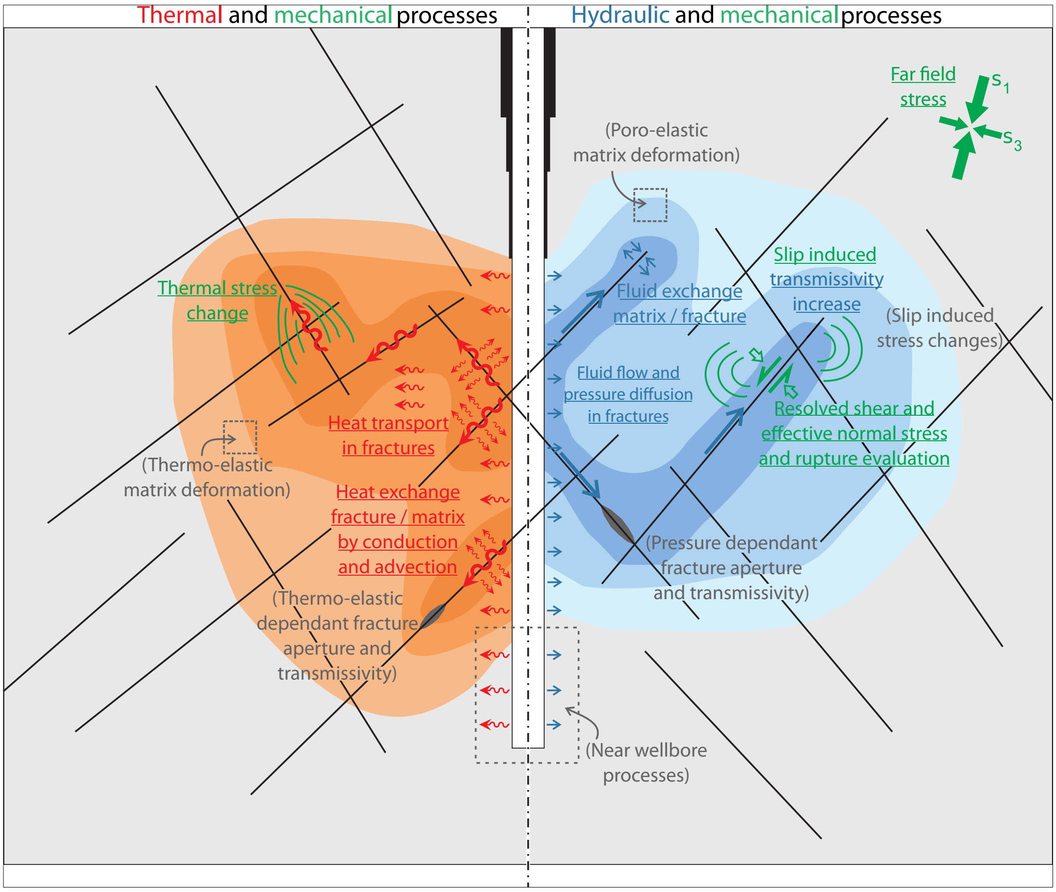

Figure 3.2: A conceptual model of a fractured domain with relevant thermo-hydro-mechanical processes. Underlined processes are included in THERMAID's current implementation. Processes in brackets are considered relevant but are currently not included mainly due to ambiguity in the simplified geomechanical model.

tation of fracture effective normal stress. This is an important parameter to evaluate fracture stability. If a fracture becomes unstable it will slip, and the associated dilation slip will thus increase the fracture transmissivity. The assessment of fracture stability is included in the code, and the transmissivity increase is introduced in a simplified manner: if a fracture segment reaches the slip condition, its transmissivity is multiplied by a fixed permeability enhancement factor. In reality, slip on a fracture perturbs local the stress state, potentially affecting the stability of other fractures. This process is not implemented in the code because the direction and amount of slip is ambiguous. However, stress change induced by thermal changes is implemented, not yet in a fully coupled way, but instead computing the thermal stresses and superposing thermal stresses onto the ambient stresses.
In addition to the processes shown in Figure 3.2, THERMAID properly accounts for gravity effects, internal pressure and heat sources, and the pressure- and temperature-dependence of fluid density and viscosity. The corresponding equations of state are given by (Sun et al., 2008) for density and (Al-Shemmeri, 2012) for the viscosity of water.

To summarize, THERMAID is a thermo-hydraulic code for fractured media that accounts for mechanical stability of the fractures, slip-induced transmissivity increase and thermally induced stresses. In the following, we introduce the governing equations for fluid flow and heat transport, couplings between fracture and matrix, and the implemented fracture stability analysis.

3.2.2 Governing equations

Flow in naturally fractured reservoirs is often described by the equations for slightly compressible single-phase flow. We include gravity effects in the formulation because gravity can play an important role in the flow field evolution of a reservoir fluid with variable densities. We assume that the equations for nearly incompressible single-phase flow are valid in both matrix and the fractures. This simplification might not yield an adequate description of the flow in some fractured reservoirs where very large fracture apertures result in non-Darcian flow. The methodology presented here is however easily modifiable to extended Darcy flow models.

The pressure equation, derived from continuity and total mass balance equations for single-phase fluid flow, is:

$$\phi\left(\beta_f+\beta_r\right)\frac{\partial p}{\partial t}=\nabla\cdot\left[\frac{\mathbf{k}}{\mu}(\nabla p-\rho_f g)\right]+Q \tag{3.1}$$

where ϕ [-] is the porosity, ρ_f $[\frac{kg}{m^3}]$ is the fluid density, p [Pa] is the fluid pressure and Q $[\frac{m^3}{s}]$ a source term. The compressibilities β [Pa^{-1}] are denoted with the subscripts f for fluid and r for rock, respectively, $\mathbf{k}$ $[m^2]$ is the permeability and μ $[\frac{1}{s}]$ the fluid viscosity. We consider only isotropic permeability k. Permeability is often linked to fracture aperture through the Cubic law, which has been shown to be useful in predicting fluid transport through fractured reservoirs and fractured porous media in general. However, it does not account for the roughness of the fracture or flow adjacent to the fracture walls due to the rock permeability. From the fluid pressure p, the fluid velocity is calculated using Darcy's law, i.e.

$$\mathbf{v} = -\frac{k}{\mu}\left[\nabla p - \rho_f g\right] \tag{3.2}$$

The total mass balance equation derived above is separated into parts for the matrix and the fracture domains, i.e.

$$\phi^m \left(\beta_f + \beta_r\right) \frac{\partial p^m}{\partial t} = \nabla \cdot \left[\frac{k^m}{\mu^m}(\nabla p^m - \rho_f g)\right] + \Psi^{mf} + Q^m \tag{3.3}$$

and

$$\phi^f \left(\beta_f + \beta_r\right) \frac{\partial p^f}{\partial t} = \nabla \cdot \left[\frac{k^f}{\mu^f}(\nabla p^f - \rho_f g)\right] + \Psi^{fm} + Q^f \tag{3.4}$$

where Ψ^{mf} and Ψ^{fm} are the flux transfer functions between the matrix and the fractures. Superscripts m and f denote matrix and fracture quantities respectively.

The heat transport equation is derived similarly to the pressure equation by balancing the heat transport mechanisms. We assume local thermal equilibrium so that $T = T_r = T_f$ where T_r and T_f are the temperatures of solid rock and fluid respectively. Taking average over an elemental volume we find

$$\overline{c_p\rho}\frac{\partial T}{\partial t} + c_{p_f}\rho_f \mathbf{v}\nabla T - \overline{\lambda}\nabla^2 T = \overline{q} \tag{3.5}$$

where over-lined properties denote volume averaged mean values for the porous medium.

$$\overline{c_p\rho} = \phi(c_{p_f}\rho_f) + (1-\phi)(c_{p_r}\rho_r) \tag{3.6}$$

$$\overline{\lambda} = \phi\lambda_f + (1-\phi)\lambda_r \tag{3.7}$$

$$\overline{q} = \phi q_f + (1-\phi)q_r \tag{3.8}$$

In equations 3.5 to 3.8 the heat capacity $c_p\,[\frac{J}{kgK}]$, the thermal conductivity $\lambda\,[\frac{W}{mK}]$ and internal heat source $q\,[\frac{W}{m^3}]$ of solid rock and fluid have been introduced. The fluid velocity $\mathbf{v}$ used in the heat transport equation is the Darcy velocity given by equation 3.2.

The heat transport equation is separated into matrix and fracture parts according to the same procedure as for the fluid pressure equation

$$\overline{c_p\rho}^m \frac{\partial T^m}{\partial t} + (c_{p_f}\rho_f\mathbf{v})^m \nabla T^m - \overline{\lambda}^m \nabla^2 T^m = \overline{q}^m + \mathcal{X}^{mf} \tag{3.9}$$

and

$$\overline{c_p\rho}^f \frac{\partial T^f}{\partial t} + (c_{p_f}\rho_f\mathbf{v})^f \nabla T^f - \overline{\lambda}^f \nabla^2 T^f = \overline{q}^f + \mathcal{X}^{fm} \tag{3.10}$$

where $\mathcal{X}^{mf}$ and $\mathcal{X}^{fm}$ are the heat transfer functions between the matrix and the fractures.

3.2.3 Fracture matrix coupling

To obtain a conservative set of equations, we apply a transfer function governing the mass and heat exchange between the two domains because flow and transport in the damaged matrix is treated separately from the fractures. The transfer function is treated as a source/sink term in the pressure and heat transport equations for damaged matrix and fracture, respectively, similar to classical well models (Peaceman, 1978).
The transfer function for the pressure equation is defined as

$$\Psi^{fm} = CI \cdot \Xi \cdot (p^f - p^m) \tag{3.11}$$

with Ξ being the mean total mobility of the fluid, defined as the fraction of permeability and viscosity (Lee et al., 2001). CI is the connectivity index between matrix and fracture that is dependent on the numerical discretization and will be defined in the next section. From the separated mass balance equations, it becomes immediately clear that the total flux between matrix and fracture has to be conserved:

$$\int \Psi^{mf} dV = -\int \Psi^{fm} dA \tag{3.12}$$

The transfer function for the heat equation is similarly defined. However, as two heat transport mechanisms are present in the equation, the transfer function needs to account for both mechanisms. Thus, the transfer function is defined as:

$$\mathcal{X}^{fm} = \mathcal{X}^{fm^{\nabla}} + \mathcal{X}^{fm^{\nabla^2}} \tag{3.13}$$

where the superscript ∇ denotes the heat advection contribution and ∇^2 denotes the heat conduction contribution. The heat conduction contribution $\mathcal{X}^{fm^{\nabla^2}}$ is derived using the same approach as in the pressure transfer function.

$$\mathcal{X}^{fm^{\nabla^2}} = CI \cdot \Lambda \cdot (T^f - T^m) \tag{3.14}$$

Here, Λ is the thermal conductivity at the fracture-matrix interface which can be calculated as

$$\Lambda = \frac{2 \cdot \lambda^f \cdot \lambda^m}{\lambda^f + \lambda^m} \tag{3.15}$$

using the definition of the averaged thermal conductivity λ given in equation 3.7. The advection contribution χ_{fm}^{∇}, on the other hand, explicitly shows the coupling to the pressure equation based on the Darcy velocity:

$$\mathcal{X}^{fm^{\nabla}} = \Upsilon \cdot \mathbf{v}^{fm} \tag{3.16}$$

In equation 3.16 we introduce the fluid velocity $\mathbf{v}^{fm}$ and specific heat capacity Υ at the matrix-fracture interface. Υ is calculated analogous to equation 3.15 and based on the averaged specific heat capacity given in equation 3.6. The fluid velocity at the matrix-fracture interface is defined as

$$\mathbf{v}^{fm} = -CI \cdot \Xi \cdot (\nabla p)^{fm} \tag{3.17}$$

where $(\nabla p)^{fm}$ is the pressure gradient at the interface of matrix and fracture. As discussed for the pressure transfer function also the heat transfer flux has to be conserved:

$$\int \mathcal{X}^{mf} dV = -\int \mathcal{X}^{fm} dA \tag{3.18}$$

3.2.4 Fracture stability

Within THERMAID, the equations governing the poro- and thermo-elastic deformation of the rock matrix and the deformation process during fracture slip are not solved. Nevertheless, a simplified analytical approach to fracture slip enables us to estimate fracture stability based on slip tendency analysis. Following Amonton's law for purely frictional fault reactivation

$$\tau = \mu_s \cdot \sigma_{\mathrm{n}eff} \tag{3.19}$$

with τ as shear stress, $\sigma_{\mathrm{n}eff}$ as effective normal stress ($\sigma_{\mathrm{n}} - p$ and p as fluid pressure), and μ_s as sliding friction coefficient (Byerlee, 1978), slip tendency is the ratio of shear stress to effective normal stress on a surface (Morris et al., 1996), i.e.

$$T_s = \frac{\tau}{\sigma_{\mathrm{n}eff}} \tag{3.20}$$

Fracture failure or slip is likely to occur if the shear stress to effective normal stress ratio equals or exceeds the frictional sliding resistance μ_s. Thus we define the stability of a fracture as follows

$$T_s = \begin{cases} \frac{\tau}{\sigma_{\mathrm{n}eff}} < \mu_s & \text{(stable)} \\ \frac{\tau}{\sigma_{\mathrm{n}eff}} \geq \mu_s & \text{(unstable)} \end{cases} \tag{3.21}$$

Shear and effective normal stress acting on a given fracture depend on the orientation of the fracture plane within the effective principal stress field. If the effective principal stress field $(\vec{l}, \vec{m}, \vec{n})$ and the reference coordinate system $(\vec{x}, \vec{y}, \vec{z})$ of the simulation match, shear and normal stress can be calculated by simple expressions based on the dip angle of the fracture (e.g. Miller et al., 2004). If the reference coordinate system is oriented e.g. with the groundwater flow direction, which does not coincide with the principal stress field, stress transformations are needed in order to calculate the correct normal and shear stress in the fracture coordinate system $(\vec{u}, \vec{v}, \vec{w})$. In order to express the state of stress within the reference coordinate system we use the following transformation

$$\mathbf{S}_{xyz} = \mathbf{R^T}_{lmn}\mathbf{S}_{lmn}\mathbf{R}_{lmn} \tag{3.22}$$

where $\mathbf{R}_{lmn}$ is the matrix of direction cosines of $(\vec{l}, \vec{m}, \vec{n})$ relative to $(\vec{x}, \vec{y}, \vec{z})$. $\mathbf{R}_{lmn}$ can easily be calculated if the orientations of the principal stresses are known (e.g. Allmendinger et al., 2011).

We obtain the stress state in the fracture coordinate system $(\vec{u}, \vec{v}, \vec{w})$ by a second transformation

$$\mathbf{S}_{uvw} = \mathbf{R}_{uvw}\mathbf{S}_{xyz}\mathbf{R^T}_{uvw} \tag{3.23}$$

with $\mathbf{R}_{uvw}$ is the matrix of direction cosines of $(\vec{u}, \vec{v}, \vec{w})$ relative to $(\vec{x}, \vec{y}, \vec{z})$. $\mathbf{R}_{uvw}$ can be expressed as a function of fracture azimuth ϕ and dip θ

$$\mathbf{R}_{uvw} = \begin{pmatrix} -\cos(\phi)\cos(\theta) & -\sin(\phi)\cos(\theta) & sin(\theta) \\ \sin(\phi) & -\cos(\phi) & 0 \\ \cos(\phi)\sin(\theta) & \sin(\phi)\sin(\theta) & \cos(\theta) \end{pmatrix} \tag{3.24}$$

Finally we compute the normal and shear stress on the fracture

$$\sigma_{\mathrm{n}} = \mathbf{S}_{uvw}(3,3) \tag{3.25}$$

$$\tau = \sqrt{\mathbf{S}_{uvw}(1,3)^2 + \mathbf{S}_{uvw}(2,3)^2} \tag{3.26}$$

Figure 3.3 shows a series of configurations of the reference coordinate system within the principal stress field. If we fix the orientation of the fractures in the reference system, the state of stress changes and thus fault criticality with the configurations (cf. Figure 3.3).

An important addition to the effects of pore pressure and far field stresses for fracture stability is thermal stress. A body will change its shape and/or volume when exposed to a temperature change ΔT. If the body's deformation is restricted, as it would be the case for a small volume inside a rock mass, the strain results in thermal stress.

$$\sigma_{T_{ij}} = \frac{E}{1-2\nu} \cdot \alpha \Delta T \delta_{ij} \tag{3.27}$$

where α is the coefficient of linear thermal expansion in $\frac{1}{K}$, E is the Young's modulus (Pa) and ν the Poisson ratio (-). δ_{ij} is the Kronecker delta, which is 1 for identical indices i and j, and 0 otherwise. The thermal stress is positive (relative compression) if the temperature difference is positive ($\Delta T > 0$), and if the temperature difference negative, the thermal stress is negative (relative tension). In the following we assume that the thermal stress is independent of the fluid pressure and the in-situ stress state of the rock. Thus, the resulting stress can be obtained by superposition of the effective stress ($\sigma_{eff} = \sigma_{tot} - p$) and the thermal stress. We formulate the superposed effective stress as

$$\sigma_{eff} = \sigma_{tot} - p + \sigma_T \tag{3.28}$$

which can be used in equation 3.19 in order to account for thermal stress during the fracture stability analysis.

Clearly, other stress contributions as slip induced stresses and stresses induced by chemical reaction have to be considered in a general case. However, especially the estimation of slip induced stress changes is ambiguous as the amount of slip and slip

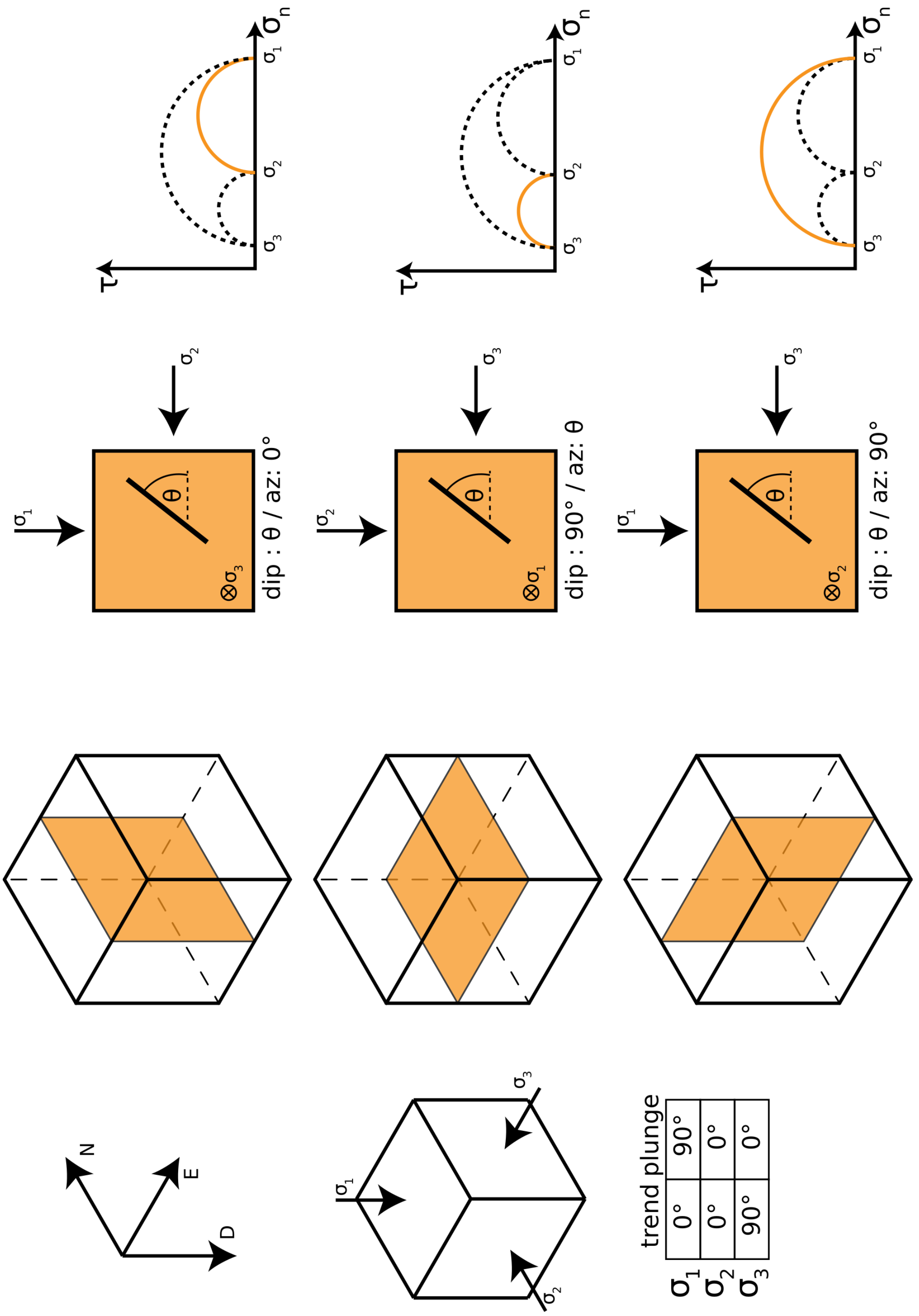

	trend	plunge
σ_1	0°	90°
σ_2	0°	0°
σ_3	90°	0°

Figure 3.3: Possible reference system orientations and their influence on the fracture stability depending on the principal stress field. **1st column** The principal stress field is aligned with a NED coordinate system. The trend and plunge of the principal stresses are given. **2nd column** Three basic orientations of the reference plane (simulation plane) within the principal stress field. **3rd column** Resulting stress orientations in 2D view. A fracture with angle θ to the horizontal in the reference plane is shown. The corresponding dip and azimuth of the fracture in the principal stress field is given. **4th column** Mohr-Coulomb diagrams for each case. In color the 'active' plane is shown for each case. The dashed circles show the remaining Mohr-Circles resulting from the principal stress field.

direction for potentially failing fractures is not known a-priori unless the underlying governing equations for fracture slip are solved explicitly. Thus, for reasons of simplicity we restrict ourselves to only pore pressure and thermally induced stress changes.

As fractures are reactivated they generally show an increase in aperture as the fracture surfaces are not smooth but have many asperities. Due to a strong aperture dependence of permeability (e.g. Nemčok et al., 2002), where small changes in aperture result in very large changes in permeability, it can be assumed that unstable (or sliding) fractures undergo a stepwise change in fracture permeability (Miller and Nur, 2000). Here we adopt the most simple model

$$k^f = \begin{cases} k^f & \text{if } T_s < \mu_s \\ \gamma \cdot k^f & \text{if } T_s \geq \mu_s \end{cases} \tag{3.29}$$

where γ is an permeability enhancement factor. This model successfully described the distribution of the induced seismicity in the Basel EGS site, and fluid-driven aftershock sequences (Miller et al., 2004; Miller, 2015). It should be noted, that the sudden permeability increase potentially has a great impact on the flow field evolution during the simulation of a EGS stimulation. In cases without the impact of fracture stability on the flow simulation, the permeability enhancement factor can be set to $\gamma = 1$.

3.3 Implementation

Here we describe the discretization of the governing equations by the finite volume method and implementation of the two-dimensional embedded discrete fracture method in MATLAB. Our implementation if based on the concepts used in *MAFLOT*, an open source MATLAB flow and transport solver (Künze and Lunati, 2012). As briefly discussed in the introduction, the matrix and fracture domains are discretized by regular Cartesian grids in 2D for the matrix and 1D for the fractures respectively (cf. Figures 3.1 and 3.4).

3.3.1 Numerical discretization in space

Using a finite volume approach, we discretize the domain Ω as the integration over finite control volumes Ω_{ij} with $\Omega = \sum_{ij=1}^{N} \Omega_{ij}$. Using the Gauss theorem, the divergence integral over the volume can be rewritten as the surface integral normal to the boundary of the volume.

Pressure equation Applied to a matrix grid cell on the right hand side (RHS) of the pressure equation 3.3 this yields

$$\int_{\Omega_{ij}} \nabla \cdot \left(\frac{k}{\mu} \cdot \nabla p\right)^{m} + \Psi^{mf} + Q^{m} dV \Rightarrow \int_{\partial\Omega_{ij}} \left(\left(\frac{k}{\mu} \cdot \nabla p\right)^{m} + \Psi^{mf}\right) \cdot \mathbf{n} ds + \int_{\Omega_{ij}} Q^{m} dV \tag{3.30}$$

Note that gravity is neglected here and in the remains of this section to better facilitate comprehension of the implementation. The pressure gradient over the cell boundary $\partial\Omega_{ij}$ is approximated by a two-point flux approximation that is similar to the central difference scheme of the finite difference method and is second-order accurate in space. As the domain is generally heterogeneous in terms of rock properties, a harmonic averaging technique is used to calculate the appropriate values at the cell boundaries. This leads to the discretized expression for the RHS of the matrix pressure

$$\begin{aligned}
&\frac{\Delta y \left(\frac{k}{\mu}\right)^{m}_{i-\frac{1}{2},j}}{\Delta x}(p^{m}_{i,j} - p^{m}_{i-1,j}) + \frac{\Delta y \left(\frac{k}{\mu}\right)^{m}_{i+\frac{1}{2},j}}{\Delta x}(p^{m}_{i,j} - p^{m}_{i+1,j}) \\
+&\frac{\Delta x \left(\frac{k}{\mu}\right)^{m}_{i,j-\frac{1}{2}}}{\Delta y}(p^{m}_{i,j} - p^{m}_{i,j-1}) + \frac{\Delta x \left(\frac{k}{\mu}\right)^{m}_{i,j+\frac{1}{2}}}{\Delta y}(p^{m}_{i,j} - p^{m}_{i,j+1}) \\
&\qquad = Q^{m}_{i,j} + \sum_{\Omega_{ij} \cap \Omega_{k}} CI_{k} \left(\frac{k}{\mu}\right)_{ij,k} (p^{f}_{k} - p^{m}_{i,j})
\end{aligned} \tag{3.31}$$

where Δx and Δy represent the lengths of the grid cells in x and y direction, respectively. All other notations are adopted from the elemental literature of the Finite Volume Method. Note that the matrix-fracture interaction term has already been moved to the right-hand side using $\int \Psi^{mf} = -\int \Psi^{fm}$.
The RHS for the fracture pressure can be expressed using the same approach as

$$\begin{aligned}
&\frac{b \left(\frac{k}{\mu}\right)^{f}_{k-\frac{1}{2}}}{\Delta x^{f}}(p^{f}_{k} - p^{f}_{k-1}) + \frac{b \left(\frac{k}{\mu}\right)^{f}_{k+\frac{1}{2}}}{\Delta x^{f}}(p^{f}_{k} - p^{f}_{k+1}) \\
&\qquad = Q^{f}_{k} - \sum_{\Omega_{ij} \cap \Omega_{k}} CI_{k} \left(\frac{k}{\mu}\right)_{ij,k} (p^{f}_{k} - p^{m}_{i,j})
\end{aligned} \tag{3.32}$$

Here, Δx^{f} is the discretization lengths of the fracture segments and b the aperture of the fracture.

The discretization of the RHS of the temperature equation is analogous to the pressure equations and omitted here for brevity. It is worth noting, however, that the advection term must be treated with special care. This is not a limitation of the EDFM but a consistent issue in a wide range of numerical methods. In this EDFM implementation, we use an upwind method in the fractures in combination with a *minmod*-flux limited QUICK scheme in the matrix (Courant et al., 1952; Leonard, 1979; Roe, 1986).

3.3.2 Connectivity index

The connectivity index CI between matrix and fracture is discretization-dependent, and defined based on the linear pressure distribution assumed within a grid cell intersected by a fracture (Hajibeygi et al., 2011). It is defined as the length fraction $A_{ij,k}$ of fracture segment k inside matrix cell ij divided by the average distance $\langle d \rangle_{ij,k}$ between matrix cell ij and fracture segment k.

$$CI_{ij,k} = \frac{A_{ij,k}}{\langle d \rangle_{ij,k}} \tag{3.33}$$

The average distance $\langle d \rangle_{ij,k}$ can be calculated as

$$\langle d \rangle_{ij,k} = \frac{\int x_k(x')dx'}{V_{ij}} \tag{3.34}$$

where x_k is the distance from the fracture within the matrix cell and V_{ij} the volume of the matrix cell. This allows a proper accounting for the reduced influence of a fracture segment on a matrix cell if the fracture segment does not cross the matrix cell through its center. Figure 3.4 shows the numerical discretization of a single fracture within a regular matrix and helps to understand the concept of the connectivity index. In many cases equation 3.34 has to be evaluated by numerical integration. For rectangular grids however, there exists an analytical solution for fracture intersections horizontally, vertically or on the diagonal to a grid cell (Hajibeygi et al., 2011). This has later been extended to arbitrary intersections with rectangular grid cells by (Pluimers, 2015). For enhanced efficiency, the analytical expressions given in (Hajibeygi et al., 2011; Pluimers, 2015) are used in the present implementation.

3.3.3 Fracture intersections

Fractures often intersect other fractures in naturally fractured reservoirs, which potentially significantly impacts flow dynamics in the reservoir. Therefore, we must also consider fracture-fracture coupling in the model. The additional transmissivity at a fracture intersection can be obtained using an approach similar to that in electrical

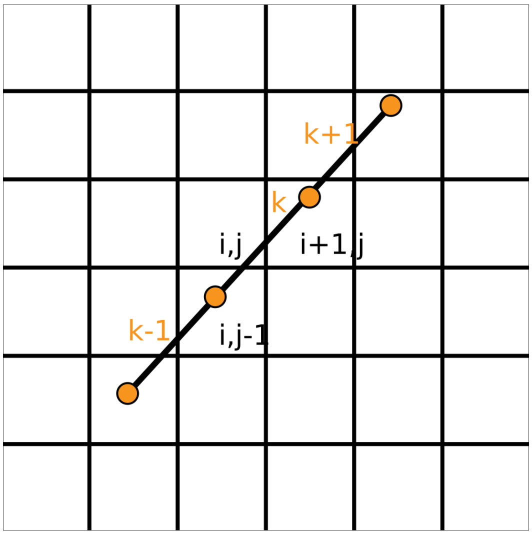

Figure 3.4: Discretization of a single fracture within a regular matrix. Black indices denote matrix cells whereas colored indices belong to the fracture discretization. The fracture segment k is intersecting cells $i, j-1$, i, j and $i+1, j$. It is obvious that the fracture's influence on the matrix cells is not equal. This is captured by the connectivity index CI, which depends on the lengths and position of the fracture intersection with the matrix cell.

engineering and known as the star-delta transformation in circuits (Karimi-Fard et al., 2003). The additional fracture-fracture transmissivity can be calculated as

$$T_{i,j} = \frac{\alpha_i \cdot \alpha_j}{\alpha_i + \alpha_j} \quad \text{with } \alpha_i = \frac{b_i \Xi_i}{0.5 \cdot \Delta x^f} \tag{3.35}$$

where b_f^i denotes the fracture aperture, Ξ_i the total mobility and Δx^f the numerical discretization spacing in the fracture. This approach can be generalized to more than two fractures intersecting in a single point on a fracture segment, but is omitted here due to its rare occurrence.

3.3.4 Time-discretization

The time derivatives in equations 3.1 and 3.5 are treated using the backward Euler method, which is an implicit time-discretization of order one. This means that the local truncation error (defined as the error made in one step) is $\mathcal{O}(h^2)$. The backward Euler method is an unconditionally stable implicit time-discretization scheme that theoretically allows arbitrarily large time steps. In practice, when encountering non-linear behavior, such as the temperature- and pressure-dependent evolution of fluid density, issues with non-convergence might appear and place an indirect restriction on the time-step. Nonetheless, much larger time steps are allowed in the implemented method when compared to explicit schemes.

3.3.5 System of equations

The discretized equations for pressure and transport can be assembled separately as linear systems of equations of the form $A \cdot x = b$. Since the matrix and fracture domains are strongly coupled, the solution for both domains must be found either in iteratively where the fracture and matrix systems are solved independently until reaching convergence, or implicitly at the same time. The implicit solution can be achieved through the assembly of a block matrix of the pressure or the transport systems respectively, i.e.

$$A = \begin{pmatrix} A^{mm} & A^{mf} \\ A^{fm} & A^{ff} \end{pmatrix} \tag{3.36}$$

Assuming that A has been assembled for the pressure equation, then the diagonal submatrix block A^{mm} contains the matrix transmissivities. A^{ff} contains the fracture transmissivities, including the additional transmissivities due to fracture-fracture intersections, and the off-diagonal submatrix blocks contain the fracture-matrix and matrix-fracture transmissivities A^{fm}/A^{mf} . The block matrix structure for the heat transport equation remains unchanged. Of course the transmissivities are replaced by the appropriate coefficients of the heat transport equation. Due to the numerical treatment of the advection term a different sparse pattern arises. In any case, the solution of the assembled block matrices is performed by the backslash operator of MATLAB in the current implementation.

3.3.6 Solution strategy

We adapt a serial iterative scheme in order to accurately account for the coupling between the pressure and transport equations. Instead of assembling and solving a very large system for pressure and transport in a single step, the problem is divided in two parts. In a first step, the pressure system is assembled and solved. Using Darcy's law, the fluid velocities can be calculated in an intermediate step. Once the fluid velocities are found, the transport system can be assembled and subsequently solved. At this point the fracture stability is evaluated. As this is an analytical analysis no additional system of equations is involved. In strongly coupled problems, multiple iterations must be used to capture any arising nonlinearities. In most cases, the flow and transport exhibit rather loose coupling in which only a few iterations are needed to converge to the solution. If on the other hand, fracture stability ceases and permeability enhancement in unstable fracture parts is used, the number of iterations might increase significantly and even place a limit on the allowable timestep.

Flowchart THERMAID consists of multiple parts that are involved in the solution of a coupled flow, heat transport and fracture stability problem. The general structure of the main function that controls the simulation and calls most of the sub functions is presented in a simplified flow chart in Figure 3.5. Throughout the flowchart the following terms are used: *time* denotes the current point in time in the simulation, *timeEnd* is the specified duration of the simulation, *err(p,T)* is the residual error of the pressure and temperature solutions between iterations and *tol* a user specified tolerance of the acceptable residual error. The sub functions that deal with specific parts of the program, such as initialization, discretization and solution of the flow and transport equations, are further explained throughout the user manual and in the inline documentation.

Interface for user defined calculations As shown in the flowchart in Figure 3.5, there are two points in the procedure where users can introduce additional calculations easily without having to modify the general implementation. This allows users to add their own visualization procedures, model calculations such as e.g. the implementation of time-dependent boundary conditions and even interfaces to third-party programs. This interface is presented as two additional MATLAB scripts that can be specified during the simulation startup that are executed at the specified positions in each time-step. Using conditionals, it is possible to restrict the additional computations only at certain times during the simulations. Examples of how to use the interfaces are provided with the package and in the user manual.

3.4 Results

We present the results of three benchmark experiments and an application experiment that provide insight into the capabilities of THERMAID and validate the implemented method. The effect of gravity is neglected in the numerical experiments presented in this paper, as well as the pressure and/or temperature dependence of the fluid density and viscosity. Fracture permeability and aperture are treated as independent from each other in the following. This allows simulating also ’filled’ fractures with relatively high aperture and comparably small permeability and allows fracture permeability estimates independent of Cubic law.

First we validate the implemented model with a simple flow problem independently. We then evaluate the coupled results of fluid flow and heat transport on the same geometry over a long time period. The last benchmark validates the solution of a coupled flow and heat transport problem on a more realistic complex fracture network over a similarly long time period. The final numerical experiment is the application of the implemented approach to a field scale problem were we take advantage of the implemented fracture stability analysis in order to characterize the stimulated reservoir during injection of a geothermal reservoir. We combine results

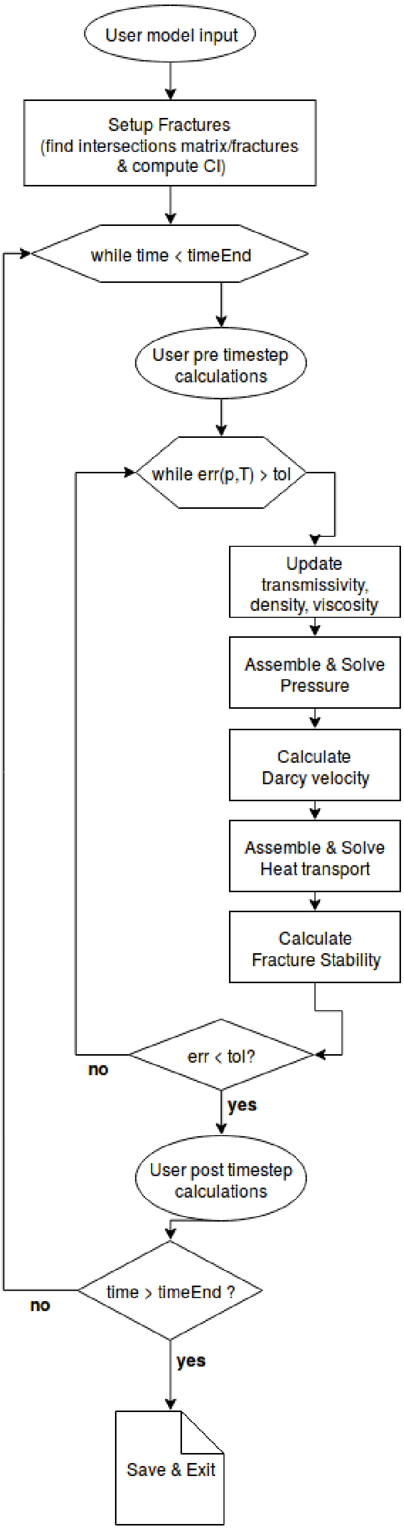

Figure 3.5: The simplified flowchart of the implemented solution strategy for coupled flow and transport problems including fracture stability analysis. *time* denotes the current point in time in the simulation, *timeEnd* is the specified duration of the simulation, *err(p,T)* is the residual error of the pressure and temperature solutions between iterations and *tol* a user specified tolerance of the acceptable residual error. Round objects denote parts of the code where the user has (optional) abilities to perform additional calculations and add runtime visualization.

and their discussion to emphasize each experiment's outcome. A more general discussion of the results as well as a conclusion is provided in the final section.

3.4.1 Validation of the pressure equation: Steady-state flow in the presence of a fracture

In order to validate the implementation of flow equations of the model, we use an analytical solution for the steady-state flow in a porous medium in the presence of a fracture (Strack, 1982; Kolditz et al., 2012). Figure 3.6a shows the benchmark geometry, a square with a length of 10m with a 2m-long inclined fracture in its center. The aperture of the fractures is fixed at $b = 0.05$m. Uniform flow is maintained by imposing a specific discharge q_0 from the left boundary into the domain. To compare numerical results with the analytical solution, pressures calculated by the analytical solution are used at the lateral boundaries, i.e. $p_{in} = 49646$Pa and $p_{out} = -49646$Pa (cf. Figure 3.6). On the top and bottom a no-flow Neumann boundary is applied. The remaining material properties of the numerical model are shown in Table 3.1.

Table 3.1: Model parameters used for the inclined fracture solution.

	Parameter	Value	Unit
α	Fracture angle	45	°
b_{max}	Maximum fracture aperture	0.05	m
L	Fracture length	2	m
k^m	Matrix permeability	$1 \cdot 10^{-12}$	m^2
k^f	Fracture permeability	$1 \cdot 10^{-10}$	m^2
μ	Fluid viscosity	$1 \cdot 10^{-3}$	Pa s
q_0	Specific discharge	$1 \cdot 10^{-4}$	m s^{-1}

The pressure distribution obtained by THERMAID is shown in Figure3.6a. The lateral uniform flow is disturbed in the vicinity of the inclined fracture where the flow is faster than in the surrounding porous media. Figure 3.7b shows the pressure profile along a diagonal line from the bottom-left to the top-right. The results show very good agreement between the numerical solution obtained by THERMAID and the analytical solution.

3.4.2 Validation of the pressure equation: Flow field with intersecting fractures

Additionally we validate the implementation of flow equations of the model by using a benchmark experiment first presented by (Hajibeygi et al., 2011). The same benchmark is also used by (Pluimers, 2015) to study the sensitivity of the EDFM with respect to numerical resolution and fracture position within the intersecting grid cells. Figure 3.8 shows the benchmark geometry that consists of two perpendicular

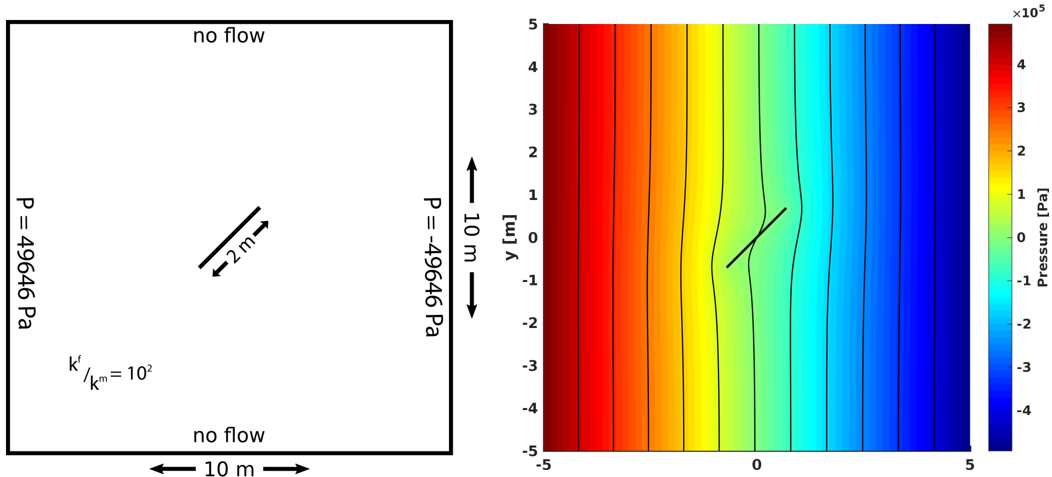

(a)

(b)

Figure 3.6: a) Numerical setup to evaluate the performance of the flow equations solution. Incompressible fluids are assumed in this benchmark experiment. On the left boundary a constant pressure of 49646Pa is assumed. The right boundary is set to -49646Pa to enforce the specific discharge q_0. On the other boundaries a no-flow boundary condition is applied. b) Pressure field computed for the flow field including a single inclined fracture.

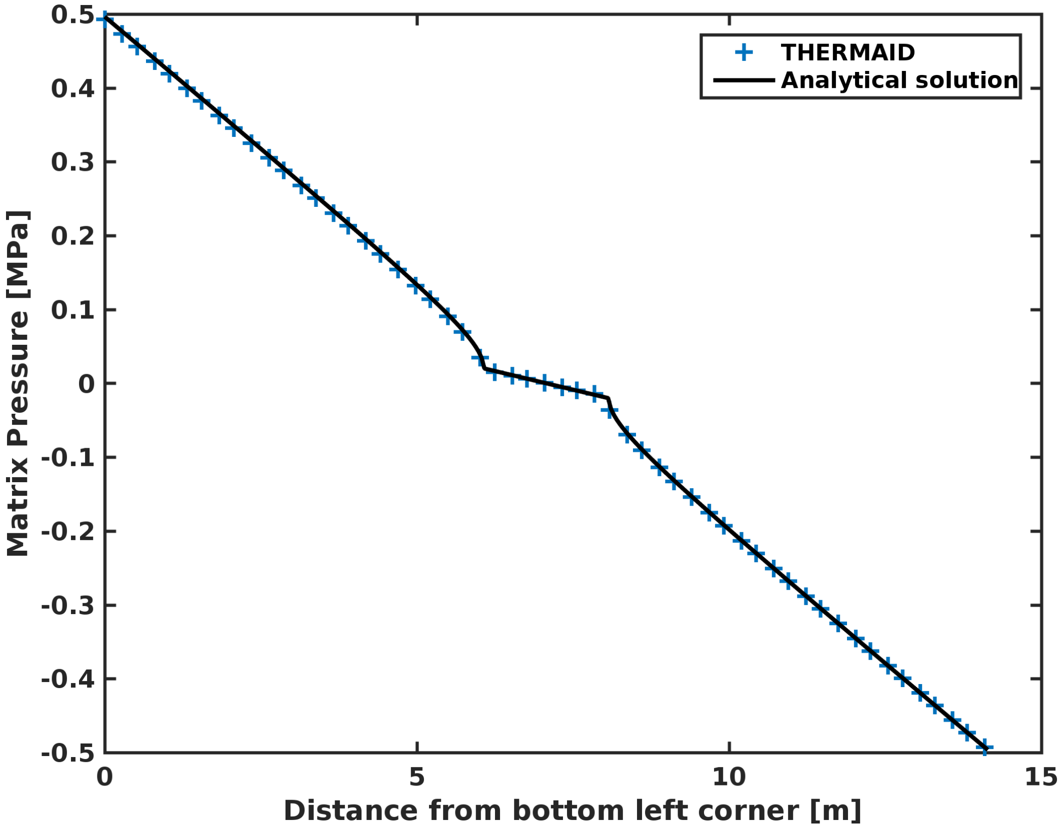

Figure 3.7: Comparison between simulated (continuous red curve) and analytical derived (empty black circles) pressure distribution along diagonal from bottom left to top right of the model

5m-long fractures intersecting in the middle of a square domain. The aperture of the fractures is fixed at $b = 4mm$. The domain is 9m by 9m square domain with Dirichlet boundary conditions on the left and right sides. On the left, a constant pressure of 1Pa is applied, whereas the right side is fixed to 0Pa. On the top and bottom a no-flow Neumann boundary is applied. The matrix domain is discretized by 301x301 cells while the fractures are modelled by 304 fracture segments (152 each). As fracture permeability and permeability contrast between fracture and matrix are some of the most important variables to be determined in EGS reservoirs to accurately predict flow in the reservoir, we evaluate our method with two different permeability contrast values, namely $\frac{k^f}{k^m} = 10^3$ and $\frac{k^f}{k^m} = 10^5$. We compare the solution at steady state obtained by THERMAID to a reference solution computed by *COMSOL Multiphysics*, which is a widely used finite element package with subsurface flow and transport capabilities (Comsol Inc., 2017). It should be noted that we use the implementation of the governing equations of the subsurface flow module of *COMSOL*. This established and independent implementation provides the basis for the validation of our model. The reference solution is computed on a conforming discrete fracture network were the matrix elements are aligned exactly on the grid with a total of 1'750'693 degrees of freedom (dof).

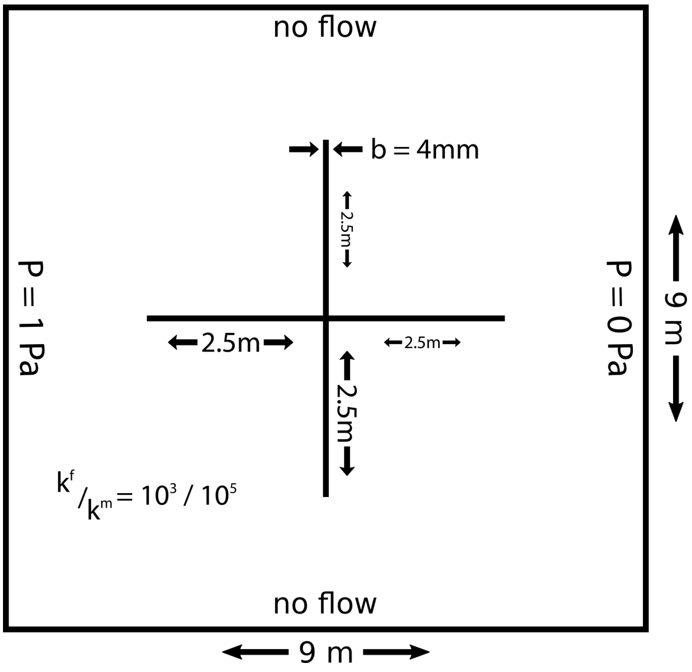

Figure 3.8: Numerical setup to evaluate the performance of the flow equations solution. Incompressible fluids are assumed in this benchmark experiment. On the left boundary a constant pressure of 1Pa is assumed. The right boundary is set to 0Pa. On the other boundaries a no-flow boundary condition is applied.

The fracture pressure shown in Figure 3.9 shows a very good match between the reference and the implemented model. However, if the results are compared in detail, a slight offset between the reference solution and the current implementation

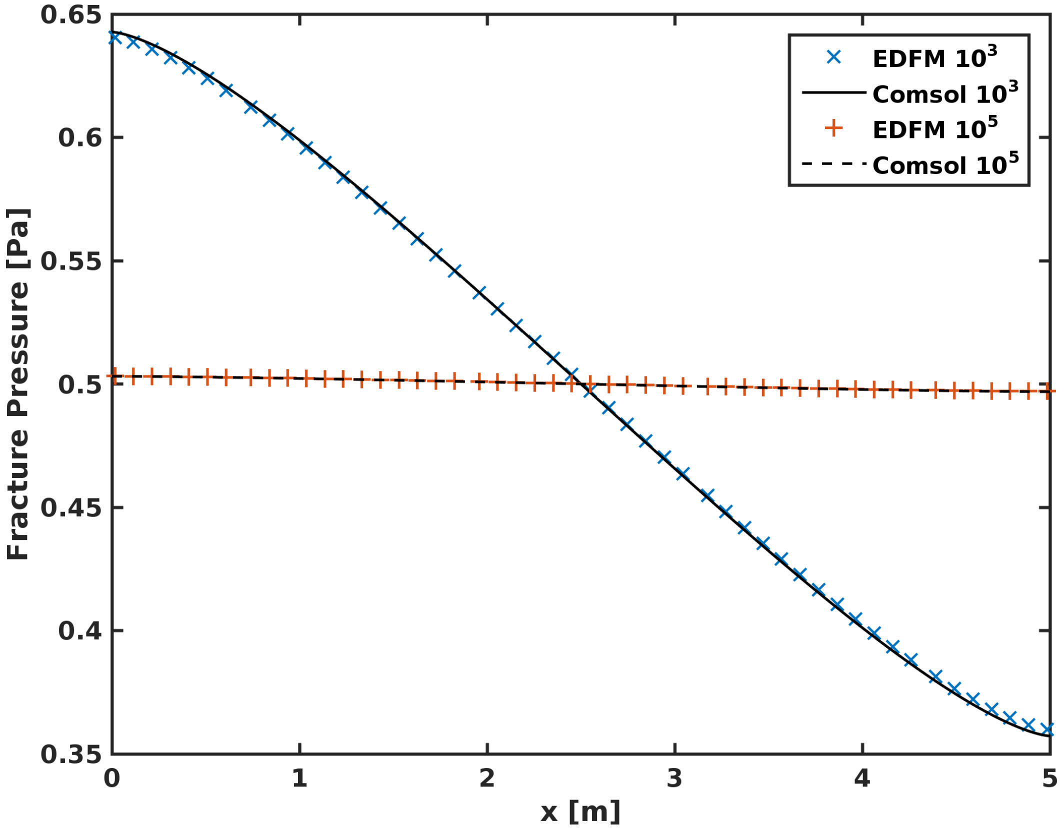

Figure 3.9: Steady-state fracture pressure through the horizontal fracture. For both permeability contrasts we see very good agreement between the implemented method and the reference solution.

becomes visible. We quantify the difference between our model with the reference by the 'normalized root mean squared error (NRSME)' as well as the 'normalized mean absolute error (NMAE)'.

$$NRSME = \frac{\sqrt{\frac{\sum_{i=1}^{n}\left(x_i - x_i^{ref}\right)^2}{n}}}{max(x_i^{ref}) - min(x_i^{ref})} \tag{3.37}$$

$$NMAE = \frac{\frac{\sum_{i=1}^{n}|x_i - x_i^{ref}|}{n}}{max(x_i^{ref}) - min(x_i^{ref})} \tag{3.38}$$

We decided to use two measures of performance due a recent scientific debate on both measures (e.g. Willmott and Matsuura, 2005; Chai and Draxler, 2014). Especially (Chai and Draxler, 2014) suggest that a combination of measures is required to assess model performance.

The results are shown in Table 3.2. We observe errors of well below 2% compared to the pressure range in the benchmark setup. Both NRSME and NMAE show slightly bigger fracture pressure errors for a permeability contrast of $\frac{k^f}{k^m} = 10^5$.

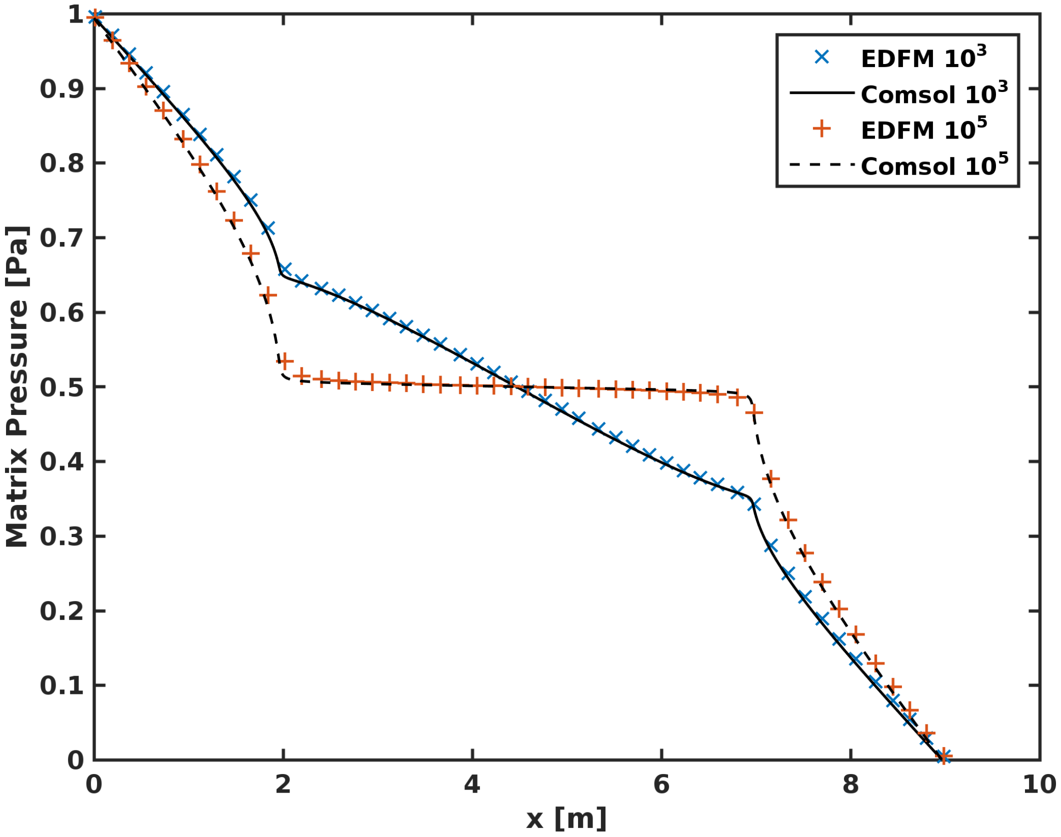

Figure 3.10: Steady state matrix pressure at y=4.5m - the position of the horizontal fracture. We evaluated two permeability contrast between matrix and fracture. In both cases we see very good consistency between the implemented method and the reference solution.

Especially the fracture pressure at this permeability contrast shows, with a deviation of $\sim 1.5\%$, the largest observed error in this benchmark. Figure 3.10 shows the matrix pressure at y = 4.5m, which corresponds to the matrix cells intersected by the horizontal fracture. Again, the reference case and the THERMAID solutions are in good agreement. Slight deviations from the reference solution ($\sim 0.5\%$) are visible and the error quantification is shown in Table 3.2. Based on the overall good agreement of the implemented model and the reference solution, the implementation of the fluid flow equations is validated in this benchmark experiment.

Table 3.2: NRSME and NMAE errors for the fluid flow equation benchmark (presented in Fig. 3.9 and 3.10) showing pressure difference in the fracture (p^f) and in the matrix (p^m) with respect to the model. Both permeability contrast ratios r are shown.

	$\mathbf{p^f\ (r = 10^3)}$	$\mathbf{p^m\ (r = 10^3)}$	$\mathbf{p^f\ (r = 10^5)}$	$\mathbf{p^m\ (r = 10^5)}$
NRMSE [%]	0.5	0.47	1.58	0.67
NMAE [%]	0.43	0.40	1.50	0.49

3.4.3 Validation of the heat transport equation

We validate the coupled flow and heat transport equations using a similar geometry of the benchmark to the previous benchmark (Figure 3.11). The aperture of the fractures is fixed at $b = 1mm$. The domain is 100m by 100m square domain with Dirichlet boundary conditions on the left and right sides. On the left a constant pressure of 10MPa is applied, whereas the right side is fixed to 0MPa. On the top and bottom a no-flow Neumann boundary is applied. The domain is initially at $T_0 = 180°C$, which is a typical temperature for economic heat extraction in a geothermal reservoir. The inflow temperature at the left side of the domain is set to $T_{in} = 50°C$ (cf. Figure 3.11). As shown in the previous section, the flow solver is accurate for both investigated permeability contrasts. Here we restrict ourselves to the case of $\frac{k^f}{k^m} = 10^5$. The material parameters for this benchmark were chosen realistically and are shown in Table 3.3. The benchmark's results are evaluated after 40 years of simulation. Consistent with the previous benchmark the matrix domain is discretized by 301x301 cells while the fractures are modeled by 304 fracture segments (152 each). The reference solution is computed by *COMSOL* on a conforming discrete fracture network with a high resolution grid. As the pressure in the fractures and matrix of this geometry have already been investigated in the previous section, here we focus on the temperature solutions.

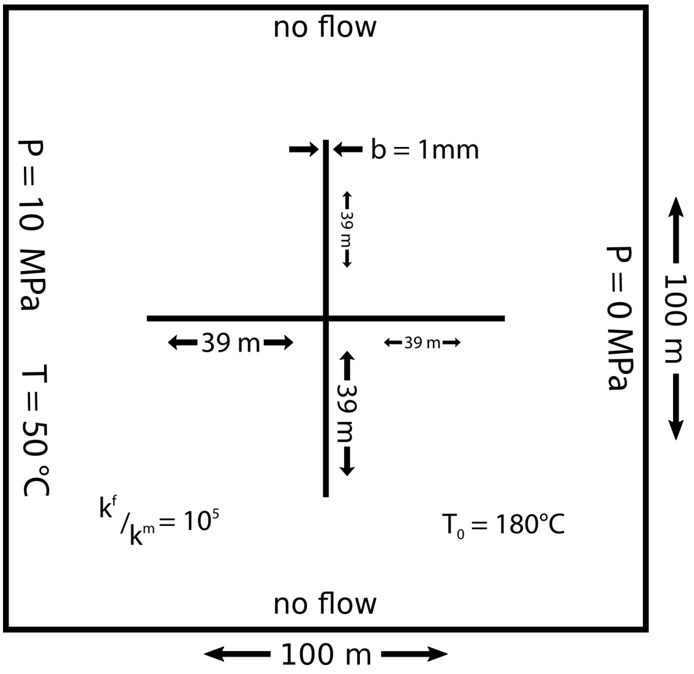

Figure 3.11: Numerical setup to evaluate the performance of the coupled flow and heat transport solution. A simple fracture geometry and incompressible fluids are used. On the left boundary a constant pressure of 10MPa at 50°C is applied. The right boundary is set to 0Pa. On the other boundaries a no-flow boundary condition is applied. The interior has an initial temperature of 180°C. All parameters for this model setup are shown in Table 3.3.

Table 3.3: Properties used in the coupled flow and heat transport models. Superscripts: f - fracture, m - matrix. Subscripts: f - fluid, r - rock.

Permeability	$k^f = 1 \cdot 10^{-11} m^2$	$k^m = 10^{-16} m^2$
Porosity	$\phi^f = 0.3$	$\phi^m = 0.3$
Density	$\rho_f = 1 \cdot 10^3 \frac{kg}{m^3}$	$\rho_r = 2.5 \cdot 10^3 \frac{kg}{m^3}$
Viscosity	$\mu_f = 1 \cdot 10^{-3} Pa \cdot s$	
Specific heat	$c_{p_f} = 4000 \frac{J}{kg \cdot K}$	$c_{p_r} = 1000 \frac{J}{kg \cdot K}$
Thermal conductivity	$\lambda_f = 0.5 \frac{W}{m \cdot K}$	$\lambda_r = 2.0 \frac{W}{m \cdot K}$

Figure 3.12 shows the temperature in both fractures after 40 years of coupled flow and heat transport simulation. Additionally, Table 3.4 shows the quantitative error analysis for the fracture temperatures. We observe a very good agreement between the temperature distribution in both fractures with the reference solution. The horizontal fracture presents changes in temperature over most its extent, which is in accordance with the principal flow direction. As the vertical fracture is not aligned with the flow, a rather homogeneous temperature decrease is observed to about $140°C$ after 40 years. This is in good agreement with the matrix temperatures at the position of the fracture. Nevertheless, a significant change in temperature is observed close to the intersection of both fractures. Here the fracture-fracture interaction is clearly visible as both fractures show nearly identical temperatures at the intersection (cf. Figure 3.12). The quantitative error analysis shows differences between our solution and the reference of $\sim 0.8\%$ for the vertical fracture and $\sim 0.1\%$ for the horizontal fracture although the two error measures differ slightly (cf. Table 3.4).

Table 3.4: NRSME and NMAE errors for the first coupled fluid flow and heat transport equation benchmark.

	$\mathbf{T}_{\mathbf{vertical}}$	$\mathbf{T}_{\mathbf{horizontal}}$
NRMSE [%]	0.89	0.16
NMAE [%]	0.71	0.11

Ultimately, the benchmark shows that our model accurately solves the coupled flow and heat transport equations for this geometry. The simulated time-frame is consistent with the estimated lifetime of a typical enhanced geothermal reservoir. The agreement of our model and the reference solution shows additionally that the implemented time-marching scheme is accurate for the problem at hand. With these results we can evaluate the model on a more complex geometry in the next section.

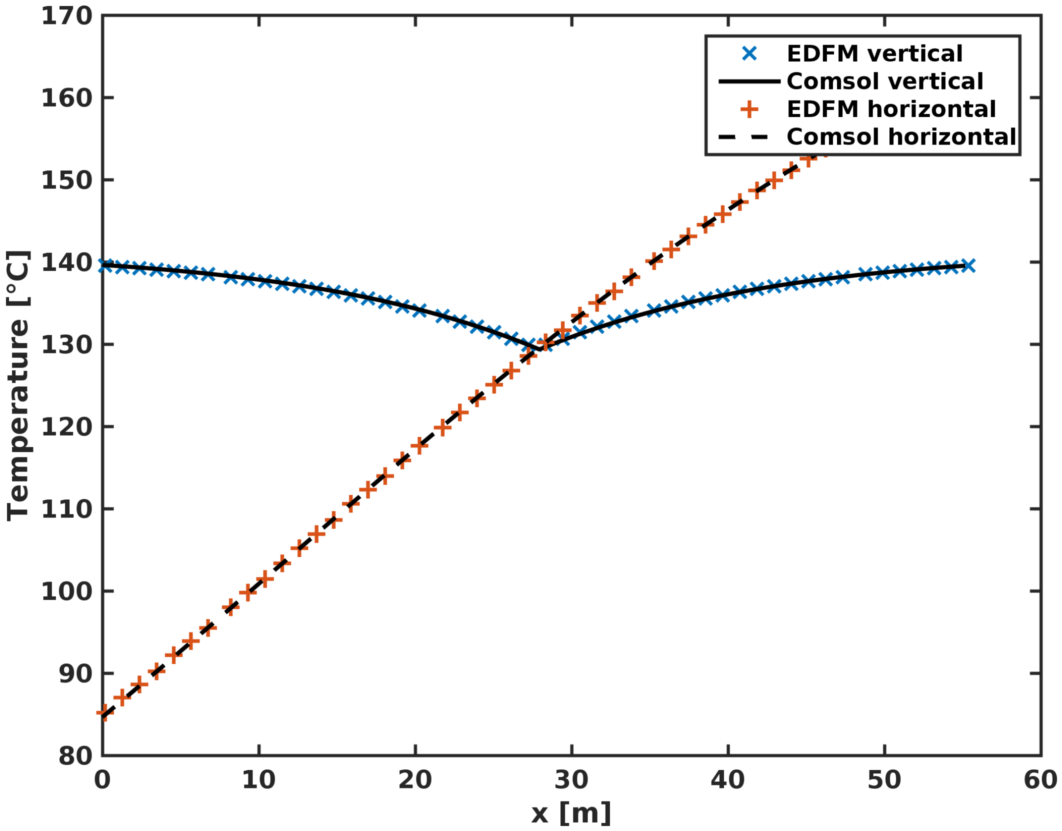

Figure 3.12: Fracture temperatures through vertical and horizontal fractures. For both fractures we see very good agreement between the implemented method and the reference solution.

3.4.4 Validation of the heat transport equation on a complex fracture network

We evaluate the coupled flow and heat transport on a more complex fracture geometry. The geometry (Figure 3.13) consists of a total of 13 fractures within a square domain. Boundary and initial conditions are equal to the previous experiment. The fracture aperture is set to $b = 0.5mm$. The remaining parameters governing the heat transport are consistent with the benchmark in the last section and shown in Table 3.3. We evaluate the results after 40 years of simulation. The reference solution computed by *COMSOL* contains 419'594 DOF. In this experiment we evaluate also grid dependence of the implemented model by comparing the results for different resolution simulations with the reference.

In the previous section we focused on the temperature distributions in the fractures. Here we take a closer look at the matrix temperature distributions. Figure 3.14a shows the final pressure distribution for a matrix grid resolution of 301x301. As we still consider the fluids to be incompressible in this benchmark, the pressure distribution does not change throughout the simulation and is obtained as the steady-state solution. The temperature distribution in the domain after 40 years

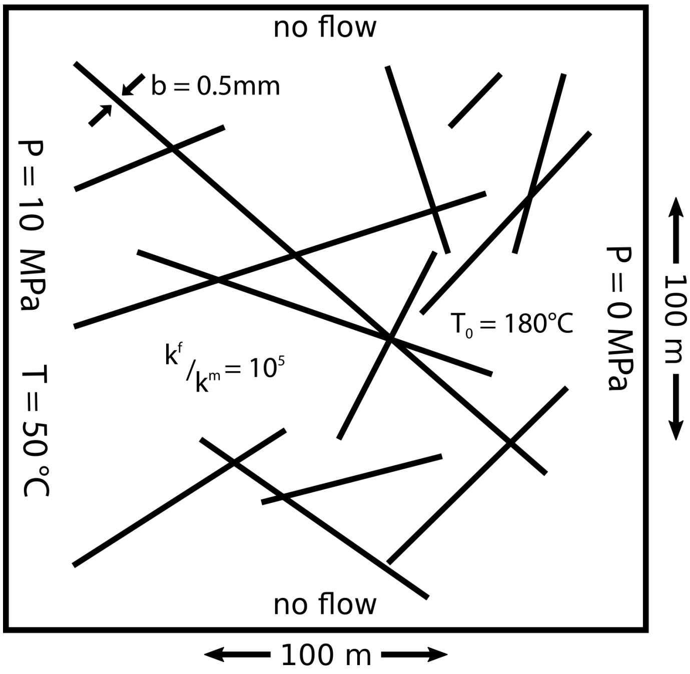

Figure 3.13: Numerical setup to evaluate the performance of the coupled flow and heat transport solution with a more realistic complex fracture geometry. Incompressible fluids are used. On the left boundary a constant pressure of 10MPa at 50°C is applied. The right boundary is set to 0Pa. On the outer boundaries a no-flow boundary condition is applied. The interior has an initial temperature of 180°C. All parameters for this model setup are shown in Table 3.3.

of simulation is shown in 3.14b. Both pressure and temperature fields show a heterogeneous distribution due to the influence of the fractures.

Figures 3.15a and 3.15b show the percental deviation of our solution from the reference for the matrix grid resolution of 301x301 of our model. The pressure solution shows only small errors with a NRMSE of 0.35%. In the lower third of the domain between 20m and 60m in x-direction, a region of elevated error ($\sim 1\%$) is present (cf. Figure 3.15a). Bigger deviations are visible close to some fracture tips where typically on the high-pressure (inflow) side of the fracture our model overestimates the matrix pressure compared to the reference. The low-pressure (outflow) sides of the fractures show predominantly underestimations of pressure. Interestingly, fractures that exhibit error concentration around one of the tips, do not necessarily show the opposite error on the other side of the fracture. Maximum pressure deviations from the reference are below $\pm 5\%$.

The errors in the temperature distribution are generally larger than for the pressure as the additional error occurs due to the time-stepping. Figure 3.15b shows the percentage error at the final stage of the simulation for a matrix grid discretization of 301x301. Compared with the error in the pressure solution, we find that our model seems to always overestimate the matrix temperature compared to the reference. We find the same region of elevated error in the temperature as in the pressure

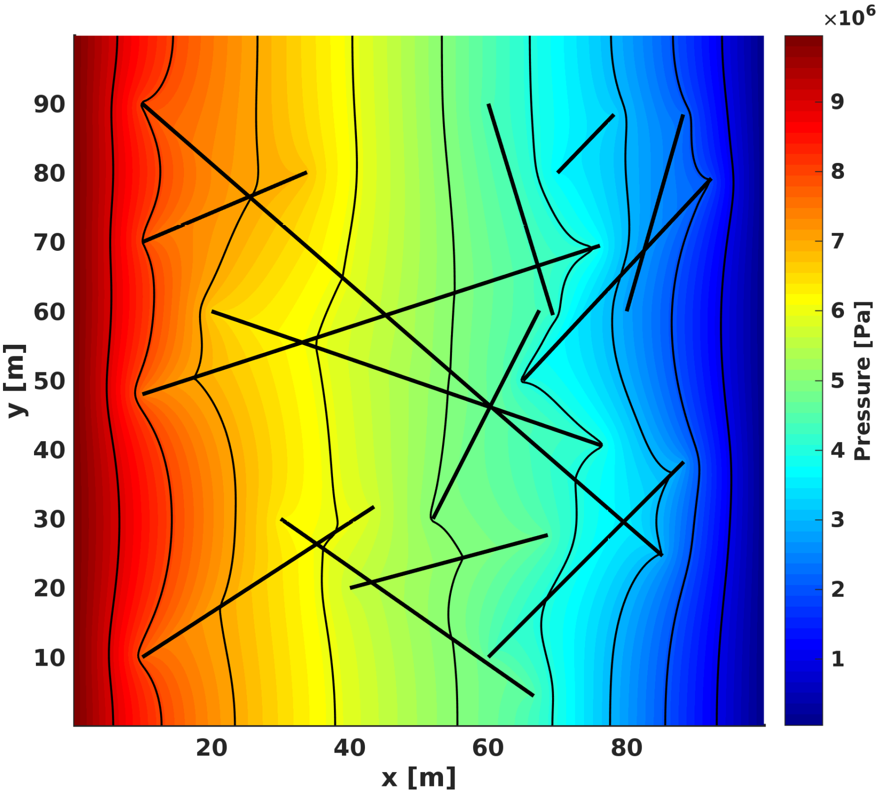

(a) Pressure distribution for the complex fracture geometry.

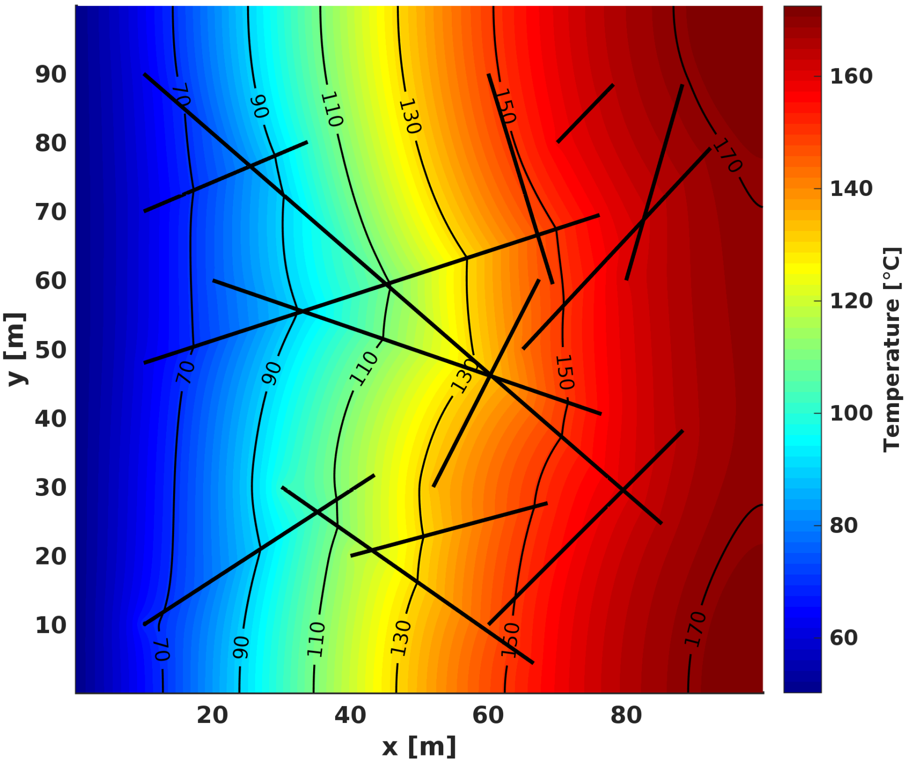

(b) Final temperature distribution in the matrix for the complex fracture geometry

Figure 3.14: The heterogeneous pressure distributions shows the significant influence of the fractures and leads to inhomogeneous fluid velocities, which is consequently shown in the temperature evolution. Resolution: 301x301.

with deviations of up to 10% close to fracture tips that lie in this region. However, the normalized RMS error for this resolution over the whole domain is comparably low at 2.22%. We suspect that the elevated temperature deviations are caused by the relatively small error in the pressure solution. The small error in the pressure leads to comparably larger differences in flow velocities that are controlling heat advection. Thus, over a simulation of 40 years this error accumulates to the values observed here.

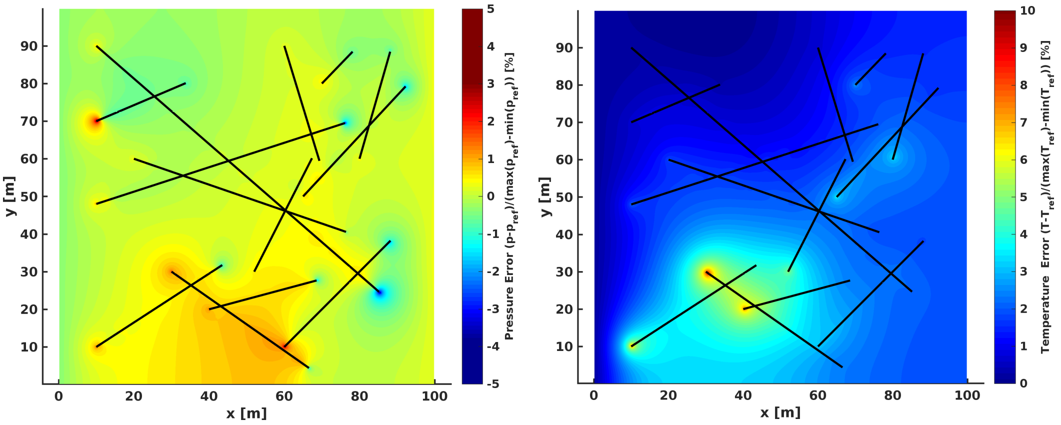

(a) **(b)**

Figure 3.15: Deviation of THERMAID (resolution 301x301) from reference solution: **a)** Pressure. A region of elevated error is visible in the lower part of the domain. Significant deviations are also visible at some fracture tips. **b)** Temperature. Measured at the final stage of the simulation. The error in the pressure solution are reproduced in the temperature solution. The matrix temperatures are generally overestimated compared with the reference.

We further want to investigate the influence of the resolution on the accuracy of the results, so we compare four different resolutions (101x101, 301x301, 501x501 and 1001x1001). We investigate the improvement of solution accuracy in the pressure and heat transport solutions by using the NRMSE and NMAE values compared to the high resolution solution obtained by *COMSOL*. Table 3.5 shows both error measurements for all resolutions. We find a general improvement of the accuracy with an increase in resolution. For the temperature, this is a decrease in NRMSE from 4.6% (101x101) to 1.2% (1001x1001). The pressure error is consistently about one magnitude smaller, showing a decrease from 0.78% (101x101) to 0.15% (1001x1001). Overall we find a significant increase in accuracy with an increase in resolution. Nevertheless, the deviation is not changing significantly between 501x501 and 1001x1001 (1.74% vs 1.22% in case of the temperature). This indicates a systematic difference between the reference solution and our method. There are multiple possible origins of this systematic error. Since we observe the systematic deviation also in the pressure, we think it is likely to be a difference in methodology concerning the fluid flow equation. These differences could include the treatment of fracture-fracture intersections, the definition of matrix-fracture

Table 3.5: NRSME and NMAE errors for the second coupled fluid flow and heat transport equation benchmark in dependence of resolution.

	$\mathbf{p^m}$		$\mathbf{T^m}$	
	NRMSE [%]	**NMAE [%]**	**NRMSE [%]**	**NMAE [%]**
101 x 101	0.78	0.64	4.59	4.0
301 x 301	0.35	0.26	2.22	1.87
501 x 501	0.23	0.17	1.74	1.51
1001 x 1001	0.12	0.12	1.11	1.02

interface permeability, and inherent numerical differences between finite element and finite volume methods. As mentioned above, the time discretization is further causing additional errors, magnifying them with time.

Although the observed deviations are larger than in the previous benchmark experiments, we nevertheless find very good agreement between the reference simulation and our implementation for large parts of the model. Even in regions of significantly elevated deviation, we find acceptable agreement with differences below 10% between the two methods. The definitive source of the difference is currently not resolved but presents excellent future research opportunities.

3.4.5 Utilization of the fracture stability analysis

We present the fracture stability analysis to show the influence of permeability enhancement, thermal stress, and the orientation of the simulation plane on fracture stability. We model fluid injection into a complex fracture network with a range of fracture orientations. The geometry consists of a total of 196 fractures within a square domain (Figure 3.16). The borehole is located in the middle of the domain with an open hole section of 6m. Above the injection region of the well, its influence on the reservoir is neglected here for simplicity. The fracture aperture in the reservoir is set to $b = 0.1mm$. The remaining parameters used in this section are shown in Table 3.6. The upper limit of the fractured reservoir domain is assumed to be at 5km depth. The injection pressure is held constant at 25MPa overpressure. To all sides of the domain a no-flow Neumann boundary is applied. The principal stresses are oriented as shown in Figure 3.3, which corresponds to a normal faulting regime. The magnitudes of the principal stresses are 125MPa, 107.5MPa and 81.25 MPa respectively, which corresponds to a relative stress ratio of $R = 0.4$. The in-situ pore pressure is assumed to be hydrostatic ($\sim$ 50MPa). The stress conditions roughly resemble the relative conditions at the Fenton Hill and Hijiori geothermal projects although both projects were situated above 4km depth (Xie et al., 2015; Barton et al., 1988; Oikawa and Yamaguchi, 2000).

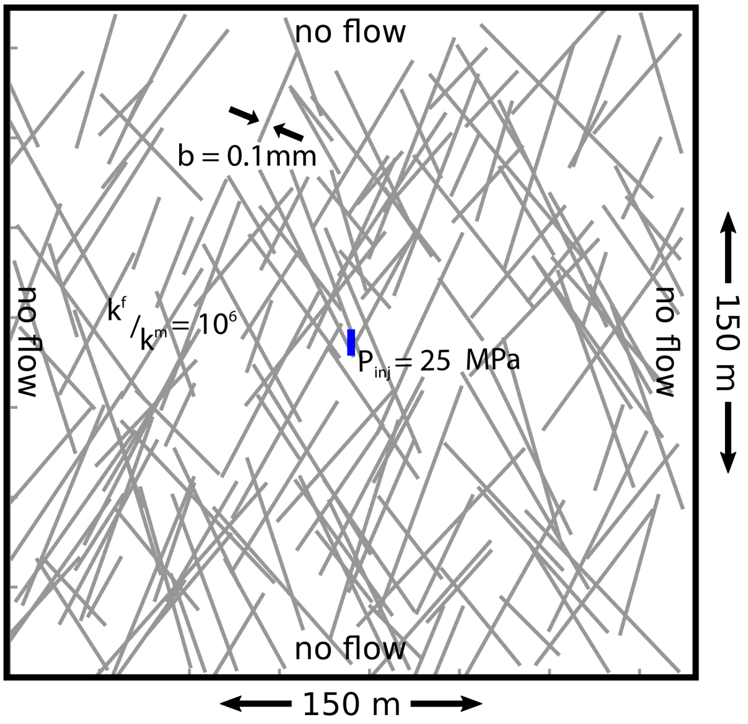

Figure 3.16: Numerical setup to evaluate the fracture stability on a realistic complex fracture geometry. A constant injection pressure of 25MPa is applied in the borehole (blue line). On the outer boundaries a no-flow boundary condition is applied. All parameters for this model setup are shown in Table 3.6.

Table 3.6: Properties used in the fracture stability analysis model. Superscripts: f - fracture, m - matrix. Subscripts: f - fluid, r - rock.

Permeability	$k^f = 1 \cdot 10^{-12} m^2$	$k^m = 10^{-18} m^2$
Porosity	$\phi^f = 0.9$	$\phi^m = 0.1$
Density	$\rho_f = 1 \cdot 10^3 \frac{kg}{m^3}$	$\rho_r = 2.5 \cdot 10^3 \frac{kg}{m^3}$
Viscosity	$\mu_f = 1 \cdot 10^{-3} Pa \cdot s$	
Specific heat	$c_{p_f} = 4000 \frac{J}{kg \cdot K}$	$c_{p_r} = 1000 \frac{J}{kg \cdot K}$
Thermal conductivity	$\lambda_f = 0.5 \frac{W}{m \cdot K}$	$\lambda_r = 2.0 \frac{W}{m \cdot K}$
Thermal expansion. coeff.	$\alpha = 7.9 \cdot 10^{-6} K^{-1}$	
Shear modulus	$G = 29.0 GPa$	
Poisson ratio	$\nu = 0.25$	

Simulation in a sub-critical stress state In a sub-critical stress state, the local coordinate system is in the $\sigma_1 - \sigma_3$ plane as shown in the last row in Figure 3.3. Within this orientation the maximal shear stress values will be observed and thus high fracture slip potential is expected. We evaluate the results after 10 days of continuous fluid injection.

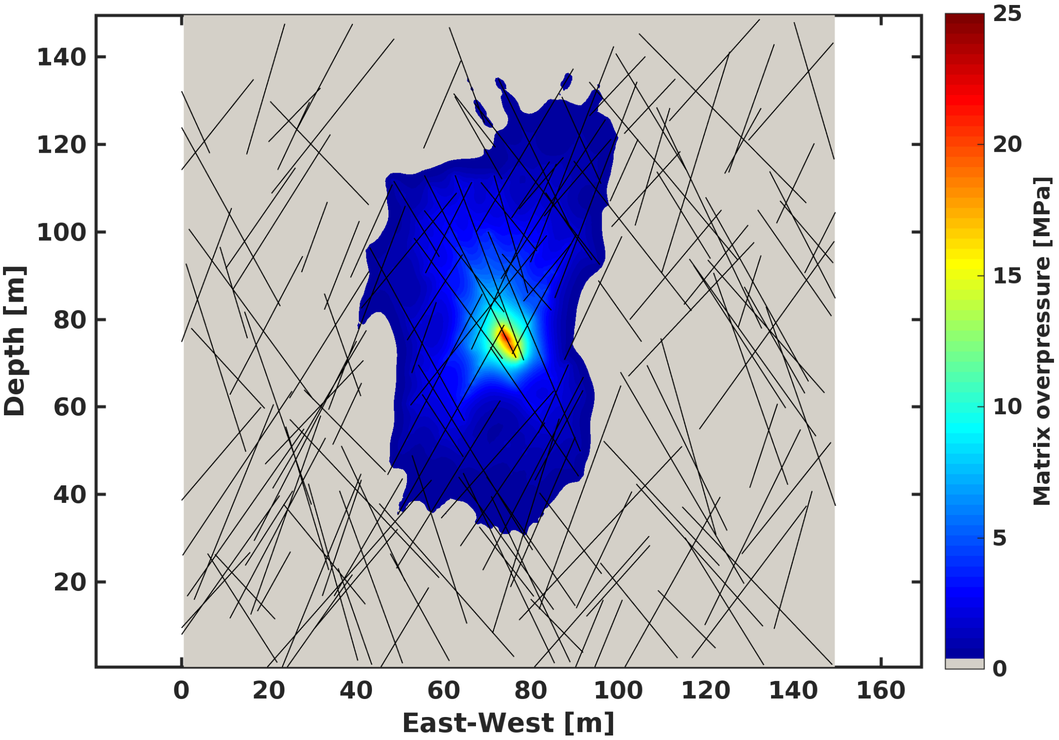

Figure 3.17: Matrix pressure in the reservoir after 10 days of injection. Due to the orientation of the fractures a preferential flow direction in the vertical direction is visible.

Figure 3.17 shows the pressure distribution after 10 days of injection. Due to the orientation of the pre-existing fractures, a preferential flow direction in the vertical direction is visible. Slight pressure changes due to the injection are measured at distances up to 55m in the vertical and 35m in the horizontal directions from the injection point. The zone of 10MPa pressure changes extends roughly 10m around the borehole. Very high pressures $> 20\text{MPa}$ are concentrated in the direct vicinity of the injection.

The in-situ fracture stability is influenced by the additional injected fluid pressure. Figure 3.18 shows the final normalized fracture slip tendency. Note that a normalized slip tendency value of 1 represents a fracture that is eligible for failure and slip. We observe a range of values in the reservoir based on the fractures' orientations. The average fracture stability is high with values well below the failure condition. However, closer to the injection the increased slip tendency due to the injection is visible. Zones with fluid overpressure of $> 5\text{MPa}$ show significant increase in slip tendency (yellow colors in the plot). The region with at least 10MPa additional fluid pressure is very close to or eligible for slip on the fracture.

Permeability enhancement in the sub-critical stress state In the previous section fracture segments eligible for slip did not have any feedback on the fluid pressure distribution. Here we investigate this feedback by introducing the stepwise permeability enhancement for failing fractures. The setup used is identical to the previous section

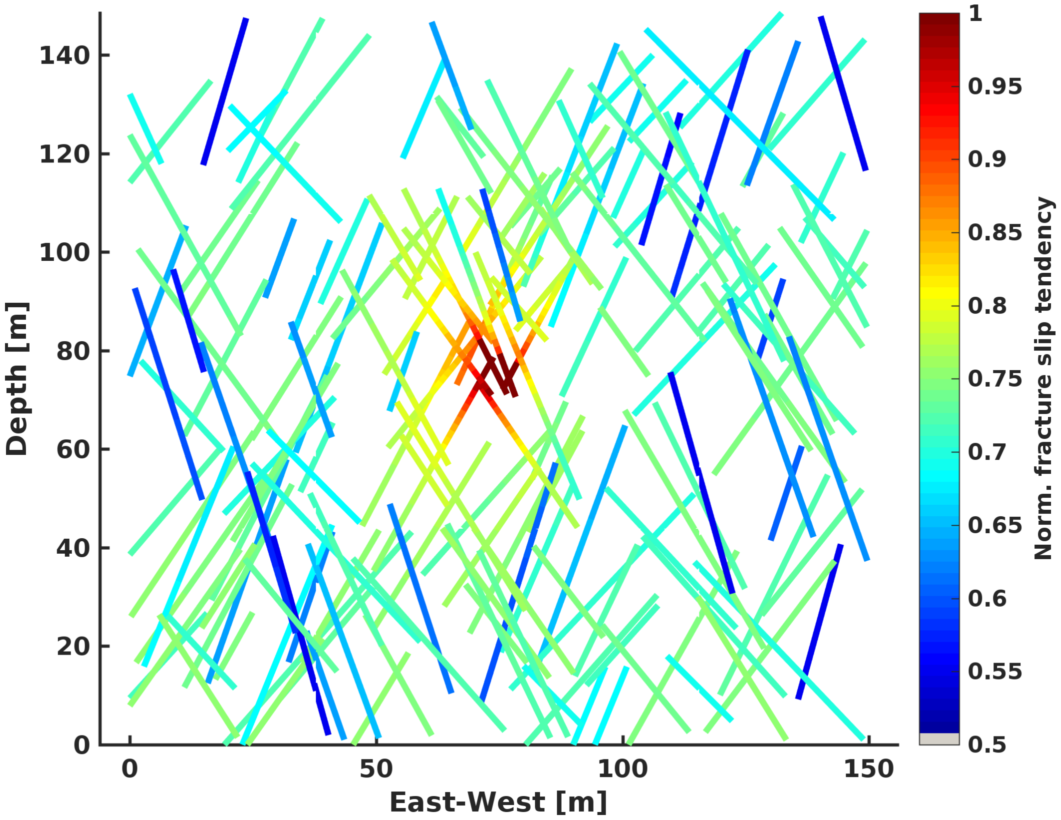

Figure 3.18: Fracture stability in terms of normalized slip tendency in the reservoir after 10 days of injection. Values are normalized by the friction coefficient $\mu = 0.6$. High values denote higher slip tendency. The general fracture stability is good at levels well below the instability condition. Stability reduces closer to the injection. Very close to the injection point high fluid pressures lead to unstable fracture segments (red).

except a 10-fold increase in permeability is assumed for failing fracture segments. Figure 3.19 shows the pressure distribution after 10 days of injection if permeability enhancement is considered. Although the general flow directions remain unchanged, the fluid pressure distribution shows significant differences in extent and magnitude. Small pressure variations are visible over the whole vertical extent of the domain. The horizontal extent has increased as well, but appears to be more non-symmetric in this case. As fracture density is a little higher on the left side of the injection point, the extent of the pressurized zone is larger on the left than on the right side of the borehole. Very high fluid pressures (> 20MPa) are concentrated at the borehole. However, a large zone of $\sim 10 - 15$MPa overpressure is now present up to 35m from the borehole due to permeability enhancement.

Fracture stability is changed drastically if permeability enhancement is considered (cf. Figure 3.20a). The in-situ fracture stability remains unchanged in the outer regions of the domain at very stable levels. On the other hand, most of the fractures within the overpressured regions show elevated slip tendency with fractures closer to the injection being eligible for slip. Compared to the previous simulation, 20-times more fracture segments are unstable and capable of slip. Failing fractures, which have increased in permeability allow fluid to propagate more easily. As we assume a constant pressure injection, the amount of injected fluid is increased significantly. In this way a much larger stimulated area is observed compared to the case without permeability enhancement.

Thermal stress has only a small influence during the relatively short injection period of 10 days in this simulation. The resulting thermal stress distribution is shown in Figure 3.20b and shows thermal stresses concentrated at the borehole. As the fractures within the vicinity of significant thermal stress are eligible for slip also by the injection fluid pressure, no additional unstable fracture segments are observed. In the following we will present a rotated model in which the thermal stress becomes important for reservoir stimulation.

Simulation in a stable stress state We demonstrate the influence of stress field orientation on fracture stability in this section. The local reference system is rotated by 90° compared to the previous example so that the simulation takes place in the $\sigma_1 - \sigma_2$ plane. This corresponds to a stable stress state and is shown in the first row of Figure 3.3. Note that the fractures' orientations remain unchanged in the local reference system. Within this orientation the maximal normal stresses will be observed and thus comparably low fracture slip potential is expected.

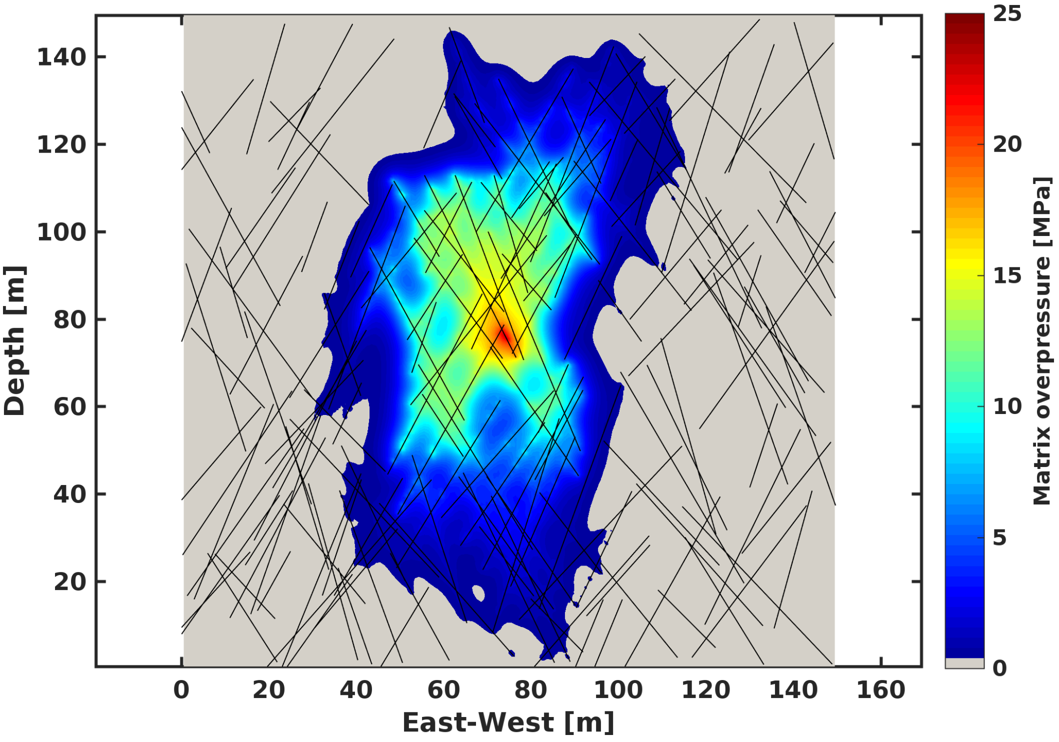

Figure 3.19: Matrix pressure in the reservoir after 10 days of injection if permeability enhancement is used. Here a enhancement factor of $\gamma = 10$ is used. Due to the constant injection pressure and increased permeability in unstable fracture segments, the high-pressure zone is increased drastically.

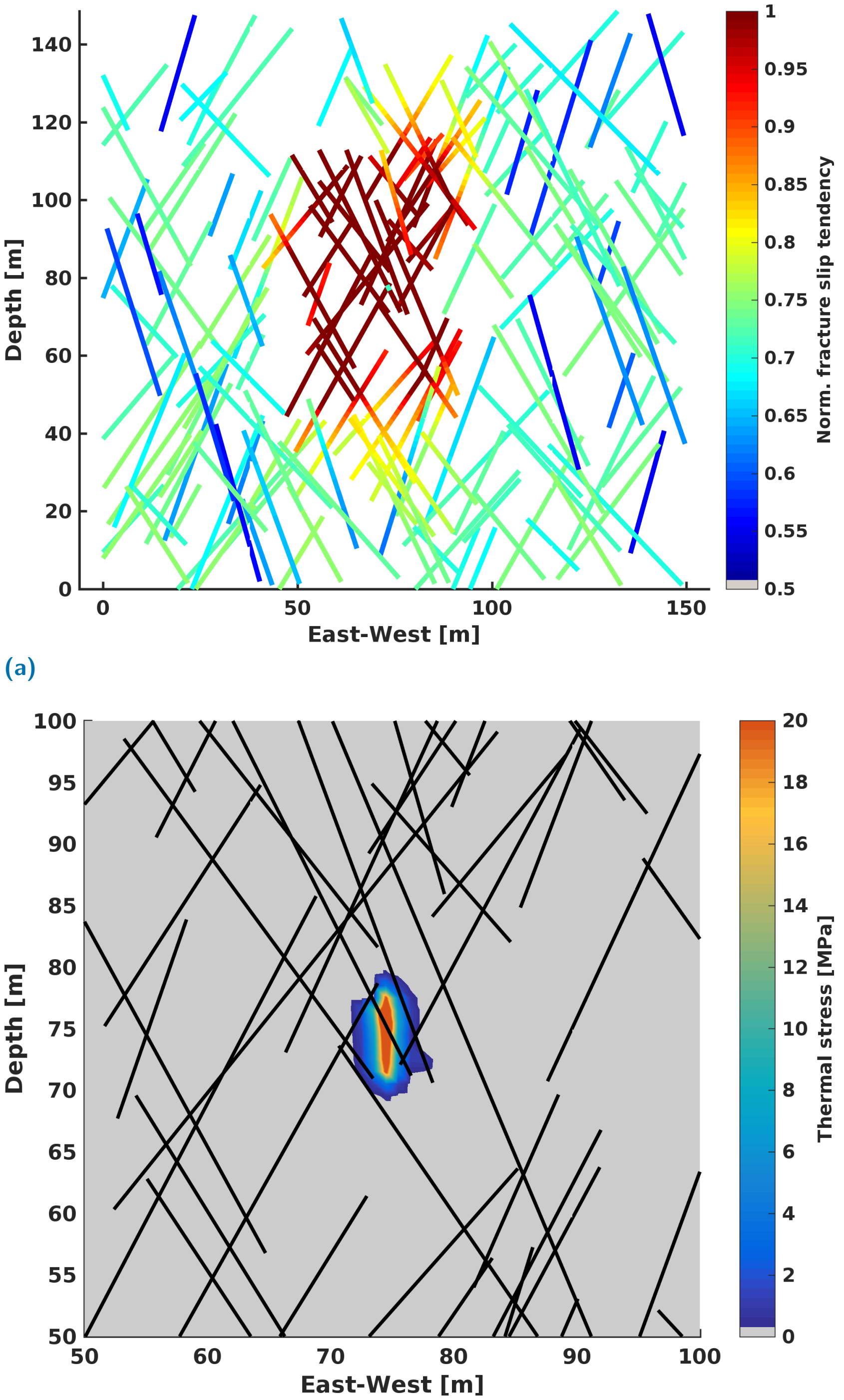

(a)

(b)

Figure 3.20: **a)** Fracture stability in terms of normalized slip tendency in the reservoir after 10 days of injection for the case of permeability enhancement. Values are normalized by the friction coefficient $\mu = 0.6$. High values denote higher slip tendency. Stability drastically reduces closer to the injection as the high fluid pressure zone is much bigger if permeability enhancement is used (red). **b)** Thermal stress after 10 days of injection into the fracture network. The thermal stress is concentrated close to the injection well. The color-scale in the figure starts at 0.25MPa with the darkest blue. Everything below is neglected in the graphical representation and shown in the background color. Note that the absolute value of the thermal stress is shown and all thermal stress here is tensional.

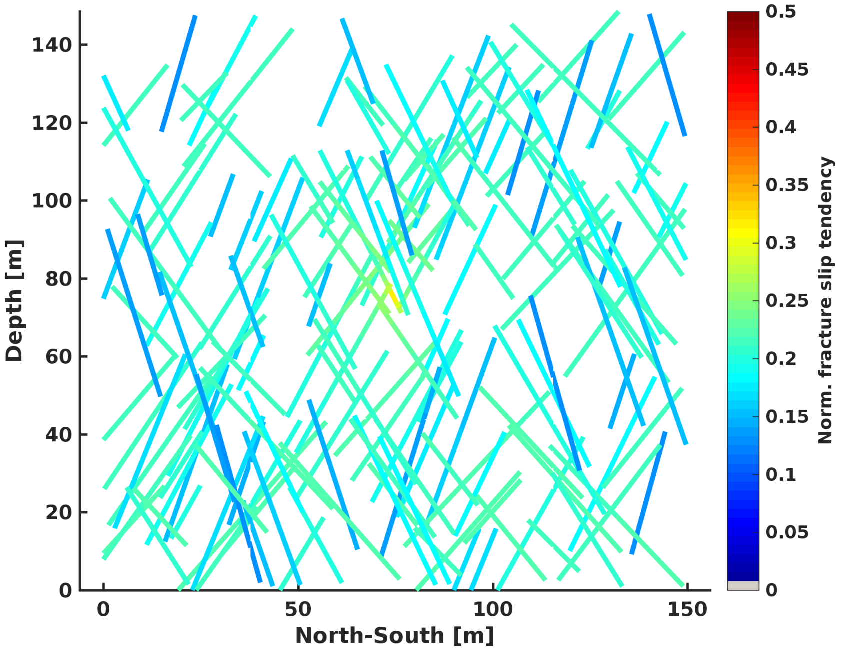

Figure 3.21: Fracture stability in terms of normalized slip tendency in the reservoir after 10 days of injection for the rotated reference system. None of the fractures are close to unstable conditions. Stability reduces closer to the injection but remains completely intact.

Figure 3.21 shows the normalized fracture slip tendency in the $\sigma_1 - \sigma_2$ plane if thermal stresses are neglected. Throughout the whole domain very high stability (i.e. very low slip tendency values) is visible. Note that in Figure 3.21, the range of the color-bar has been changed from [0.5 - 1.0] to [0.0 - 0.5]. This shows that all fractures, even in direct vicinity of the injection, are less likely to slip as the least well oriented fracture in the $\sigma_1 - \sigma_3$ plane. Very close to the borehole a slight increase in fracture slip tendency is visible. Nevertheless, the fracture network remains completely stable during the injection experiment.

The pressure distribution is identical to the pressure distribution obtained in the case without permeability enhancement from the previous section. Although permeability enhancement is allowed in this setup, the fracture stability is very high and no fractures are eligible for slip. Thus the fluid pressure behaves identically to the first example as no further stress - fluid pressure interactions are taken into account.

In a separate simulation, we found that the injection pressure in order to induce any failure in the reservoir under these stress conditions without thermal stress contributions would be at least $50\mathrm{MPa}$. This would lead to fracture instability in the fracture segments that intersect the injection point. An even higher injection pressure of $65\mathrm{MPa}$ would lead to a significant increase in fracture failure and stimulated reservoir volume. However, the stimulated region remains smaller than presented in the previous section and shown in Figure 3.19.

Thermal stress in the stable stress state In a recent study (Jansen and Miller, 2017), we investigated the role of thermal stress in a geothermal reservoir during fluid injection. We found that thermal stresses can facilitate slip on non-optimally oriented fractures, and this is especially important in long-term injection scenarios where the thermal stress changes become more significant with time.

In the previous section we showed that the reservoir remains intact for an injection pressure of 20MPa without thermal stress contributions. Accounting for thermal stress leads to thermal stresses concentrated around the borehole. After 10 days of fluid injection significant increase in failure potential is observed at distances of 5m from the borehole with two fracture segments becoming unstable and eligible for slip.

We further investigate the effect of thermal stress during a one year duration fluid injection in the stable stress state. The results from the previous section suggest that without thermal stress effects the reservoir should remain completely stable also for such long-term injections. Figure 3.22 shows the normalized fracture slip tendency in the $\sigma_1 - \sigma_2$ plane if thermal stresses are explicitly taken into account. Throughout most of the domain very high stability (i.e. normalized slip tendency values < 0.3) is visible. In the vicinity of the injection and distances up to 15m from the borehole, fracture stability is significantly reduced. Note that the color-bar still ranges from [0.0 - 0.5]. After one year of continuous injection, 32 fracture segments exhibit unstable fracture stability values. Interestingly, the propagation of thermal stress appears to be rather homogeneous and mainly driven by heat diffusion from the matrix (cf. Figure 3.22). (Jansen and Miller, 2017) show that thermal stress propagation is largely influenced by the hydraulic properties of both fracture and matrix, and a more fracture-driven thermal stress development is likely to be linked to higher permeability of the surrounding matrix.

The experiments presented here show the importance of stress field orientation and fracture stability analysis. We showed that a stepwise permeability increase in potentially failing fracture segments has a major impact on the stimulated reservoir volume and allows fracture slip in larger parts of the domain. Additionally, thermal stress contributions can lead to reduced fracture stability especially for longer periods of injection. This emphasizes the importance of coupling thermo-hydraulic models with the mechanical changes during fracture slip.

3.5 Conclusion

We developed, implemented and validated a fractured reservoir modeling framework in *MATLAB* for investigating coupled thermo-hydraulic problems including fracture stability analysis in geothermal reservoirs and other naturally fractured systems. The numerical benchmark experiments show the capabilities and accuracy of THERMAID.

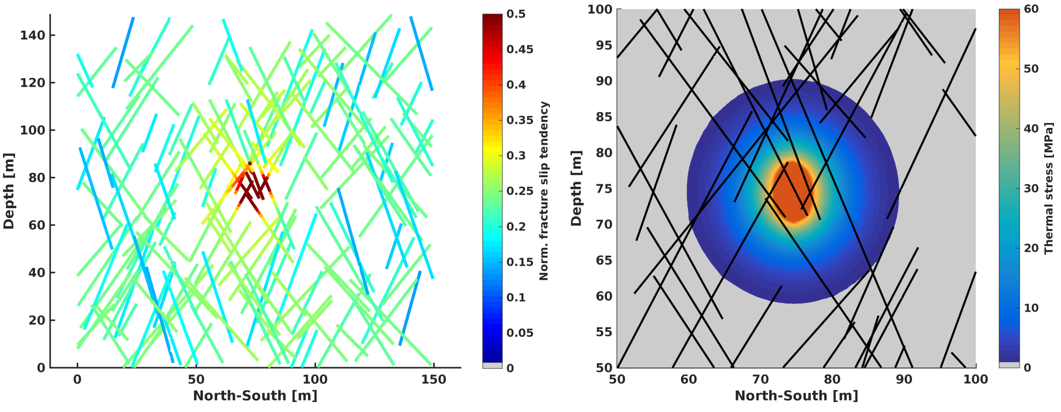

(a) **(b)**

Figure 3.22: **a)** Fracture stability in terms of normalized slip tendency in the reservoir after 1 year of injection for the rotated reference system. Values are normalized by the friction coefficient $\mu = 0.6$. High values denote higher slip tendency. Stability drastically reduces closer to the injection as thermal stress propagates through the reservoir (red). **b)** Thermal stress after 1 year of injection into the fracture network in the rotated reference system. The propagation of thermal stress appears to be rather homogeneous and mainly driven by heat diffusion from the matrix. The color-scale in the figure starts at 0.9MPa with the darkest blue. Note that the absolute value of the thermal stress is shown and all thermal stress here is tensional.

Our results show with high confidence that the accuracy of the implemented *MATLAB* package are within the limits of commercial simulators for fractured reservoirs. Especially the results of the coupled flow and heat transport on a complex fracture network show the importance of discrete fractures in numerical analysis of fractured reservoirs. Both pressure and temperature distributions show heterogeneities due to fracture-matrix interactions. Although the benchmark experiments present slight differences to the reference solutions, the benefits of our open source implementation outweigh these differences. THERMAID presents easy access to the underlying implementation that enables the user to further investigate the embedded discrete fracture model and coupled processes in naturally fractured reservoirs.
As discussed earlier in the results, the deviations in the pressure solution could be caused by different treatment of fracture-fracture intersections or the definition of matrix-fracture interface permeability between the models. Currently there is no clear indication about which weighting to use at fracture-matrix interfaces, which presents an excellent future research opportunity for combined laboratory and numerical experiments. We assume that differences in the temperature solutions are caused by the deviations in the pressure solution that are magnified with time. However, also differences in the numerical treatment of the heat advection term can cause significant errors. The optimal choice of the appropriate numerical scheme remains an open question and should be studied in detail in the future.

We showed that the embedded discrete fracture model is a viable alternative to the existing methods. As numerical discretization is simplified compared to conforming discrete fracture models, dynamic changes of the fracture network are possible without large numerical overhead. The extension of the embedded discrete fracture model to three dimensions has not been discussed so far in this article. Due to the relatively simple numerical discretization, the grid generation process in three dimensions becomes trivial. Additionally, as the two computational domains are independent except for the transfer functions, also the extension of the discretized equations is straight forward. The treatment of the transfer functions involves the intersection of planes instead of lines in three dimensions. Increased flow is expected along the intersection of fractures, which has to be included in the transfer functions. Although the extension to three dimensions is feasible, THERMAID is currently only developed in a 2D version. This is however not a limitation of the embedded fracture model but a computational limitation of the implementation in *MATLAB*. Nevertheless, the approach taken in THERMAID could be efficiently re-implemented and extended to 3D in a high-performance computing environment. The embedded discrete fracture model is not necessarily restricted to regular grids and can be extended to general geometries. However, using regular grids can be advantageous for the application of massively parallel computation techniques to further increase computational efficiency and enable large scale, high resolution simulations.

Our results further show the importance of including the mechanical behavior of fractures and the reservoir in thermo-hydraulic simulations. Although the deformation process during fracture slip was not explicitly taken into account, the assumed step-wise increase in fracture permeability during slip provides a necessary feedback for the pressure equation in order to capture the often observed increase in injectivity during hydraulic stimulation. We propose that changes in permeability and aperture should be incorporated in all models that seek to fully understand the thermo-hydraulic evolution during fluid injection in fractured reservoirs. Although our model exhibits a very simplified view on the complex fracture mechanics, it still provides important insight into reservoir stimulation that helps in identifying some challenges and opportunities for future studies. More advanced models currently under development will consider both pre-existing fractures as in the present work, but also the generation of new fractures in response to the evolving stress state from both thermo-and hydraulic perturbations. Future models might also include fracture roughness and morphology, and solving the full equilibrium equations to estimate aperture changes that influence permeability. Recently, progress in this direction has been made using boundary element methods, multi-point stress approximations (MPSA) and the novel extended finite volume method (XFVM) (Norbeck et al., 2016; Ucar et al., 2016; Deb and Jenny, 2016). However, these models are not yet as computationally efficient as to allow an adaption for THERMAID. A method to estimate magnitude from computed slip (e.g. Heinze et al., 2015), is currently not implemented, but is essential for a mechanistic assessment of seismic hazard associated with injection. Currently, induced seismicity can not be quantified in terms of magnitude because slip on the fracture is not computed. Moreover, fracture slip can occur in a seismic or aseismic manner, thus further complicating the assessment of

induced seismicity. These are all areas that we are currently pursuing in order to extend and refine THERMAID's capabilities.
Although this paper focuses on the application of enhanced geothermal systems, other possible applications for THERMAID include seasonal thermal energy storage in fractured aquifers, and natural or anthropogenic fluid-driven earthquake sequences. Furthermore, a wide range of research questions related to fractured reservoirs and their properties can be addressed using THERMAID. Even beyond the current model capabilities, we expect further applications and research opportunities because the open source code will allow a community to evolve and contribute to this common platform.

THERMAID is an accurate and efficient modeling framework for a broad range of applications in the fractured subsurface. The open source distribution and GNU GPL v3.0 license enables the scientific community to use and modify THERMAID to their needs. The implementation in *MATLAB* ensures that even novice programmers can easily understand the underling equations and their implementation and develop their own numerical models based on the examples provided with THERMAID. Simulation of coupled processes in fractured reservoirs is becoming increasingly important in today's research as it is connected to many possible remedies of climate change. With THERMAID we present a starting point from which new insight can be gained into the complex coupled processes in fractured domains in the subsurface.

On the role of thermal stresses during hydraulic stimulation of geothermal reservoirs

4

> *Nothing has such power to broaden the mind as the ability to investigate systematically and truly all that comes under thy observation in life.*
>
> — **Marcus Aurelius**
> (Roman Emperor from 161 to 180)

The contents of this section are published as: Gunnar Jansen and Stephen A. Miller, “On the Role of Thermal Stresses during Hydraulic Stimulation of Geothermal Reservoirs,” Geofluids, 2017. doi:10.1155/2017/4653278.

4.1 Introduction

One of the primary driving mechanisms for permeability creation in engineered geothermal systems (also known as enhanced geothermal systems), or EGS, involves shear failure induced by fluid injection at high pressures. In environments with low differential stress, tensile fractures may develop if the injection pressure exceeds the minimal principal stress (e.g. fracking). The injection of cold water into a reservoir at substantially higher temperature also induces thermal stress changes that contribute to the overall evolution of the local stress and failure potential. The cooling of the reservoir can lead to thermal fracturing and thus further enhance permeability (Wang et al., 1989; Harlow and Pracht, 1972; Gringarten, 1980; Pearson et al., 1983). On the other hand, thermal fracturing and thermal fracture propagation or fracture reactivation may also contribute to premature cold water breakthrough into producing wells.

The basis for EGS are usually geothermal plays of the "hot dry rock" type where the available water in the porous medium is considered negligible. These conditions are found primarily in metamorphic or igneous terrains with low permeability and porosity containing fractures and faults that provide the major pathways for fluid flow. In geothermal energy systems, the fracture’s surfaces serve as the main heat exchanger. Clearly, pre-existing, critically stressed and optimally oriented fractures provide the most favorable conditions for enhancing permeability of EGS (Ghassemi and Kumar, 2007; Combs et al., 2004).

In this paper we focus on the role of thermal stresses during cold fluid injection and stimulation of an EGS site. Of special interest here is the interplay of hydraulic and thermally induced stresses. The processes involved in permeability creation during hydraulic stimulation act on different timescales. While the poro-mechanical coupling is active throughout the injection, its dominance over thermo-mechanical effects depends on the state of the injection. Thermo-mechanical coupling plays a particularly important role during prolonged periods of injection (weeks to years) because the variation of injectivity with injection water temperatures can be attributed to thermal stress (Ghassemi et al., 2005).
A major concern in EGS is induced seismicity at levels above that tolerated by the local population, in either frequency or magnitude. Usually induced seismic events are attributed to the change in effective stress due to the change in fluid pressure (Shapiro and Dinske, 2009; Goertz-Allmann and Wiemer, 2012; Miller, 2015). However, thermal stress also significantly contributes to induced seismicity in petroleum and geothermal fields (Ghassemi et al., 2005; Sherburn, 1984; Stark, 1990). Stark, (1990) found that in the Geysers geothermal field in northern California, USA, half of the measured earthquakes appear associated with cold water injection.

In this paper we present the theoretical basis for thermal stresses, evaluate the temperature distribution during injection in a borehole, and determine a modeling framework for evaluating the influences of thermal stress generation and propagation in a hypothetical reservoir. We describe the numerical method, and present results of numerical experiments focusing on the influence of thermal stress on permeability, fracture orientation and failure potential. We discuss the results in terms of thermal influence on induced seismicity and reservoir characteristics.

4.2 Theory

Here we present the mathematical basis for the formulation of thermal stresses. In addition, the temperature profile in an injection well is considered because this has a significant impact on the initial conditions of the numerical simulations.

4.2.1 Mathematical description of thermal stress

A body will change its shape and/or volume when exposed to a temperature change ΔT. This change is called *thermal strain* and can be expressed as

$$\epsilon_T = \alpha \Delta T \tag{4.1}$$

where α is the coefficient of linear thermal expansion in $\frac{1}{K}$. In most solids α is positive and on the order of $10^{-6}\frac{1}{K}$. In isotropic materials the thermal strain acts only on the normal strains with the same magnitude. If the body's deformation is restricted, as it would be the case for a small volume inside a rock mass, the strain results in thermal stress.

$$\sigma_T = C \cdot \epsilon_T \tag{4.2}$$

where C is the elastic stiffness tensor of the material. If we restrict ourselves to isotropic conditions, the thermal strain has only normal components with equal magnitude in which case we can simplify the previous expression to

$$\sigma_{T_{ij}} = \frac{E}{1-2\nu} \cdot \alpha \Delta T \delta_{ij} \tag{4.3}$$

where E is the Young's modulus (Pa) and ν the Poisson ratio (-). It is important to note that equation 4.3 is only nonzero for the three normal stresses $\sigma_{Txx}, \sigma_{Tyy}, \sigma_{Tzz}$. It is immediately obvious that larger temperature differences will result in higher thermal stress changes. Additionally, the thermal stress is positive (relative compression) if the temperature difference is positive ($\Delta T > 0$), and if the temperature difference negative, the thermal stress is negative (relative tension). The magnitude of thermal stress can change widely depending on the material. Assuming a constant thermal expansion coefficient $\alpha = 10^{-6} \frac{1}{K}$ and and fixed temperature difference of $\Delta T = -10°C$ the resulting thermal stress for an elastic sandstone ($E =\sim 20GPa$) is 60% smaller than the resulting thermal stress in a typical granite ($E =\sim 50GPa$). The granite would undergo a stress change of 1MPa in this case compared to a 0.4MPa stress change in the sandstone.
Thermal expansion coefficients are well-constrained by experiments, and show only minor influences of temperature and pressure on the thermal expansion coefficients (Richter and Simmons, 1974; Wong and Brace, 1979). Cooper and Simmons, (1977) attributed some change in the thermal expansion coefficient to the formation of micro-cracks by differential expansion of mineral grains. Considering the small magnitude in the change of the thermal expansion coefficient compared with the order of magnitude expected in temperature and pressure change, it is a valid assumption that the thermal expansion coefficient is constant.

In the following we assume that the thermal stress is independent of the fluid pressure and the in-situ stress state of the rock. Thus, the resulting stress can be obtained by superposition of the effective stress ($\sigma_{eff} = \sigma_{tot} - p$) and the thermal stress. Changes in the far-field in-situ stress of the rock are negligible on the timescales of interest for hydraulic stimulation. Considering only stress changes resulting from pore pressure and thermal expansion, we can formulate the total stress change as

$$\Delta\sigma = \Delta p + \Delta\sigma_T \tag{4.4}$$

Other stress contributions as slip induced stresses and stresses induced by chemical reaction have to be considered in a general case. However, for reasons of simplicity we restrict ourselves to only pore pressure and thermally induced stress changes.

4.2.2 Induced shear failure potential

Induced shear failure potential is estimated by a Mohr-Coulomb failure condition. We restrict ourselves to a cohesion-less material with a friction coefficient of $\mu = 0.6$. A fracture segment is able to slip and is thus categorized as "potential slip" if the following condition is met:

$$\tau - \mu\overline{\sigma_n} > 0 \tag{4.5}$$

The effective normal stress $\overline{\sigma_n}$ is defined as

$$\overline{\sigma_n} = \sigma_{eff} + \sigma_T = \sigma_n - p_f + \sigma_T \tag{4.6}$$

where σ_n is the normal stress, p_f is the fluid pressure and σ_T the thermal stress as introduced in the previous section. The effective normal stress $\overline{\sigma_n}$ and shear stress τ acting on a fracture segment are:

$$\overline{\sigma_n} = \frac{\sigma_1 + \sigma_3 - 2p_f + 2\sigma_T}{2} + \frac{\sigma_1 - \sigma_3}{2}\cos 2\theta \tag{4.7}$$

$$\tau = \frac{\sigma_1 - \sigma_3}{2}\sin 2\theta \tag{4.8}$$

where σ_1 and σ_3 are the maximum and minimum principal stresses acting in the far field and θ is the angle between σ_1 and the fracture segment measured from the normal to the σ_1 plane.

The poro-elastic deformation of the fractured reservoir during the injection as well as the deformation due to fracture slip is not included in the present model. Consequently, this simple model does not predict magnitudes or estimation of the amount of slip, but rather identifies when a frictional failure condition is met, similar to other approaches in modeling EGS (Goertz-Allmann and Wiemer, 2012; Miller, 2015).

4.2.3 Heat distribution in a geothermal well

The temperature inside an injection well is not constant with depth. The injected water is heated by the rock mass surrounding the borehole while moving downwards through the borehole. Although the heat distribution in geothermal boreholes can be measured, in many cases it is still useful to describe it mathematically. Such calculations can be used in numerical simulations and aid the drilling crews during their operation. In most cases description of well bore heat transmission is based on a well bore heat balance equation. Most of the literature is based on the initial work of Ramey, (1962) in which he derived the temperature distribution in a well used for hot fluid injection. The work was later enhanced by the rate of heat loss from the well to the formation by Ramey, (1964). The main assumptions of Ramey's model are a homogeneous and isotropic formation, constant fluid properties and fluid flow at constant flow rate in the direction of the well only. Recent work from Hagoort, (2004) re-evaluated Ramey's classical work and found that it is an excellent approximation.

Following Satman and Tureyen, (2016) the temperature in an injection well into which a single phase fluid is injected is given by

$$T(z) = T_{surf} + \alpha \cdot z + (T_{inj} + T_{surf} + \alpha A) \cdot e^{(-\frac{z}{A})} \tag{4.9}$$

Here, z is the distance downwards from surface in meters, α the geothermal gradient in $\frac{°C}{m}$, T_{surf} is the surface temperature in $°C$ and T_{inj} the temperature in $°C$ of the injected fluid. A is a variable defined as

$$A = \frac{Q c_{pf} f(t)}{2\pi\lambda} \tag{4.10}$$

where Q is the mass flow rate in $\frac{kg}{s}$, c_{pf} the heat capacity of the fluid (assumed constant) and λ the thermal conductivity of the formation (also assumed constant with depth). The dimensionless function $f(t)$ describes the transient heat transfer to the formation. There are a number of different formulations for the function $f(t)$ available. Here we assume that the temperature at the boundary between the fluid in the well and the formation is constant and that the heat flow in the formation is conductive. For simplicity, we further assume a single-phase liquid flowing in a casing without tubing.Kutun et al., (1981) provide a simple formulation for this case

$$f(t) = \ln\left(1 + 1.7\sqrt{t_D}\right), \tag{4.11}$$

which is based on a best curve fit of the data provided by Ramey, (1962), Ramey, (1964), and Ramey, (1981). According to Satman and Tureyen, (2016) it is accurate within 1% for the relevant time scales. In equation 4.11 t_D is a dimensionless time defined by

$$t_D = \frac{\kappa \cdot t}{r_w^2}; \tag{4.12}$$

where κ is the mean thermal diffusivity of the formation in $\frac{m^2}{s}$ and r_w the well radius in meters.

A detailed review on the methods to describe well bore heat distributions, prevalent assumptions and different formulations for the transient heat transfer function $f(t)$ can be found in Satman and Tureyen, (2016).

Based on equations 4.9 to 4.12 the general characteristics of fluid injection in the well are presented and examined in detail. The model parameters are given in Table 4.1. Figure 4.1 shows the temperature distribution with depth of well bore temperature during prolonged fluid injection. The profiles are plotted for different

injection times: 1d, 10d, 30d, 365d. The geothermal gradient shown as a dashed line represents also the static (long term) temperature distribution in the well bore. It is clearly visible that it is not a static profile but contains a dynamic evolution with time. During the first days of injection, the temperature profile changes most rapidly. After about 10 days of continuous injection, the rates of the temperature profile change decreases. After 365 days of continuous injection, the bottom hole temperature has decreased from $70°C$ after 1 day of injection to $52°C$ in the case of an injection rate of $40\frac{kg}{s}$. Is the injection rate lower at $20\frac{kg}{s}$ the temperature decreases from initially $93°C$ after 1 day of injection to $63°C$ after one year. This demonstrates the highly dynamic temperature distribution during injection with respect to time and injection rates.
The dynamic behavior is driven by advective heat transfer during injection of the fluid at the well-head, and conductive heat exchange with the formation. Initially heat transfer from the formation to the fluid is high, leading to a rapid increase in the fluid temperature. During the course of injection, the formation is cooled by the injected fluid leading to reduced conductive heat transfer from the formation to the fluid. This subsequently lowers the overall temperature distribution in the well bore.

Figure 4.1 shows that the temperature within the wellbore varies greatly with depth and time of the injection. This shows that the assumption of a constant temperature distribution in the well in numerical modeling of fluid injection is generally not valid. Especially for very low injection rates (not shown here), the thermal gradient in the borehole is comparable to the static geothermal gradient. In long duration high injection rate scenarios a constant temperature at the borehole becomes more acceptable as the formation is cooled quickly and the well bore temperature approaches the injection temperature. From the findings of this section we can conclude that the temperature change in the well bore is significant and must be taken into account when thermal stresses are to be evaluated accurately.

Table 4.1: Properties used in estimation of well temperature profiles.

Surface temperature	$20°C$
Injection temperature	$40°C$
Geothermal gradient	$0.04\frac{°C}{m}$
Well depths	$5000m$
Well radius	$0.11m$
Injection rate	$20/40\frac{kg}{s}$
Rock density	$2650\frac{kg}{m^3}$
Mean thermal conductivity (formation)	$2.92\frac{J}{ms°C}$
Mean thermal diffusivity (formation)	$1.102 \cdot 10^{-6}\frac{m^2}{s}$
Specific heat capacity (fluid)	$3160\frac{J}{kg°C}$

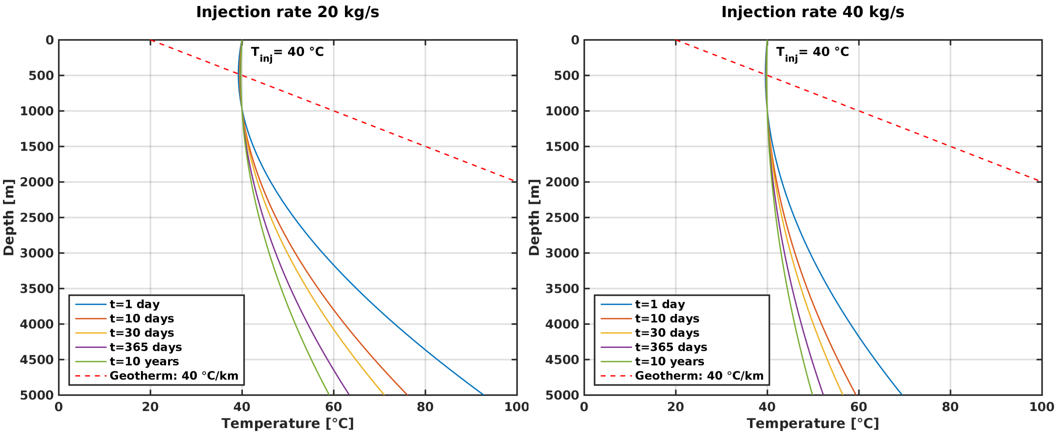

(a) **(b)**

Figure 4.1: Temperature profiles in a 5km deep injection well for an injection temperature of $40°C$ and an injection rate of $20\frac{kg}{s}$ (left) and $40\frac{kg}{s}$ (right).

4.3 Methods

We developed an embedded discrete fracture model (EDFM) using the phenomenology described in other studies (Hajibeygi et al., 2011; Karvounis, 2013; Pluimers, 2015). The conceptual idea of the EDFM is the distinct separation of a fractured reservoir into a fracture and a damaged matrix domain. We introduce a transfer function to account for coupling effects between the two domains, so the fracture and matrix domains are computationally independent except for the transfer function. As the fractures are generally very thin and highly permeable compared to the surrounding matrix rock, the gradient of fracture pressure normal to the fracture is negligible. This allows for a lower dimensional representation of fractures (i.e. 1D objects within a 2D reservoir).

The flow in naturally fractured reservoirs is often described by the equations for nearly incompressible single-phase flow. We note that the following equations are assumed valid in both the damaged matrix and the fractures. From mass balance and single-phase fluid flow, the pressure equation is,

$$\phi\left(\beta_f + \beta_r\right)\frac{\partial p}{\partial t} = \nabla \cdot \left[\frac{k}{\mu}(\nabla p - \rho_f g)\right] + q \tag{4.13}$$

Where ϕ [-] is the porosity, ρ [$\frac{kg}{m^3}$] is the fluid density and p [Pa] is the fluid pressure. The compressibilities β [Pa^{-1}] are denoted with the subscripts f for fluid and r for rock, respectively. Moreover, k [m^2] is the permeability and μ [$\frac{1}{s}$] the fluid viscosity. From the fluid pressure p, the fluid velocity is calculated using Darcy's law, i.e.

$$\mathbf{v} = -\frac{k}{\mu}\nabla p \tag{4.14}$$

The velocity can subsequently be used in the heat transport equation. The heat transport equation is derived similarly to the continuity equation by the balancing the heat transport mechanisms and described as

$$\overline{c_p}\rho_f \frac{\partial T}{\partial t} + c_{p_f}\rho_f \mathbf{v}\nabla T - \overline{\lambda}\nabla^2 T = 0 \tag{4.15}$$

if local thermal equilibrium is assumed. Over-lined properties denote volume averaged mean values for the porous medium (i.e. $\overline{c_p} = \phi c_{p_f} + (1-\phi)c_{p_r}$).

As the methodology and its implementation is described in detail in chapter 3 further details are omitted at this point.

4.4 Results & Discussion

We present the results of three numerical experiments that provide insight into the effects of thermal stress on the stimulation of a geothermal reservoir. First we evaluate the influence of contrasts in the fracture permeability and the fracture-matrix permeability. We then investigate the influence of the fracture orientation on potential slip in combination with thermal stress. In a final numerical experiment, we simulate fluid injection into a complex fracture network over a prolonged period to evaluate the temporal evolution of thermal stress and failure potential. In all experiments the pressure and/or temperature dependence of the fluid density and viscosity is taken into account. The underlying equation of state is given by Sun et al., (2008) for density and Al-Shemmeri, (2012) for the viscosity of water. In this section we combine results and their discussion to emphasize each experiment's outcome. A more general discussion of the results as well as a conclusion is provided in section 4.5.

4.4.1 Influence of fracture & matrix permeability on thermal stress

Fracture permeability is one of the most important variables to be determined in EGS reservoirs to accurately predict flow in the reservoir. Here we evaluate to what degree the fracture permeability has an impact on thermal stress. To this end we model the fluid injection in a well that is intersected by a single fracture as depicted in Figure 4.2.

Table 4.2 lists the physical parameters for the matrix and fracture used in this study. In this experiment, we investigate the results after a continuous injection of 30 days. In contrast to the previously presented temperature distribution in the well, we assume a homogeneous temperature distribution in the open hole section throughout the injection as the open hole section is short (100m) compared to the length of the borehole. The injection temperature is variable with time and obtained by a

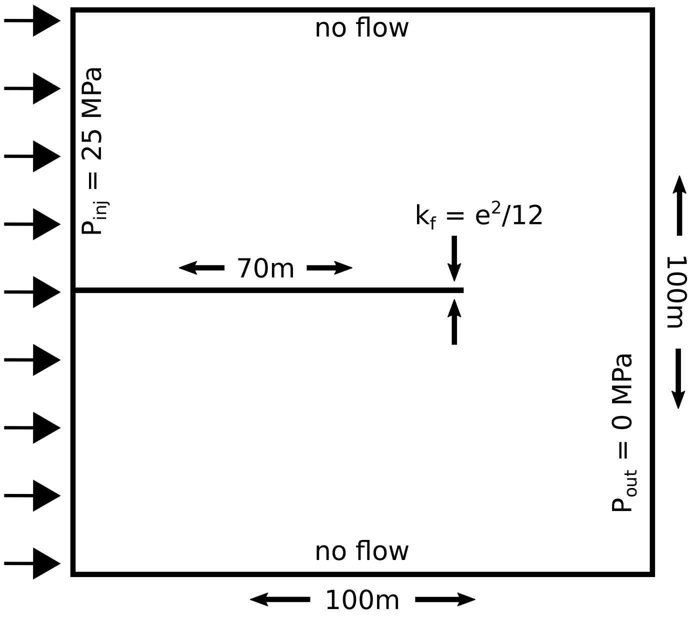

Figure 4.2: Numerical setup to evaluate the influence of fracture permeability on thermal stress. A constant injection pressure is applied to the left side of the domain. The right side serves as a zero pressure outflow well.

least-squares fit of the data presented in Figure 4.1 for a depth of 5km. The initial temperature is set at $T_0 = 200°C$. The injection pressure is constant at 25 MPa. Gravity is neglected in this experiment. We vary the fracture permeability in five steps over a range from $8.33 \cdot 10^{-8} - 1 \cdot 10^{-12} m^2$. Further we evaluate two matrix permeabilities $10^{-16} m^2$ and $10^{-18} m^2$.

Figure 4.3 shows the temperature distribution and resulting thermal stress after 30 days of fluid injection for a matrix permeability of $10^{-16} m^2$. The temperature profiles along the fracture show significant differences based on fracture permeability. For the two highest fracture permeabilities ($k_{fr} = 10^{-12}/10^{-11} m^2$) the profiles are very similar and show temperature variations only within the first 10 meters of the frac-

Table 4.2: Properties used in the fluid injection simulation.
Subscripts: fr - fracture, m - matrix, f - fluid, r - rock.

Permeability	$k_{fr} = 8.33 \cdot 10^{-8} - 10^{-12} m^2$	$k_m = 10^{-16/-18} m^2$
Porosity	$\phi_{fr} = 1.0$	$\phi_m = 0.1$
Compressibility	$\beta_f = 5 \cdot 10^{-10} \text{Pa}^{-1}$	$\beta_r = 1 \cdot 10^{-10} \text{Pa}^{-1}$
Specific heat	$c_{p_f} = 4000 \frac{J}{kg \cdot K}$	$c_{p_r} = 1000 \frac{J}{kg \cdot K}$
Thermal conductivity	$\lambda_f = 2.92 \frac{W}{m \cdot K}$	$\lambda_r = 0.5 \frac{W}{m \cdot K}$
Thermal expansion. coeff.	$\alpha = 7.9 \cdot 10^{-6} K^{-1}$	
Shear modulus	$G = 29.0 GPa$	
Poisson ratio	$\nu = 0.25$	

ture. At the injection point the temperature dropped down to approximately $140°C$. The resulting thermal stress is approximately -70MPa. An intermediate fracture permeability of $k_{fr} = 10^{-10}m^2$ shows a further propagation of the thermal front within the 30 days. We observe temperature change on almost 60m of the fracture resulting thermal stress perturbations along the same length. At an approximate distance of 30m from the injection point, the thermal stress reaches -9MPa. The two highest tested permeabilities ($k_{fr} = 8.33 \cdot 10^{-8}/8.33 \cdot 10^{-10}m^2$) show distinctively different profiles compared to the lower permeability values. Here the temperature propagates the full length of the fracture with an almost linear profile. The temperature at the injection point however is greater than for the other permeabilities with approximately $150°C$. Due to the temperature profiles, the thermal stress is significantly larger along the whole length of the fracture for these very permeable fractures.

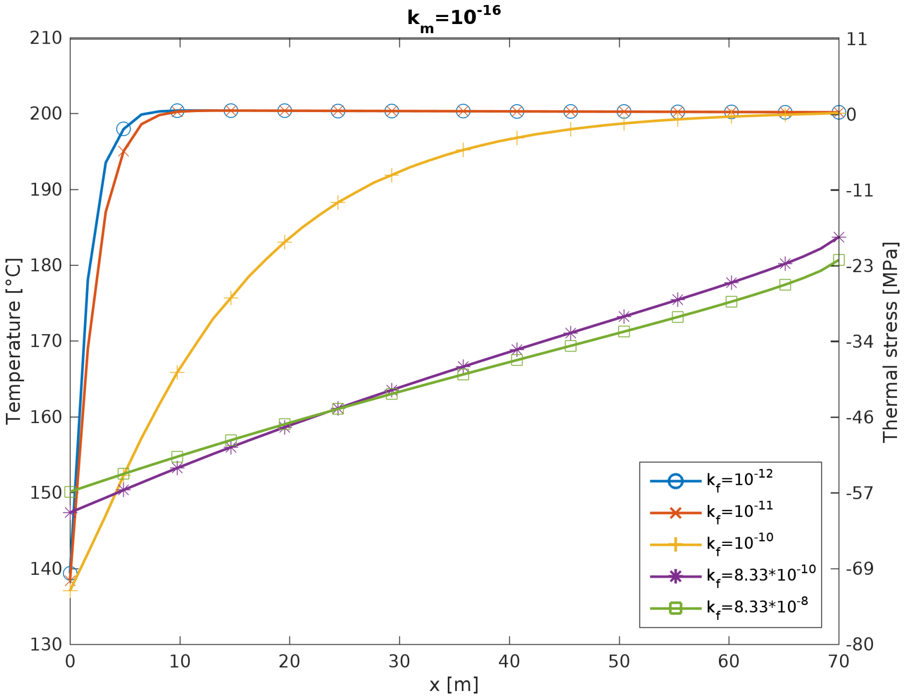

Figure 4.3: Temperature and thermal stress distributions after 30 days of injection for a matrix permeability of $k_m = 10^{-16}m^2$.

We further evaluated the mean velocity in the fracture throughout the 30 days of injection. The result is shown in Figure 4.4. Overall the mean velocity varies over four orders of magnitude due to the wide range of fracture permeabilities. For all fracture permeabilities an initial decline in the fracture velocity is visible. This is more pronounced for high fracture permeabilities ($k_{fr} = 8.33 \cdot 10^{-8}/8.33 \cdot 10^{-10}m^2$) with a "stabilization time" of only a couple of days. Lower fracture permeabilities show less variability in the mean fracture velocity.

Figure 4.5 shows the temperature distribution and resulting thermal stress after 30 days of fluid injection for a matrix permeability of $10^{-18}m^2$. The temperature

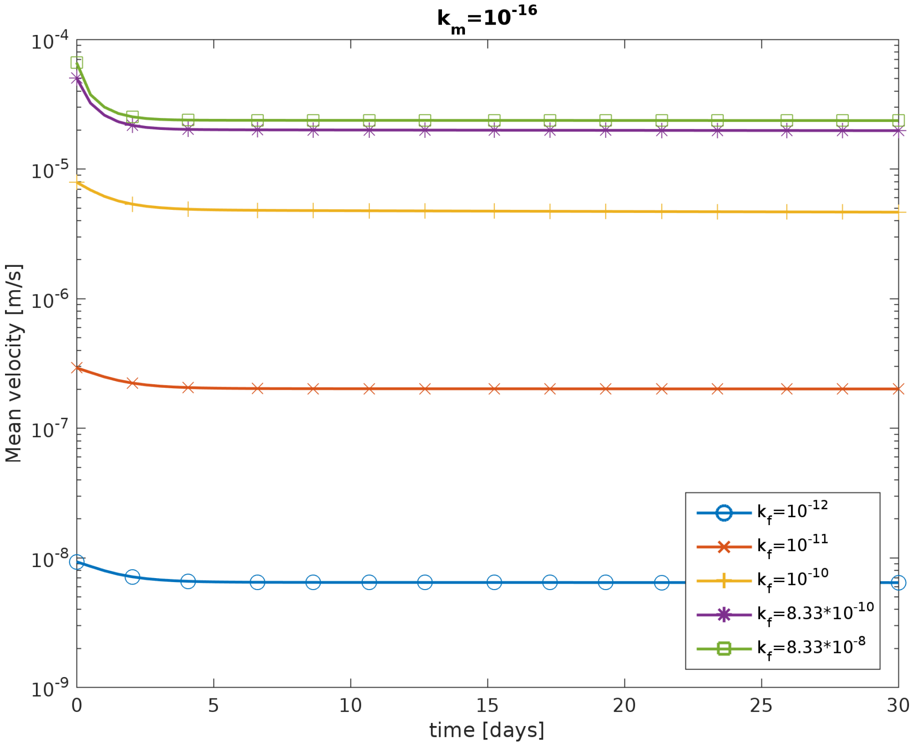

Figure 4.4: Mean fracture velocity during the simulated 30 days of injection.

profiles along the fracture show significantly fewer differences compared to higher matrix permeability. The three highest permeabilities show nearly identical behavior. The temperature front advanced as far as 25m, which is the maximum for a matrix permeability of $k_m = 10^{-18}m^2$. The two higher fracture permeabilities ($k_{fr} = 10^{-12}/10^{-11}m^2$) show less temperature change after 30 days compared to the other permeabilities as well as the higher matrix permeability. All profiles exhibit a temperature at the injection point of $150 - 155°C$.

A comparison of thermal stress distribution for the fracture permeability $k_{fr} = 10^{-10}m^2$ with both matrix permeabilities is shown in Figure 4.6. As already discussed earlier the different propagation depths of the temperature and thus thermal stress is visible. Additionally, the matrix effect is also shown. For the higher matrix permeability the thermal stress front propagates as far as 6m into the reservoir, and we observe a wedge-shaped thermal stress disturbance close to the fracture. In the case of the lower matrix permeability, the thermal stress front barely penetrates the matrix. The 1MPa isoline is already at a distance of approximately 2 meters from the injection well. Close to the fracture a more pronounced thermal stress alteration zone is visible. In contrast to higher matrix permeability this zone is relatively small.

Figure 4.7 shows that the pressure diffusion for the higher matrix permeability is much more homogeneous than for a lower matrix permeability, leading to a significant pressure gradient in the fracture. If the matrix permeability is very

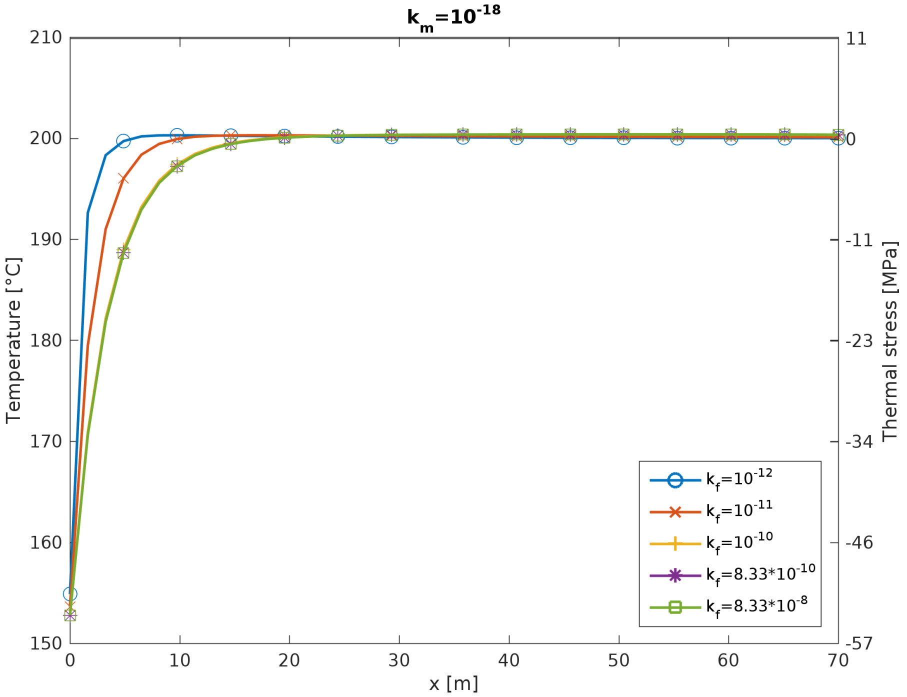

Figure 4.5: Temperature and thermal stress distributions after 30 days of injection for a matrix permeability of $k_m = 10^{-18} m^2$.

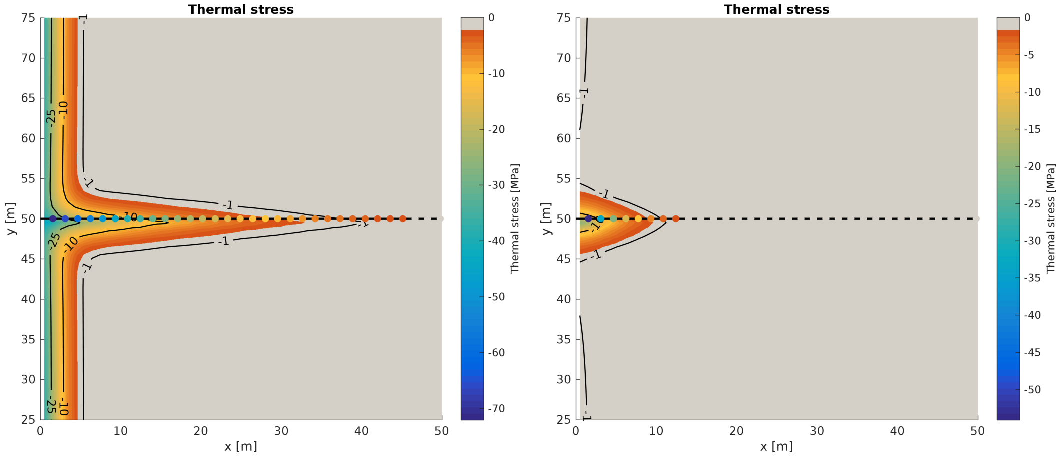

Figure 4.6: Thermal stress distribution after 30 days of injection. Fracture permeability $k_{fr} = 10^{-10} m^2$ Left: higher matrix permeability $k_m = 10^{-16} m^2$. Right: lower matrix permeability $k_m = 10^{-18} m^2$

low, a high pressure zone develops around the fracture causing a smaller pressure gradient in the fracture. This is also observable in the mean fracture velocities. For high fracture permeabilities the difference in fracture velocity increases one order magnitude with increasing matrix permeability. For low fracture permeabilities there is no significant change in observed mean fracture velocity with respect to matrix permeability. The observed "stabilization time" in the fracture velocities is caused by the initial pore pressure diffusion through the matrix and fracture.

The differences in the pressure field and the fracture velocities can, however, not fully explain the observed thermal stress distributions. In order to explain these differences we examine the heat transport in more detail. It is clear that the matrix-fracture interaction plays an important role in the thermal stress propagation. With increasing matrix and fracture permeabilities, also the interface permeability between matrix and fracture is increased allowing heat transfer by advection between matrix and fracture. Only by advection has the fluid in the fracture a chance to cool down the surrounding matrix. Once the surrounding matrix is cooled to a certain extent, the temperature front can also advance within the fracture. In case of a low matrix permeability, the main heat transfer mechanism between matrix and fracture is heat diffusion. Here heat diffusion from the matrix into the fracture dominates, leading to a heating of the fracture and thus significantly slowing down the thermal stress propagation. The second scenario is favorable in terms of sustainability of an geothermal reservoir. Here the heat is efficiently extracted from the matrix rather than prematurely cooling down the matrix surrounding the fractures.

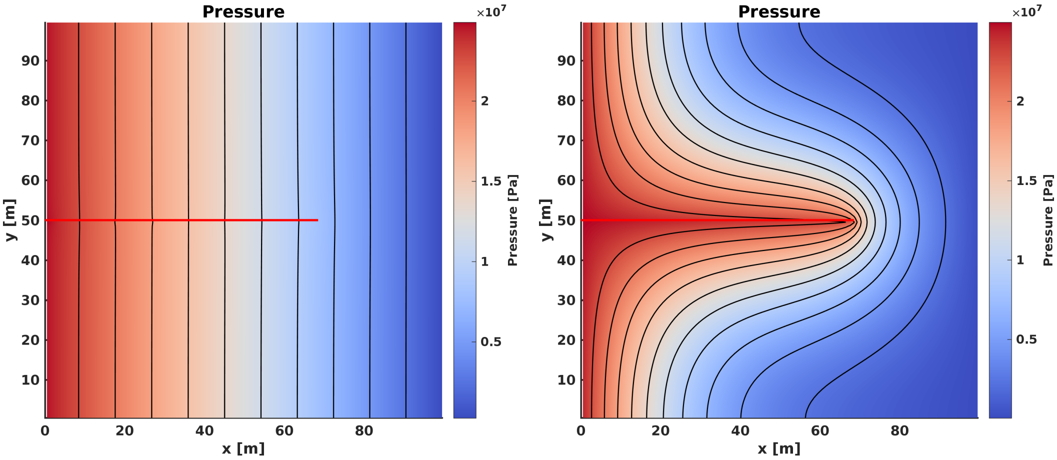

Figure 4.7: Pressure distribution after 30 days of injection. Fracture permeability $k_{fr} = 10^{-10} m^2$ Left:higher matrix permeability $k_m = 10^{-16} m^2$. Right: lower matrix permeability $k_m = 10^{-18} m^2$

4.4.2 Influence of thermal stress on shear failure potential

In this section we investigate the thermal stress influence on shear failure potential. As mentioned in the introduction and methods, shear failure in the reservoir occurs mainly on optimally oriented fractures. Here we investigate whether thermal stress leads to earlier onset of slip and how this is influenced by fracture orientation, and model the fluid injection into a single fracture (Figure 4.8).

All parameters except for the matrix and fracture permeabilities are identical to the previous experiment and shown in Table 4.2. We apply a fracture permeability of $k_{fr} = 10^{-10} m^2$ with a matrix permeability of $k_m = 10^{-17} m^2$. The injection pressure is constant at 9MPa. The minimum and maximum principal stresses are 45MPa and 20MPa, respectively. Stresses are oriented in alignment to the coordinate axis as

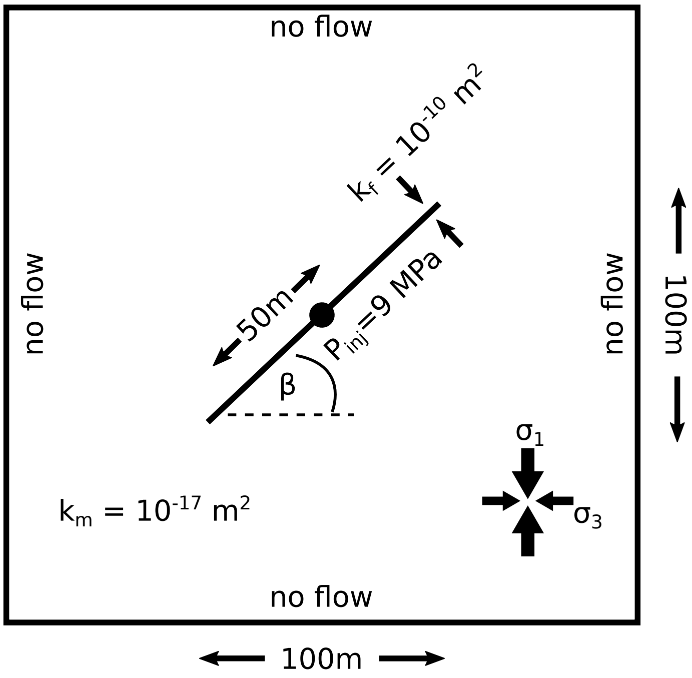

Figure 4.8: Numerical setup to evaluate the influence of fracture orientation and thermal stress on shear failure potential. A constant injection pressure is applied to the middle of the fracture. On the outer boundaries a no-flow boundary condition is applied.

shown in Figure 4.8. We vary the fracture orientation (measured in degree from the normal to the maximum principal stress) from $35°$ to $85°$ in steps of $2.5°$. The injection pressure was chosen so that only very close to optimally oriented fractures at $60°$ are eligible for slip. In this experiment we investigate the results after a continuous injection of 10 days. The injection temperature is variable with time and obtained as presented in the previous experiment. The initial temperature is set again at $T_0 = 200°C$ and we neglect gravity.

Figure 4.9 shows the result for a rotation of $45°$ after 10 days of injection. It shows a pressure ellipse with its principal axis aligned with the fracture. The initial point source is not recognizable in the matrix pressure after 10 days of continuous injection. This can be explained by the fast pressure diffusion in the fracture and consequential pressure diffusion from the fracture to the matrix. The thermal stress is distributed symmetrically around the injection point in the fracture. The temperature front propagates roughly 10m in each direction. The maximum cool-down and consequently maximum thermal stress is found at the injection point. Thermal stress in the matrix is propagated again from the fracture. The propagation direction is normal to the fracture leading to an elliptic thermal stress alteration zone surrounding the injection point. The rotation of the fracture barely influences the pressure and thermal stress distributions. Minor differences were observed but can be attributed to numerical effects.

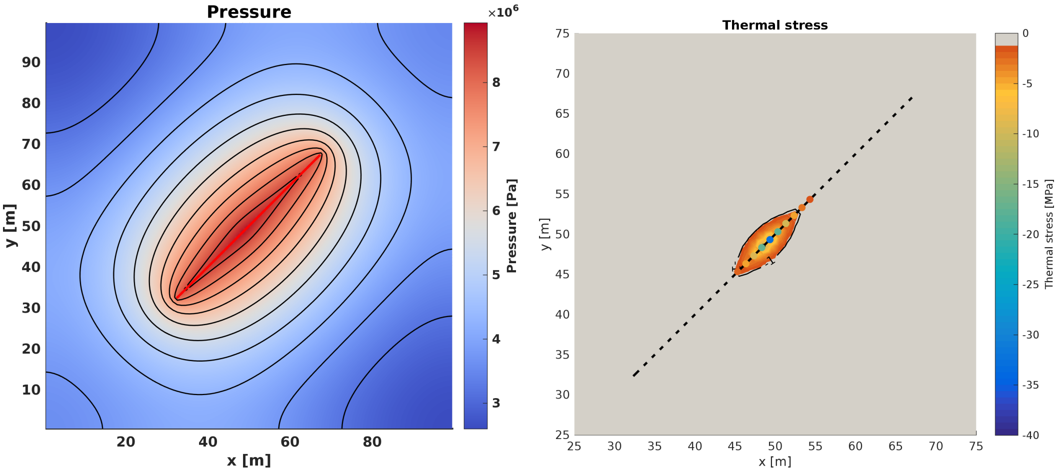

Figure 4.9: Results after 10 days of injection into the fracture. Fracture permeability $k_{fr} = 10^{-10} m^2$. Matrix permeability $k_m = 10^{-17} m^2$. Left: Pressure distribution. Right: Thermal stress distribution.

We use the Mohr-Coulomb diagram to evaluate the failure potential due to thermal stress with respect to fracture orientation. Figure 4.10 shows the failure potential for each fracture orientation, where each point in the diagram is the mean normal and shear stress calculated over the whole fracture length. We show the effective stress modified solely by the fluid pressure as well as modified by thermal stress and fluid pressure combined. Figure 4.10 shows that accounting only for fluid pressure in the effective normal stress only fractures oriented at $55° - 65°$ are able to slip. All other orientations do not meet the failure condition. If we further consider the effects of thermal stress we observe a wide range of fracture orientations that fulfill the failure condition and are able to slip. The results after 10 days of injection show that fractures orientated up to $17.5°$ from the optimum $(42.5° - 77.5°)$ are critically stressed. As Figure 4.10 only considers the average stress state in the fracture we evaluate the failure potential in greater detail with a histogram. Figure 4.11 shows the percentage of fracture segments for each orientation that could demonstrate slip. Considering only fluid pressure effects, we find that the injection pressure of 9MPa propagated as far as necessary to induce slip over the whole length of the optimally oriented fracture. Fractures oriented at $5°$ from the optimum already show significantly less segments with failure potential $(-(25 - 50)\%)$. Adding the thermal stress effect we observe a broad spectrum of potential slip in up to 35% of the fracture segments (at $\pm 7.5°$). However, also fractures with an orientation further from the optimum show a significant ability to slip with $\sim 20\%$ at $\pm 15°$ and $\sim 5 - 10\%$ for fracture oriented at $\pm 25°$ from the optimum.

The observed asymmetry in the failure potential is of numerical origin because as the fracture is rotated the number of matrix grid cells intersected by the fracture is changing. Consequently, this leads to small differences in the solution that propagate to the failure potential.

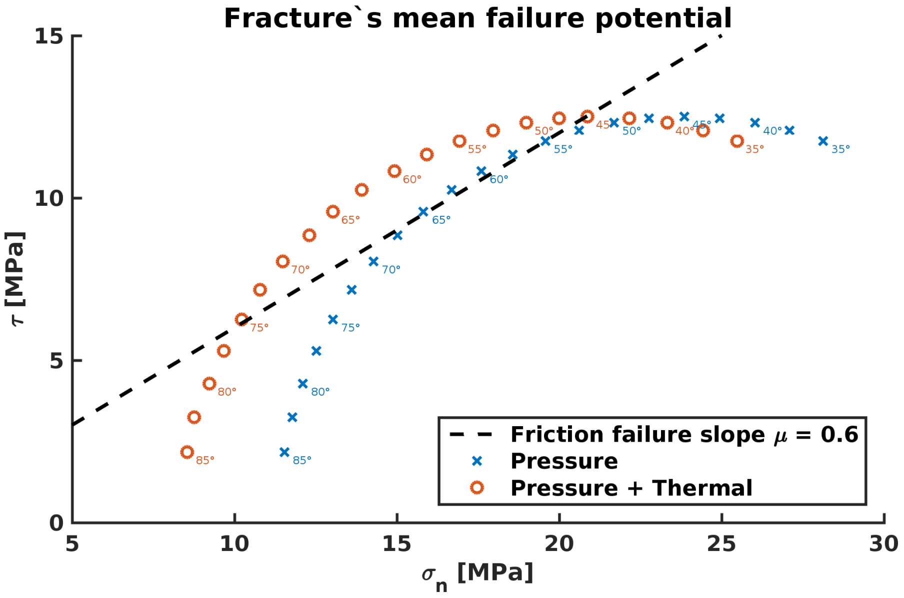

Figure 4.10: Failure potential for rotated fractures due to thermal stress. The failure potential is depicted in the classical Mohr-Coulomb diagram. A fracture is eligible for slip if its corresponding point in the diagram touches/crosses the failure line (black dashed). Failure occurs only in a narrow range of orientations with the selected injection pressure. After 10 days of injection thermal stress leads to possible slip in a wide range of orientations.

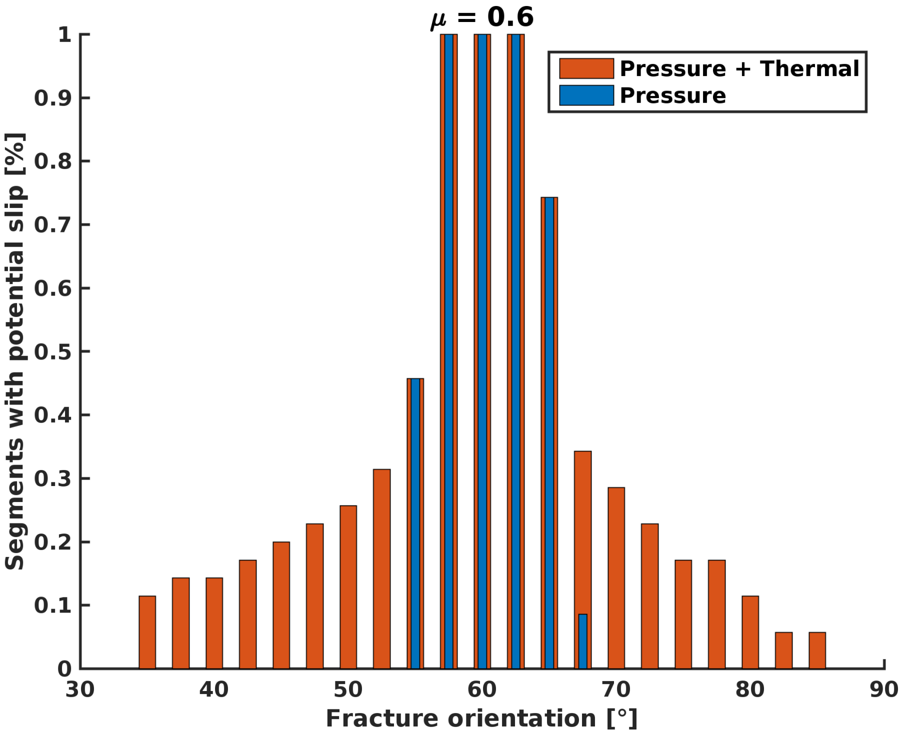

Figure 4.11: Failure potential for rotated fractures due to thermal stress in a bar diagram. It shows the percentage of fracture segments eligible for slip. Again, failure occurs only in a narrow range of orientations with the selected injection pressure. After 10 days of injection, thermal stress leads to possible slip in a wide range of orientations.

This experiment shows that thermal stress can greatly enhance the range of fracture orientations eligible for slip. This has a potentially large impact for the stimulation of geothermal reservoirs with a complex tectonic history and multiple fracture sets. If one or more fracture sets are non-optimally oriented and unsuitable for hydraulic stimulation, they might still be suitable for thermal stimulation. However, due to different propagation speeds of the fluid pressure and thermal front, thermal stimulation might be challenging for short stimulation scenarios. The significantly slower propagation of the thermal front suggest that enhanced slip on close to optimally oriented fractures is unlikely. Nevertheless, thermal stresses can be expected to add to slip in the reservoir on non-optimally oriented fractures and on fractures with highly heterogeneous frictional properties in the long run. The role of the different timescales of fluid pressure and thermal stress will be examined in more detail the third numerical experiment.

4.4.3 Cold water fluid injection into a complex fracture network

In the third numerical experiment we investigate the spatial and temporal evolution of potential failure due to fluid pressure and thermal stress. We model the fluid injection into a complex fracture network with a range of fracture orientations. The initial setup is shown in Figure 4.12. The domain represents a fractured reservoir at a depth of 5km. We used the fracture network generator *FracSim3D* (Xu and Dowd, 2010) to create the fracture network used in this study. It consists of a total of 310 large scale fractures within a damaged rock matrix. The borehole is located in the middle of the domain with an open hole length of 50m (cf. 4.12).

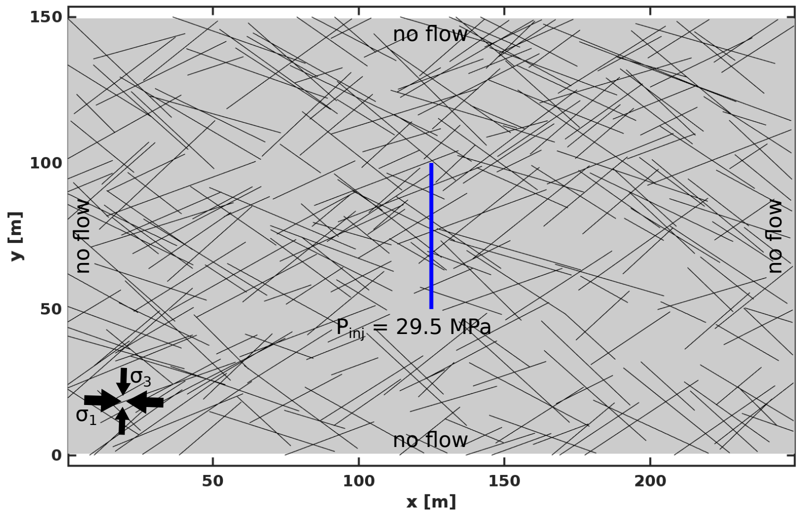

Figure 4.12: Numerical setup to evaluate the spatial and temporal evolution of potential slip due to fluid pressure and thermal stress. A constant injection pressure is applied to the borehole in the middle of the domain (blue). On the outer boundaries a no-flow boundary condition is applied.

All parameters except for the matrix and fracture permeabilities are identical to the previous experiments (cf. Table 4.2). We apply a fracture permeability of $k_{fr} = 10^{-11}m^2$ with a matrix permeability of $k_m = 10^{-18}m^2$. The injection pressure is constant at 31.1MPa. The minimum and maximum principal stresses are 113MPa and 175MPa respectively. The in-situ pore pressure is assumed to be hydrostatic at 50 MPa. We neglect the hydrostatic gradient within the reservoir due to the relatively small vertical extent of the model. Stresses are oriented with $2°$ rotation to the coordinate axis as shown in Figure 4.12. In this experiment we investigate the results during a continuous injection of 30 days. The injection temperature is variable with time and obtained as discussed previously. The initial temperature is set to $T_0 = 200°C$, and we include gravity effects.

An important addition to this experiment is a stepwise change in fracture permeability when a fracture segment reaches the failure condition (Miller and Nur, 2000). That is, when the failure condition is reached, then the permeability adopts $k_{fr} = x \cdot k_{fr}$, where x is a multiplication factor. For the simulations presented here, the enhancement factor x is set to 100. The geological basis for stepwise change in permeability (Miller and Nur, 2000) rests with the strong aperture dependence of permeability (e.g. Nemčok et al., 2002), where small changes in aperture result in very large changes in permeability. The proposed model has been used to successfully describe the distribution of the induced seismicity in the Basel EGS site, and for modeling fluid-driven aftershock sequences (Miller et al., 2004; Miller, 2015).

Figure 4.13 shows the pressure distribution after 30 days of injection. Due to the heterogeneity of the fracture network the pressure distribution is complex. As is also visible in Figure 4.12, the fracture density on the left side of the injection well is much higher than on the right side. This leads to more flow towards the left side of the reservoir as clearly indicated by the pressure field. The pressure distribution is dominated by the fracture network. After 30 days of injection, a pressure change of at least 1MPa is measured in the whole domain. The maximum extent of the area with at least 30 MPa is approximately 30m on the right side of the injection and up to 75m on the left side of the well. A distinct anisotropy is visible between the horizontal and vertical extents of the high pressure zone. Vertically the pressure propagates slower compared to the horizontal direction and is caused by the main direction of the fracture set.

Figure 4.14 shows the thermal stress caused by the fluid injection into the reservoir. As predicted by the results of the previous experiments, the thermal stress alteration is concentrated to a region close to the injection well. Thermal stress evolves around the fractures intersecting the well as most of the fluid enters the reservoir here. The color-scale in the figure starts at 0.65MPa with the darkest blue. Everything below is neglected in the graphical representation and shown in the background color. This low cutoff shows the extent of the thermal stress alterations in the

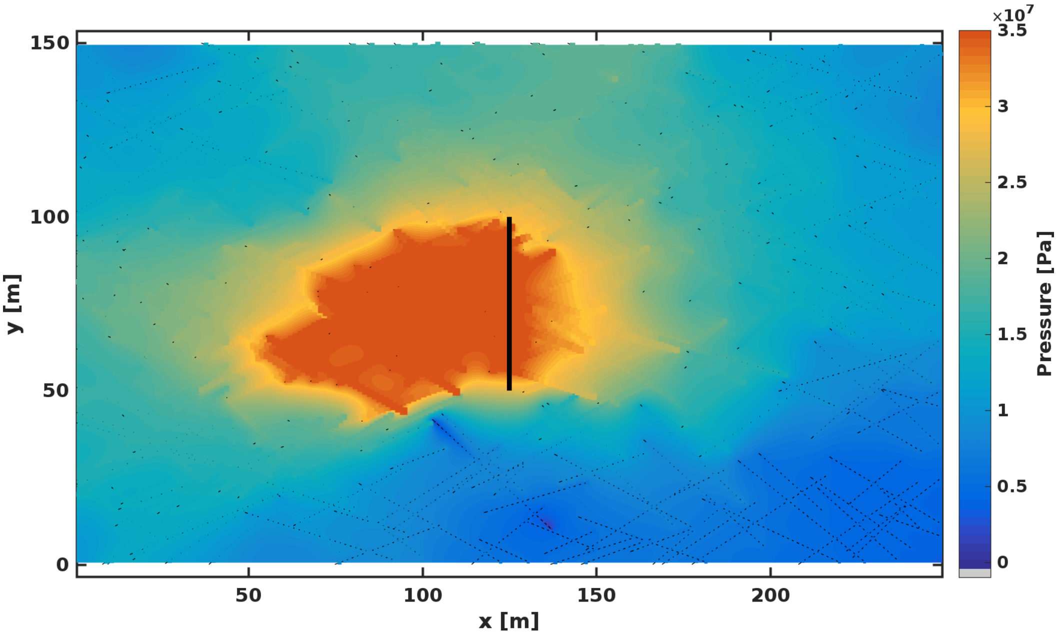

Figure 4.13: Pressure distribution after 30 days of injection into the fracture network. The heterogeneous fracture distribution influences the pressure field and leads to preferential flow directions in the reservoir. Fracture permeability $k_{fr} = 10^{-11} m^2$. Matrix permeability $k_m = 10^{-18} m^2$.

domain. The propagation of thermal stress in the matrix is rather homogeneous and mainly driven by heat diffusion. Additional thermal stress of 0.65MPa occurs in a distance of 6 - 10m from the borehole. Close to the borehole thermal stress in the matrix reaches up to 20MPa. The thermal stress in the fractures differs from the thermal stress in the matrix. Maximal thermal stress perturbation is measured at the fracture intersections at the borehole with up to 40MPa additional stress. Due to the complex flow pattern, the thermal stress propagation in the fractures is equally strong. Some fractures show stress perturbations up to 10m from the borehole while for others alterations do not reach 5m into the reservoir. This shows that heat in the fractures is transported also by advection. A distinctive separation of the heat transfer mechanisms as previously performed for a single fracture is not possible here due to the interplay of the various effects.

We further evaluate failure potential in the reservoir due to the fluid injection. Figure 4.15 shows the distribution of potentially slipping failure segments in the reservoir at the end of the injection period. Each fracture segment is tested for potential failure based on equation 4.5. If the failure criterion is met, a star is shown in the figure to indicate potential slip on this segment. The color indicates the failure mechanism. Symbols in red indicate potential shear failure solely due to the fluid pressure. Blue symbols, on the other hand, signal failure due to the combined effects of increased fluid pressure and thermal stress. Pressure induced shear failure (or hydraulic failure) occurs mainly on the left side of the injection well and up to 65m away from the well. Note that not all fractures are hydraulically stimulated as their

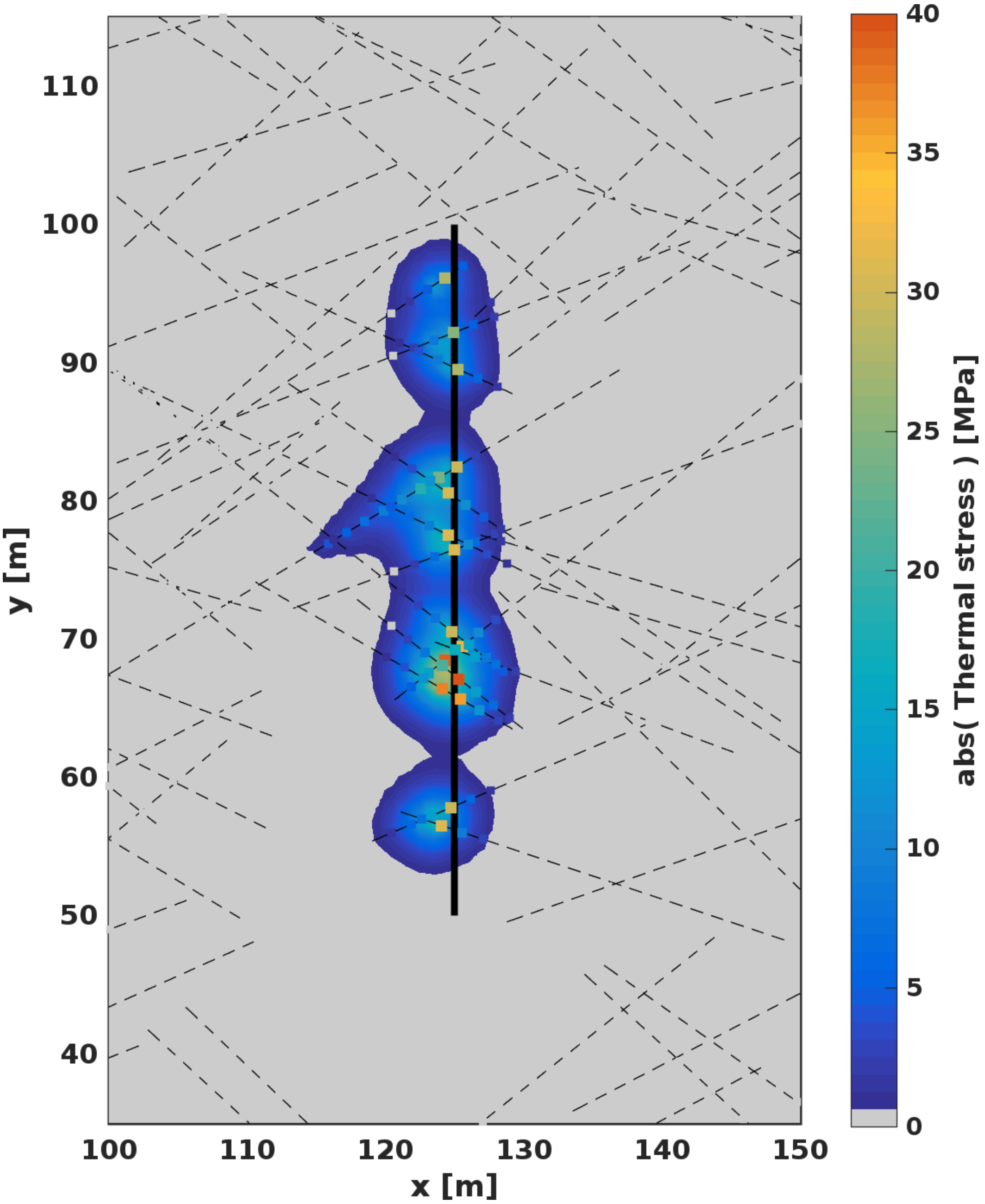

Figure 4.14: Thermal stress after 30 days of injection into the fracture network. The thermal stress is concentrated close to the injection well. Note that the absolute value of the thermal stress is shown and all thermal stress here is tensional.

orientation is not suitable for slip although the fluid pressure inside the fractures is comparable (cf. Figure 4.13). Close to the well thermo-hydraulic failure is visible. The extent corresponds to the size of the thermal-stress alteration zone. These fractures are not aligned optimally for slip and thus do not show potential failure with hydraulic stimulation alone. Once thermo-hydraulic stimulation is taken into account, the reduction in effective normal stress on these fractures is high enough to make them eligible for slip as indicated by the blue symbols in Figure 4.15.

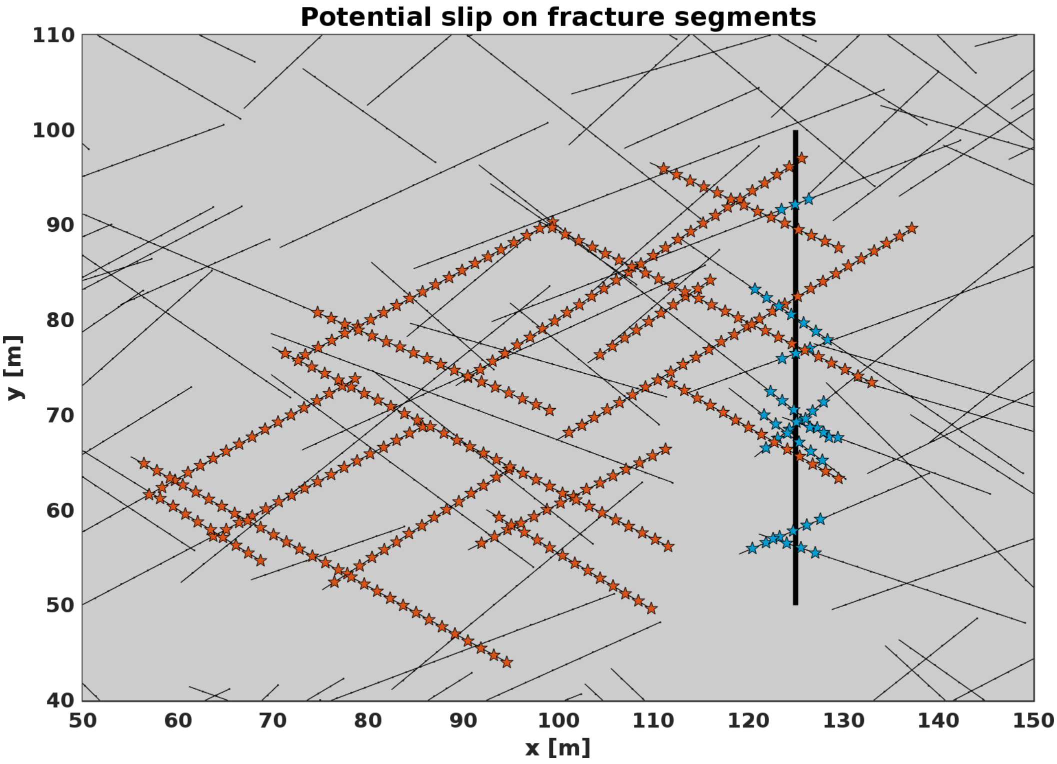

Figure 4.15: Potentially slipping fracture segments after 30 days of injection into the fracture network. The two colors indicate the mechanism of failure. Red: Fracture segments failing due to fluid pressure alone. Blue: Failure due to the combined effects of fluid pressure and thermal stress.

The temporal evolution of the failure potential has been neglected so far. In Figure 4.16, we evaluate the simulated seismic events to gain more insight into the mechanisms at play and their evolution. An event is counted if the corresponding fracture segment is eligible for slip. In the present numerical model we assume that all events are seismogenic. Due to the simplified failure model, the separation of seismic and aseismic slip is not possible within the scope of this study. So-called *H*-events indicate failure only due to fluid pressure. The *TH*-events are all events including both hydraulic failure and thermo-hydraulic failure. Initially, during the first days of injection both event curves are close to each other. Later in the injection cycle, the difference between the curves grows larger, indicating the increased significance of the thermo-hydraulic failure events. Throughout the 30 days of fluid injection the difference between *H* and *TH* events is about 15%. With continued injection this difference is expected to increase as the fluid pressure propagation slows down the higher the radial distance from the well and thermal-stress propagation continues. Note that both curves share many of the sharp gradients and subsequent plateaus. This indicates that hydraulic failure dominates the shape of the measured event curves. Steep gradients indicate abrupt failure in many connected fracture segments possibly leading to microseismicity. Overall, the microseismicity is likely to increase due to combined thermo-hydraulic failure. However, large felt microseismic events are not a necessary consequence as there are no sharp gradients in the difference between the two curves (black dashed line in Figure 4.16) during the 30 days of injection into the reservoir.

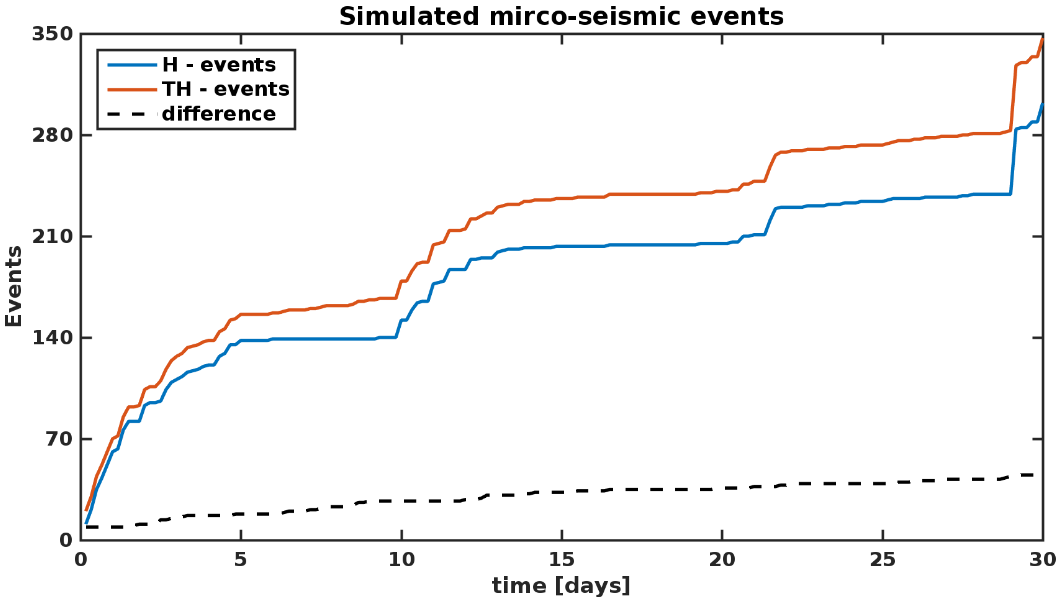

Figure 4.16: Temporal evolution of the simulated seismic events during the injection period. An event is counted if the corresponding fracture segment is eligible for slip. The two colors indicate the mechanism of failure. Blue: Fracture segments failing due to fluid pressure alone (H). Red: Failure due to the combined effects of fluid pressure and thermal stress (TH).

This third numerical experiment shows that thermal stress can play and important role in shear stimulation of a fractured reservoir close to the well. Figure 4.15 showed that two distinct stress domination regimes can be defined. In one region only hydraulic failure is observed, while in the other region (more or less confined close to the well) thermo-hydraulic failure occurs. We showed that these regions act on different timescales. Fractures that are not optimally oriented for failure and are not prone to slip early in the injection cycle might be triggered due to the combined thermo-hydraulic stress changes later during the injection. This could help to explain the sometimes non-intuitive temporal evolution of micro-seismicity observed during fluid injection. We can compare our results to typical changes in the static Coulomb stress transfer model that is widely used. Typical changes in Coulomb stress during fluid injection are observed in the range of -2MPa to 1MPa

(Schoenball et al., 2012; Catalli et al., 2013). In our experiments we showed that thermally induced stress changes can easily exceed these changes in proximity to the fractures and the injection point. This further emphasizes the importance of thermal stress during reservoir stimulation.

4.5 Conclusion

We developed and implemented a fast and efficient methodology for investigating the role of thermal stress in a geothermal reservoir. The numerical experiments presented in this study give insight into the role of thermal stress during hydraulic stimulation over short and long periods. We showed that thermal stresses can facilitate slip on non-optimally oriented fractures and that thermal stress propagation is largely influenced by the hydraulic properties of both fracture and matrix. We found that thermal stress change is spatially more concentrated and generally propagates much slower than fluid pressure. Nevertheless, thermal stress changes can exceed fluid pressure especially close to the well.

Some of our simulations showed that the combination of pore-pressure and thermal stress can exceed the minimum principal stress, which would thermally induce tensile cracks. However, these tensile cracks are not self-propping, so hydraulic pressurization would be needed to facilitate flow. This is not considered in our current model, but could be introduced as shown e.g. in Ghassemi, (2012) Figure 6 using a damage methodology for the matrix blocks surrounding the fracture. Including these effects would lead to an enhanced heat exchange between matrix and fracture in addition to that discussed previously. We also identified two different failure regimes that act on different timescales. The hydraulic failure regime acts on the timescale of days to weeks whereas the thermo-hydraulic regimes acts on the scale of weeks to years. Future studies should aim to determine whether this can be observed in micro-seismic data from real-world fluid injection experiments.

Finally we showed that thermal stress changes can be significantly larger than the injected fluid pressure as well as the slip-induced Coulomb stress change in some situations. This is especially important in long-term injection scenarios where the thermal stress changes become more significant with time and during the production phase of high flow rate geothermal systems.

Although we assumed water as the working fluid, it would be interesting to observe how the model behaves by implementing an equation of state for CO_2 as the working fluid. Since CO_2 is typically at super-critical conditions in the reservoir, we would expect similar hydraulic outcomes. However, specific heat capacity, density, and viscosity of super-critical CO_2 differ significantly from those of water, which could affect the spatial evolution and heat flow, consequently influencing thermal stress propagation within the reservoir.

Our model using simplified mechanics provided important insight into the dominant thermo-elastic effects, and helped to identify some challenges and opportunities for future studies. More advanced models currently under development will consider both pre-existing fractures as in the present work, but also the generation of new fractures in response to the evolving stress state from both thermo-and hydraulic perturbations. Future models might also include fracture roughness and morphology, and solving the full equilibrium equations to estimate aperture changes that influence permeability. Finally, including a method to estimate magnitude from computed slip (Heinze et al., 2015), not currently modeled, is essential for a mechanistic assessment of seismic hazard associated with injection. Induced seismicity can not be quantified in terms of magnitude as fracture slip in the fractures is not computed. These are all areas that we are currently pursuing.

We conclude that thermal stress changes in the reservoir should be incorporated in models that seek to fully understand the processes at play during fluid injection (covering initial stimulation as well as the production phase) in fractured reservoirs over long-periods.

5 Fluid pressure triggered foreshock sequence of the 2008 Mogul earthquake sequence

> *Water its living strength first shows,*
> *when obstacles its course oppose.*
>
> — **Johann Wolfgang von Goethe**

The contents of this section are currently in preparation for submission as: Gunnar Jansen, Christine J. Ruhl and Stephen A. Miller, "Fluid pressure triggered foreshock sequence of the 2008 Mogul earthquake sequence".

5.1 Introduction

Many shallow earthquakes were generated by the Mogul earthquake sequence that began in late February 2008, 10 km west of Reno, Nevada, USA. Although the earthquakes were relatively small, they were widely felt by the local population due to their shallow occurrences. A temporary network of seismic stations was installed directly above the sequence just prior to the first significant increase in activity (Ruhl et al., 2016b). Over a two month period earthquake activity increased resulting in a M_L 5.1 ($M_W = 4.9$) main shock on April 25, 2008. Thousands of well recorded events present an excellent opportunity to investigate the role of fluid pressure during the earthquake sequence. A previously suggested role of high-pressure fluid (Ruhl et al., 2016b) in this sequence was left unquantified.

Prior to the mainshock and the succeeding aftershock sequence, seismicity presented itself similarly to typical earthquake swarms. Thus, in the literature the Mogul earthquake sequence is sometimes also referred to as *Mogul swarm*. Seismic swarms are often attributed to fault creep, magmatic events and fluid flow (e.g. Hill, 1977; Sibson, 1996; Lohman and McGuire, 2007; Shelly et al., 2013; Wei et al., 2015; Heinze et al., 2017). The distinction of seismicity bursts as either foreshock sequences or seismic swarms mainly relies on the occurrence of a significantly larger seismic event at later stages of the sequence. Their connection however remains unclear. It is possible that foreshocks and seismic swarms share the same underlying processes that eventually trigger an unusually large event in the former case.

Since foreshocks are one of the few well-documented precursors to large earthquakes, understanding their nature is very important. Therefore, in this paper we take the opportunity to investigate the role of fluid pressure especially during the foreshock period of the sequence using a combination of analytical and numerical methods. We use stress inversion to infer the local stress field and estimate the required fluid overpressure to trigger the sequence. This allows us test the physical feasibility of the proposed fluid pressure trigger. Numerical simulations are then used to develop and evaluate a scenario for the spatio-temporal evolution of the Mogul earthquake sequence. The results provide strong evidence that at least the foreshock sequence of the Mogul earthquake sequence is fluid-driven.

This paper is structured as follows. In the remainder of the introduction we present the current state of research for the Mogul earthquake sequence its tectonic setting, regional hydrothermal activity and the data used in this study. The following section is concerned with the determination of the local stress field and excess fluid pressure. Based on this we develop a numerical model for the foreshock period of the Mogul swarm and presents its results. We conclude the paper by a discussion of the findings and a conclusive statement.

5.1.1 The Mogul Earthquake sequence

Beginning in late February 2008, many shallow earthquakes (< 6 km depth) were generated by an earthquake sequence west of Reno, NV, USA. Many of the earthquakes were felt in the residential Mogul and Somersett neighborhoods which lead to significant public concern. Locatable seismicity occurred on 21-22 February 2008 and was preceded by around 30 micro-earthquakes that were detected in January and early February 2008. The nearby Nevada Seismological Laboratory (NSL) at the University of Nevada, Reno, installed a temporary, telemetered instrument array by 3 March 2008, several days before the first significant increase in activity (Ruhl et al., 2016b). Over the next two months distinct bursts in seismicity grew in spatial extent and seismic intensity culminating in the $M_W = 4.9$ main shock on 26 April 2008 06:40 (UTC). Seismicity rates following the main shock decayed similarly to typical aftershock sequences, following the modified Omori's law (Ruhl et al., 2016b; Utsu, 1961). Ruhl et al., (2016b) estimate the Gutenberg-Richter magnitude-frequency b-value of the Mogul sequence at 0.94. This is similar to typical main schock - aftershock earthquake sequences. The Mogul earthquake sequence is also referred to as Mogul swarm (e.g. Ruhl et al., 2016b; Bell et al., 2012). Earthquakes swarms linked to magmatic or volcanic intrusions often show b-values much greater than 1 (e.g. Farrell et al., 2009; Jakobsdóttir et al., 2008). However, close to 1 b-values were recognized in e.g. the Voigtland swarms that are assumed to be fluid driven by the degassing of CO_2 (Heinze et al., 2017; Hainzl, 2004). Lower b-values (0.8-1) have been found in seismic swarms hosted in extensional environments (Ibs-von Seht et al., 2008; Ruhl et al., 2010). Previous studies on the Mogul sequence show consistently that the main shock was caused by right-lateral slip on a concealed, steeply dipping, northwest-striking fault (cf. Figures 5.1 and 5.2) that was not previously identified by published geological mapping (Anderson et al., 2009; Bell et al., 2012). Figure 5.1 further shows the focal mechanisms of the ten largest events of the sequence. Three of these events occurred during the foreshock period showing predominantly strike-slip. The largest six events of the aftershock sequence include strike-slip as well as normal faulting. The measured line of sight (LOS) deformation was ± 3 cm from April to August 2008 using InSAR data which suggests that the earthquake sequence was generated by 25-75 cm of right-lateral displacement on a fault with $\sim$3 km rupture length and a rupture depth of $\sim$2 km (Bell et al., 2012). Bell et al., (2012) further show that the total seismic moment modeled using InSAR is approximately twice the cumulative moment of the main shock and all $M_W \geq 3.0$ events. This suggests significant aseismic slip, which is found to be primarily post-seismic (Bell et al., 2012). However, limitations in data collection (e.g. InSAR satellite image coverage) may mask the presence of slow slip in the days prior to the main shock (Ruhl et al., 2016b). Ruhl et al., (2016b) perform statistical clustering to quantitatively isolate spatio-temporal clusters which they interpret to be fluid driven based on observations of event migration, fault-fracture mesh geometry and fault-valve behavior. Fault-Valve behavior is suggested based on the observed upward migration of clusters after the largest foreshock cluster, indicating a rupture into a suprahydrostatic fluid reservoir at very shallow depths (Ruhl et al., 2016b). The fault-fracture mesh is revealed as a network of en echelon strike-slip faults, extending from $\sim$2.5 km depth to 4 km depth, activated by clustered and background earthquakes (Ruhl et al., 2016b). Seismicity is found to spread at velocities near 30m/d or a diffusivity of 0.25 m^2/s consistent with pore pressure changes related to fluid flow (Ruhl et al., 2016b). Recently, Ruhl et al., (2017) investigated the variation of stress drop during the earthquake sequence. The observed variability can best be explained by a difference in rheology along the fault plane (Ruhl et al., 2017). They also found increasing stress drop with distance from the first relocated events for the foreshock period, which is interpreted to be a result from pore pressure diffusion with patterns very similar to fluid-driven seismicity in geothermal fields (e.g. Kwiatek et al., 2014; Goertz-Allmann et al., 2011).

5.1.2 Tectonic Setting

The Mogul earthquake sequence occurred within the transtensional Walker Lane (cf. Figure 5.2), a broad zone (~ 100km width and ~ 700km length) of predominantly northwest-striking right-lateral strike slip and normal faulting (Stewart, 1988). The Walker Lane parallels the San Andreas fault system and accommodates northwest translation of the Sierra Nevada (GPS models suggest 7 - 10mm/yr (Hammond and Thatcher, 2007)) as well as 20 - 25% of relative plate motion between the Pacific and North American plates (Surpless, 2008). Regardless of the measured strain, there is little geological evidence for continuous northwest-striking right-lateral strike slip faulting in the Reno-Carson City-Lake Tahoe area (cf. Figure 5.2) (Surpless, 2008; Wesnousky et al., 2012). The area is dominated by large westward titled en echelon

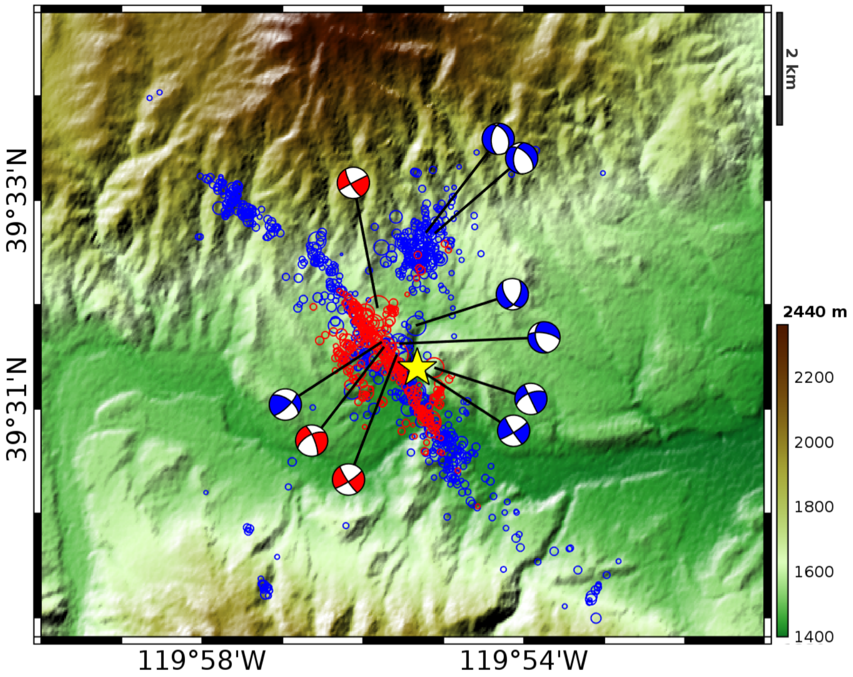

Figure 5.1: Map of the relocated seismicity in the Mogul earthquake sequence west of Reno, NV sized by magnitude. Events are colored by their occurrence with respect to the Main shock (yellow star). Events that occured during the foreshock period are denoted by red circles while events of the aftershock sequence are shown in blue. Additionally, the focal mechanism solution of the ten largest events of the sequence are shown. The coloring follows the aforementioned convention.

normal-fault-bounded range blocks (Surpless, 2008; Wesnousky et al., 2012; Ruhl et al., 2016b). Abundant regional seismicity occurs often in the transition zones between major normal faults at seismogenic depths between 5 and 17 km (Ichinose et al., 1998; Ruhl et al., 2016a). A long history of moderate earthquakes, where stronger events were preceded by energy foreshock periods, were suggested from historical accounts in the Reno area (dePolo et al., 1997).

Directly above the Mogul sequence area, discontinuous surface faults are cutting Tertiary sediments, volcanic units and older granites at a variety of orientations (Bell and Garside, 1987; Ruhl et al., 2016b). In addition, local quaternary faults are mapped at various orientations which suggests a long history of overprinting and deformation in a highly fractured shallow subsurface (Bell and Garside, 1987; Cashman et al., 2012).

5.1.3 Hydrothermal activity

In addition to a highly fractured shallow subsurface, the presence of fluids is evident by the occurrence of hot springs. Multiple hot springs are located in proximity to the Mogul sequence area with the Lawton hot springs being just at the southern end of the observed seismicity. Other geothermal areas within a 20km radius from Mogul

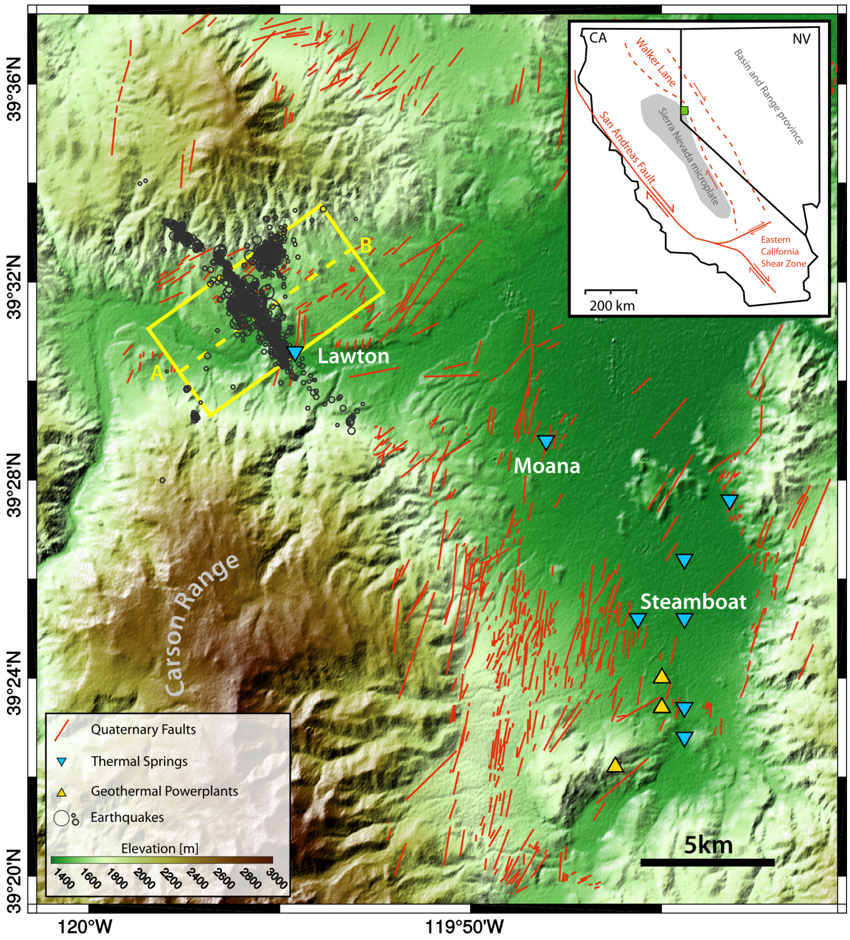

Figure 5.2: Regional overview of the Reno area on a color-coded elevation map. The Mogul earthquake sequence (grey circles) occurred west of Reno on a concealed strike-slip fault between the Peavine mountain and the Carson range. The studied cross-section A-B is shown in yellow. Quaternary faults of the region are shown in red. The three main geothermal fields of the region are shown. Natural hot springs are denoted by blue symbols and geothermal power-plants as yellow triangles. The inset shows the tectonic setting of the region within the Walker lane at the border between California (CA) and Nevada (NV).

are the Moana and Steamboat hot springs (cf. Figure 5.2).

Lawton hot springs flows with a surface temperature of 45 - 50°C that originates from fractured granite with an estimated minimum reservoir temperature of 117°C (Stearns et al., 1937; Scheibach, 1975). Outflow at the spring is estimated at 1000L/min according to Waring and Blankenship, (1965). As the spring is located approximately 10m away from the Truckee river along a north-south trending fault, a considerate amount of mixing is expected (Scheibach, 1975).

The Moana geothermal area, southwest of Reno, supports the largest low to moderate direct heat usage development in Neveda. Over an approximately 3km^2 area more than 250 wells ranging from 3m to 3000m with temperatures ranging from 40° C to 100° C have been drilled since the early 1900s (Flynn and Enterprises, 2001). However, the Moana hot springs have not flowed at the surface since at least 1979

(Garside and Hess, 1994). The Moana geothermal area is structurally-controlled by at least two near-vertical faults, striking northwest and north-northeast respectively (Flynn and Enterprises, 2001). The reservoir constitutes of Tertiary sediments and hydrothermally altered andesite (Flynn and Ghusn Jr, 1983).

The Steamboat geothermal area is Nevada's best known and most intensively studied geothermal area with a history going back to the 1860s (Garside and Schilling, 1979). The local geology has been described in detail in White, (1964), Thompson and White, (1964), and Bonham and Bell, (1993). The basement consists of fractured granodiorite overlain by faulted andesite and other volcanic and sedimentary rocks. There are at least three prominent fault systems, trending north-south, northeast-southwest and northwest-southeast. Geothermal production for the Steamboat power-plants is primarily from the fractured granodiorite along the northeast-southwest trending fault system (Skalbeck et al., 2002). Production testing at the Steamboat power plant indicates that flow of thermal water is fracture controlled (Skalbeck et al., 2002). The springs exhibit temperatures close to boiling and exploration wells have reported temperatures as high as 187°C (Garside and Schilling, 1979). A reservoir temperature of 230°C is estimated from geothermometers (Nehring, 1980). There is evidence for a magmatic source of heat for the Steamboat geothermal system, yet disagreement about the conceptual model exists (Arehart et al., 2003; Skalbeck et al., 2002). Recharge has been identified to be mainly precipitation in the Carson range at a mean elevation of 2100m based on stable isotope analysis (Nehring, 1980). However, a small portion of magmatic water ($\sim 5\%$) has been suggested to explain the observed discharge in CO_2, Li, B and heavy metals (White, 1968; Nehring, 1980).

In addition to the geothermal areas mentioned here, at least 7 other areas of hydrothermal occurrences are present in Washoe County alone (Garside and Schilling, 1979). The region reveals numerous fracture-driven geothermal areas that originate mainly from highly fractured basement rocks. The presence of natural geothermal fluids also at supra-hydrostatic conditions, evident by the occurrence of flowing hot springs, is one of the driving motivations to investigate the role of fluid pressure in the 2008 Mogul earthquake sequence.

5.1.4 Conceptual model

The presence of fractures and excess fluids in the subsurface motivates the investigation of the role of fluids in the earthquake sequence. These aspects have also been recognized by previous studies (e.g. Ruhl et al., 2016b; Ruhl et al., 2017). However, no study on whether it is physically possible to trigger the earthquake sequence by fluids in this setting and the prevailing tectonic conditions exists. Therefore, in this paper we take to opportunity to investigate the role of fluid pressure especially during the foreshock period of the sequence. We seek to provide insight using a combination of analytical and numerical methods. The first objective is whether

fluid pressure triggering is physically possible in the local tectonic setting. To this end, we use stress inversion to infer the local stress field and estimate the required fluid overpressure to trigger the sequence. This will allow us to test the physical feasibility of the proposed fluid pressure trigger.
Numerical simulations are used to evaluate a scenario for the spatio-temporal evolution of the Mogul earthquake sequence based on the conceptual model for this study (Figure 5.3). The model is similar to the conceptual model for the Steamboat Hills geothermal system that lies 15-20km to the south. We consider a system where meteoric water from the Carson range and Peavine mountains is able to deeply infiltrate the subsurface through steep fractures. Possibly, additional fluids might result from a magmatic source at depth. Deep magmatic injection events were recently inferred just west of the Mogul area beneath Lake Tahoe and the Sierra valley (Smith et al., 2004; Smith et al., 2016). In contrast to the Steamboat hills we suggest that these fluids are initially trapped within a confined reservoir at supra-hydrostatic conditions. Within numerical simulations we then evaluate the evolution of fluid pressure and fluid-driven seismicity if the seal is broken and fluids are migrating towards the surface through pre-existing faults and fractures.

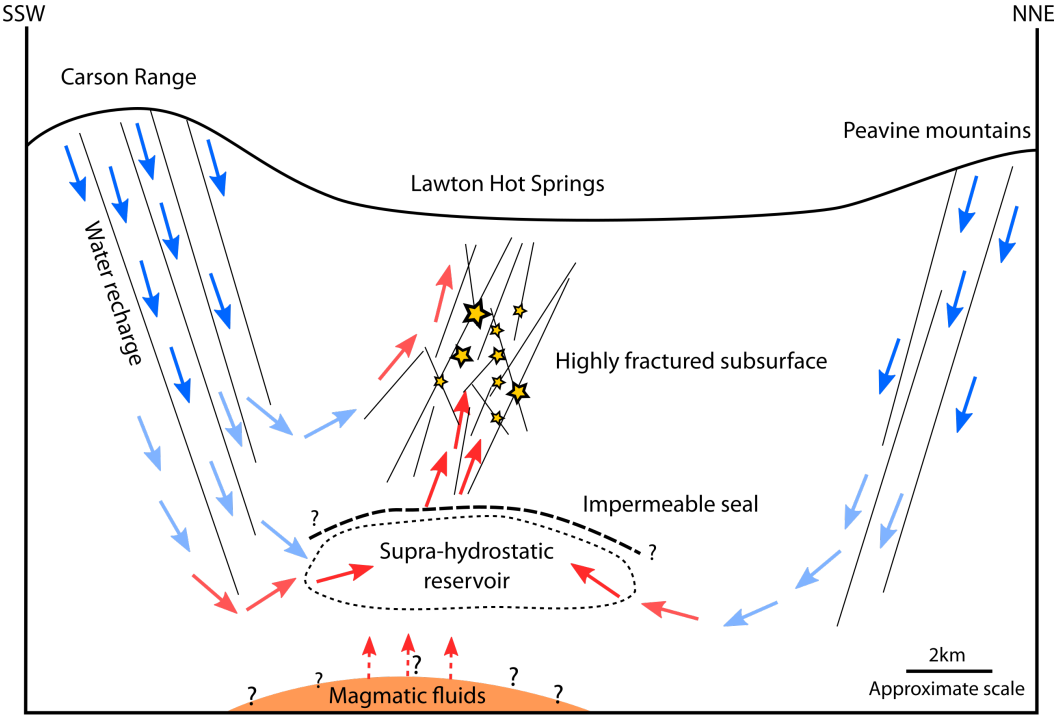

Figure 5.3: Conceptual model for fluid-driven seismicity in the 2008 Mogul earhquake sequence. The conceptual model is similar to the Steamboat Hills (e.g. White, 1968; Skalbeck et al., 2002).

5.1.5 Data

We use the data set originally presented in Ruhl et al., (2016b) with a total of 7752 relocated events comprising 1082 well-constrained focal mechanism solutions events. Absolute earthquake relocation, double-difference relocation with cross correlation and determination of the focal mechanism as well as a clustering analysis were performed by Ruhl et al., (2016b). Here we use the data resulting from event relocation and the focal mechanisms. Absolute earthquake relocation in this dataset was performed using *HYPOINVERSE* (Klein, 1978). Due to the high-density monitoring network, uncertainties in absolute vertical and horizontal location are less than 1.2 and 2.0km, respectively. Relative relocation uncertainties, defining the accuracy of observed structures in the seismicity, are $\sim$1 order of magnitude less than absolute uncertainties (~ 100m).

Stress inversion analysis requires knowledge of the focal mechanisms. The double-couple earthquake focal mechanism were computed from the full catalog of relocated events from P wave polarities using the USGS program *HASH* (Hardebeck and Shearer, 2002). The available 1082 events show fault-plane uncertainties $< 35°$, include events with $M_L = 0 - 4.14$ and are located between 0.7 and 6.1km depth (Ruhl et al., 2016b). The large data set additionally allows us to classify the focal mechanisms in detail according to the criteria set forth by Johnston et al., (1994) using *FMC* (Álvarez-Gómez, 2014).

5.2 Analytical analysis: Determining the local stress field and excess fluid pressure

We determine the local stress field orientation by stress inversion of 1082 well-constrained focal mechanism solutions using *MSATSI* (Martínez-Garzón et al., 2014). Although earthquake focal mechanism parameters (i.e. strike, dip, rake) often have fairly large uncertainties, a large enough data set (>30 mechanisms) can provide an accurate stress tensor orientation (Hardebeck and Michael, 2006). The estimation of stress-field orientation is a nonlinear inverse problem that is often solved in a linearized least-squares inversion scheme (Martínez-Garzón et al., 2014; Hardebeck and Michael, 2006; Michael, 1984). The inversion method used in *MSATSI* is based on one of the standard methods for determining a single stress tensor that best fits a set of focal mechanisms. The implemented method in *MSATSI* minimizes the differences between the slip vector and the resolved shear stress vector on each fault plane (Martínez-Garzón et al., 2014; Michael, 1984). The use of focal mechanisms to determine the stress field orientation assumes a uniform stress field and that traction on the fault plane is parallel to the slip direction (Wallace, 1951; Bott, 1959; Michael, 1987). The inversion provides the orientations of the three principal stress axes and the relative stress magnitude $R = \frac{(\sigma_1 - \sigma_2)}{(\sigma_1 - \sigma_3)}$.

Stress inversion yields the orientation of the principal stresses: The maximum and minimum principal stresses are trending north ($0°$) and east ($90°$) on nearly horizontal planes, respectively. The intermediate principal stress σ_2 is trending NW on a $83°$-dipping sub-vertical plane (cf. Figure 5.4a). The optimal R-value from the inversion is 0.22, indicating similar magnitudes for vertical and maximum principal stress (cf. Figure 5.4b). The orientations of the local stress field are consistent with the regional stress field determined in previous studies (Ruhl et al., 2016a).

From the distribution of focal mechanisms, we have determined the regional stress field to be primarily characterized by strike-slip ($S_{Hmax} > S_v > S_{hmin}$). For simplicity, we assume a uniform stress field with $S_v = \sigma_2 = \rho g z$ (vertical) where ρ is the crustal density (2600 $\frac{kg}{m^3}$), g is acceleration of gravity, and z is depth. We constrain the horizontal principal stress magnitudes assuming that the ratio of shear to normal stress on pre-existing faults does not exceed the frictional strength of the faults (Jaeger et al., 2009):

$$\frac{\sigma_1 - p_f}{\sigma_3 - p_f} = \left[(1+\mu^2)^{\frac{1}{2}} + \mu\right]^2. \tag{5.1}$$

Using reasonable values for μ of $0.6 \leq \mu \leq 1.0$ (Byerlee, 1978), upper and lower bounds on the horizontal stresses may be placed. Note that we constrain S_{hmin} by replacing σ_1 in equation 5.1 with an expression solely depending on σ_3 and σ_2 and R. We assume $\mu = 0.6$ and a to some degree overpressured subsurface ($\sim 15\%$) as indicated by the occurrence of multiple hot springs. This suggests a minimum principal stress magnitude $S_{hmin} = \sigma_3 = 0.65 \cdot S_v$. Note that the approach to estimate the minimum principal stress taken here differs from related works. Terakawa et al., (2010) assume that an optimally oriented fault is eligible for slip under hydrostatic fluid pressure. Here we argue that this does not apply to the Mogul sequence as elevated fluid pressure levels in the region are evident (hot springs) and can be sustained in the subsurface without continuous fault slip.
The focal mechanisms of the Mogul earthquake sequence show coexistence of strike-slip and normal faulting events (cf. Figure 5.6). This implies that σ_1 and σ_2 interchange in the region. Based on the relative stress ratio R estimated from stress inversion, the difference between intermediate and maximum principal stress is estimated to be small. From this, the maximum principal stress σ_1 can be constrained using the relative stress ratio R at $\sigma_1 = 1.1 \cdot S_v$.

We estimate the excess fluid pressure necessary to trigger seismic events from Amonton's law of purely frictional fault reactivation:

$$\tau = \mu(\sigma_n - p_f), \tag{5.2}$$

where τ is the shear stress, σ_n is the normal stress, p_f is the fluid pressure, and μ the friction coefficient taken as 0.6 (Byerlee, 1978).

We use the orientation of the local stress field calculated by stress inversion and the corresponding estimated principal stress magnitudes to determine the shear and normal stresses acting on any plane through Cauchy's relation. The excess fluid pressure required to induce failure is obtained by re-arranging equation 5.2. The lower and upper physical limits of the calculated fluid pressure are given by the hydrostatic and lithostatic pressures (cf. Figure 5.7). We attribute the observation of fault planes at varying orientations (determined from focal mechanisms) within the prevailing stress field to variations of fluid pressure within the causative fault (Terakawa et al., 2010). This concept is illustrated by a 3-D Mohr diagram (Figure 5.5). The Mohr diagram shows the normal and shear stress acting on any fault plane within a uniform stress field. Any fault plane orientation exhibits unique levels of shear and normal stress and is represented by a unique point within the Mohr diagram. Seismic slip occurs when shear stress reaches the fault strength, so that the necessary excess fluid pressure to induce slip for any point is represented by the horizontal distance of this point to the failure condition line.

5.2.1 Results

The fluid pressures calculated by equation 5.2 show that the majority of foreshock events occurred at significantly elevated fluid pressure levels (Figure 5.5). While most of the events show $p_f < \sigma_3$, consistent with our hypothesis, some events

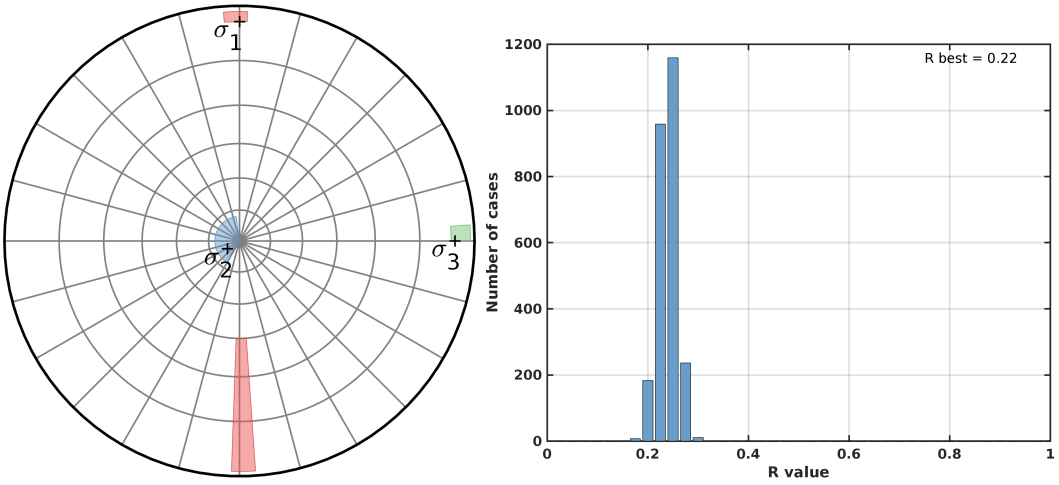

(a) (b)

Figure 5.4: Results of the stress inversion of 1082 focal mechanism of the Mogul sequence. **a)** The orientation of the local stress field is defined with high confidence. Maximum and minimum principal stresses are trending north (0°) and east (90°) on nearly horizontal planes, respectively. The intermediate principal stress σ_2 is trending NW on a 83°-dipping sub-vertical plane. **b)** Distribution of the inverted R-value. The best-fit solution yields R=0.22.

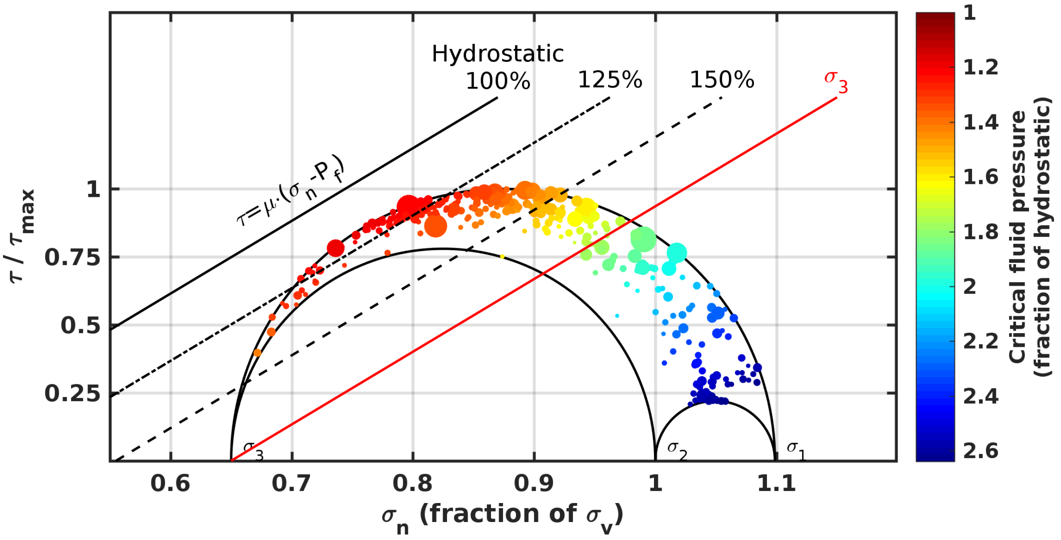

Figure 5.5: Mohr diagram for the critical fluid pressure analysis in the strike-slip regime. The principal stresses are shown in fractions of the vertical stress. Lines show fault strength for hydrostatic, moderate overpressure, high overpressure and lithostatic fluid pressure, respectively.

indicate fluid pressure values above the hydro-fracture condition.

The required fluid pressure to facilitate slip on optimally oriented faults is nearly constant with depth (Figure 5.7), suggesting a relatively homogeneous overpressure distribution. Nevertheless we observe a wide range of required fluid pressures from close to hydrostatic up to pressures nearly as large as the vertical stress. Notably, the number of events with $p_f > \sigma_3$ increases with depth, exhibiting a maximum around 4km depth. Figure 5.7 also shows the slip tendency as ratio of shear to effective normal stress normalized by the friction coefficient and assuming hydrostatic fluid pressure. We observe that events within the physical limits of fluid overpressure exhibit the highest undisturbed slip tendency, while events with fluid pressures $p_f > \sigma_3$ should have been stable under the prevailing stress conditions. Noting the position of such hydro-fracturing events within the Mohr diagram (Figure 5.5), indicates slip on very far from optimally oriented fault planes.

Figure 5.6 shows the distribution of focal mechanism types classified according to the criteria set forth by Johnston et al., (1994) on a ternary diagram. Further we distinguish between events with $p_f < \sigma_3$ from others by color. We observe that ~ 80 percent of the strike-slip dominated events are events that show $p_f < \sigma_3$. Even more striking, $70 - 90$ percent of the events where a normal faulting focal mechanism was detected show $p_f > \sigma_3$ (cf. Figure 5.6 and Table 5.1). This discrepancy suggests the presence of other, masked trigger mechanisms for these events.

The analytical analysis strengthens the hypothesis for a fluid pressure triggered earthquake sequence. Overall, about 70% of all observed foreshocks present required overpressures that are physically possible. The required overpressure varies greatly between close to hydrostatic levels up to the vertical stress. We observe that the majority of events that are likely to be fluid pressure triggered are strike-slip dominated. On the other hand, improbable events are predominantly linked to normal faulting mechanisms.

Table 5.1: Foreshock events classified according to the criteria set forth by Johnston et al., (1994) and further separated into physically possible and impossible events due to their estimated required triggering fluid pressure.

	Detected events	$p_f < \sigma_3$ (physical)	$p_f \geq \sigma_3$ (impossible)
all foreshocks	328	67.9%	32.0%
strike-slip	98	**83.7%**	16.3%
strike-slip-normal	91	**81.3%**	18.7%
strike-slip-reverse	52	**80.8%**	19.2%
normal	42	11.9%	**88.1%**
normal-strike-slip	33	27.3%	**72.7%**
reverse	3	**66.7%**	33.3%
reverse-strike-slip	9	**100%**	0%

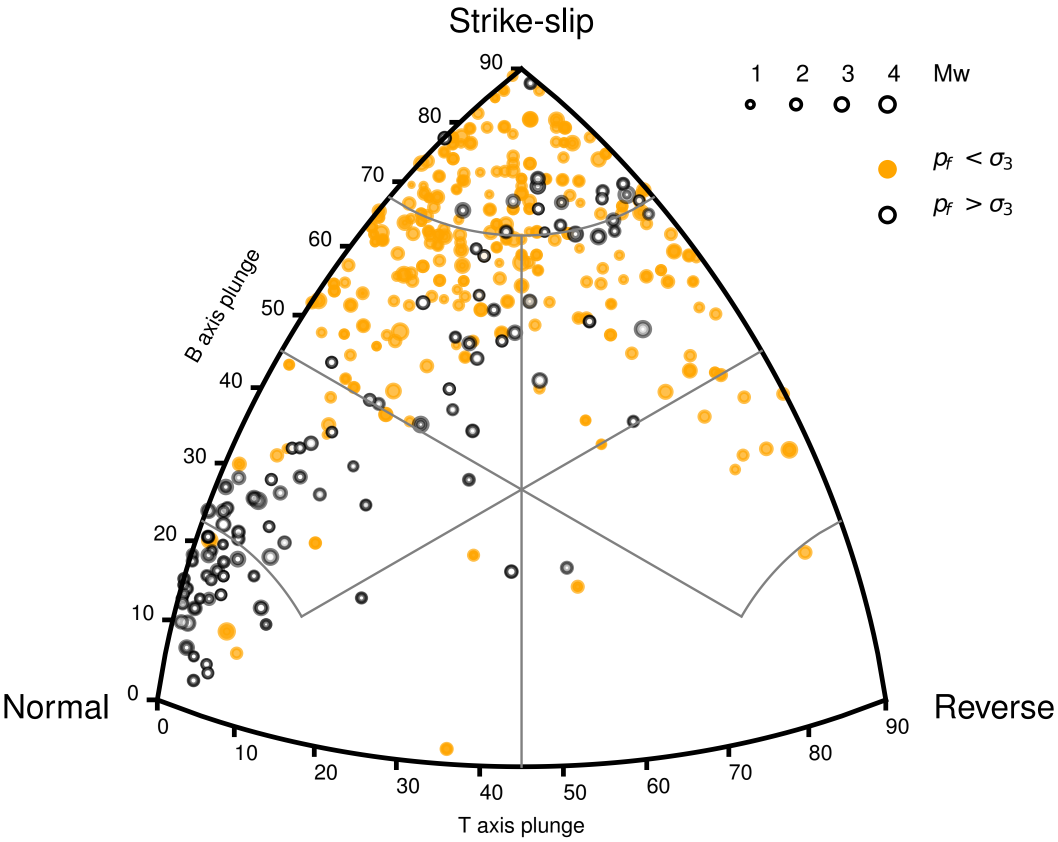

Figure 5.6: Ternary diagram of focal mechanisms during the foreshock period. Foreshocks are further separated into physically possible and impossible events due to their estimated required triggering fluid pressure. Events are classified according to the criteria set forth by Johnston et al., (1994). The ternary diagram was generated with FMC (Álvarez-Gómez, 2014).

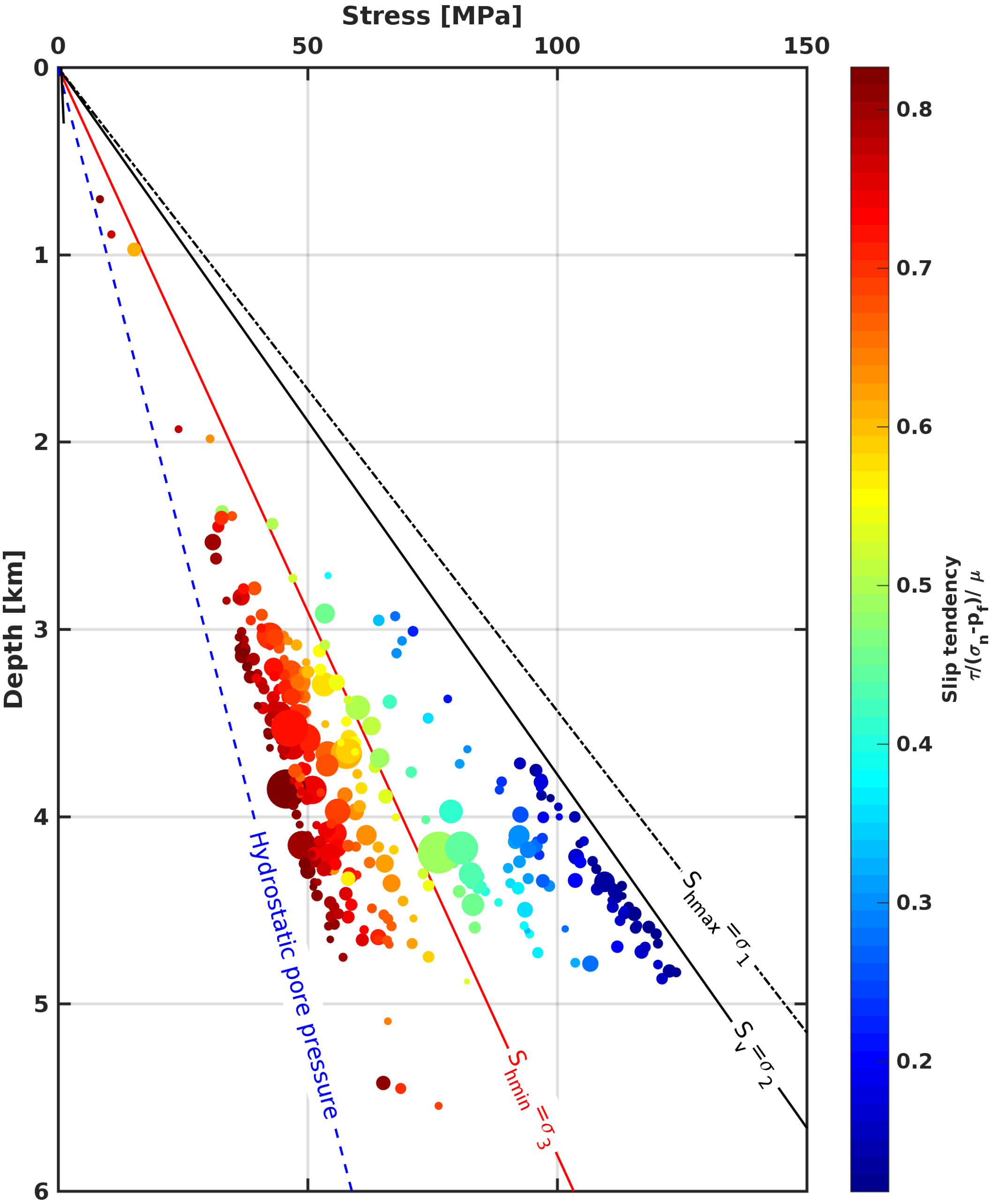

Figure 5.7: Excess (above hydrostatic) fluid pressure analysis. Critical fluid pressure for the foreshock events with depth. Lines show the hydrostatic and principal stresses with depth. Events are sized by magnitude and color-coded by frictional slip tendency.

5.3 Numerical simulation: A model for fluid pressure triggering

We use numerical simulations to evaluate whether the spatio-temporal evolution of the Mogul earthquake sequence can be reproduced based on our conceptual model of a deep supra-hydrostatic fluid source. We numerically model the foreshock sequence by solving a nonlinear diffusion equation in a highly fractured porous medium and evaluate fault slip based on fracture stability analysis. We use an embedded discrete fracture model (EDFM) following the phenomenology described in other studies (Hajibeygi et al., 2011; Karvounis, 2013) to determine the evolution the fluid flow evolution in the fractured subsurface. The conceptual idea of the EDFM is the distinct separation of the fractured subsurface into a fracture and a matrix domain. We introduce a transfer function to account for coupling effects between the two domains, so the fracture and matrix domains are computationally independent except for the transfer function.

The flow in the naturally fractured subsurface is often described by the equations for slightly compressible single-phase flow. From mass balance, assuming single-phase fluid flow, the pressure equation is,

$$\phi\left(\beta_f+\beta_r\right)\frac{\partial p}{\partial t}=\nabla\cdot\left[\frac{k}{\mu}(\nabla p-\rho_f g)\right]+Q \tag{5.3}$$

Where ϕ [-] is the porosity, ρ $[\frac{kg}{m^3}]$ is the fluid density and p [Pa] is the fluid pressure. The compressibilities β [Pa^{-1}] are denoted with the subscripts f for fluid and r for rock, respectively. Moreover, k $[m^2]$ is the permeability and μ $[\frac{1}{s}]$ the fluid viscosity.

From the fluid pressure p, the fluid velocity is calculated using Darcy's law, i.e.

$$\mathbf{v}=-\frac{k}{\mu}\nabla p \tag{5.4}$$

The total mass balance equation derived above is separated into for the matrix and the fracture domains, i.e.

$$\phi^m\left(\beta_f+\beta_r\right)\frac{\partial p^m}{\partial t}=\nabla\cdot\left[\frac{k^m}{\mu^m}(\nabla p^m-\rho_f g)\right]+\Psi^{mf}+Q^m \tag{5.5}$$

and

$$\phi^f\left(\beta_f+\beta_r\right)\frac{\partial p^f}{\partial t}=\nabla\cdot\left[\frac{k^f}{\mu^f}(\nabla p^f-\rho_f g)\right]+\Psi^{fm}+Q^f \tag{5.6}$$

where Ψ^{mf} and Ψ^{fm} are the flux transfer functions between the damaged matrix and the fractures. Superscripts m and f denote matrix and fracture quantities respectively.

We apply a transfer function governing the mass exchange between the two domains since flow in the damaged matrix is treated separately from flow in the fractures. The transfer function is treated as a source/sink term in the pressure equation for damaged matrix and fracture, respectively, similar to classical well models (Peaceman, 1978). As the methodology and its implementation is described in detail elsewhere (e.g. Jansen and Miller, 2017) further details are omitted at this point.

A simplified analytical approach to fracture slip enables us to estimate fracture stability based on slip tendency analysis. Following Amonton's law for purely frictional fault reactivation in equation 5.2, slip tendency is the ratio of shear stress to effective normal stress on a surface (Morris et al., 1996). Fracture failure or slip is likely to occur if the shear stress to effective normal stress ratio equals or exceeds the frictional sliding resistance μ. We define the stability of a fracture as follows

$$T_s = \begin{cases} \frac{\tau}{(\sigma_n - p_f)} < \mu & \text{(stable)} \\ \frac{\tau}{(\sigma_n - p_f)} \geq \mu & \text{(unstable)} \end{cases} \tag{5.7}$$

Reactivated fractures generally show an increase in aperture. Due to a strong aperture dependence of permeability (e.g. Nemčok et al., 2002), where small changes in aperture result in very large changes in permeability, it can be assumed that unstable (or sliding) fractures undergo a stepwise change in fracture permeability (Miller and Nur, 2000). Here we adopt the most simple model

$$k^f = \begin{cases} k^f & \text{if } T_s < \mu \\ \gamma \cdot k^f & \text{if } T_s \geq \mu \end{cases} \tag{5.8}$$

where γ is an permeability enhancement factor. This model successfully described the distribution of the induced seismicity in the Basel EGS site, and fluid-driven aftershock sequences (Miller, 2015; Miller et al., 2004). Quantification of the modeled seismicity in terms of magnitude is not possible within this approach because slip on the fault is currently not explicitly resolved.

5.3.1 Initial conditions

We numerically model the foreshock sequence by solving the nonlinear diffusion equation as presented in the previous section. We use the dataset originally presented in Ruhl et al., (2016b) to compare our numerical results with the data. The initial conditions are determined as a qualitative best fit from a series of more than 800 simulations.

The numerical analysis is simplified by considering the two-dimensional profile A-B shown in Figure 5.8 (cf. Figure 5.2). All foreshock events within 2km to each side

(1372 of 1409 relocated foreshock events) of the profile are projected onto the two-dimensional domain for comparison with model results (cf. Figures 5.2 and 5.8). The two-dimensional model domain covers an area of 8km x 8km. The profile was chosen so that 73% (5630 of 7752 relocated events) including the main shock are included in the comparison.

Although the occurrence of thermal springs suggests slightly elevated fluid pressures, the domain is assumed to rest at hydrostatic fluid pressure in the initial conditions. We use this approximation due to a lack of detailed information on the in-situ fluid pressure distribution. The source region below the modeling domain is initialized at 52% of lithostatic (130% of hydrostatic). The depth dependence of the hydrostatic pressure limits the theoretically observable overpressure to 40% at 6km and 60% at 4km depth. These bounds are in agreement with the previously estimated required excess fluid pressures in section 5.2.

Flow initiates when the over-pressured fluid from below enters the numerical domain in a zone approximately 2km in width in the beginning of the simulation. Faults and fractures are modeled as 1m wide damaged shear zones within the domain (Figure 5.8). Orientations (e.g. strike and dip) follow a distribution determined from the observed focal mechanisms (assuming the correct mechanism was chosen in the data). Fault locations are chosen consistent with the assumed fault structure. Following Faulkner et al., (2011), damage zone thickness is linked to the amount of deformation. As the Mogul fault structure was not previously identified and no surface rupture occurred, we infer deformation mainly in the deeper parts of the faults. Consequently, we decrease shear zone thickness above 3km depth. We estimate the damage zone permeability to be $k^f = 1.99 \cdot 10^{-10} m^2$ using the Cubic law (e.g. Witherspoon et al., 1980) assuming highly fractured damage zones and fracture aperture estimates from laboratory experiments (Kulatilake et al., 2008). We adopt the model of Ingebritsen and Manning, (1999) to estimate matrix permeability where permeability is a function of depth.

As introduced in the previous section, we assume that sliding fractures undergo a stepwise change in fracture permeability. We have chosen $\gamma = 100$, that is a 100-fold increase in permeability consistent with observations from fluid injection sites (Evans et al., 2005; Miller, 2015).

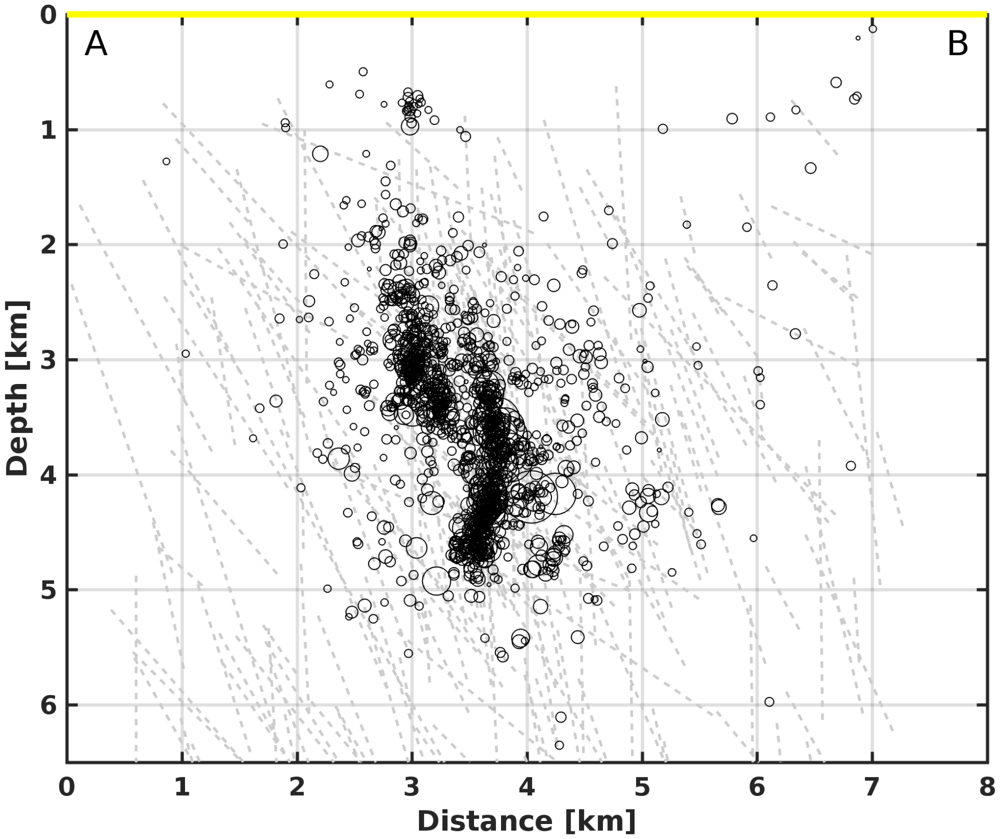

Figure 5.8: Vertical cross section of A-B (cf. Figure 5.2) with the hypocenters of all foreshock events for the 2008 sequence, sized by magnitude. In the background, the faults and fractures modeled as 1m wide damaged shear zones for the numerical model are shown in light gray.

Table 5.2: Properties used in the foreshock simulation.
Superscripts: f - fracture, m - matrix; Subscripts: f - fluid, r - rock.

Matrix permeability	$k^m = 10^{-14-3.2\cdot\log_{10}(z)}\, m^2$
Mean fracture permeability	$k^f = 1.99 \cdot 10^{-10}\, m^2$
Permeability enhancement	$\gamma = 100$
Porosity	$\phi = 0.1$
Density	$\rho_f = 1000\, \frac{kg}{m^3}$
	$\rho_r = 2600\, \frac{kg}{m^3}$
Fluid viscosity	$\mu_f = 0.001\, Pa \cdot s$
Compressibility	$\beta_f = 5 \cdot 10^{-10}\, Pa^{-1}$
	$\beta_r = 1 \cdot 10^{-10}\, Pa^{-1}$

5.3.2 Results

Figure 5.9 shows the results of the subjectively chosen best fit simulation. The evolution of the propagating fluid pressure field is superposed with the modeled seismic events and the data hypocentres of the foreshocks. The results are shown for four respective points in time after the first modeled seismicity occurs.

Prior to any seismic events, our simulation shows a rapid propagation of fluid pressure into the model domain along the shear zones. Pressure propagation into the surrounding matrix is much less pronounced and more diffuse. Diffusion into the matrix is enhanced with decreasing depth due to the decrease in σ_n and consequent increase in permeability. The invading fluid pressure front extends to a depth of approximately 1km below the surface with an average width of 2km.

The evolution of the excess fluid pressure in the system presents a significant correlation with the observed seismicity in space and through time. The high-pressure fluid front triggers the first events at a depth of around 3km, similar to the observed data, at approximately 10MPa excess pore pressure (Figure 5.9a). Continuous recharge from depth allows the fluid pressure front to propagate upward, triggering further events (Figure 5.9b). A very shallow cluster of seismic events occurred approximately 16 days from the beginning of the sequence, which is not captured by our simulation. We observe a clustering of modeled seismicity at 2-4 km depth. This coincides well with a similar clustering in the data. Additionally, modeled seismicity also begins to significantly migrate down- and outwards (cf. Figure 5.9b & c). With progressing fluid inflow and increased permeability in failing fault segments, seismicity spreads throughout the domain in a diffusive pattern until the main shock. (Figure 5.9d). The fluid pressure within the main fault zone continually increases throughout the sequence. Most of the modeled seismicity falls into regions with fluid pressure levels between 10-15 MPa over hydrostatic conditions. In the lower parts of the domain, we observe fluid overpressures >20MPa but only little modeled or measured seismicity. On the right hand side of the main fault zone, a branch where fluid pressure has propagated further into the domain than elsewhere is clearly visible (Figure 5.9d). In general, we find that most of the measured seismicity lies within regions where our simulation shows overpressures of at least 1-5MPa. However, overpressures in that order don't trigger seismicity within our simulation. Finally, some measured seismicity occurs in regions where the simulation does not show any change in fluid pressure during the sequence (e.g. upper right parts of the domain).

In order to compare the spatial extent and temporal evolution of modeled seismic events and foreshock data we determine a confidence ellipse. It is calculated so that it encloses 95% of the foreshocks at a given point in time. The resulting ellipse is also shown in Figure 5.9. In the first snapshot (Figure 5.9a) all modeled events are located well within the confidence ellipse. However, due to a relatively remote foreshock (∼6km depth) the confidence ellipse is rather large. The shallow cluster

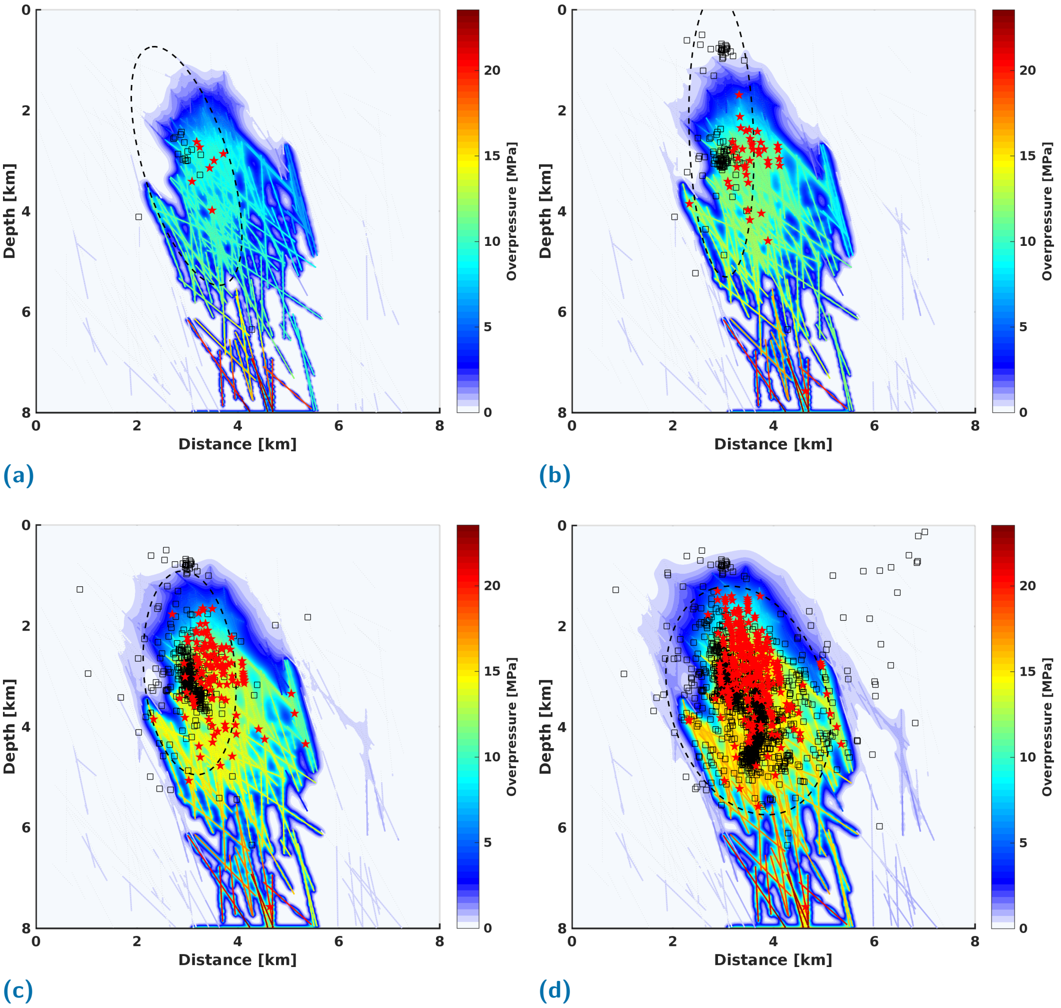

Figure 5.9: Evolution of the seismicity, modeled excess fluid pressure, and modeled events during the foreshock sequence of the 2008 Mogul sequence. All hypocenters of fore-shocks within 2km of each side of the cross-section A-B are shown (black squares) for different times. The dashed ellipse is the 95% confidence best fit approximation surrounding the hypocenters. Red stars indicate modeled slip events. The tiles show the evolution for (a) 5 days, (b) 20 days and (c) 40 days after the first locatable seismicity and (d) ∼63 days, immediately before the main shock on April 25, 2008.

of seismic events in Figure 5.9 distorts the ellipse so that some modeled events are located on the outside. In Figure 5.9c& d most of the modeled seismicity lies within the best-fit ellipse calculated based on the data. Overall, we find good agreement between data and simulation results, especially for later stages of the foreshock sequence (Figure 5.9c& d).

Figure 5.10 shows the migration of foreshock events with time. Migration is measured by the signed radial distance of foreshocks with respect to the first event. The corresponding sign is computed based on the event's depth with respect to the first event. The observed seismicity and modeled fault-slip events migrate roughly on the same parabolic distance envelope that corresponds to linear fluid pressure diffusion from a point source. Yet different diffusivities seem necessary to describe the upward and downward migrations respectively. In both simulation and data we observe more downwards migration than in the opposite direction. Additionally, deviations from linear behavior are visible through seismicity bursts in both foreshock data and simulation. Between 25 and 40 days from the beginning of the sequence, many spatially and temporally clustered foreshocks were observed in the data. This variability in earthquake location and seismicity rate is reasonably well captured by the numerical simulation. Towards later stages of the foreshock sequence, larger deviations between the model and simulations appear. While the modeled seismicity rate remains rather constant and shows mainly homogeneous migration in the days prior to the mainshock, the data shows significant seismic bursts as well as rapid downwards migration. Nevertheless, for the largest part of the foreshock sequence (up to ~50 days) we see good agreement between simulation and the foreshock data.

The numerical analysis further strengthens the hypothesis for a fluid pressure triggered earthquake sequence. Overall, both Figures 5.9 and 5.10 show that the simulation is reproducing the spatio-temporal behavior of the observed seismicity. Nevertheless, not all observed seismicity can be reproduced by the numerical simulation. Especially foreshocks at larger distances to the main fault zone and some distinct bursts of seismicity at high migration rates in the days preceeding the mainshock are not captured in the simulation.

5.4 Discussion

The 2008 Mogul foreshock sequence presents a complex spatial and temporal evolution. This is certainly true for numerous sequences, however accurate and extensive datasets are rare. A high-density coverage of seismic stations provided a large dataset of accurately relocated events and focal mechanism solutions. We have performed analytical and numerical simulations based on this dataset in order to provide insight into the sequence.

The analytical analysis shows that the local stress conditions are generally in favor of

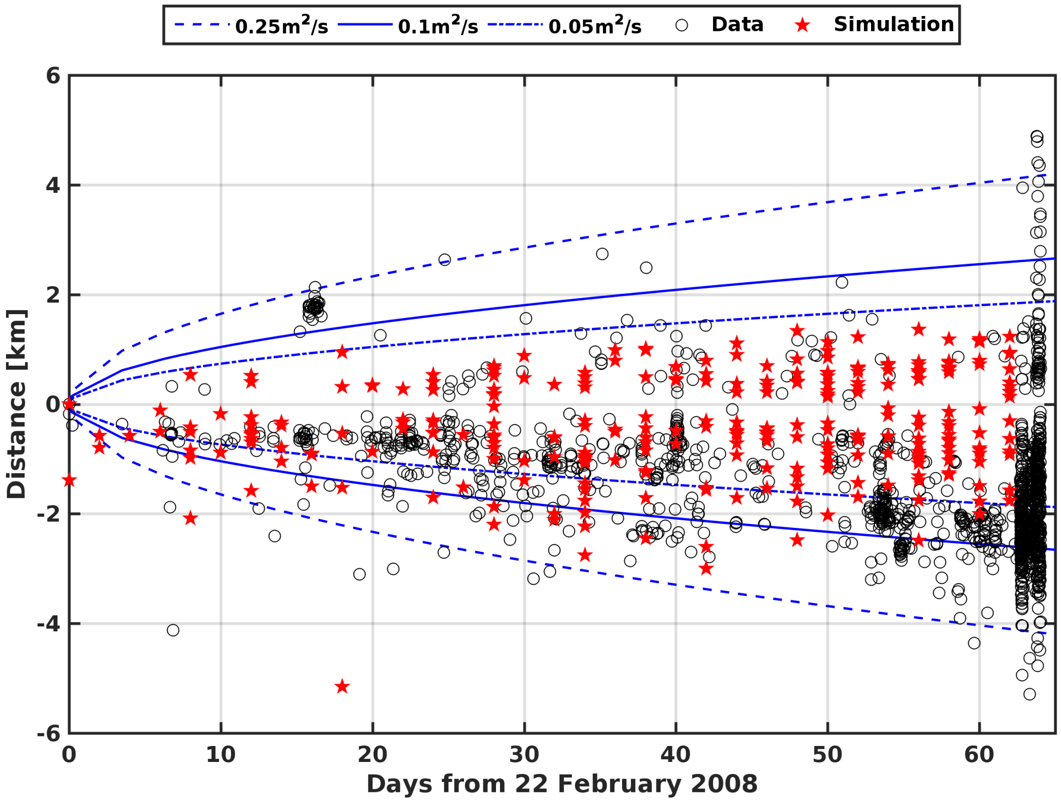

Figure 5.10: Seismicity migration during the foreshock period. Distances are measured radially from the first event for the sequence events (black circles) and the results of the simulation (red stars). Distances are located in the upper/lower half of the domain relative to their vertical occurrence. Lines represent event migration curves following the linear diffusion model (Shapiro et al., 1997) for diffusion rates of $0.05m^2/s$ (point-dashed), $0.1m^2/s$ (solid) and $0.25m^2/s$ (dashed), respectively. On the far right side the mainshock-cluster is visible.

a fluid-pressure trigger. We show that the majority of events that are likely to be fluid pressure triggered are strike-slip dominated. Improbable events are predominantly linked to normal faulting mechanisms. The simultaneous occurrence of physically possible and improbable seismic events indicates a combination of fluid-pressure triggering and kinematic processes. Alternatively, a shift in the local stress regime from strike-slip to normal faulting could permit slip on these otherwise unlikely fault planes. However, we believe that kinematic processes on the regional scale (e.g. pull aparts in en echelon strike-slip segments) were more likely to have triggered these events. Although significant amounts of seismicity were observed on non-critically stressed fault planes, we find strong evidence suggesting the fluid pressure triggering of the foreshock sequence. The occurrence of Lawton hot springs within the area of the earthquake sequence indicates a permeable and likely highly fractured sub-surface and ubiquitous fluids.

Our numerical model is based on the conceptual model of Ruhl et al., (2016b) and follows the general idea of Sibson, (1996), where fault-fracture meshes are related to fluid-driven earthquake swarms in a variety of tectonic settings. The simulation reproduces the spatio-temporal behavior of the observed seismicity. Yet, a distinctive number of foreshocks do not coincide with our modeling results. We link this misfit to a lack of knowledge on the fault geometry and general model uncertainty. We acknowledge that a large amount of model uncertainty remains, so we do not seek to fully reproduce the observed foreshock pattern in detail. Accordingly, we focus on general behavior rather than individual structures. In this regard, our model produced exceptionally good correlation in terms of extent, location and migration of the observed seismicity.

Accounting for the faults and fractures discretely in the numerical model allows rapid fluid pressure propagation within the fault zone at rates exceeding classical linear diffusion models. This is potentially important as the observed branching in Figure 5.9c & d could explain how seismicity far away from the main fault zone is triggered. The branching in our simulations did not trigger seismicity as fluid pressure levels remained low. Nevertheless, pre-existing permeable fractures that provide fluid pathways towards the outer regions of the fault zone might be missing form our fault geometry.

Model uncertainty does not only persist in the fault geometry, but also in the constraints of the physical properties used in our model. The results presented in this study were subjectively determined to be the best fit to the data from a series of more than 800 simulations. Within these simulations we have determined several other parameter combinations of fault zone width, permeability and pressure of the supra-hydrostatic reservoir at depth that were reproducing the foreshock data reasonably well. Consequently, definitive conclusions about fault zone geometry and properties remain elusive. On the other hand, this further strengthens our hypothesis since fluid-pressure triggering is not tied to a single set of parameters.

In combination with the analytical analysis, the numerical simulations provides strong evidence for a likely fluid-driven foreshock sequence. In the following we will highlight the impact of our findings and discuss questions of special interest that result from our study.

5.4.1 Event migration

In order to test for fluid diffusion as triggering mechanism, the equation of Shapiro et al., (1997) is often used.

$$r = \sqrt{4\pi D t} \tag{5.9}$$

It calculates the distance r of a propagating fluid pressure front diffusing at rate D through a homogeneous isotropic saturated poroelastic medium from a point source. The solution is parabola-shaped and utilized in Figure 5.10. The model is based on a point source injection and assumes linear diffusion as main driving mechanism. Observed seismicity suggests spreading rates that correlate well to linear diffusivities between 0.05m^2/s and 0.25m^2/s. Migration rates on this order are associated with fluid flow through a fractured volume (e.g. Parotidis et al., 2003; Shelly et al., 2015). However, deviations from the parabolic envelope (e.g. bursts in seismicity, differences in migration direction) suggest significant contribution from nonlinear fluid pressure diffusion. Especially bursts are visible in both the simulation results as the original dataset. We observed a discrepancy of event migration between simulation and data in the days preceeding the main shock (cf. Figure 5.10). The data shows significant seismic bursts as well as rapid downwards migration, which is not completely captured by our numerical model. This suggests that a different driver (e.g. aseismic slip, dynamic triggering) is taking over.

The Mogul foreshock sequence presents significant differences in upward and downward migration. During the first foreshock phase only weak downwards migration is visible. More apparent and rapid downward migration is visible later in the foreshock sequence. While upward migration is intuitive for a high pressure fluid source at depth, our simulation shows that downwards migration can similarly be triggered by fluid-pressure. Downwards migration in our simulations is caused by recharge. In lower parts of the fault system the required overpressure to induce fault slip is generally higher (cf. Figure 5.7). However, with continuous fluid inflow from the source at the base of the model, excess pore pressure accumulates over time. At critical levels, this induces fault slip at depths below the initial seismicity (cf. Figure 5.9c). Since the described mechanism requires a certain build-up time, the delayed downward migration, observed in the Mogul foreshock sequence, can be explained.

5.4.2 Source of fluids

Despite the evidence of a fluid-driven foreshock sequence for the 2008 Mogul sequence provided in this study, the source of these fluids remains unclear. Lawton hot springs in the area of the Mogul earthquakes shows the presence of fluids and permeable fractures in the subsurface.

Although seismicity appears to migrate at velocities consistent with linear fluid pressure diffusion of a point source in a fractured volume (e.g. Parotidis et al., 2003; Shelly et al., 2015), we do not find any plausible argument for an intrinsic fluid source around the hypocenters of the first events. This indicates an alternative origin of the excess fluids that could be present at depth as suggested by our model results. One possible explanation for the fluid flow and sudden occurrence of seismic activity is the perturbation of an extensive and overpressured reservoir at depth. The origin of this reservoir remains elusive. Geothermal reservoirs in the region are believed to be supplied from a deep magmatic intrusion recharged by meteoric water (Nehring, 1980; Arehart et al., 2003) that could be the origin of large amounts of fluid within the crust. We suggest that meteoric water from the Carson range and Peavine mountains is able to deeply infiltrate the subsurface through steep fractures. In contrast to the Steamboat hills we propose that fluids are initially trapped within a confined reservoir leading to supra-hydrostatic conditions. Although the Nevada Seismological Laboratory dismissed volcanic activity as a cause for the Mogul sequence at the time, a magmatic intrusion beneath the Mogul area could provide extensive amounts of fluids. There is evidence for a deep magmatic intrusion to the west and northwest of the Mogul area (Smith et al., 2004; Smith et al., 2016). Nevertheless, there is no supporting evidence (e.g. surface uplift) of such an intrusion beneath the Mogul area up to date.

The results of our study suggest that a reservoir at supra-hydrostatic conditions exists beneath Mogul; however, the origin of this reservoir remains hypothetical and should become a research focus in the future.

5.4.3 Aseismic slip & kinemetic processes

A distinctive number of foreshocks do not coincide with our numerical modeling results. In addition to transient mechanisms such as dynamic triggering that are very effective in fluid-rich environments (Hill et al., 1993); static stress transfer, aseismic slip and local changes to the stress-regime are likely to contribute to the triggering of foreshocks, especially on non-optimally oriented faults. In fact, as indicated by the in-situ stress conditions determined in the analytical analysis, not all observed foreshock events could have been triggered by excess fluid pressure. The required pore pressure would exceed the minimum principal stress for these events. This indicates kinematic processes, local heterogeneities in the stress field, dynamic poro-elastic effects, as well as aseismic slip are likely to be important. These processes are currently not captured by our model. InSAR data suggests significant aseismic slip, primarily in the aftershock phase (Bell et al., 2012). However also for the foreshock clusters immediately prior to the main shock, speeds consistent with aseismic slip ($\sim$1km/h) were inferred (Ruhl et al., 2016b). In the present numerical model we assume that all fault instability is seismogenic. Due to the simplified fault failure model, the separation of seismic and aseismic slip is not possible within the realm of this study.

5.4.4 Main shock & aftershock sequence

In this sutdy we have focused on the foreshock sequence. The main shock or the aftershock sequence were not yet investigated. Our results suggest that the main shock resulted from the consequences of the foreshock fluid intrusion and migration. The observed diffusion-like spreading of the seismicity until the main event corresponds well to the hypothesis of Ruhl et al., (2017) that the opening of fluid pathways and continued fluid migration could have caused the main shock. The aftershock sequence exhibits the characteristics of typical mainshock-aftershock sequences (Ruhl et al., 2016b) where triggering is expected to be the consequence of various triggering possibilities including fluid-pressure (e.g. Miller et al., 2004).

Dynamic and static stress transfer can be expected to be controlling parameters of aftershock location and intensity (Toda et al., 2012; Kilb et al., 2000). Since our results show that fluids were of major importance during the foreshock period, we expect a significant fluid-driven contribution to the aftershock sequence as well.

5.5 Conclusion

Comparisons between model and observations provide strong evidence for a predominantly fluid-driven foreshock sequence. The structural, seismic and modeling response of the 2008 Mogul earthquake sequence support a scenario where high pressure fluid infiltrates a highly fractured shallow subsurface leading to fault slip throughout the domain. Our combined analytical and numerical analysis provides important insight on foreshock sequences. Stress inversion and overpressure estimations are well suited to evaluate the feasibility of fluid-pressure triggering based on the regional stress conditions. Our numerical simulation further shows that the lack of dominant upward migration of seismicity does not exclude fluid-pressure as the driving mechanism. Finally, we expect that the approach presented can be applied to other studies of swarms or swarm-like earthquake sequences.

6 Simple and fast generation of structured hexahedral meshes for improved subsurface simulations

> Loki: *I have an army.*
> Iron Man: *We have a Hulk.*
>
> — **Marvel's The Avengers**
> 2012

This Section is published as: Gunnar Jansen, Reza Sohrabi, Stephen A. Miller, HULK - Simple and fast generation of structured hexahedral meshes for improved subsurface simulations, In Computers & Geosciences, Volume 99, 2017, Pages 159-170, doi:10.1016/j.cageo.2016.11.011.

6.1 Introduction

A geological model should incorporate structural information and rock properties for any kind of subsurface simulation because simulation accuracy strongly depends on the relevant rock properties and their distribution in space. Therefore, reliable results can only be expected when well-constrained structural and lithological information is used in the simulation. Due to complexities in both the geological modeling and subsurface simulation, an integrated approach of modeling the geology and the physics of the subsurface (e.g. flow, deformation, etc.) is in many cases not available. Commercial software exists that provides integrated modeling and simulation, especially in the oil/gas industry, but often requires months of expert training and their usage might be unsuited for academic purposes. Unfortunately most researchers are only expert in a single field. Thus, they might be either experts in geological modeling or very good in simulators, but rarely both. Consequently, this often leads the situations where very detailed geological models are never used to simulate physics, while simulators with highly sophisticated physics are often only applied to simple and over-simplified geologies. We address this problem for simulators using hexahedral grids by proposing an efficient mesh generation method. The method is based on octree refinement and provides for direct transfer of structural geological information to the numerical simulator of the underlying physics.

6.1.1 Discretization of geological models

Most meshing algorithms focus on aligning the mesh exactly with the boundaries of the structural geological model. This is inevitable in some cases, such as the prototyping of engineering parts. In other cases, such as structural geological models, this requirement of a so-called *conforming* mesh is too strict and not always necessary because of the uncertainties associated with the geological model itself (Bárdossy and Fodor, 2001; Thore et al., 2002; Lindsay et al., 2012; Wellmann et al., 2014). A well-discretized geological model therefore does not necessarily follow the exact boundaries of the geological model, but more importantly enables the simulator to capture the most relevant aspects and to properly model the underlying physics.

Structural geological models can be built using several different methods if the amount of data (e.g. geological, geophysical or seismic surveys) is sufficient and are readily implemented in widely used commercial software packages *Geomodeller (Intrepid-Geophysics), GOCAD (Paradigm)* or *Petrel (Schlumberger)*. In cases where the geological information available is sparse, solely the interpretation of the geologist might be used to build a structural model using a computer aided design (CAD) program. Of course, with less data available, the accuracy of the structural model and thus ultimately of the subsurface simulation is limited.

The type of discretization requested by the wide variety of subsurface simulators varies largely due to the different underlying numerical methods that impose different restrictions on the geological model's discretization. Finite Element simulators are often based on triangular or tetrahedral meshes, while many finite volume based tools require quadrilateral or hexahedral meshes (Pruess et al., 1999; Hammond et al., 2012; Jasak et al., 2007; Trefry and Muffels, 2007; Li et al., 2009). Automatic high quality mesh generation software is available for triangular and tetrahedral elements using Delaunay triangulation (Ho-Le, 1988; Chan and Anastasiou, 1997; Du and Wang, 2006). However, many simulators exist, especially in the field of computational fluid dynamics in general and in high performance computing, that are based on quadrilateral discretizations. Unfortunately, where a quadrilateral / hexahedral mesh is required or beneficial, a general and stable automatic solution method for the generation of a conforming mesh is not available and a field of ongoing research (Yu et al., 2015; Botella et al., 2014; Owen and Shelton, n.d.). Significant progress was made in recent years and also applied to geological models (e.g. (Xing et al., 2009; Zehner et al., 2015; Botella et al., 2016)). However, these methods share a certain complexity in terms of automatism and are rather time-consuming (Stupazzini, 2004; Casarotti et al., 2008).

The methods previously described (including most methods from tetrahedral meshing) have their "bottom-up" approach in common. First, two dimensional surfaces based on the vertices on the geological formation boundaries are meshed by quadrilateral elements. The model is then divided into different meshable regions, which are meshed separately by one of the methods in hexahedral meshing such as sweep-

ing or the advancing front technique (Scott et al., 2005; Löhner, 1996). These separated volumes are connected in a last step to a complete discretization.
As outlined previously, a conforming discretization as targeted by these algorithms is not completely necessary. Octree-based meshing algorithms are generally considered very efficient if a good but non-conforming discretization is targeted. Octree methods were introduced in (Yerry and Shephard, 1984) and further enhanced by various authors (e.g. (Schneiders, 1996; Schneiders, 1997; Shephard and Georges, 1991; Marechal, 2001; Tu and O'Hallaron, 2004; Maréchal, 2009)). In general, octree based discretization have good mesh quality , are adaptive and support automatic generation (Xing et al., 2009). The Los Alamos Grid Tool Box (LaGriT) is specifically designed to generate meshes for geological applications and also supports meshing procedures based on octree refinement. Using the octree refinement method, (Miller et al., 2007) used LaGriT to discretize a geological model that demonstrated good performance.

6.1.2 Outline and scope

The purpose of this work is to present a new and simple-to-use tool to reduce the gap between numerical simulators based on structured or octree grids and geological modeling. Short for Hexahedra from Unique Location in (K)convex Polyhedra - *HULK* is a simple and efficient algorithm to generate hexahedral meshes from geological models. We achieve rapid mesh generation by binary space partitioning and the octree refinement. While the method of octree refinement is not enhanced in this work, we present an alternative approach for handling all geological formations at the same time, classifying their position in space efficiently. We therefore utilize a "top-down" approach in our method, in contrast to most of the meshing procedures mentioned previously.

In the following, we focus on the underlying theory of the implemented algorithm. We first describe the discretization procedure, followed by the theory of binary space partitioning that is essential for method efficiency. We briefly introduce the methods to evaluate its performance and provide insight into the implementation. The *HULK* algorithm is then applied a series of test cases, including an irregularly shaped two component system, a sedimentary basin, and a complex example from the Swiss Jura Mountain range. We then evaluate the method's overall performance (e.g. different input mesh sizes for the same model), and conclude with some perspectives for future research.

6.2 Theory

A fundamental target of geological modeling is to identify the boundaries between geological formations in the subsurface. Consequently, the output of any geological modeler is in most cases a discretized (triangulated) boundary volume representation of the formations. This discretized boundary representation can be used as the input for the meshing preprocessor of the subsurface simulator. We use this representation to generate a binary space partitioning and successively refine a hexahedral background mesh as further described in this section.

6.2.1 Octree-based meshing

The grid generation process in *HULK* is based on the octree refinement technique (Yerry and Shephard, 1984; Schneiders, 1996; Schneiders, 1997; Shephard and Georges, 1991; Marechal, 2001; Tu and O'Hallaron, 2004; Maréchal, 2009). Initially, a structured background mesh is generated circumscribing all of the volumes to be discretized. In the next step, each cell is associated with the corresponding geological formation. In *HULK* this cell-to-formation mapping is performed by binary space partitioning of the input volumes, discussed in detail below.

Once the correct position within the input model is determined, cells can be flagged for refinement (or coarsening) based on their affiliation in a third step. Several refinement criteria can be used. Here we chose to flag all cells whose neighbors have non-matching material identifiers for refinement, and cells which have only matching-id neighbors for coarsening (Figure 6.1). The refinement is then executed according to the flags that were previously set. If these two steps are repeated until a desired accuracy or number of mesh cells has been generated, it forces a cyclic refinement towards the boundaries of the geological formations (c.f. figure 6.2). The actual implementation in *HULK* differs slightly from the general approach introduced here and is further explained in section 6.3.

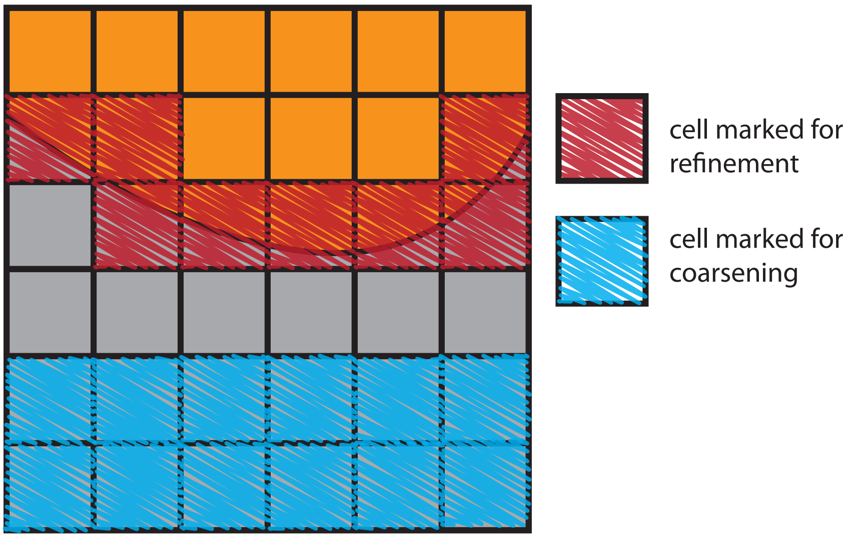

Figure 6.1: A simple model with two materials. All cells which are at the interface of the two materials are flagged for refinement. In the lower part of the model, were many cells do not have neighbors close to the interface, the cells are marked for coarsening.

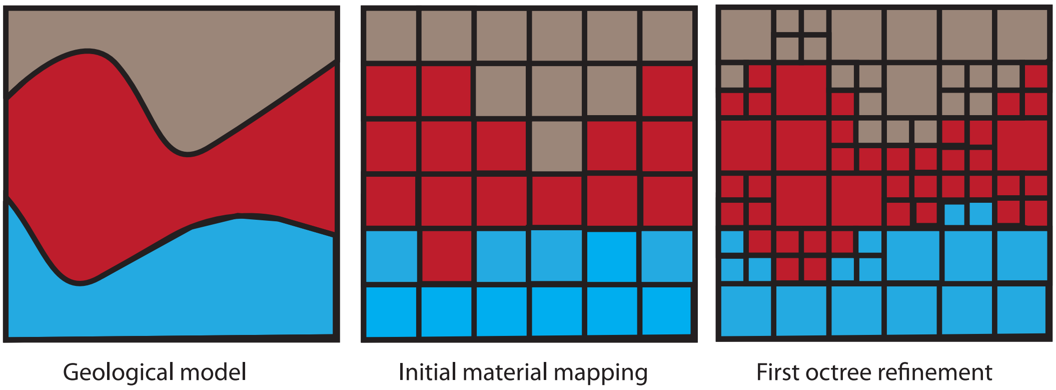

Figure 6.2: Conceptual model of octree based mesh refinement in the context of geological models. Left: Geological model to be discretized. Middle: In a first step the material properties from the geological model are mapped onto the initial grid. Right: Cells are marked for refinement if any of its neighbors belong to another geological formation. This shows the result after the first cycle of octree refinement, and shows that the initial input are better resolved. With increasing number of refinement cycles, the approximation will become very close to the input geometry.

6.2.2 Binary space partitioning

A key element in the efficiency, and the main novelty of our approach, is the efficient mapping of a cell to the corresponding geological formation. Unlike many other meshing algorithms, all input geometries are treated in a single step. This requires an algorithm that is able to swiftly decide whether or not a point (such as the center of a cell) is contained in a geometry. This test is often called “collision detection” and is a well-studied field in computational geometry (Lin and Gottschalk, 1998; Ericson, 2004). A simple and common technique of collision-detection is ray-tracing, where multiple rays are sent out from the query point in arbitrary directions. Each ray is then tested for its number of intersections with the geometry in order to determine its relative position as “inside” or “outside” of the geometry. Unfortunately, the ray-tracing approach has non-optimal efficiency and is prone to errors due to a number of special cases that need to be treated accordingly (Smits, 2005). Another popular approach is binary space partitioning. Binary space partitioning trees (or BSP trees for short) are structures that can be used to recursively partition n-dimensional boundary representations into subspaces with respect to dividing hyperplanes. They are one of many spatial partitioning methods, but considered to be the most versatile and powerful in collision detection algorithms (Ericson, 2004). Originally, BSP trees were developed to address the "hidden surface problem" (Fuchs et al., 1980), but also the computer game engine community takes advantage of the tree structure due to their ability to perform fast collision tests even for a very large number of polygons. If the space to be partitioned is three dimensional, the dividing hyperplanes become regular two dimensional planes. The two partitions or half-spaces generated by a dividing plane are usually called positive and negative half-spaces. We use the convention that the positive half-space lies in front of the dividing plane and the negative half-space behind the dividing plane. In two dimensions the specification of front and back-sides is ambiguous, but as our target geometries are three dimensional the definition is useful. Henceforth, the front side is the side of the geometry's discretized elements whose normal points outward from the geometry.

Generation of a binary space partitioning tree A quick and easy separation of inside and outside the volume ("collision test") is accomplished with BSP trees. Unlike other types of BSP trees, in our method, the dividing planes must be identical with the input geometry's polygons. This selection of the dividing planes is also known as auto-partitioning. Furthermore, all polygons have to be selected exactly once as dividing planes in order to correctly represent the geometry. Note that no actual geometry is stored in the nodes - merely the information pointing to the next nodes in the tree. The end-nodes of a tree partitioning are often called leaves. The leaves store whether the half-space in front / behind the last dividing plane is within the geometry (solid) or outside (empty).

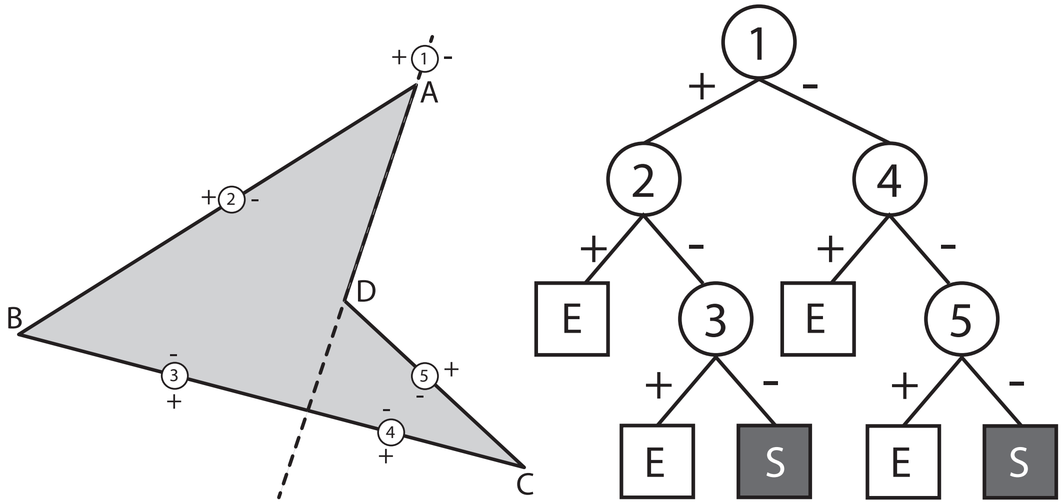

(a) **(b)**

Figure 6.3: A dart shaped geometry represented by a solid leaf BSP tree. a) Geometry consisting of 4 vertices and 4 edges resulting in 5 dividing planes as the dividing plane along $\overline{DA}$ divides edge $\overline{BC}$ into two pieces. b) The final corresponding BSP tree when all edges are chosen exactly once as dividing plane. Boxes with E signal empty (meaning outside) and dark boxes with S are solid (inside the geometry).

The generation of a BSP tree is illustrated in figure 6.3 for a simple dart shaped geometry in 2D. The initial geometry is composed of four vertices (*A,B,C,D*) connected by four edges ($\overline{AB}$, $\overline{BC}$, $\overline{CD}$ and $\overline{DA}$). Now, an edge is arbitrarily chosen to serve as the first dividing plane ①, in this example $\overline{DA}$. All remaining edges are classified according to ①. On the positive side of ①, edge $\overline{AB}$ is found and which is going to be the next dividing plane ② and a part of edge $\overline{BC}$. In order to continue the decomposition, edge $\overline{BC}$ has to be split into its parts on the positive sides respectively ($\overline{BC}^+ \rightarrow$ ③ & $\overline{BC}^- \rightarrow$ ④). The generation of the tree is continued with ②, which will produce a leaf on its positive side (pointing to empty space) and the third dividing plane on the negative side. ③ points to empty space on its positive side. Since all other dividing planes on the negative side of ③ have already been considered, it can concluded that it points to solid volume inside the geometry. The tree construction is continued in the same manner until all polygons have been chosen once as dividing plane. With this the BSP tree generation is complete and can be used to query for a location of a arbitrary point with regard to the geometry. Figure 6.4 shows a graphical representation of such queries for the cases that the query-point is located within and outside of the geometry. Finally note that, although the initial geometry in figure 6.3 is concave, the spatial regions corresponding to the leaves are always convex.

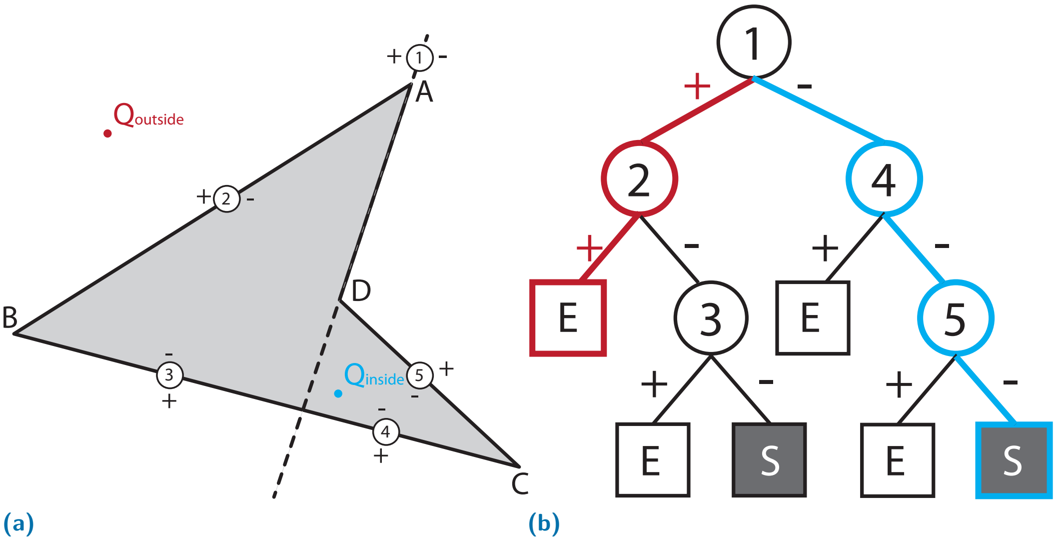

Figure 6.4: Two query points Q_{inside} and $Q_{outside}$ are tested against a collision of the dart-shaped geometry to obtain a result for the relative position of the query point with respect to the geometry. a) Geometry with the two query points - the first outside and the second inside the geometry. b) The corresponding BSP tree query path is visualized for both query points. At each node, the query point is tested against the corresponding plan and sent down in the respective direction. The red path belongs to the outside point, whereas the blue path is assigned to the inside query point. It is evident, that not all nodes of the geometry have to be tested for a collision query. This figure visualizes the optimal complexity of the BSP tree algorithm (c.f. 6.2.2)

Complexity of binary space partitioning Due to the hierarchy formed by a BSP tree with n objects in the tree, only on the order of $\mathcal{O}(\log(n))$ objects need to be tested by a query (Ericson, 2004). This is due to the fact that typically half of the possibilities can be disregarded with each test. However, in poorly balanced trees the query can cost up to the order of $\mathcal{O}(n)$. It is worth noting that the ray-tracing approach is also

$\mathcal{O}(n)$, yet having higher computational cost per element than the corresponding worst case BSP tree. Auto-partitioning of a square yields in fact a worst case BSP tree and is shown in figure 6.5a. Since none of the dividing planes actually divides the square, no possibilities can be disregarded during queries, leading to an $\mathcal{O}(n)$ cost. With this in mind the BSP tree generation of our geological model benefits from complexities in the model as the number of self-intersections is greatly increased. On the other hand, it is clear that we can not expect to generate perfectly balanced BSP trees from our input geometries with auto-partitioning. Thus a query cost in between $\mathcal{O}(log(n))$ and $\mathcal{O}(n)$ can be expected.

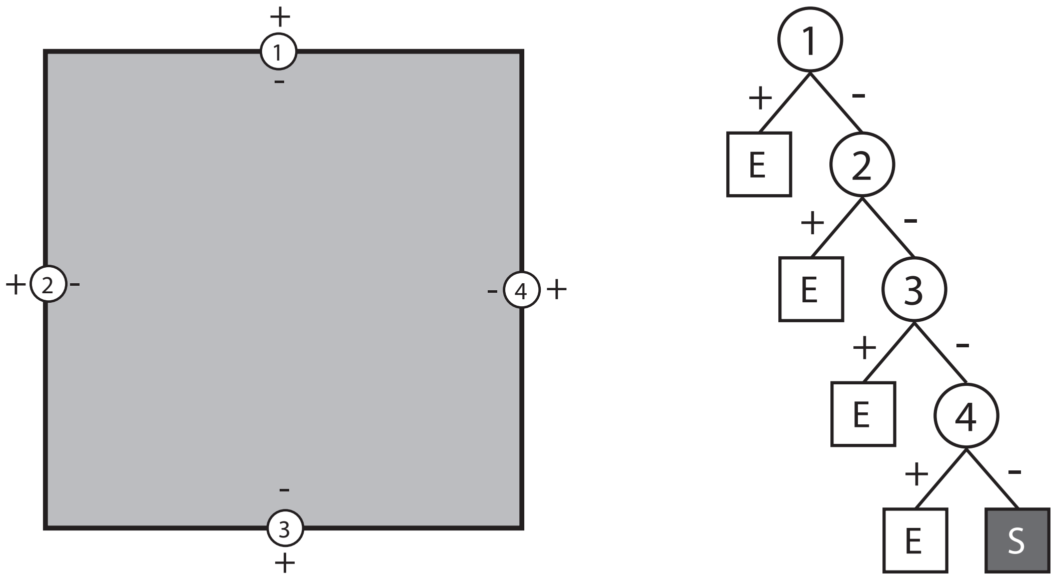

(a) **(b)**

Figure 6.5: The square geometry. This shows how auto-partitioning can lead to unfavorable BSP tree structures. No part of the tree can be neglected after each test. Real world geometries are not likely to suffer from this problem to the same degree, as irregularities in the domain boundaries will most likely provide suitable dividing planes.

6.3 *HULK* - combining octree meshing and space partitioning

The theory is implemented into an efficient and rapid mesh generator. As our primary targets are finite element simulations on adaptively refined grids, we build the mesh generator based on the finite element library *deal.II* (Bangerth et al., 2016; Bangerth et al., 2007). This library has already previously been used for multiphase flow and transport simulations in the subsurface (Chueh et al., 2010; Chueh et al., 2013). Using these subsurface simulators on adequate geological domains is a logical extension of the previous work.

In the following specific parts of the implementation are presented in depth. The pseudo-code for the currently implemented *HULK* procedure is given in algorithm 1.

```
for all input geometries do
    read input data from file;
    generate BSP tree;
end
while cycle < maxCycles and number of cells < MaxCells do
    for all cells do
        for all BSP trees do
            if is inside current BSP tree then
                set id = corresponding material identifier;
                break loop;
            else
                continue with BSP tree for next input geometry;
            end
        end
        if (neighbor's id ≠ cell's id ) for any neighbor then
            flag cell for refinement;
        end
        if (neighbor's ID = cell's ID) for all neighbors then
            flag cell for coarsening;
        end
        if cell's distance to cell's corresponding BSP tree $\leq \epsilon \cdot \max(L_x, L_y, L_z)$
         then
            remove cell's flag for refinement;
        end
    end
    execute refinement;
end
```

Algorithm 1: Pseudo-code for the algorithm used in HULK using octree refinement to resolve complex geometries in hexahedral cells.

6.3.1 Preparation of the input data

There is currently no standard in the output format of geological modelers or CAD programs. Rather, a set of widely used formats has evolved. A well known format is the STereoLithography (STL) format, which is available as an export format in almost any of the relevant programs from the geological modeling or CAD environments. The STL format is based on triangulated surfaces describing only the boundaries of the domain. Due to its wide availability, we use the STL output format as input to our mesh generator. STL files contain only an information header, the overall number triangles to be expected, and then a list of all individual triangles. Each triangle is defined by three vertices and a normal vector, and no information is given about the connectivity. While the data format is fairly simple, a number of issues may arise during their creation. Evidently, the input geometry must be an orientable surface for which a system for determining a normal vector can be consistently defined. In other words, it must not contain any holes, self-intersections or multiple shells. Furthermore, any triangle can not share more than two vertices. This ensures that at least a minimal distance is maintained between all triangles. Fortunately, a number of STL repair methods exist, that can detect and often fix these defects automatically (e.g. implemented in the open-source software *MeshLab* and the freeware *netfabb* and recently (Chong et al., 2007)). Note that a BSP tree can be generated also if these defects are left unaccounted for, but it is clear that a valid "collision" query on the BSP tree is only possible for orientable geometries. In general, the quality of the input STL does not so much influence the final resulting mesh, but more the generation of the BSP tree structures.

6.3.2 Generation of the BSP trees

The BSP tree generation is performed once at the beginning of the program execution after the corresponding geometry has been read from a file. For each input geometry an individual BSP tree is generated. The pointers to the root nodes of the trees are stored in a shared vector to allow easy queries for all geometries. The current implementation does not cover the selection of a preferable splitting plane to guarantee the generation of a balanced BSP tree. Rather, the first polygon (triangle) from the STL is chosen as a root node of the tree, and generation is performed accordingly until all polygons of the input file are used once as splitting planes. Clearly, the time to generate the tree structure is directly related to the number of triangles in the geometry. But since it is performed previously to the actual mesh refinement, the overhead is kept small. During refinement the optimal complexity of the BSP tree queries minimizes the dependence on the tree size, largely contributing to the efficiency of *HULK*.

6.3.3 Refinement criteria

Flagging cells for coarsening or refinement is the main control on the cell size and count in the final discretization. A number of different criteria could be used. In *HULK* relatively basic criteria are implemented at the current state. As the name octree suggests, in the uniform case where all cells are refined, the total number of cells is increased by a factor of 8. Thus, choosing cells to be refined has to be performed cautiously to prevent an unpleasantly large number of cells. On the other hand, cells must be refined enough to resemble the input geometry as close as possible. To this end the following criteria based on each cell's geometric affiliation in terms of an material identifier (id) are used:

- Refinement: if $id \neq id_i$ for any i neighbors → refine
- Coarsening: if $id = id_i$ for all i neighbors → coarsen

Additionally, a suitable criterion to cease refinement has to be defined. Here, the generation stops once the distance d of the query point x is sufficiently close to the BSP tree.

- Evaluate Distance: if $d(x) \leq \epsilon \rightarrow$ clear refine flag

Here ϵ is the only actual tuning parameter in *HULK*. From experience, good results are achieved when $\epsilon \approx 0.005 \cdot \max(L_x, L_y, L_z)$ where L_i are the model extents in the coordinate directions.

In order to assure numerical accuracy, the maximum level difference in refinement between adjacent cells may not be greater than one. This implies that also cells that are not directly associated to the interface might be flagged for refinement in a second internal step. Furthermore, due to the implemented criteria, the number of cells in the initial mesh has to be chosen appropriately to the smallest geometric feature that is to be resolved in the final grid.

6.4 Methods for mesh quality analysis

Measuring the quality of the generated discretized domain is an important part of a meshing algorithm. Standard procedures include the measurement of element skewness, aspect ratio and distortion. These quantities are mainly used to determine the quality based on the degree of conformity and to identify degenerate elements. Since we do not seek a conforming discretization of the input geometries and the discretization is based on regular octree meshes, some techniques of defining mesh quality no longer apply; for example element skewness and aspect ratio become constant and attack optimal value in this case. In order to give a measure of the degree of conformity nonetheless, we compute the "mean distance" between the triangulated input and our hexahedral approximation as well as the volumetric space filling.

Measuring the distance or similarity of two discretized surfaces is not straightforward. Many of the more sophisticated theories developed are used in the field of automatic face recognition (Abate et al., 2007). A simpler approach is used here which computes the minimum distance between the cell centers of cells at the interfaces and the BSP tree of the corresponding geological formation. From this, the mean distance is calculated. Ideally, the BSP tree - cell center distance distribution should have it’s maximum at zero. However, since we compare the cell centers we expect a shift of the mean distance towards the half the size of the largest element on the boundary. In any case, with progressing refinement of the mesh the mean distance is expected to decrease continuously.
Further, the accuracy in volume of the mesh is considered. To this end, the percentage

deviation between the volume of the input V_0 and the final discretized mesh V is calculated:

$$Deviation_{vol}(\%) = \frac{V}{V_0} \cdot 100\% - 100\% \qquad (6.1)$$

The deviation by itself is not a good indicator for the mesh quality, as no information about the shape of the geometries is incorporated and in fact could lead to very poor discretizations. However, in combination with the mean distance it becomes a viable indicator for mesh accuracy.

The quality of octree-based discretization in general is known to be good (e.g. Xing et al., 2009), but the accuracy of the numerical method depends on the overall distribution of the cell sizes. Assuming the numerical accuracy is ideal if all cells are of the same size, the utilization of octree refinement can increase computational efficiency while maintaining the same numerical accuracy only if the cell size distribution is only mildly altered. In other words, smooth cell size distributions with a single peak should always be preferred. Again, this is not a direct measurement of mesh quality, but serves as an important indicator for the expectable accuracy of the applied numerical simulators.

6.5 Results

The implemented algorithm is validated against three test geological scenarios. The first is a 3D model of an artificial dike intrusion into a single constituent host rock to demonstrate the general performance of the algorithm. We then present an example of a simplified three-dimensional model of the newly born hydrothermal system called 'LUSI' in Indonesia (Mazzini et al., 2012; Lupi et al., 2013). This model already consists of multiple geological layers of a sedimentary basin. A third example is a full scale geological model of a part of the Swiss Jura Mountains. The models vary in size and complexity. Table 6.1 shows detailed information on the test geometries used.

Table 6.1: Three model types from different settings are used to evaluate *HULK*'s performance. They vary in size, amount of shells and their underlying complexity.

Model name	**Setting**	**Volumes**	**Input size (triangles)**	**Complexities**
Dike intrusion	Volcanic	1	$1.9 \cdot 10^5$	Locally steep gradients
LUSI	Sedimentary basin	5/7	$4.5 - 7.5 \cdot 10^5$	None/Large scale faults zones
GeoNE	Swiss Jura	25	$1.5 - 11.9 \cdot 10^6$	Folding & faulting including offset

6.5.1 Dike intrusion

Figure 6.6 shows the initial model for the first example. As the model consists only of two geological formations, the volcanic intrusion at the bottom and a host rock on top, only the resulting hexahedral mesh for the volcanic intrusion layer is shown. Note that the input consists only of one shell which describes the geometry of the dike. We assume that the region of interest is a rectangular box around the dike, thus making a second input geometry for the host rock unnecessary.

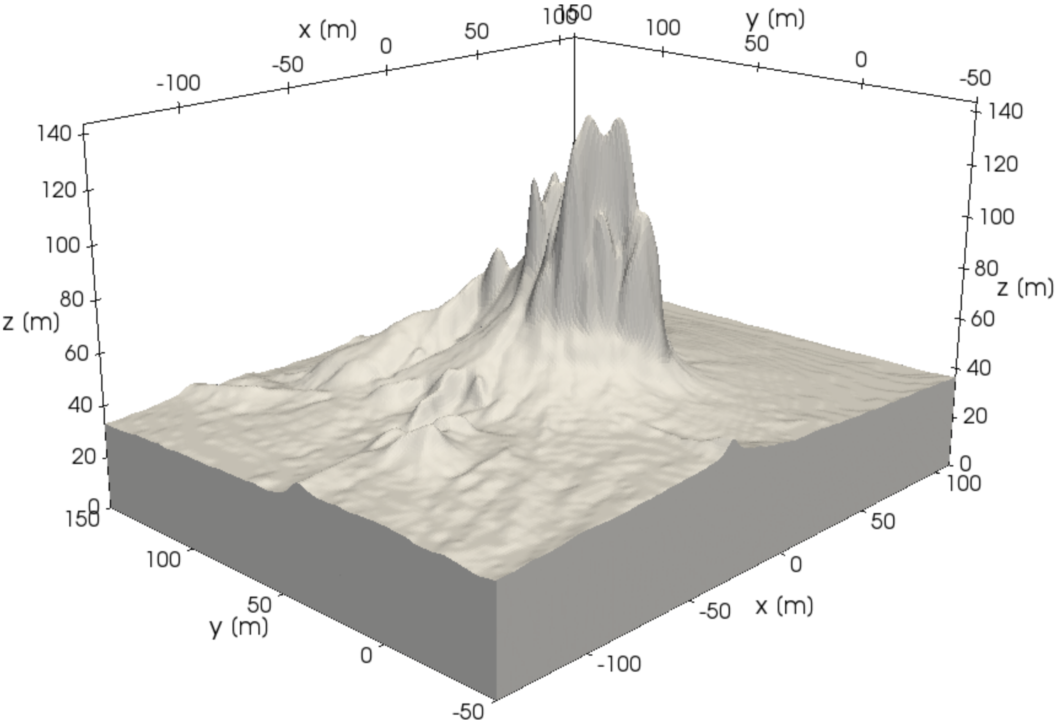

Figure 6.6: The geological model and input for the dike model. The dike has a non-trivial shape with steep gradients to evaluate the implemented algorithm.

The geometry was discretized using four refinement cycles. In table 6.2 the resulting number of cells in the whole (both volcanic intrusion and host rock) are shown for all cycles. Furthermore we evaluated the performance of volumetric filling for the dike intrusion model. To this end we compared the meshed volume against the computed volume of the input STL file. The resulting deviation in volume as well as the distance (measured to the BSP tree) from the input geometry are also presented in table 6.2. The accuracy of the upper layer can easily be computed by $(\delta\%)^1 = 1 - (\delta\%)^0$.

As mentioned in section 6.4 the volumetric filling is not a sufficiently good indicator by itself. This is clearly visible as it is already very high even when the visual accuracy of the mesh is still unsatisfying. Regardless, a clear trend towards the correct theoretical volume is visible. In combination with the measured distance to the BSP tree we can conclude that the mesh accuracy increases with the number of refinement cycles.

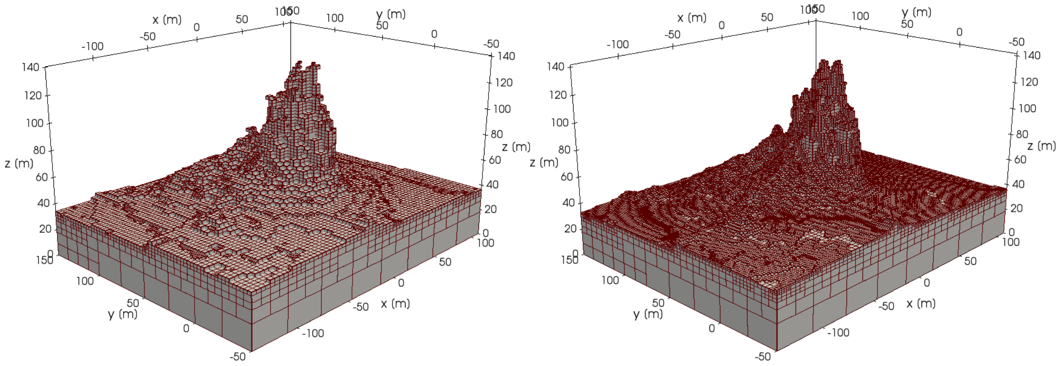

(a) (b)

Figure 6.7: The generated mesh for the dike model after different refinement cycles. a) After the 2nd cycle. The general shape of the dike is already captured but its extends are slightly overestimated and smaller features not yet captured. b) Mesh after the 3rd cycle of refinement. The peak shape is still not matching the input model completely. Yet on the rather flat zones of the interface refinement towards smaller features is visible.

Table 6.2: Mesh statistics for the dike model. The number of cells, volumetric filling accuracy as well as the distance to the corresponding BSP tree can was analyzed for all performed refinement cycles on the dike intrusion model. The volumetric deviation alone is not a sufficient indicator but shows in combination with the BSP distance an overall increase in mesh accuracy with refinement cycles.

Cycles	Cells	Deviation(%)	BSP distance (-) $\cdot 10^{-3}$
0	32768	0.04	23.8
1	21715	1.33	52.6
2	77708	0.47	34.3
3	269746	0.13	22.6
4	861617	0.19	13.8

Figures 6.7a and 6.7b show the mesh after different cycles. Clearly the refinement towards the boundaries is visible. The final model is shown in figure 6.8, which shows that all important features of the initial model were captured by the algorithm. Note that due to the selection of refinement criteria the cell size distribution is not uniform at the interface. Rather flat regions of the model are less refined, whereas areas with steeper geological features exhibit a stronger refinement to capture the curvature of the geometry correctly. After the last cycle the mesh contains roughly 1 million cells which might be too big for initial simulations. However, the accuracy of the preceding cycles is also good and yield a cell count of maximum a few hundred-thousand cells, which can be handled by modern parallel computing systems (Hammond et al., 2014).

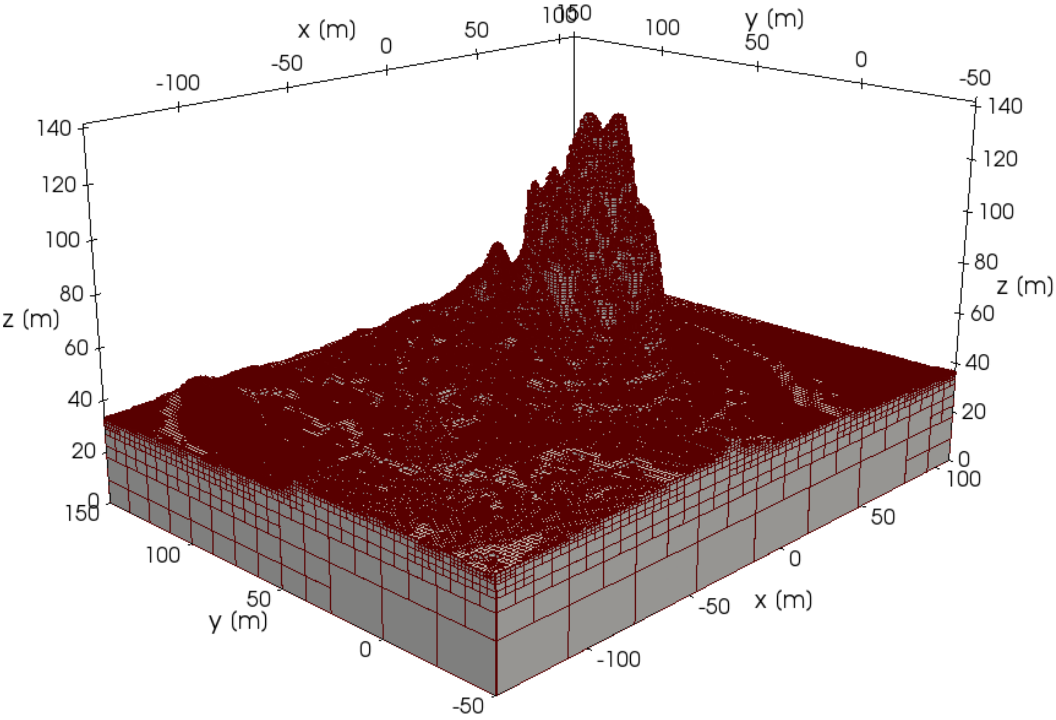

Figure 6.8: The final mesh of the dike model after 4 cycles of refinement by HULK. All important geometric features of the input geometry are captured and provide a good hexahedral approximation to the initial geometry (cf. also 6.2 for detailed accuracy evaluation). Different levels of refinement are visible depending on the curvature of the dike's shape. Flat regions are slightly less refined than the peak for which cells are highly refined to capture its extends.

6.5.2 LUSI

The second example is a simplified model of the LUSI mud eruption in Eastern Java, which appeared in 2006 and continues today as a geyser system Mazzini et al., (2012), Lupi et al., (2013), and Sawolo et al., (2009). LUSI is located in a back-arc sedimentary basin that is likely influenced by nearby active volcanism. The eruption is located at the intersection of two major regional faults which were included in the geological model as finite width faults. In the following we present the model with and without the faults to increase the clarity in analyses. In general, the model does not show many complexities, as the sedimentary basin is mostly undisturbed except for the intersecting strike-slip faults. We generated a model based on seismic and borehole data obtained in the framework of the LUSI Lab project and computed with *Geomodeller* Lajaunie et al., (1997) and Calcagno et al., (2008). The number of input geometries range from 5 formations up to 7 formations if the two major faults are included. The initial model is shown in figure 6.9.

The final discretizations of the LUSI model consist of 346,991 hexahedral cells without and 513,409 cells including the faults. The final meshes without and including the faults are shown in figure 6.10. A visual comparison of the input geometry and the final discretization shows that all important geological features

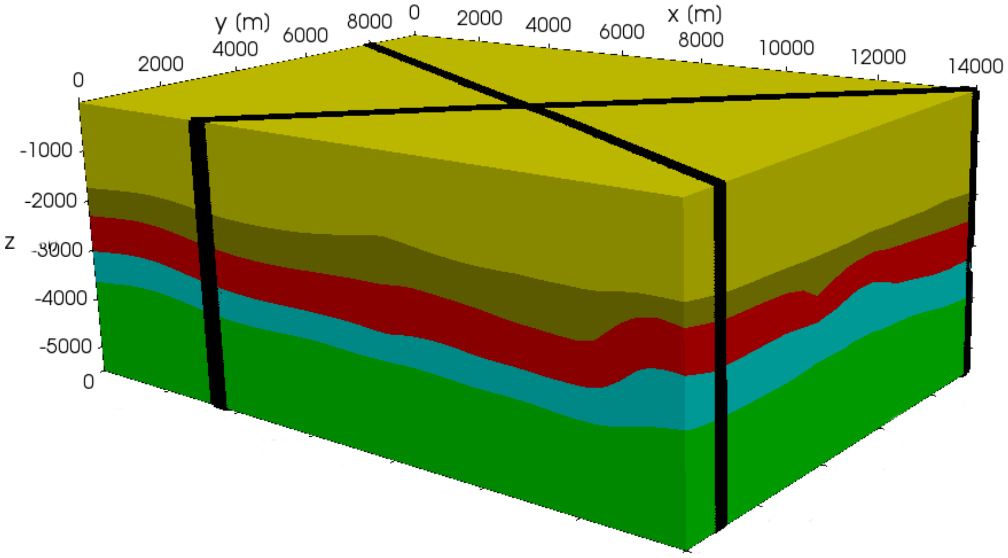

Figure 6.9: The geological model for LUSI used to generate a hexahedral mesh with HULK. Note that the two faults are implemented a posteriori into the model which makes certain analysis unavailable for this model.

of the sedimentary basin are preserved. The LUSI geological model was discretized using five refinement cycles in HULK. For each cycle all volumes are compared to the reference volume of the input geometry. Unlike the dike model, the accuracy of the volumetric filling is not as high during the first refinement cycles. This is mostly due to a different refinement strategy chosen in this example. For this model we decided to change the refinement strategy to a uniform refinement without coarsening or removal of refinement flags in order to show the excellent refinement towards the models boundaries. However, as shown in figure 6.11 the accuracy is greatly increased in later refinement cycles. The final accuracy can also be seen in the y-slice view of the model which is shown in figure 6.12 for the final mesh where the boundary cells for each layer and the outline of the corresponding input geometry are shown. Here it is very well visible that the boundary cells coincide very well with the input geometry after the last refinement step.

6.5.3 GeoNE

The GeoNE model is by far the most complex model that we use to evaluate the performance of *HULK*. Between May 2010 and July 2012, the Laboratory of Geothermics at the University of Neuchâtel studied the potential of deep geothermal resources in the Canton of Neuchâtel in Switzerland (cf. CREGE Laboratoire de Géothermie, 2014). As part of the project a detailed 3D geological model was built. We present a part of this geological model here to generate a hexahedral mesh. This model is going to be used also for the input mesh scaling in the next section. In this section the GeoNE50 model containing a total of 5.9 million triangles is used. The geological model as we use it here is shown in figure 6.13a. The model features geological

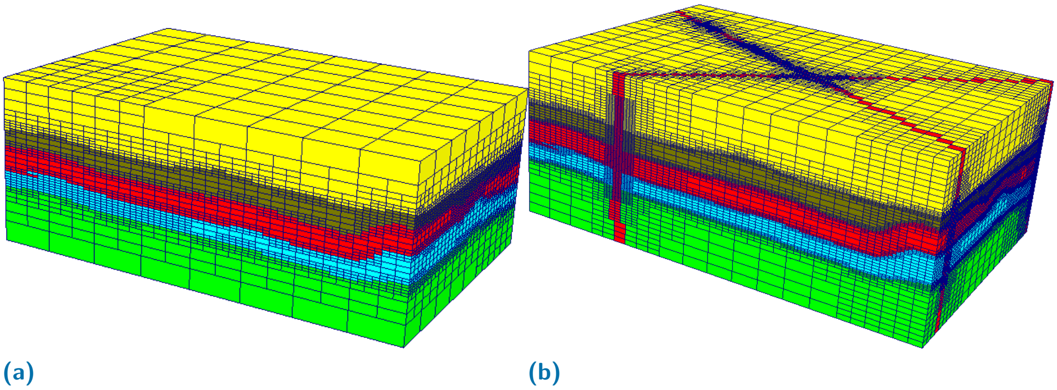

Figure 6.10: The final LUSI model based only on the geological layers of the sedimentary basin with and without big scale faults. The successive refinement into the boundaries of the geological formations is visible and working well. yellow - Sandstone formation, brown - Clay formation, red - Volcanoclastic formation, blue - Carbonate formation and green - Mudstone formation. a) without faults b) with faults

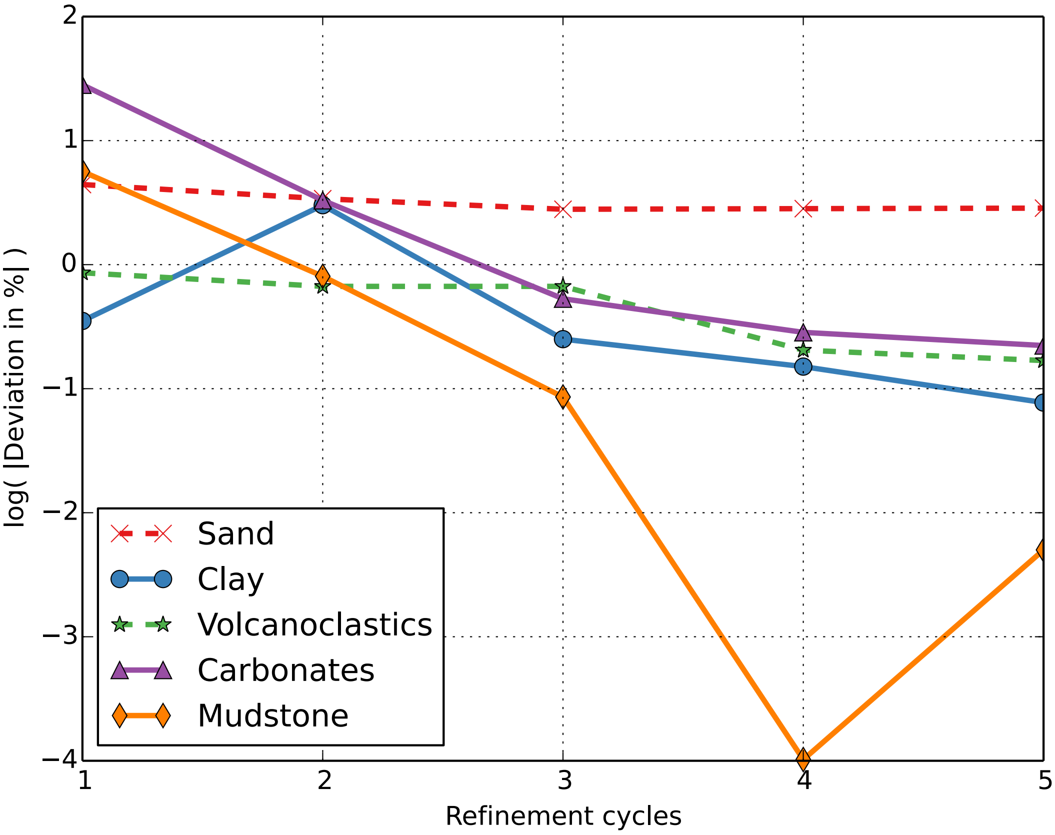

Figure 6.11: The deviation of volumetric filling for the LUSI model is shown for the refinement cycles used. The accuracy is increased by one or two order of magnitude for all formations.

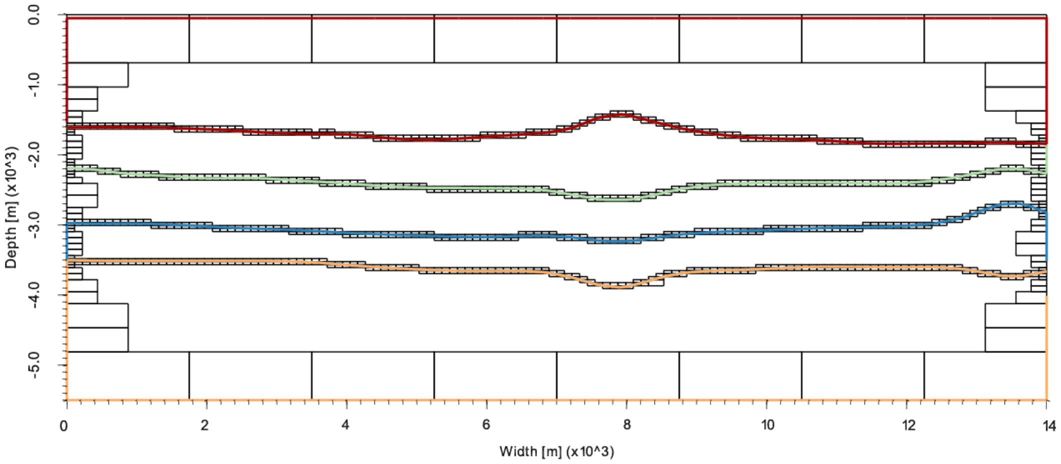

Figure 6.12: The accuracy around the formation boundaries after the 5th and final cycle of refinement is greatly increased as visible in this slice through the model. The achieved accuracy is sufficient for a structured hexahedral approximation of the input geometries.

formations of different sizes as well as folds and faults including offset. Figure 6.13b shows a cross section through the model, were the intersection of multiple faults in a fold is visible. This provides an excellent opportunity to investigate the algorithm's performance in complex settings. The model consists of overall 25 parts which are all included in the meshing procedure.

Due to the high complexity of this model the final discretization includes 1.4 million hexahedral cells. The final result for the whole model and the cross section through the model are shown in figures 6.14 and 6.15 respectively. A visual comparison of the input geometry and the final discretization shows very good agreement. The GeoNE50 geological model was discretized using 4 refinement cycles in HULK. The high complexity of the model prohibits a meaningful volume analysis as performed in the other examples. However, the mean distance to the BSP tree of the corresponding geological formation could be calculated and shown in table 6.3. The overall decrease in the distance indicates a distinct increase in accuracy with later refinement cycles.

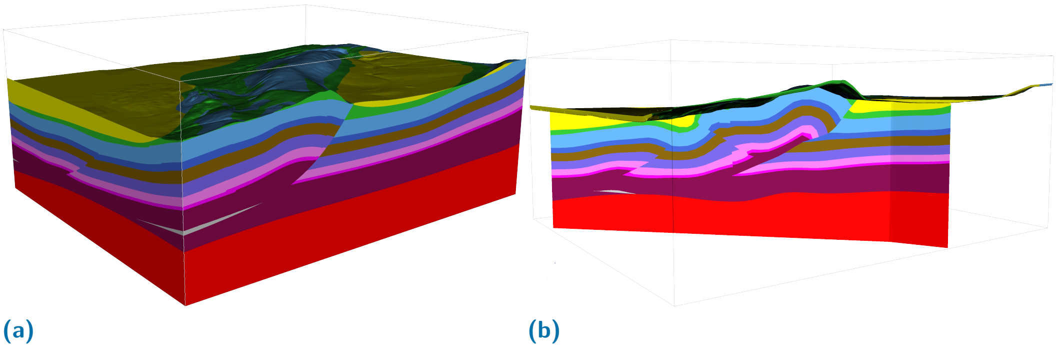
(a) **(b)**

Figure 6.13: The GeoNE model containing 11 formations in a total of 25 parts. a) An outside view of the complete model. b) Cross section through the model showing the complex interior including multiple faults including offset.

This further supports the conclusion of the visual analysis of the final discretization. A detailed comparison on the cross section through the geological model (cf. figure 6.13b) and the discretization (cf. figure 6.15) shows how detailed the hexahedral approximation by *HULK* really is. Although the faults in the model could not be included in the meshing process as they were modeled as 2D surfaces instead of finite width faults, their resulting offset is clearly visible. Overall, all 11 formations were resolved with very good accuracy, capturing also the complex interior with intersecting fault offsets in a folding environment.

Table 6.3: Simple mesh statistics for the GeoNE50 model. The number of cells as well as the distance to the corresponding BSP tree was analyzed for all performed refinement cycles on the complex geological model. The BSP distance indicates an overall increase in mesh accuracy with refinement cycles.

Cycles	Cells	BSP distance (-)
0	32768	1.91
1	40489	2.84
2	135290	2.74
3	459040	1.91
4	1408975	1.20

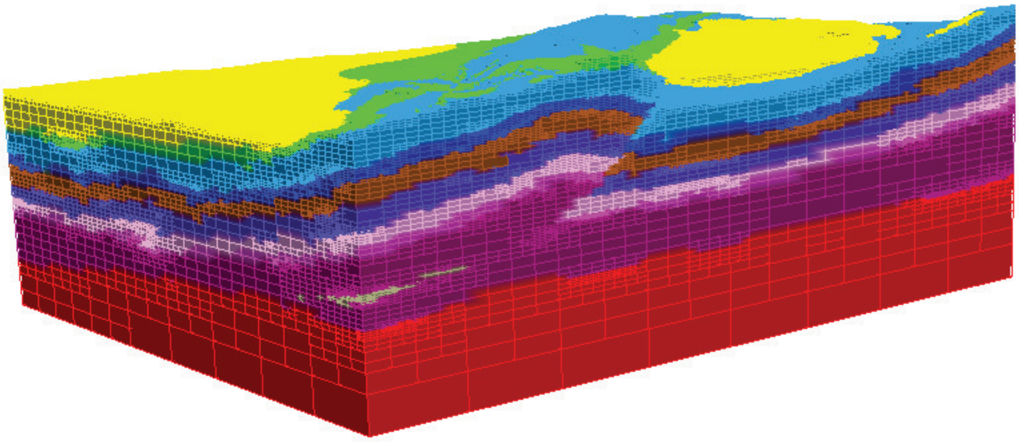

Figure 6.14: The final mesh of the GeoNE50 model after 4 cycles of refinement by HULK and contains 1.4 million cells. All important geometric features of the input geometries are captured and provide a good hexahedral approximation to the initial geometry. Even smaller features such as a small intrusion (shown in gray at the front corner) as well as the very fine quaternary deposits at the top of the model are well-resolved. Dynamic cell size changes are visible especially in vicinity of the large offset fault visible on the right face of the model.

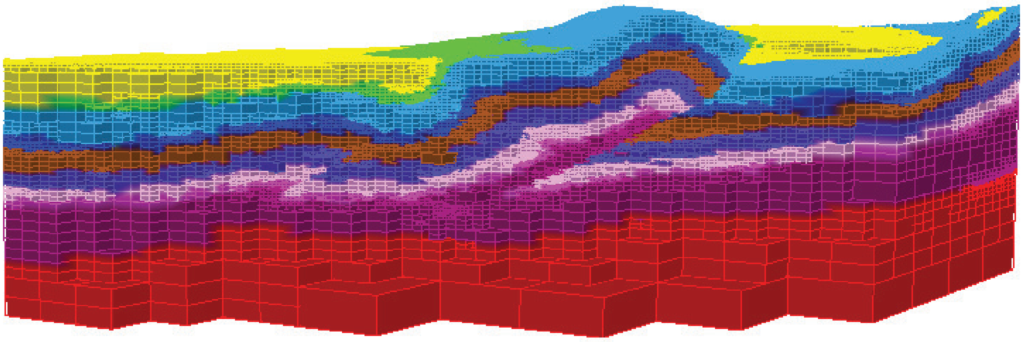

Figure 6.15: Cross section through the complex interior of the final mesh of the GeoNE50 model after 4 cycles of refinement by HULK. The whole model contains roughly 1.4 million hexahedral cells. In comparison with figure 6.13b the accuracy is very good. All three main offset faults visible in the cross section are resolved by the mesh. Solely, a small intrusion (shown in gray in figure6.13b is not resolved by the hexahedral approximation. Note that the adaptivity of the octree mesh is not as clearly visible in this section through the mesh as many complexities have to be resolved, leaving little room for cell number optimization through mesh coarsening.

6.6 Discussion

In the previous section, three models with varying degree of complexity were used. However, in order to evaluate execution timings as well as scalability a more reliable basis needs to be created. To this end the GeoNE model is used. We use the quadric edge collapse decimation technique to reduce and increase the number of triangles in the input geometries while conserving all formations and faults in the model (Hoppe, 1999). The initial model is the GeoNE50 model consisted of roughly 6 million triangles. In the following we will consider two down-sized models (GeoNE25 ~ 3 million and GeoNE13 ~ 1.5 million triangles) as well as one up-sized model GeoNE100 with a total of ~ 12million triangles in the input geometries in addition to the initial GeoNE50 (~ 6 million), LUSI ($\sim 0.5 - 0.8$ million) and Dike (~ 0.2 million triangle models.

6.6.1 Mesh quality

As discussed in section 6.4 the quality of octree based meshes is in general quite good. However, for accurate simulation results the cell size distribution within the model might be important. In order to guarantee high accuracy the maximum level difference between neighboring cells is set to 1. Here we present the distribution of refinement levels for the cells in the different models. Figure 6.16 shows the distributions for all three models presented in the previous section and additionally the largest version of the GeoNE model. In general, smooth distributions are visible for all models, which indicates good quality with respect to the expected numerical accuracy. The dike model's distribution has its peak at the highest level of refinement, which is due to the high curvatures in the input geometry. The effect of the curvature of the input geometries is also visible in the LUSI model that contains only moderate curvatures and which leads to a more widened distribution of the cell sizes within the model. Both GeoNE models show a similar distribution of cell sizes indicating that the resolution of the input geometries - given that it is reasonably good - does not significantly influence the distribution of cell sizes in the final discretization.

The distance to the BSP tree is also an indicator for the accuracy of the discretizations. Figure 6.17 shows the calculated mean distances to the corresponding BSP tree structures for all cells in each refinement step for the dike and GeoNE models. The mean distance is decreasing continuously after the first cycle for the GeoNE models. This is due to the fact that indeed within the first refinement cycle more cells are coarsened than refined, leading to an initial shift in the medium distance towards bigger distances. For the final models the distances are well below the initial distances, indicating the overall increase in accuracy as already indicated by the volumetric deviation and the visible confirmation.

6.6.2 Computing timings

We show the performance and efficiency of the proposed method by a series of execution timings. All simulations were run in serial, single threaded on a Intel Xeon E5-2650 CPU with 2.3GHz clock speed. Figure 6.18 shows the time needed to generate the BSP trees for all models used in this article. The generation of the BSP tree shows a linear scaling with size of the input geometry. Solely for small inputs small deviations from the linear behavior are visible. This in however not related to the BSP tree construction but due to a small computational overhead when generating multiple BSP trees from different geological formations. With increasing size of each formation this overhead is relatively reduced, showing better linear scaling.

The overall timings for the generation of the final discretization for all models is shown in figure 6.19. Output of the final discretization as well as the actual refinement are the main contributors to the overall runtime of the execution. Again, the near-linear scaling of the generation of the BSP trees is visible, particularly for the four GeoNE models. We observe that the time consumed by the refinement procedure does not appear to strongly depend on the size of the BSP tree, and also not strongly dependent on the number of triangles in the input. The figure further shows that the a main contributor to overall execution time is the output. This time is shared also with other mesh generators and needs to be taken into account when comparing execution timings. In general, the execution times range from less than one minute for the simple LUSI model without faults up to about 12 minutes for the largest of the GeoNE models with an overall input size of roughly 12 million triangles.

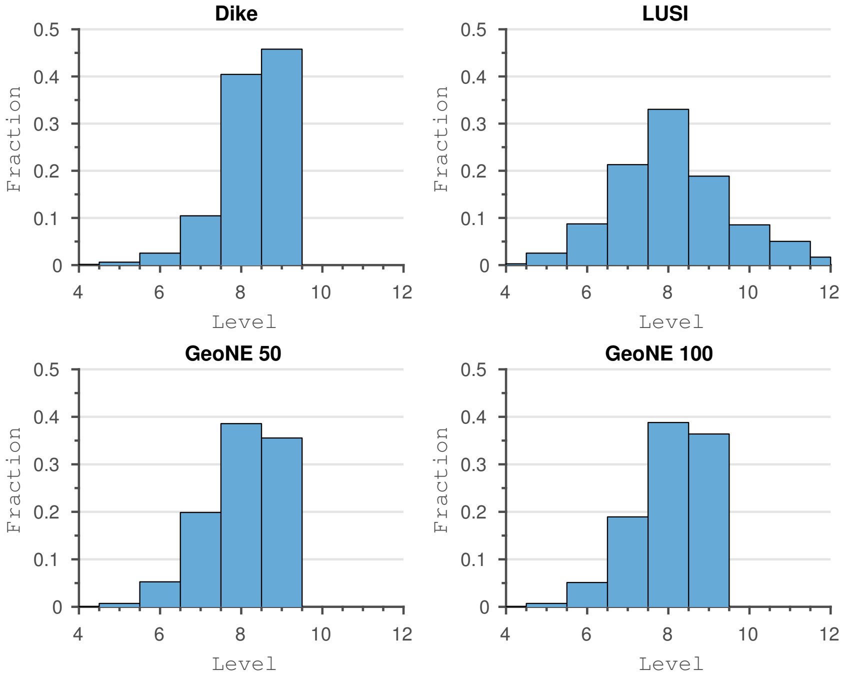

Figure 6.16: Mesh quality analysis based on the refinement level distribution of the cells in four different models. Sharp distributions are likely due to sharp gradients in the input geometries, as for example the dike model. Rather smooth distributions as seen for the LUSI model also indicate rather smooth input geometries.

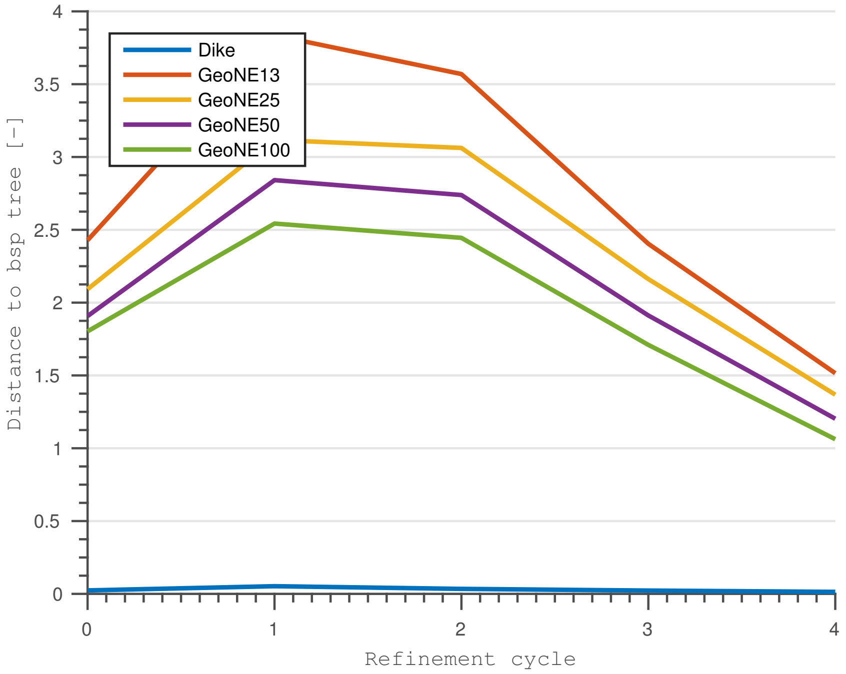

Figure 6.17: The mean distance to the BSP tree is shown for the dike and GeoNE models. The initial increase in distance is caused by a dominating cell coarsening in the first refinement cycle of the GeoNE models. The final discretizations exhibit distances well below the initial value.

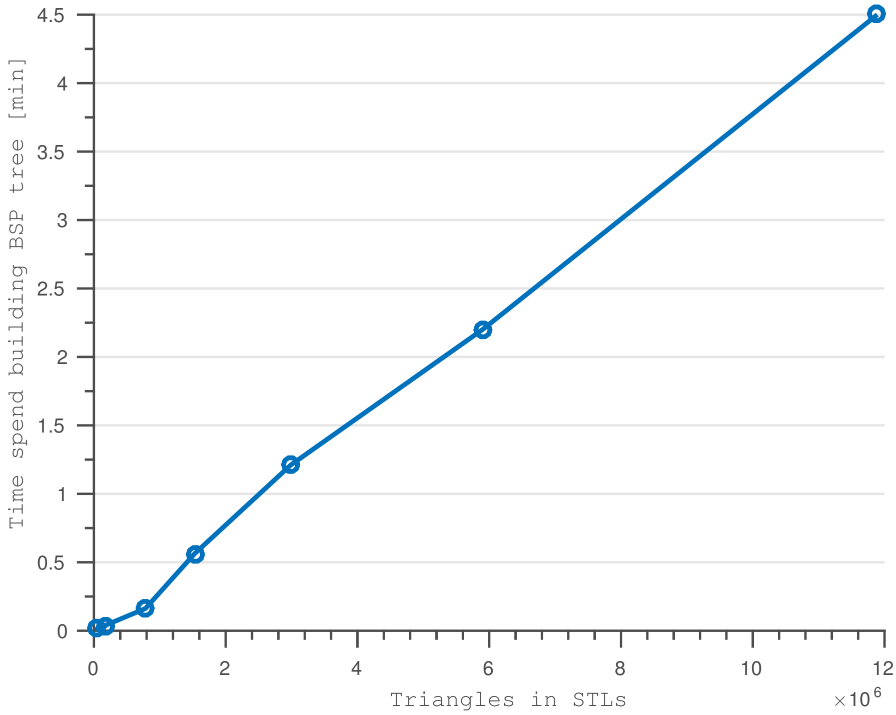

Figure 6.18: The BSP generation shows excellent linear scaling for moderate to large input files. Small input files suffer from a slight computational overhead if multiple BSP trees are generated for a series of geological formations such as the smallest GeoNE model.

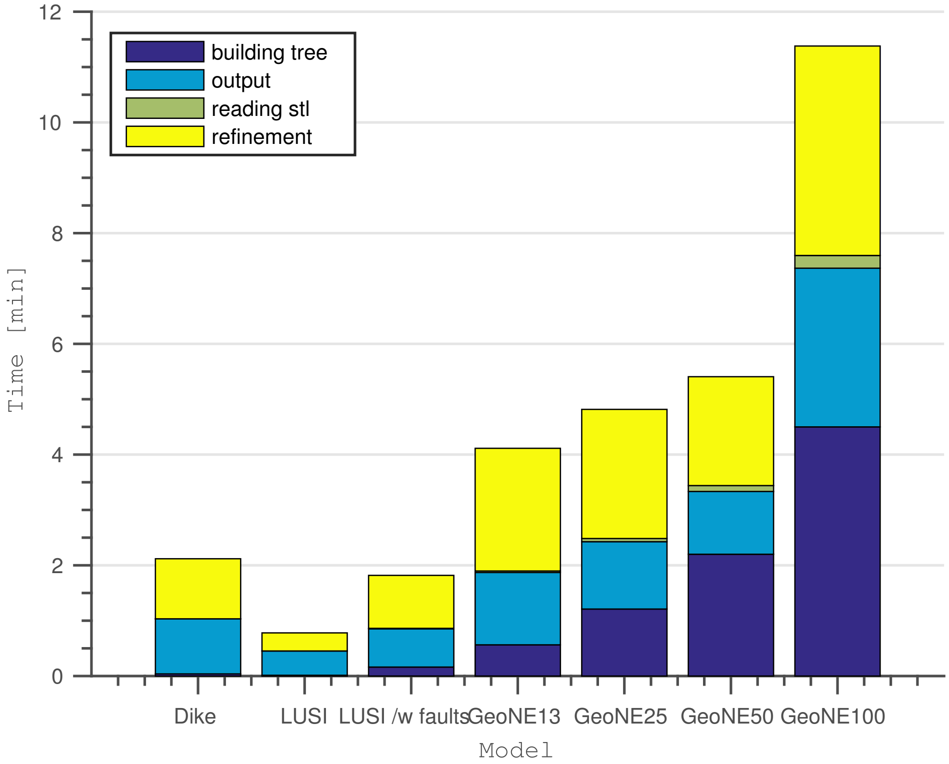

Figure 6.19: Comparison of the execution times of the different models discretized by *HULK*. All models were executed in a single threaded on a Intel Xeon E5-2650 CPU with 2.3 GHz clock speed. The execution time strongly depends on the complexities in the geological model (cf. table 6.1).

It becomes evident that the execution time strongly depends on the complexities in the model. Better refinement criteria might mitigate this effect in the future.

6.6.3 Comparison with uniform refinement

We can further evaluate the efficiency of our refinement technique by comparing the refinement behavior of all models compared to uniform global refinement. The refinement curves in figure 6.20 show the number of cells depending on the refinement cycle. Two theoretical curves for uniform global refinement with different number of initial cells are also shown. It can be seen that the proposed method is effective in terms of refinement cost as both models have a refinement factor much less than the uniform refinement. Nevertheless, the possibility to utilise the algorithm also on a structured grid with uniform refinement is very useful because many reservoir simulators still utilise this type of grid, and where our algorithm can simplify and speed up the grid generation process. In cases where the structured grid is coarse, our algorithm can be interpreted as a very simple upscaling technique mapping the geological domains and properties on the structured grid.

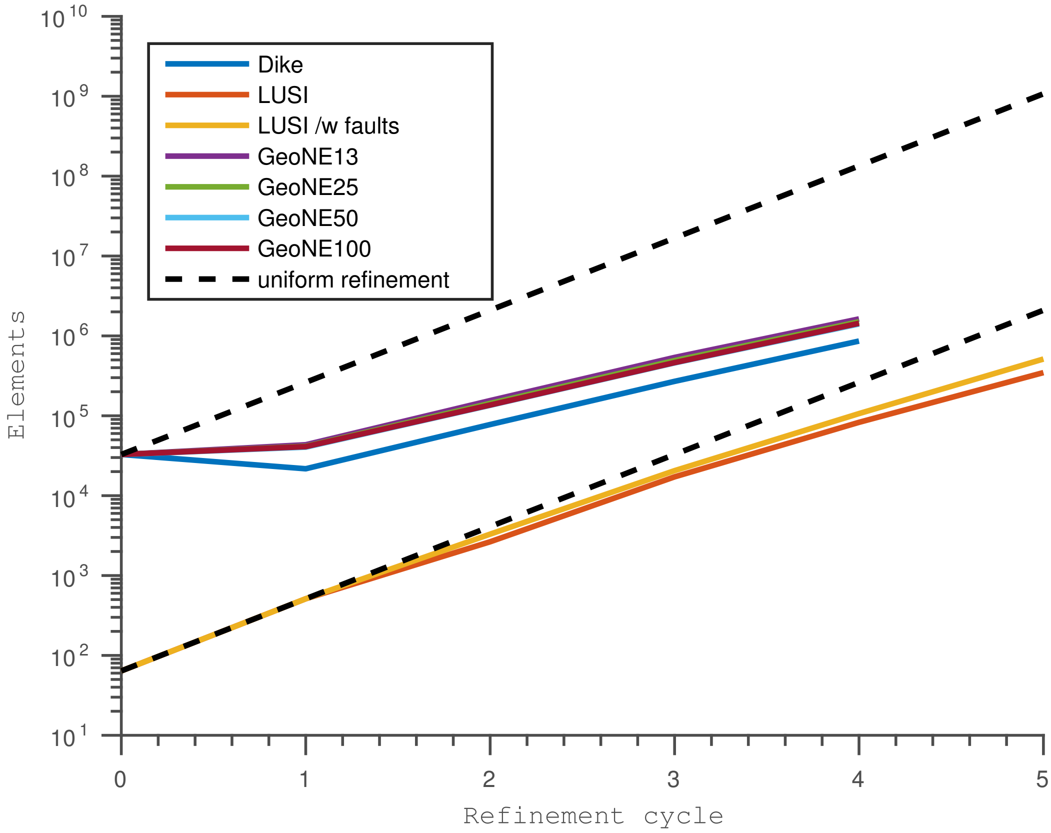

Figure 6.20: Comparing the refinement factor for the models under consideration. The dashed lines represent uniform global refinement. All models show a slope much lower than the unfavorable uniform refinement curve, showing the efficiency of the chosen octree refinement in the algorithm. (Note the logarithmic scale on the y-axis.)

6.7 Conclusion

All three examples demonstrate that the implemented algorithm works very well. The input geometries are reasonably well represented in the hexahedral discretizations. In general the number of cells needed for a satisfying model is on the order of a few hundred thousand to roughly 1.5 million cells. This is quite a large number, but compared to the grid resolution used in classical benchmark models (e.g. Johannsen formation with 149 x 189 x 16 = 450,576 cells and SPE10 with 60 x 220 x 85 = 1,122,000 cells) it is competitive Eigestad et al., 2009; Christie and Blunt, 2001. A common solution strategy for these large full field models is the division into smaller sections and a successive solution of each section. This procedure could also be applied to the mesh constructed by our algorithm if the required number of cells is too big for a full field solution. Nonetheless, state-of-the-art parallel subsurface simulators such as *pflotran* are able to handle large number of elements (Hammond et al., 2014). With the utilization of new programming techniques and the advances in hardware accelerators will enable and promote simulations with multi-million cells. The number of hexahedral cells necessary for the models is also comparable to the number of cells in a corresponding tetrahedral triangulation. To compare against a tetrahedral discretization, we used the open source software *gmsh* and computed a conforming tetrahedral triangulation on each formation of the LUSI model Geuzaine and Remacle, 2009. We find that in this case the number of tetrahedral cells (gmsh: 421,392) needed is even greater than the hexahedral approximation by HULK (346,991). It is important to note that the tetrahedral discretization algorithm builds a conforming mesh which coincides exactly with the input geometry. Thus the quality, namely the number of elements of the input geometries' discretization, is directly linked to the number of cells in the final mesh. In HULK however, the accuracy of the initial boundary description is not directly linked to the number of cells as we are only interested in a good quality non-conforming approximation.

The implemented algorithm could be improved by a technique called *edge-snipping*, which would result in a conforming mesh by moving the outer boundary vertices to the exact position of the input geometry surface. This procedure, however, comes at a high computational effort, and even prohibits some parallelization techniques such as scalable adaptive mesh refinement that performs better on structured octree grids (Burstedde et al., 2011). Therefore it has been omitted in the current work but yields a possible extension of the algorithm for the future.

Accounting for structures in the subsurface using a geological model efficiently helps increase the accuracy of any kind of numerical subsurface simulation. We developed and implemented a fast and efficient hexahedral mesh generator for subsurface simulations. The underlying theory and the simple structure of the algorithm makes it also possible to implement the algorithm directly in the discretization part of other simulation software. However, it can also be used as a stand-alone preprocessing unit. Simulators that use adaptive mesh refinement based on the physics can utilize our method within their simulations to dynamically resolve only those parts of the input geometry that are of interest in the current state of the simulation.

Conclusion

7

> *In theory there is no difference between theory and practice. But, in practice, there is.*
>
> — **Attributed to multiple authors**

Simulation of coupled processes in fractured reservoirs is becoming increasingly important in today's research as it is connected to many applications. These include possible remedies of climate change such as geothermal energy production and CO_2 sequestration. This thesis compiles applied case studies and theoretical-numerical studies of fluid flow and heat transport through fractured systems. The outcome is a fractured reservoir modeling framework that is open source and distributed under the GNU GPL v3.0 license that enables the scientific community to use and modify it according to their needs. The developed model finds application in a broad range of applications in the fractured subsurface. Throughout this thesis the focus has been the investigation of coupled thermo-hydraulic problems including fracture stability analysis in geothermal reservoirs and other naturally fractured systems. Nevertheless, I expect further applications and research opportunities beyond the current model capabilities because the open source code will allow a community to evolve and contribute to this common platform.

The presented studies show that the embedded discrete fracture model is a viable alternative to the existing methods. As numerical discretization is simplified compared to conforming discrete fracture models, dynamic changes of the fracture network are possible without large numerical overhead. Numerical benchmark experiments presented in this thesis validate the model and its capabilities, and demonstrate the accuracy of the implemented *MATLAB* package within the limits of commercial simulators for fractured reservoirs. The results presented in this thesis show further the importance of including the mechanical behavior of fractures and the reservoir in thermo-hydraulic simulations. Although the deformation process during fracture slip was not explicitly taken into account, the assumed step-wise increase in fracture permeability during slip provides the necessary feedback for the pressure equation. In this way the developed model is able to capture the observed increase in injectivity during hydraulic stimulation and inferred permeability increase in natural fluid driven seismicity. Although the model exhibits a very simplified view on the complex fracture mechanics, it still provides important insight into reservoir stimulation that helps in identifying some challenges and opportunities for future studies.
I investigated the role of thermal stress during the stimulation of geothermal reservoirs in a numerical study . The results suggest that thermal stress can facilitate slip

on non-optimally oriented fractures and that thermal stress propagation is largely influenced by the hydraulic properties of both fracture and matrix. Thermal stress is found to be more concentrated and much slower propagating than fluid pressure. Nevertheless, thermal stress changes can exceed fluid pressure and even minimal principal stress, especially close to the well. In the latter case, thermally induced tensile cracks can form, which would lead to an enhanced heat exchange between the matrix and the fluid in the fractures. Two different failure regimes were identified that act on different timescales. The hydraulic failure regime acts on the timescale of days to weeks whereas the thermo-hydraulic regime acts on the scale of weeks to years. Finally, the study shows that thermal stress changes can be significantly larger than the slip-induced Coulomb stress change. This lead to the conclusion that thermal stress changes in the fractured subsurface should be incorporated in models that seek to fully understand fluid injections over long-periods.
The case study of the 2008 Mogul earthquake sequence presents an application of the implemented model to fluid-driven seismicity in a naturally fractured system. The structural, seismic and modeling response supports a scenario where high pressure fluid infiltrates a highly fractured shallow subsurface leading to consecutive and sustained fault slip. The occurrence of multiple hot springs in the region and the analysis of focal mechanisms suggest the presence of excess fluids. The model results present strong evidence for the fluid pressure triggering of the foreshock sequence of the 2008 Mogul sequence. Both the Omori and Gutenberg-Richter laws are satisfied by this sequence, which suggests that similar fluid-driven foreshock sequences may be found elsewhere. This study presents important insight on foreshock sequences and demonstrates the broad range of utility provided by the modeling framework developed in this thesis.

In addition to the numerical model for coupled thermo-hydraulic problems, a novel discretization technique was introduced in this thesis. The algorithm called HULK, short for "Hexahedra from Unique Location in (K)convex Polyhedra", is simple and efficient, and generates hexahedral meshes from generic STL files describing a geological model. Using a geological model efficiently helps to increase the accuracy of numerical subsurface simulations by constraining structures in the subsurface. The three tested geological models with varying complexity demonstrate that the implemented algorithm works very well. In general the number of cells needed for a satisfying model is on the order of a few hundred thousand to roughly 1.5 million cells. Nonetheless, state-of-the-art parallel subsurface simulators such as *pflotran* are able to handle large number of elements (Hammond et al., 2014). The utilization of new programming techniques and the advances in hardware accelerators will enable and promote simulations with multi-million cells in the future.

The numerical modeling framework for coupled thermo-hydraulic simulations distinguishes itself from related works by the included fracture stability analysis that accounts for thermal and porous effects by efficient superposition, a user friendly MATLAB implementation and an open source distribution of the source code. Sanyal et al., (2000) present a review on the state-of-the-art of numerical simulation of enhanced geothermal systems. Although the review does not include the most recent advances EGS modeling, the key features desired in a practical simulator for enhanced geothermal systems remain unchanged. These features include the ability to handle two-phase fluid flow, heat transfer and tracer transport in porous and fractured media, explicit representation of fractures, change in fracture aperture due to effective stress, thermo-elastic effects, a relationship between fracture aperture and fracture conductivity, shear deformation of fractures, channeling of fluid flow within fractures and chemical reaction between water and rock (Sanyal et al., 2000). The majority of these features is included in the current version of the modeling framework delivered with this thesis. However, certain aspects are currently covered in a simplified manner while others are only meaningful in a 3D implementation or are missing altogether. Thus the following final section of this thesis will point out possible research directions and opportunities for future work with the aforementioned desirable features in mind.

Future Work

The numerical modeling framework developed in this thesis uses a simplified approach on the mechanical processes in the reservoir. This can be regarded as one of the biggest advantages and disadvantages of the model at the same time. The simplification allows important insight into reservoir stimulation that helps in identifying challenges and opportunities for more complex models. On the other hand the simplified model allows a very efficient implementation and solution of the coupled thermo-hydraulic equations. Future models might solve the full equilibrium equations to fully resolve the shear deformation process of fractures. However the required degree of complexity of the geomechanical model is still under research and part of the scientific discussion (e.g. Hoedeman and Zee, 2016). In state-of-the-art coupled thermal-hydraulic-mechanical-chemical (THMC) simulations, the geomechanical model requires most of the computational effort (B. Galvan, personal communication, 2017). Nevertheless, more advanced models could consider both pre-existing fractures as in the present work, but also the generation of new fractures and their propagation in response to the evolving stress state from both thermo-and hydraulic perturbations.

While validating the numerical model against a commercial simulator, slight differences in solutions became visible. As discussed earlier the exact source of the deviation remains elusive. This could be addressed in the future using a systematic

study of different numerical advection schemes and the definition of matrix-fracture interface properties between the models. Currently there is no clear indication about what weighting to use at fracture-matrix interfaces, which presents an excellent future research opportunity for combined laboratory and numerical experiments.
Tracer transport is mathematically very similar to heat transport. Therefore, the implementation of a simple tracer transport module is feasible. Additionally, chemical reaction between fluid and rock could either be implemented in terms of a reactive flow module or through the coupling of the model with an external chemical simulator using one of the provided interfaces. Currently there is only single-phase flow available in the model. The extension to a two phase flow model in the future should be envisioned as it will allow the simulation of a broader spectrum of applications. Applications where multiphase flow in fractured systems is considered relevant, include CO_2 sequestration and hydrothermal systems in volcanic environments.
A natural extension of the work presented in this thesis is the efficient implementation of the model in three dimensions. Currently the modeling framework is implemented in *MATLAB*. This enables a broad audience to the developed model without deepened programming knowledge. On the other hand the *MATLAB* platform is not particularly well suited for large scale 3D simulations. Omlin, (2016) presents a promising new approach for the automated transfer of *MATLAB* code to modern parallel computation techniques. However the methodology is not as sophisticated yet as to allow the transfer of my modeling framework. Nevertheless, a manual re-implementation of the model in a high-performance environment based on the *MATLAB* implementation could be efficiently extended to 3D.
Currently the developed fractured reservoir framework is restricted to regular numerical grids. The embedded discrete fracture model can in principle be implemented for general unstructured grids as well. However, using regular grids can be advantageous for the application of modern parallel computation techniques that will be required in a 3D extension of the model.
Finally, the combination of the numerical modeling framework with the mesh generation algorithm presented in this thesis would be desirable in order to facilitate the integration of detailed information about the subsurface in the numerical simulator. As previously mentioned, this would be particularly beneficial for 3D simulations in a high-performance computing environment where a high degree of spatial complexity of the subsurface geology can be resolved.

The different research opportunities presented here may vary in their required effort and complexity. Prioritizing any of the aspects over the others remains to the researcher and largely depends on the focus of the corresponding work and partly personal preferences. In theory all the aforementioned open research directions can be addressed in the future. Ultimately the scientific community as potential users of the open source coupled TH(m) fractured reservoir simulator presented in this thesis will decide on the prevailing research directions.

Bibliography

Abate, A. F., M. Nappi, D. Riccio, and G. Sabatino (2007). „2D and 3D face recognition: A survey“. In: *Pattern Recognition Letters* 28.14, pp. 1885–1906.

Allmendinger, R. W., N. Cardozo, and D. M. Fisher (2011). *Structural geology algorithms: Vectors and tensors*. Cambridge: Cambridge University Press.

Álvarez-Gómez, J. A. (2014). „FMC: a one-liner Python program to manage, classify and plot focal mechanisms“. In: *EGU General Assembly Conference Abstracts*. Vol. 16.

Anderson, J. G. et al. (2009). „Exceptional ground motions recorded during the 26 April 2008 Mw 5.0 earthquake in Mogul, Nevada“. In: *Bulletin of the Seismological Society of America* 99.6, pp. 3475–3486.

Annewandter, R., I. Main, and S. Geiger (2013). „High-Resolution Numerical Simulations of Capillary Trapping of CO2 in Fractured Formations“. In: *SPE Reservoir Characterization and Simulation Conference and Exhibition*. Society of Petroleum Engineers.

Arehart, G. B., M. F. Coolbaugh, and S. R. Poulson (2003). „Evidence for a magmatic source of heat for the Steamboat Springs geothermal system using trace elements and gas geochemistry“. In: *Transactions-Geothermal Resources Council*, pp. 269–274.

Bangerth, W., R. Hartmann, and G. Kanschat (2007). „deal.II – a General Purpose Object Oriented Finite Element Library“. In: *ACM Trans. Math. Softw.* 33.4, pp. 24/1–24/27.

Bangerth, W. et al. (2016). „The deal. II library, version 8.3“. In: *Archive of Numerical Software* 4.100, pp. 1–11.

Bárdossy, G. and J. Fodor (2001). „Traditional and new ways to handle uncertainty in geology“. In: *Natural Resources Research* 10.3, pp. 179–187.

Barenblatt, G., I. P. Zheltov, and I. Kochina (1960). „Basic concepts in the theory of seepage of homogeneous liquids in fissured rocks [strata]“. In: *Journal of applied mathematics and mechanics* 24.5, pp. 1286–1303.

Barton, C. A., M. D. Zoback, and K. L. Burns (1988). „In-situ stress orientation and magnitude at the Fenton Geothermal Site, New Mexico, determined from wellbore breakouts“. In: *Geophysical Research Letters* 15.5, pp. 467–470.

Barton, C. A., M. D. Zoback, and D. Moos (1995). „Fluid flow along potentially active faults in crystalline rock“. In: *Geology* 23.8, pp. 683–686.

Bauer, S. et al. (2012). „Modeling, parameterization and evaluation of monitoring methods for CO_2 storage in deep saline formations: the CO_2-MoPa project“. In: *Environmental Earth Sciences* 67.2, pp. 351–367.

Bear, J. (1972). *Dynamics of Fluids in Porous Media*. Courier Corporation.

Bell, J. W., F. Amelung, and C. D. Henry (2012). „InSAR analysis of the 2008 Reno-Mogul earthquake swarm: Evidence for westward migration of Walker Lane style dextral faulting“. In: *Geophysical Research Letters* 39.18.

Bell, J. W. and L. J. Garside (1987). *Verdi Quadrangle: Geologic Map*. Nevada Bureau of Mines and Geology, University of Nevada-Reno.

Benato, S. and J. Taron (2016). „Desert Peak EGS: Mechanisms influencing permeability evolution investigated using dual-porosity simulator TFReact“. In: *Geothermics* 63, pp. 157–181.

Berkowitz, B. (2002). „Characterizing flow and transport in fractured geological media: A review“. In: *Advances in water resources* 25.8, pp. 861–884.

Bertani, R. (2007). „World geothermal generation in 2007“. In: *GHC Bulletin* 7, p. 19.

— (2016). „Geothermal power generation in the world 2010–2014 update report“. In: *Geothermics* 60, pp. 31–43.

Bodvarsson, G., C. Ho, and B. Robinson (2003). „Yucca mountain project“. In: *Journal of contaminant hydrology* 62-63, Special issue.

Bonham, H. and J. Bell (1993). „Geologic map of the Steamboat Quadrangle“. In: *Nevada: Nevada Bureau of Mines and Geology Map 4Fg* 1.24,000.

Botella, A., B. Lévy, and G. Caumon (2014). „Indirect unstructured hex-dominant mesh generation using tetrahedra recombination“. In: *ECMOR XIV-14th European conference on the mathematics of oil recovery*.

Botella, A., B. Lévy, and G. Caumon (2016). „Indirect unstructured hex-dominant mesh generation using tetrahedra recombination“. In: *Computational Geosciences* 20.3, pp. 437–451.

Bott, M. H. P. (1959). „The mechanics of oblique slip faulting“. In: *Geological Magazine* 96.2, pp. 109–117.

Bower, K. and G. Zyvoloski (1997). „A numerical model for thermo-hydro-mechanical coupling in fractured rock“. In: *International Journal of Rock Mechanics and Mining Sciences* 34.8, pp. 1201–1211.

Breede, K., K. Dzebisashvili, and G. Falcone (2015). „Overcoming challenges in the classification of deep geothermal potential“. In: *Geothermal Energy Science* 3.1, pp. 19–39.

Brown, D. W., D. V. Duchane, G. Heiken, and V. T. Hriscu (2012). *Mining the earth's heat: hot dry rock geothermal energy*. Berlin Heidelberg: Springer Science & Business Media.

Burstedde, C., L. C. Wilcox, and O. Ghattas (2011). „`p4est`: Scalable Algorithms for Parallel Adaptive Mesh Refinement on Forests of Octrees“. In: *SIAM Journal on Scientific Computing* 33.3, pp. 1103–1133.

Byerlee, J. (1978). „Friction of rocks“. In: *Pure and applied Geophysics* 116.4, pp. 615–626.

Cacas, M.-C. et al. (1990). „Modeling fracture flow with a stochastic discrete fracture network: calibration and validation: 1. The flow model“. In: *Water Resources Research* 26.3, pp. 479–489.

Calcagno, P., J.-P. Chilès, G. Courrioux, and A. Guillen (2008). „Geological modelling from field data and geological knowledge: Part I. Modelling method coupling 3D potential-field interpolation and geological rules“. In: *Physics of the Earth and Planetary Interiors* 171.1, pp. 147–157.

Casarotti, E. et al. (2008). „CUBIT and seismic wave propagation based upon the spectral-element method: An advanced unstructured mesher for complex 3D geological media“. In: *Proceedings of the 16th International Meshing Roundtable*. Springer, pp. 579–597.

Cashman, P. H., J. H. Trexler, M. C. Widmer, and S. J. Queen (2012). „Post-2.6 Ma tectonic and topographic evolution of the northeastern Sierra Nevada: The record in the Reno and Verdi basins“. In: *Geosphere*.

Catalli, F., M.-A. Meier, and S. Wiemer (2013). „The role of Coulomb stress changes for injection-induced seismicity: The Basel enhanced geothermal system“. In: *Geophysical Research Letters* 40.1, pp. 72–77.

Chai, T. and R. R. Draxler (2014). „Root mean square error (RMSE) or mean absolute error (MAE)?–Arguments against avoiding RMSE in the literature“. In: *Geoscientific Model Development* 7.3, pp. 1247–1250.

Chan, C. and K. Anastasiou (1997). „An automatic tetrahedral mesh generation scheme by the advancing front method“. In: *Communications in Numerical Methods in Engineering* 13.1, pp. 33–46.

Chen, D. and D. Wyborn (2009). „Habanero field tests in the Cooper Basin, Australia: a proof-of-concept for EGS“. In: *Geothermal Resources Council Transactions* 33.1, pp. 159–164.

Chiarabba, C. et al. (2009). „The 2009 L’Aquila (central Italy) MW6. 3 earthquake: Main shock and aftershocks“. In: *Geophysical Research Letters* 36.18.

Chong, C., A. S. Kumar, and H. Lee (2007). „Automatic mesh-healing technique for model repair and finite element model generation“. In: *Finite Elements in Analysis and Design* 43.15, pp. 1109–1119.

Christie, M., M. Blunt, et al. (2001). „Tenth SPE comparative solution project: A comparison of upscaling techniques“. In: *SPE Reservoir Simulation Symposium*. Society of Petroleum Engineers.

Chueh, C., M. Secanell, W. Bangerth, and N. Djilali (2010). „Multi-level adaptive simulation of transient two-phase flow in heterogeneous porous media“. In: *Computers & fluids* 39.9, pp. 1585–1596.

Chueh, C.-C., N. Djilali, and W. Bangerth (2013). „An H-adaptive operator splitting method for two-phase flow in 3D heterogeneous porous media“. In: *SIAM Journal on Scientific Computing* 35.1, B149–B175.

Clarivate Analytics (2017). *Web of Science citation report for "discrete fracture model"*. `https://apps.webofknowledge.com`. Accessed: 12.12.2017.

Combs, J., S. K. Garg, and J. W. Pritchett (2004). „Geothermal well stimulation technology: a preliminary review“. In: *Geothermal Resources Council Transactions* 28, pp. 207–212.

Comsol Inc. (2017). *COMSOL Multiphysics User's Guide*.

Cooper, H. and G. Simmons (1977). „The effect of cracks on the thermal expansion of rocks". In: *Earth and Planetary Science Letters* 36.3, pp. 404–412.

Coumou, D., S. Matthäi, S. Geiger, and T. Driesner (2008). „A parallel FE–FV scheme to solve fluid flow in complex geologic media". In: *Computers & Geosciences* 34.12, pp. 1697–1707.

Courant, R., E. Isaacson, and M. Rees (1952). „On the solution of nonlinear hyperbolic differential equations by finite differences". In: *Communications on Pure and Applied Mathematics* 5.3, pp. 243–255.

CREGE Laboratoire de Géothermie (2014). *Programme GeoNE-Développement de la géothermie profonde dans le canton de Neuchâtel. Rapport final de la Phase 1*. Tech. rep. Université de Neuchâtel.

Darcy, H. (1856). *Les fontaines publiques de la ville de Dijon: exposition et application...* Victor Dalmont.

Deb, R. and P. Jenny (2016). „Finite volume–based modeling of flow-induced shear failure along fracture manifolds". In: *International Journal for Numerical and Analytical Methods in Geomechanics*.

— (2017). „Modeling of shear failure in fractured reservoirs with a porous matrix". In: *Computational Geosciences* 21.5-6, pp. 1119–1134.

dePolo, C. M., J. G. Anderson, D. M. dePolo, and J. G. Price (1997). „Earthquake Occurrence in the Reno-Carson City Urban Corridor". In: *Seismological Research Letters* 68.3, pp. 401–412.

Dershowitz, W. and C. Fidelibus (1999). „Derivation of equivalent pipe network analogues for three-dimensional discrete fracture networks by the boundary element method". In: *Water Resources Research* 35.9, pp. 2685–2691.

Dietrich, P. et al. (2005). *Flow and transport in fractured porous media*. Springer Science & Business Media.

Du, Q. and D. Wang (2006). „Recent progress in robust and quality Delaunay mesh generation". In: *Journal of Computational and Applied Mathematics* 195.1, pp. 8–23.

Eigestad, G. T. et al. (2009). „Geological modeling and simulation of CO2 injection in the Johansen formation". In: *Computational Geosciences* 13.4, pp. 435–450.

Ericson, C. (2004). *Real-time collision detection*. CRC Press.

Evans, D. D., T. J. Nicholson, and T. C. Rasmussen (2001). „Flow and transport through unsaturated fractured rock". In: *Washington DC American Geophysical Union Geophysical Monograph Series* 42.

Evans, K. F., A. Genter, and J. Sausse (2005). „Permeability creation and damage due to massive fluid injections into granite at 3.5 km at Soultz: 1. Borehole observations". In: *Journal of Geophysical Research: Solid Earth* 110.B4.

Evans, W. C., D. Bergfeld, J. P. McGeehin, J. C. King, and H. Heasler (2010). „Treering 14C links seismic swarm to CO2 spike at Yellowstone, USA". In: *Geology* 38.12, pp. 1075–1078.

Fairley, J., S. Ingebritsen, and R. Podgorney (2010). „Challenges for numerical modeling of enhanced geothermal systems“. In: *Ground water* 48.4, p. 482.

Farrell, J., S. Husen, and R. B. Smith (2009). „Earthquake swarm and b-value characterization of the Yellowstone volcano-tectonic system“. In: *Journal of Volcanology and Geothermal Research* 188.1, pp. 260–276.

Faulkner, D., T. Mitchell, E. Jensen, and J. Cembrano (2011). „Scaling of fault damage zones with displacement and the implications for fault growth processes“. In: *Journal of Geophysical Research: Solid Earth* 116.B5.

Fischer, T. and J. Horálek (2003). „Space-time distribution of earthquake swarms in the principal focal zone of the NW Bohemia/Vogtland seismoactive region: period 1985–2001“. In: *Journal of Geodynamics* 35.1, pp. 125–144.

Flynn, T. and M. Enterprises (2001). „Moana Geothermal Area Reno, Nevada–2001 Update“. In: *Geo-Heat Center Quarterly*.

Flynn, T. and G. Ghusn Jr (1983). *Geologic and hydrologic research on the Moana geothermal system, Washoe County, Nevada*. Tech. rep. Univ. of Nevada, Las Vegas, Reno.

Fridleifsson, I. B. et al. (2008). „The possible role and contribution of geothermal energy to the mitigation of climate change“. In: *IPCC scoping meeting on renewable energy sources, proceedings, Luebeck, Germany*. Vol. 20. 25. Citeseer, pp. 59–80.

Fu, P., S. Johnson, and C. Carrigan (2011). „An explicitly coupled hydro geomechanical model for simulating hydraulic fracturing in complex discrete fracture networks“. In: *International Journal for Numerical and Analytical Methods in Geomechanics*.

Fuchs, H., Z. M. Kedem, and B. F. Naylor (1980). „On Visible Surface Generation by a Priori Tree Structures“. In: *SIGGRAPH Comput. Graph.* 14.3, pp. 124–133.

Garside, L. J. and R. H. Hess (1994). „Nevada geothermal resource use-1993 update“. In: *Geothermal Resources Council Bulletin* 23.2, pp. 47–54.

Garside, L. J. and J. H. Schilling (1979). *Thermal waters of Nevada*. University of Nevada, Reno, NV.

Gaston, D., C. Newman, G. Hansen, and D. Lebrun-Grandie (2009). „MOOSE: A parallel computational framework for coupled systems of nonlinear equations“. In: *Nuclear Engineering and Design* 239.10, pp. 1768–1778.

Gehringer, M. and V. Loksha (2012). „Geothermal handbook: planning and financing power generation“. In: *Washington DC: World Bank Group, Energy Sector Management Assistance Program*.

Geiger, S., T. Driesner, C. A. Heinrich, and S. K. Matthäi (2006). „Multiphase thermohaline convection in the earth's crust: II. Benchmarking and application of a finite element–finite volume solution technique with a NaCl–H2O equation of state“. In: *Transport in Porous Media* 63.3, pp. 435–461.

Geiger-Boschung, S., S. K. Matthäi, J. Niessner, R. Helmig, et al. (2009). „Black-oil simulations for three-component, three-phase flow in fractured porous media“. In: *SPE journal* 14.02, pp. 338–354.

Genter, A., K. Evans, N. Cuenot, D. Fritsch, and B. Sanjuan (2010). „Contribution of the exploration of deep crystalline fractured reservoir of Soultz to the knowledge of enhanced geothermal systems (EGS)“. In: *Comptes Rendus Geoscience* 342.7-8, pp. 502–516.

Geothermie-Schweiz.ch (2018). *Geothermie Nutzungstypen*. `http://geothermie-schweiz.ch/geothermie/geothermie-uebersicht/`. Retrieved 2018-03-28. Accessed 2018-03-28.

Geuzaine, C. and J.-F. Remacle (2009). „Gmsh: A 3-D finite element mesh generator with built-in pre-and post-processing facilities“. In: *International Journal for Numerical Methods in Engineering* 79.11, pp. 1309–1331.

Ghassemi, A. (2012). „A review of some rock mechanics issues in geothermal reservoir development“. In: *Geotechnical and Geological Engineering* 30.3, pp. 647–664.

Ghassemi, A., S. Tarasovs, and A.-D. Cheng (2005). „Integral equation solution of heat extraction-induced thermal stress in enhanced geothermal reservoirs“. In: *International Journal for Numerical and Analytical Methods in Geomechanics* 29.8, pp. 829–844.

Ghassemi, A. and G. S. Kumar (2007). „Changes in fracture aperture and fluid pressure due to thermal stress and silica dissolution/precipitation induced by heat extraction from subsurface rocks“. In: *Geothermics* 36.2, pp. 115–140.

Goertz-Allmann, B. P., A. Goertz, and S. Wiemer (2011). „Stress drop variations of induced earthquakes at the Basel geothermal site“. In: *Geophysical Research Letters* 38.9.

Goertz-Allmann, B. P. and S. Wiemer (2012). „Geomechanical modeling of induced seismicity source parameters and implications for seismic hazard assessment“. In: *Geophysics* 78.1, KS25–KS39.

Gringarten, A. (1980). „Man-made geothermal reservoirs“. In: *Geophysical Aspects of the Energy Problem* 1, pp. 134–158.

Guo, B., P. Fu, Y. Hao, C. A. Peters, and C. R. Carrigan (2016). „Thermal drawdown-induced flow channeling in a single fracture in EGS“. In: *Geothermics* 61, pp. 46–62.

Hagoort, J. et al. (2004). „Ramey’s wellbore heat transmission revisited“. In: *SPE journal* 9.04, pp. 465–474.

Hainzl, S. (2004). „Seismicity patterns of earthquake swarms due to fluid intrusion and stress triggering“. In: *Geophysical Journal International* 159.3, pp. 1090–1096.

Hajibeygi, H., D. Karvounis, and P. Jenny (2011). „A hierarchical fracture model for the iterative multiscale finite volume method“. In: *Journal of Computational Physics* 230.24, pp. 8729–8743.

Hammond, G., P. Lichtner, C. Lu, and R. Mills (2012). „Pflotran: reactive flow & transport code for use on laptops to leadership-class supercomputers“. In: *Groundwater reactive transport models*, pp. 141–159.

Hammond, G., P. Lichtner, and R. Mills (2014). „Evaluating the performance of parallel subsurface simulators: An illustrative example with PFLOTRAN“. In: *Water resources research* 50.1, pp. 208–228.

Hammond, W. C. and W. Thatcher (2007). „Crustal deformation across the Sierra Nevada, northern Walker Lane, Basin and Range transition, western United States measured with GPS, 2000–2004“. In: *Journal of Geophysical Research: Solid Earth* 112.B5.

Hardebeck, J. L. and A. J. Michael (2006). „Damped regional-scale stress inversions: Methodology and examples for southern California and the Coalinga aftershock sequence“. In: *Journal of Geophysical Research: Solid Earth* 111.B11.

Hardebeck, J. L. and P. M. Shearer (2002). „A new method for determining first-motion focal mechanisms“. In: *Bulletin of the Seismological Society of America* 92.6, pp. 2264–2276.

Häring, M. O., U. Schanz, F. Ladner, and B. C. Dyer (2008). „Characterisation of the Basel 1 enhanced geothermal system“. In: *Geothermics* 37.5, pp. 469–495.

Harlow, F. H. and W. E. Pracht (1972). „A theoretical study of geothermal energy extraction“. In: *Journal of geophysical research* 77.35, pp. 7038–7048.

Heinze, T., B. Galvan, and S. A. Miller (2015). „A new method to estimate location and slip of simulated rock failure events“. In: *Tectonophysics* 651, pp. 35–43.

Heinze, T., S. Hamidi, B. Galvan, and S. A. Miller (2017). „Numerical simulation of the 2008 West-Bohemian earthquake swarm“. In: *Tectonophysics* 694, pp. 436–443.

Hickman, S. H. and N. C. Davatzes (2003). „In-situ stress and fracture characterization for planning of an EGS stimulation in the Desert Peak Geothermal Field, Nevada“. In: *Thirty-Fifth Workshop on Geothermal Reservoir Engineering*. Stanford University, Stanford, California.

Hill, D. P. (1977). „A model for earthquake swarms“. In: *Journal of Geophysical Research* 82.8, pp. 1347–1352.

Hill, D. et al. (1993). „Seismicity remotely triggered by the magnitude 7.3 Landers, California, earthquake“. In: *Science* 260.5114, pp. 1617–1623.

Hirano, N., T. Ishibashi, N. Watanabe, A. Okamoto, and N. Tsuchiya (2010). „New concept discrete fracture network model simulator, GeoFlow, and three dimensional channeling flow in fracture network“. In: *Proceedings World Geothermal Congress*.

Hoedeman, G. and W. van der Zee (2016). „How Much Complexity is Needed in Geomechanical Modelling to Get an Accurate Answer?“ In: *78th EAGE Conference and Exhibition 2016*.

Hooijkaas, G. R., A. Genter, and C. Dezayes (2006). „Deep-seated geology of the granite intrusions at the Soultz EGS site based on data from 5km-deep boreholes“. In: *Geothermics* 35.5, pp. 484–506.

Hoppe, H. (1999). „New quadric metric for simplifiying meshes with appearance attributes“. In: *Proceedings of the conference on Visualization'99: celebrating ten years*. IEEE Computer Society Press, pp. 59–66.

Hu, M., M. Veveakis, T. Poulet, and K. Regenauer-Lieb (2017). „Thermo-Hydro-Mechanics in Shear Fracturing in Geothermal Reservoirs“. In: *International Workshop on Bifurcation and Degradation in Geomaterials*. Springer, pp. 327–333.

Hubbert, M. K. and W. W. Rubey (1959). „Role of fluid pressure in mechanics of overthrust faulting I. Mechanics of fluid-filled porous solids and its application to overthrust faulting“. In: *Geological Society of America Bulletin* 70.2, pp. 115–166.

Ibs-von Seht, M., T. Plenefisch, and K. Klinge (2008). „Earthquake swarms in continental rifts—a comparison of selected cases in America, Africa and Europe“. In: *Tectonophysics* 452.1-4, pp. 66–77.

Ichinose, G. A., K. D. Smith, and J. G. Anderson (1998). „Moment tensor solutions of the 1994 to 1996 Double Spring Flat, Nevada, earthquake sequence and implications for local tectonic models“. In: *Bulletin of the Seismological Society of America* 88.6, pp. 1363–1378.

Ingebritsen, S. and C. E. Manning (1999). „Geological implications of a permeability-depth curve for the continental crust“. In: *Geology* 27.12, pp. 1107–1110.

Ishibashi, T., N. Watanabe, T. Tamagawa, and N. Tsuchiya (2015). „Mapping the Preferential Flow Paths within a Fractured Reservoir“. In: *Proceedings World Geothermal Congress*.

Ismail-Zadeh, A. and P. Tackley (2010). *Computational methods for geodynamics*. Cambridge University Press.

Jacquey, A. B. et al. (2016). „Thermo-poroelastic numerical modelling for enhanced geothermal system performance: Case study of the Groß Schönebeck reservoir“. In: *Tectonophysics* 684, pp. 119–130.

Jaeger, J. C., N. G. Cook, and R. Zimmerman (2009). *Fundamentals of rock mechanics*. John Wiley & Sons.

Jakobsdóttir, S., M. Roberts, G. Guđmundsson, H. Geirsson, and R. Slunga (2008). „Earthquake swarms at Upptyppingar, north-east Iceland: A sign of magma intrusion?“ In: *Studia Geophysica et Geodaetica* 52.4, pp. 513–528.

Jansen, G. and S. A. Miller (2017). „On the Role of Thermal Stresses during Hydraulic Stimulation of Geothermal Reservoirs“. In: *Geofluids* 2017.

Jasak, H., A. Jemcov, and Z. Tukovic (2007). „OpenFOAM: A C++ library for complex physics simulations“. In: *International workshop on coupled methods in numerical dynamics*. Vol. 1000, pp. 1–20.

Jing, Y., Z. Jing, J. Willis-Richards, and T. Hashida (2014). „A simple 3-D thermoelastic model for assessment of the long-term performance of the Hijiori deep geothermal reservoir“. In: *Journal of Volcanology and Geothermal Research* 269, pp. 14–22.

Jing, Z., J. Willis-Richards, K. Watanabe, and T. Hashida (2000). „A three-dimensional stochastic rock mechanics model of engineered geothermal systems in fractured crystalline rock“. In: *Journal of Geophysical Research: Solid Earth* 105.B10, pp. 23663–23679.

Johnston, A., L. Kanter, K. Coppersmith, and C. Cornell (1994). *The earthquakes of stable continental regions. Volume 4, Seismicity data sheets (Part 2). Final report*. Tech. rep. Electric Power Research Inst., Palo Alto, CA (United States); Memphis State Univ., TN (United States); Geomatrix Consultants, Inc., San Francisco, CA (United States); Cornell (CA), Portola Valley, CA (United States).

Karimi-Fard, M., L. J. Durlofsky, K. Aziz, et al. (2003). „An efficient discrete fracture model applicable for general purpose reservoir simulators“. In: *SPE Reservoir Simulation Symposium*. Society of Petroleum Engineers.

Karvounis, D., V. Gischig, and S. Wiemer (2014). „EGS probabalistic seismic hazard assessment with 3-D discrete fracture modeling“. In: *Proceedings of the Thirty-Ninth Workshop on Geothermal Reservoir Engineering, Stanford*.

Karvounis, D. C. (2013). „Simulations of enhanced geothermal systems with an adaptive hierarchical fracture representation“. PhD thesis. ETH Zürich.

Karvounis, D. C. and P. Jenny (2016). „Adaptive hierarchical fracture model for enhanced geothermal systems“. In: *Multiscale Modeling & Simulation* 14.1, pp. 207–231.

Karvounis, D. C. and S. Wiemer (2015). „Decision making software for forecasting induced seismicity and thermal energy revenues in enhanced geothermal systems“. In: *Decision Making* 19, p. 25.

Keilegavlen, E. and J. M. Nordbotten (2017). „Finite volume methods for elasticity with weak symmetry“. In: *International Journal for Numerical Methods in Engineering*.

Kelkar, S., G. WoldeGabriel, and K. Rehfeldt (2016). „Lessons learned from the pioneering hot dry rock project at Fenton Hill, USA“. In: *Geothermics* 63, pp. 5–14.

Kelkar, S. et al. (2014). „A simulator for modeling coupled thermo-hydro-mechanical processes in subsurface geological media“. In: *International Journal of Rock Mechanics and Mining Sciences* 70, pp. 569–580.

Kilb, D., J. Gomberg, and P. Bodin (2000). „Triggering of earthquake aftershocks by dynamic stresses“. In: *Nature* 408.6812, p. 570.

Klein, F. W. (1978). *Hypocenter locations program HYPOINVERSE*. US Department of the Interior, Geological Survey.

Kohl, T., D. Bächler, and L. Rybach (2000). „Steps towards a comprehensive thermo-hydraulic analysis of the HDR test site Soultz-sous-Forêts“. In: *Proceedings World Geothermal Congress*. Kyushu-Tohoku Japan, pp. 2671–2676.

Kohl, T. and R. Hopkirk (1995). „“FRACure”—A simulation code for forced fluid flow and transport in fractured, porous rock“. In: *Geothermics* 24.3, pp. 333–343.

Kohl, T. and T. Mégel (2005). „Coupled hydromechanical modelling of the GPK3 reservoir stimulation at the European EGS site SoultsSous-Forets“. In: *PROCEEDINGS, Thirtieth Workshop on Geothermal Reservoir Engineering*. Citeseer.

— (2007). „Predictive modeling of reservoir response to hydraulic stimulations at the European EGS site Soultz-sous-Forêts“. In: *International Journal of Rock Mechanics and Mining Sciences* 44.8, pp. 1118–1131.

Kolditz, O. et al. (2012). *Thermo-hydro-mechanical-chemical processes in fractured porous media: Benchmarks and examples*. Springer.

Kraft, T. et al. (2009). „Enhanced geothermal systems: Mitigating risk in urban areas“. In: *Eos, Transactions American Geophysical Union* 90.32, pp. 273–274.

Kulatilake, P. H., J. Park, P. Balasingam, and R. Morgan (2008). „Quantification of aperture and relations between aperture, normal stress and fluid flow for natural single rock fractures“. In: *Geotechnical and geological engineering* 26.3, pp. 269–281.

Künze, R. and I. Lunati (2012). „An adaptive multiscale method for density-driven instabilities“. In: *Journal of Computational Physics* 231.17, pp. 5557–5570.

Kutun, K., O. I. Tureyen, and A. Satman (1981). „Analysis of Wellhead Production Temperature Derivatives“. In: *Proceedings, 50th Workshop on Geothermal Reservoir Engineering, Stanford university, Stanford California*.

Kwiatek, G., F. Bulut, M. Bohnhoff, and G. Dresen (2014). „High-resolution analysis of seismicity induced at Berlin geothermal field, El Salvador“. In: *Geothermics* 52, pp. 98–111.

Lajaunie, C., G. Courrioux, and L. Manuel (1997). „Foliation fields and 3D cartography in geology: principles of a method based on potential interpolation“. In: *Mathematical Geology* 29.4, pp. 571–584.

Ho-Le, K. (1988). „Finite element mesh generation methods: a review and classification“. In: *Computer-aided design* 20.1, pp. 27–38.

Lee, S. H., M. Lough, and C. Jensen (2001). „Hierarchical modeling of flow in naturally fractured formations with multiple length scales“. In: *Water Resources Research* 37.3, pp. 443–455.

Leonard, B. P. (1979). „A stable and accurate convective modelling procedure based on quadratic upstream interpolation“. In: *Computer methods in applied mechanics and engineering* 19.1, pp. 59–98.

Li, L., S. H. Lee, et al. (2008). „Efficient Field-Scale Simulation of Black Oil in a Naturally Fractured Reservoir Through Discrete Fracture Networks and Homogenized Media“. In: *SPE Reservoir Evaluation & Engineering* 11.04, pp. 750–758.

Li, Q. et al. (2009). „COMSOL Multiphysics: A novel approach to ground water modeling“. In: *Groundwater* 47.4, pp. 480–487.

Lin, M. and S. Gottschalk (1998). „Collision detection between geometric models: A survey“. In: *Proc. of IMA conference on mathematics of surfaces*. Vol. 1, pp. 602–608.

Lindenfeld, M., G. Rümpker, K. Link, D. Koehn, and A. Batte (2012). „Fluid-triggered earthquake swarms in the Rwenzori region, East African Rift—Evidence for rift initiation“. In: *Tectonophysics* 566, pp. 95–104.

Lindsay, M. D., L. Aillères, M. W. Jessell, E. A. de Kemp, and P. G. Betts (2012). „Locating and quantifying geological uncertainty in three-dimensional models: analysis of the Gippsland Basin, southeastern Australia“. In: *Tectonophysics* 546, pp. 10–27.

Lohman, R. B. and J. J. McGuire (2007). „Earthquake swarms driven by aseismic creep in the Salton Trough, California“. In: *Journal of Geophysical Research: Solid Earth* 112.B4.

Löhner, R. (1996). „Progress in grid generation via the advancing front technique“. In: *Engineering with computers* 12.3-4, pp. 186–210.

Lucente, F. P. et al. (2010). „Temporal variation of seismic velocity and anisotropy before the 2009 MW 6.3 L'Aquila earthquake, Italy“. In: *Geology* 38.11, pp. 1015–1018.

Lupi, M., E. Saenger, F. Fuchs, and S. Miller (2013). „Lusi mud eruption triggered by geometric focusing of seismic waves“. In: *Nature Geoscience* 6.8, pp. 642–646.

Majer, E. L. et al. (1990). *Joint seismic, hydrogeological, and geomechanical investigations of a fracture zone in the Grimsel Rock Laboratory, Switzerland*. Tech. rep. Lawrence Berkeley Lab., CA (USA); Nationale Genossenschaft fuer die Lagerung Radioaktiver Abfaelle (NAGRA), Baden (Switzerland).

Majer, E. L. et al. (2007). „Induced seismicity associated with enhanced geothermal systems“. In: *Geothermics* 36.3, pp. 185–222.

Marechal, L. (2001). „A new approach to octree-based hexahedral meshing“. In: *10th International Meshing Roundtable*, pp. 209–221.

Maréchal, L. (2009). „Advances in octree-based all-hexahedral mesh generation: handling sharp features“. In: *Proceedings of the 18th International Meshing Roundtable*. Springer, pp. 65–84.

Martínez-Garzón, P., G. Kwiatek, M. Ickrath, and M. Bohnhoff (2014). „MSATSI: A MATLAB package for stress inversion combining solid classic methodology, a new simplified user-handling, and a visualization tool“. In: *Seismological Research Letters* 85.4, pp. 896–904.

Matthäi, S. K., A. A. Mezentsev, M. Belayneh, et al. (2007a). „Finite element-node-centered finite-volume two-phase-flow experiments with fractured rock represented by unstructured hybrid-element meshes“. In: *SPE Reservoir Evaluation & Engineering* 10.06, pp. 740–756.

Matthäi, S. K. et al. (2007b). „Numerical simulation of multi-phase fluid flow in structurally complex reservoirs“. In: *Geological Society, London, Special Publications* 292.1, pp. 405–429.

Mazzini, A., G. Etiope, and H. Svensen (2012). „A new hydrothermal scenario for the 2006 Lusi eruption, Indonesia. Insights from gas geochemistry“. In: *Earth and Planetary Science Letters* 317, pp. 305–318.

McClure, M. W. and R. N. Horne (2013). *Discrete fracture network modeling of hydraulic stimulation: Coupling flow and geomechanics*. Springer Science & Business Media.

— (2014). „An investigation of stimulation mechanisms in Enhanced Geothermal Systems". In: *International Journal of Rock Mechanics and Mining Sciences* 72, pp. 242–260.

Michael, A. J. (1984). „Determination of stress from slip data: faults and folds". In: *Journal of Geophysical Research: Solid Earth* 89.B13, pp. 11517–11526.

Michael, A. J. (1987). „Use of focal mechanisms to determine stress: a control study". In: *Journal of Geophysical Research: Solid Earth* 92.B1, pp. 357–368.

Miller, S. (2015). „Modeling enhanced geothermal systems and the essential nature of large-scale changes in permeability at the onset of slip". In: *Geofluids* 15.1-2, pp. 338–349.

Miller, S. A. (2013). „The role of fluids in tectonic and earthquake processes". In: *Advances in Geophysics* 54, pp. 1–46.

Miller, S. A. and A. Nur (2000). „Permeability as a toggle switch in fluid-controlled crustal processes". In: *Earth and Planetary Science Letters* 183.1, pp. 133–146.

Miller, S. A. et al. (2004). „Aftershocks driven by a high-pressure CO2 source at depth". In: *Nature* 427.6976, pp. 724–727.

Miller, T. A., V. Vessilinov, P. H. Stauffer, K. Birdsell, and C. W. Gable (2007). „Integration of geologic frameworks in meshing and setup of computational hydrogeologic models, Pajarito Plateau, New Mexico". In: *New Mex. Geol. Soc. Guid. Book, 58th F. Conf. Geol. Jemez Mt. Reg. III*.

Moeck, I., G. Kwiatek, and G. Zimmermann (2009). „Slip tendency analysis, fault reactivation potential and induced seismicity in a deep geothermal reservoir". In: *Journal of Structural Geology* 31.10, pp. 1174–1182.

Moinfar, A. (2013). „Development of an efficient embedded discrete fracture model for 3D compositional reservoir simulation in fractured reservoirs". PhD thesis. University of Texas.

Morris, A., D. A. Ferrill, and D. B. Henderson (1996). „Slip-tendency analysis and fault reactivation". In: *Geology* 24.3, pp. 275–278.

Nehring, N. L. (1980). *Geochemistry of steamboat springs, nevada*. Tech. rep. US Geological Survey,

Nelson, R. (2001). *Geologic analysis of naturally fractured reservoirs*. Houston, Texas: Gulf Professional Publishing.

Nemčok, M., A. Henk, R. A. Gayer, S. Vandycke, and T. M. Hathaway (2002). „Strike-slip fault bridge fluid pumping mechanism: insights from field-based palaeostress analysis and numerical modelling". In: *Journal of Structural Geology* 24.12, pp. 1885–1901.

Nield, D. A. and A. Bejan (2006). *Convection in porous media*. Vol. 3. Springer.

Noir, J. et al. (1997). „Fluid flow triggered migration of events in the 1989 Dobi earthquake sequence of Central Afar“. In: *Geophysical Research Letters* 24.18, pp. 2335–2338.

Norbeck, J. H., M. W. McClure, J. W. Lo, and R. N. Horne (2016). „An embedded fracture modeling framework for simulation of hydraulic fracturing and shear stimulation“. In: *Computational Geosciences* 20.1, pp. 1–18.

Norbeck, J., H. Huang, R. Podgorney, and R. Horne (2014). „An integrated discrete fracture model for description of dynamic behavior in fractured reservoirs“. In: *Proceedings of the 39th Workshop on Geothermal Reservoir Engineering, Stanford*.

Nur, A. and J. R. Booker (1972). „Aftershocks caused by pore fluid flow?“ In: *Science* 175.4024, pp. 885–887.

Oikawa, Y. and T. Yamaguchi (2000). „Stress measurement using rock core in an HDR field“. In: *Proceedings of World Geothermal Congress*, pp. 3819–3822.

Omlin, S. (2016). „Development of massively parallel near peak performance solvers for three-dimensional geodynamic modelling“. PhD thesis. Universtiy of Lausanne.

O’Sullivan, M. J., K. Pruess, and M. J. Lippmann (2001). „State of the art of geothermal reservoir simulation“. In: *Geothermics* 30.4, pp. 395–429.

Owen, S. J. and T. R. Shelton. „Evaluation of grid-based hex meshes for solid mechanics“. In: *Engineering with Computers*, pp. 1–15.

Paluszny, A. and S. K. Matthäi (2009). „Numerical modeling of discrete multi-crack growth applied to pattern formation in geological brittle media“. In: *International Journal of Solids and Structures* 46.18, pp. 3383–3397.

Parotidis, M., E. Rothert, and S. Shapiro (2003). „Pore-pressure diffusion: A possible triggering mechanism for the earthquake swarms 2000 in Vogtland/NW-Bohemia, central Europe“. In: *Geophysical research letters* 30.20.

Peaceman, D. W. et al. (1978). „Interpretation of well-block pressures in numerical reservoir simulation (includes associated paper 6988)“. In: *Society of Petroleum Engineers Journal* 18.03, pp. 183–194.

Pearson, C. F., M. C. Fehler, and J. N. Albright (1983). „Changes in compressional and shear wave velocities and dynamic moduli during operation of a hot dry rock geothermal system“. In: *Journal of Geophysical Research: Solid Earth* 88.B4, pp. 3468–3475.

Pluimers, S. (2015). „Hierarchical Fracture Modeling Approach“. MA thesis. TU Delft, Delft University of Technology.

Podgorney, R., H. Huang, and D. Gaston (2010a). „A fully coupled, implicit, finite element model for simultaneously solving multiphase fluid flow, heat transport, and rock de-formation“. In: *Geotherm Resour Counc Trans* 34, pp. 427–432.

Podgorney, R., H. Huang, and D. Gaston (2010b). *Massively parallel fully coupled implicit modeling of coupled thermal-hydrological-mechanical processes for enhanced geothermal system reservoirs*. Tech. rep. Idaho National Laboratory (INL).

Pruess, K. (1991). *TOUGH2: A general-purpose numerical simulator for multiphase fluid and heat flow*. Lawrence Berkeley Lab. Berekeley, California.

— (2004). „The TOUGH codes—a family of simulation tools for multiphase flow and transport processes in permeable media“. In: *Vadose Zone Journal* 3.3, pp. 738–746.

Pruess, K., C. Oldenburg, and G. Moridis (1999). *TOUGH2 User's Guide Version 2*. Lawrence Berkeley National Laboratory.

Quinao, J. J. D. and S. J. Zarrouk (2018). „Geothermal resource assessment using Experimental Design and Response Surface Methods: The Ngatamariki geothermal field, New Zealand“. In: *Renewable Energy* 116, pp. 324–334.

Ramey, H. et al. (1962). „Wellbore heat transmission“. In: *Journal of Petroleum Technology* 14.04, pp. 427–435.

Ramey, H. (1964). „How to calculate heat transmission in hot fluid injection“. In: *Pet. Eng* 36, p. 110.

— (1981). *Reservoir Engineering Assessment of Geothermal Systems*. Tech. rep. Department of Petroleum Engineering, Stanford university.

Richter, D. and G. Simmons (1974). „Thermal expansion behavior of igneous rocks“. In: *International Journal of Rock Mechanics and Mining Sciences & Geomechanics Abstracts*. Vol. 11. 10. Elsevier, pp. 403–411.

Roe, P. L. (1986). „Characteristic-based schemes for the Euler equations“. In: *Annual review of fluid mechanics* 18.1, pp. 337–365.

Rohner, E., S. Bassetti, and T. Kohl (2005). „New large geothermal storage project in Zurich/Switzerland for heating and cooling“. In: *Proceedings of the World Geothermal Congress*.

Romm, E. (1966). „Flow characteristics of fractured rocks“. In: *Nedra, Moscow* 283.

Ruhl, C. J., T. Seaman, K. Smith, and G. Kent (2016a). „Seismotectonic and seismic hazard implications for the Reno-Tahoe area of the Walker Lane in Nevada and California“. In: *AEG Special Volume on Applied Geology in California*, pp. 879–895.

Ruhl, C., S. L. Bilek, and J. Stankova-Pursley (2010). „Relocation and characterization of the August 2009 microearthquake swarm above the Socorro magma body in the central Rio Grande Rift“. In: *Geophysical Research Letters* 37.23.

Ruhl, C., R. Abercrombie, and K. Smith (2017). „Spatiotemporal Variation of Stress Drop During the 2008 Mogul, Nevada, Earthquake Swarm“. In: *Journal of Geophysical Research: Solid Earth*.

Ruhl, C., R. Abercrombie, K. Smith, and I. Zaliapin (2016b). „Complex spatiotemporal evolution of the 2008 Mw 4.9 Mogul earthquake swarm (Reno, Nevada): Interplay of fluid and faulting“. In: *Journal of Geophysical Research: Solid Earth* 121.11, pp. 8196–8216.

Rutqvist, J., Y.-S. Wu, C.-F. Tsang, and G. Bodvarsson (2002). „A modeling approach for analysis of coupled multiphase fluid flow, heat transfer, and deformation in fractured porous rock“. In: *International Journal of Rock Mechanics and Mining Sciences* 39.4, pp. 429–442.

Rutqvist, J. et al. (2009). „A comparative simulation study of coupled THM processes and their effect on fractured rock permeability around nuclear waste repositories“. In: *Environmental Geology* 57.6, pp. 1347–1360.

Rybach, L. (2010). „“The Future of Geothermal Energy” and Its Challenges“. In: *Proceedings of World Geothermal Congress*.

Saeid, S., R. Al-Khoury, and F. Barends (2013). „An efficient computational model for deep low-enthalpy geothermal systems“. In: *Computers & geosciences* 51, pp. 400–409.

Sandve, T., I. Berre, and J. Nordbotten (2012). „An efficient multi-point flux approximation method for Discrete Fracture–Matrix simulations“. In: *Journal of Computational Physics* 231.9, pp. 3784–3800.

Sanyal, S. K., S. J. Butler, D. Swenson, and B. Hardeman (2000). „Review of the State-of-the-Art of numerical simulation of enhanced geothermal systems“. In: *Proceedings of World Geothermal Congress*.

Sarda, S., L. Jeannin, B. Bourbiaux, et al. (2001). „Hydraulic characterization of fractured reservoirs: simulation on discrete fracture models“. In: *SPE Reservoir Simulation Symposium*. Society of Petroleum Engineers.

Satman, A. and O. I. Tureyen (2016). „Geothermal wellbore heat transmission: Stabilization times for “static” and “transient” wellbore temperature profiles“. In: *Geothermics* 64, pp. 482–489.

Sawolo, N., E. Sutriono, B. P. Istadi, and A. B. Darmoyo (2009). „The LUSI mud volcano triggering controversy: Was it caused by drilling?“ In: *Marine and Petroleum Geology* 26.9, pp. 1766–1784.

Scheibach, R. B. (1975). „Geothermal occurrences in Truckee Meadows, Washoe County, Nevada“. PhD thesis. University of Nevada, Reno.

Scheidegger, A. et al. (1974). *The physics of flow through porous media*. 3rd ed. University Of Toronto Press: London.

Schneiders, R. (1996). „A grid-based algorithm for the generation of hexahedral element meshes“. In: *Engineering with computers* 12.3-4, pp. 168–177.

— (1997). „An algorithm for the generation of hexahedral element meshes based on an octree technique“. In: *6th International Meshing Roundtable*, pp. 195–196.

Schoenball, M., C. Baujard, T. Kohl, and L. Dorbath (2012). „The role of triggering by static stress transfer during geothermal reservoir stimulation“. In: *Journal of Geophysical Research: Solid Earth* 117.B9.

Scott, M. A., M. N. Earp, S. E. Benzley, and M. B. Stephenson (2005). „Adaptive sweeping techniques“. In: *Proceedings of the 14th International Meshing Roundtable*. Springer, pp. 417–432.

Scott, S., T. Driesner, and P. Weis (2015). „Geologic controls on supercritical geothermal resources above magmatic intrusions“. In: *Nature communications* 6.

— (2016). „The thermal structure and temporal evolution of high-enthalpy geothermal systems“. In: *Geothermics* 62, pp. 33–47.

Segall, P. and J. R. Rice (1995). „Dilatancy, compaction, and slip instability of a fluid-infiltrated fault“. In: *Journal of Geophysical Research: Solid Earth* 100.B11, pp. 22155–22171.

Shakiba, M. (2014). „Modeling and simulation of fluid flow in naturally and hydraulically fractured reservoirs using embedded discrete fracture model (EDFM)“. PhD thesis. University of Texas.

Shapiro, S. and C. Dinske (2009). „Fluid-induced seismicity: Pressure diffusion and hydraulic fracturing“. In: *Geophysical Prospecting* 57.2, pp. 301–310.

Shapiro, S. A., E. Huenges, and G. Borm (1997). „Estimating the crust permeability from fluid-injection-induced seismic emission at the KTB site“. In: *Geophysical Journal International* 131.2.

Shelly, D. R. and D. P. Hill (2011). „Migrating swarms of brittle-failure earthquakes in the lower crust beneath Mammoth Mountain, California“. In: *Geophysical Research Letters* 38.20.

Shelly, D. R., T. Taira, S. G. Prejean, D. P. Hill, and D. S. Dreger (2015). „Fluid-faulting interactions: Fracture-mesh and fault-valve behavior in the February 2014 Mammoth Mountain, California, earthquake swarm“. In: *Geophysical Research Letters* 42.14, pp. 5803–5812.

Shelly, D. R. et al. (2013). „A fluid-driven earthquake swarm on the margin of the Yellowstone caldera“. In: *Journal of Geophysical Research: Solid Earth* 118.9, pp. 4872–4886.

Al-Shemmeri, T. (2012). *Engineering Fluid Mechanics*. London: Bookboon.

Shephard, M. S. and M. K. Georges (1991). „Automatic three-dimensional mesh generation by the finite octree technique“. In: *International Journal for Numerical methods in engineering* 32.4, pp. 709–749.

Sherburn, S. (1984). „Seismic monitoring during a cold water injection experiment, Wairakei Geothermal Field: preliminary results“. In: *Proc. 6th New Zealand Geothermal Workshop*. Vol. 6, pp. 129–133.

Sibson, R. H. (1996). „Structural permeability of fluid-driven fault-fracture meshes“. In: *Journal of Structural Geology* 18.8, pp. 1031–1042.

Sibson, R. H. (2007). „An episode of fault-valve behaviour during compressional inversion?—The 2004 M J 6.8 Mid-Niigata Prefecture, Japan, earthquake sequence“. In: *Earth and Planetary Science Letters* 257.1, pp. 188–199.

— (2009). „Rupturing in overpressured crust during compressional inversion—the case from NE Honshu, Japan“. In: *Tectonophysics* 473.3, pp. 404–416.

Skalbeck, J. D., L. Shevenell, and M. C. Widmer (2002). „Mixing of thermal and non-thermal waters in the Steamboat Hills area, Nevada, USA“. In: *Geothermics* 31.1, pp. 69–90.

Smith, K. D., G. M. Kent, D. P. Seggern, N. W. Driscoll, and A. Eisses (2016). „Evidence for Moho-lower crustal transition depth diking and rifting of the Sierra Nevada microplate“. In: *Geophysical Research Letters* 43.20.

Smith, K. D. et al. (2004). „Evidence for deep magma injection beneath Lake Tahoe, Nevada-California“. In: *science* 305.5688, pp. 1277–1280.

Smits, B. (2005). „Efficiency Issues for Ray Tracing“. In: *ACM SIGGRAPH 2005 Courses*. SIGGRAPH ’05. Los Angeles, California: ACM.

Stark, M. (1990). „Imaging injected water in The Geysers reservoir using microearthquake data“. In: *Geothermal Resources Council Trans* 14, pp. 1697–1704.

Stearns, N. D., H. T. Stearns, and G. A. Waring (1937). *Thermal springs in the United States*. Vol. 679. US Government Printing Office.

Stewart, J. (1988). „Tectonics of the Walker Lane belt, western Great Basin: Mesozoic and Cenozoic deformation in a zone of shear“. In: *Metamorphism and crustal evolution of the western United States* 7, pp. 683–713.

Strack, O. D. (1982). *Analytic modeling of flow in a permeable fissured medium*. Tech. rep.

Stupazzini, M. (2004). „A spectral element approach for 3D dynamic soil-structure interaction problems“. PhD thesis.

Sun, H., R. Feistel, M. Koch, and A. Markoe (2008). „New equations for density, entropy, heat capacity, and potential temperature of a saline thermal fluid“. In: *Deep Sea Research Part I: Oceanographic Research Papers* 55.10, pp. 1304–1310.

Surpless, B. (2008). „Modern strain localization in the central Walker Lane, western United States: Implications for the evolution of intraplate deformation in transtensional settings“. In: *Tectonophysics* 457.3, pp. 239–253.

Taron, J., D. Elsworth, and K.-B. Min (2009). „Numerical simulation of thermal-hydrologic-mechanical-chemical processes in deformable, fractured porous media“. In: *International Journal of Rock Mechanics and Mining Sciences* 46.5, pp. 842–854.

Ţene, M., S. B. Bosma, M. S. Al Kobaisi, and H. Hajibeygi (2017). „Projection-based Embedded Discrete Fracture Model (pEDFM)“. In: *Advances in Water Resources* 105, pp. 205–216.

Tenma, N., T. Yamaguchi, K. Tezuka, Y. Oikawa, and G. Zyvoloski (2001). „Comparison of heat extraction from production wells in the shallow and the deep reservoirs at the Hijiori HDR test site using FEHM code“. In: *Proc. 26th Stanford Workshop on Geothermal Res. Eng., Jan*.

Tenma, N., K. Yasukawa, and G. Zyvoloski (2003). „Model study of the thermal storage system by FEHM code“. In: *Geothermics* 32.4, pp. 603–607.

Terakawa, T., A. Zoporowski, B. Galvan, and S. A. Miller (2010). „High-pressure fluid at hypocentral depths in the L’Aquila region inferred from earthquake focal mechanisms“. In: *Geology* 38.11, pp. 995–998.

Tester, J. W. et al. (2006). *The future of geothermal energy: Impact of enhanced geothermal systems (EGS) on the United States in the 21st century*. Tech. rep. Massachusetts Institute of Technology.

Thompson, G. A. and D. E. White (1964). *Regional geology of the Steamboat Springs area, Washoe County, Nevada*. Tech. rep.

Thore, P., A. Shtuka, M. Lecour, T. Ait-Ettajer, and R. Cognot (2002). „Structural uncertainties: Determination, management, and applications“. In: *Geophysics* 67.3, pp. 840–852.

Toda, S., R. S. Stein, G. C. Beroza, and D. Marsan (2012). „Aftershocks halted by static stress shadows“. In: *Nature Geoscience* 5.6, p. 410.

Trefry, M. G. and C. Muffels (2007). „FEFLOW: A Finite-Element Ground Water Flow and Transport Modeling Tool“. In: *Groundwater* 45.5, pp. 525–528.

Tsang, Y. W. and C. Tsang (1987). „Channel model of flow through fractured media“. In: *Water Resources Research* 23.3, pp. 467–479.

Tu, T. and D. R. O’Hallaron (2004). „Extracting hexahedral mesh structures from balanced linear octrees“. In: *13th International Meshing Roundtable*.

Ucar, E., I. Berre, and E. Keilegavlen (2017). „Post-injection normal closure of fractures as a mechanism for induced seismicity“. In: *arXiv preprint:1705.02986*.

Ucar, E., E. Keilegavlen, I. Berre, and J. M. Nordbotten (2016). „Finite Volume Discretization for the Deformation of Fractured Media“. In: *arXiv preprint arXiv:1612.06594*.

Utsu, T. (1961). „A statistical study on the occurrence of aftershocks“. In: *Geophys. Mag.* 30, pp. 521–605.

Vitel, S., L. Souche, et al. (2007). „Unstructured upgridding and transmissibility upscaling for preferential flow paths in 3D fractured reservoirs“. In: *SPE Reservoir Simulation Symposium*. Society of Petroleum Engineers.

Vogler, D., R. Settgast, C. Annavarapu, P. Bayer, and F. Amann (2016). „Hydro-Mechanically Coupled Flow through Heterogeneous Fractures“. In: *PROCEEDINGS, 41st Workshop on Geothermal Reservoir Engineering*.

Waldhauser, F., D. P. Schaff, T. Diehl, and E. R. Engdahl (2012). „Splay faults imaged by fluid-driven aftershocks of the 2004 Mw 9.2 Sumatra-Andaman earthquake“. In: *Geology* 40.3, pp. 243–246.

Wallace, R. E. (1951). „Geometry of shearing stress and relation to faulting“. In: *The journal of Geology* 59.2, pp. 118–130.

Wang, H., B. Bonner, S. Carlson, B. Kowallis, and H. Heard (1989). „Thermal stress cracking in granite“. In: *Journal of Geophysical Research: Solid Earth* 94.B2, pp. 1745–1758.

Wang, J. (1991). „Flow and transport in fractured rocks“. In: *Reviews of Geophysics* 29.S1, pp. 254–262.

Wang, Z., W. Huang, D. Zhao, and S. Pei (2012). „Mapping the Tohoku forearc: Implications for the mechanism of the 2011 East Japan earthquake (Mw 9.0)“. In: *Tectonophysics* 524, pp. 147–154.

Waring, G. A. and R. R. Blankenship (1965). *Thermal Springs of the United States and Other Countries: A Summary*. Vol. 492. US Government Printing Office, 833pp.

Wei, S. et al. (2015). „The 2012 Brawley swarm triggered by injection-induced aseismic slip“. In: *Earth and Planetary Science Letters* 422, pp. 115–125.

Weis, P., T. Driesner, D. Coumou, and S. Geiger (2014). „Hydrothermal, multiphase convection of H2O-NaCl fluids from ambient to magmatic temperatures: a new numerical scheme and benchmarks for code comparison“. In: *Geofluids* 14.3, pp. 347–371.

Wellmann, J. F., S. Finsterle, and A. Croucher (2014). „Integrating structural geological data into the inverse modelling framework of iTOUGH2“. In: *Computers & Geosciences* 65, pp. 95–109.

Wesnousky, S. G., J. M. Bormann, C. Kreemer, W. C. Hammond, and J. N. Brune (2012). „Neotectonics, geodesy, and seismic hazard in the Northern Walker Lane of Western North America: Thirty kilometers of crustal shear and no strike-slip?“ In: *Earth and Planetary Science Letters* 329, pp. 133–140.

Whitaker, S. (1966). „The equations of motion in porous media“. In: *Chemical Engineering Science* 21.3, pp. 291–300.

White, D. E. (1964). *Rocks, structures, and geologic history of Steamboat Springs thermal area, Washoe County, Nevada*. US Geol. Surv., Washington, DC.

White, D. E. (1968). *Hydrology, activity, and heat flow of the Steamboat Springs thermal system, Washoe County, Nevada*. US Government Printing Office.

White, M. D. and B. R. Phillips (2015). „Code comparison study fosters confidence in the numerical simulation of enhanced geothermal systems“. In: *Fortieth workshop on geothermal reservoir engineering, Stanford University, Stanford, CA*.

Willis-Richards, J. and T. Wallroth (1995). „Approaches to the modelling of HDR reservoirs: a review“. In: *Geothermics* 24.3, pp. 307–332.

Willmott, C. J. and K. Matsuura (2005). „Advantages of the mean absolute error (MAE) over the root mean square error (RMSE) in assessing average model performance“. In: *Climate research* 30.1, pp. 79–82.

Witherspoon, P. A., J. S. Wang, K. Iwai, and J. E. Gale (1980). „Validity of cubic law for fluid flow in a deformable rock fracture“. In: *Water resources research* 16.6, pp. 1016–1024.

Wong, T.-f. and W. Brace (1979). „Thermal expansion of rocks: some measurements at high pressure“. In: *Tectonophysics* 57.2, pp. 95–117.

Wu, Y.-S. and K. Pruess (2000). „Numerical simulation of non-isothermal multiphase tracer transport in heterogeneous fractured porous media“. In: *Advances in Water Resources* 23.7, pp. 699–723.

Xia, Y., R. Podgorney, and H. Huang (2017). „Assessment of a hybrid continuous/discontinuous Galerkin finite element code for geothermal reservoir simulations“. In: *Rock Mechanics and Rock Engineering* 50.3, pp. 719–732.

Xie, L., K.-B. Min, and Y. Song (2015). „Observations of hydraulic stimulations in seven enhanced geothermal system projects“. In: *Renewable Energy* 79, pp. 56–65.

Xing, H., W. Yu, and J. Zhang (2009). „3D mesh generation in geocomputing“. In: *Advances in Geocomputing*. Springer, pp. 27–64.

Xu, C. and P. Dowd (2010). „A new computer code for discrete fracture network modelling“. In: *Computers & Geosciences* 36.3, pp. 292–301.

Xu, Y. et al. (2015). „Implementation and application of the embedded discrete fracture model (EDFM) for reservoir simulation in fractured reservoirs“. PhD thesis. University of Texas.

Yerry, M. A. and M. S. Shephard (1984). „Automatic three-dimensional mesh generation by the modified-octree technique“. In: *International Journal for Numerical Methods in Engineering* 20.11, pp. 1965–1990.

Yu, W., K. Zhang, and X. Li (2015). „Recent algorithms on automatic hexahedral mesh generation“. In: *Computer Science Education (ICCSE), 2015 10th International Conference on*, pp. 697–702.

Zehner, B., O. Hellwig, M. Linke, I. Görz, and S. Buske (2015). „A Method for Converting Triangle-Mesh-Based 3D Geological Models into Hexahedral Grids for Parallel Finite Difference Simulation.“ In: *35th Gocad Meeting - 2015 RING Meeting*. ASGA.

Zyvoloski, G. (2007). *FEHM: A control volume finite element code for simulating subsurface multi-phase multi-fluid heat and mass transfer*. Tech. rep. Los Alamos Unclassified Report LA-UR-07-3359.